

İSTANBUL TECHNICAL UNIVERSITY ★ GRADUATE SCHOOL OF SCIENCE
ENGINEERING AND TECHNOLOGY

**SYNTHESIS AND CHARACTERIZATION OF HAFNIUM BORIDE-BASED
CERAMIC POWDERS**



Ph.D. THESIS

Nazlı AKÇAMLI

Department of Metallurgical and Materials Engineering

Metallurgical and Materials Engineering Programme

MAY 2016

İSTANBUL TECHNICAL UNIVERSITY ★ GRADUATE SCHOOL OF SCIENCE
ENGINEERING AND TECHNOLOGY

**SYNTHESIS AND CHARACTERIZATION OF HAFNIUM BORIDE-BASED
CERAMIC POWDERS**



Ph.D. THESIS

Nazlı AKÇAMLI
(506092425)

Department of Metallurgical and Materials Engineering

Metallurgical and Materials Engineering Programme

Thesis Advisor: Prof. Dr. İsmail DUMAN

MAY 2016

İSTANBUL TEKNİK ÜNİVERSİTESİ ★ FEN BİLİMLERİ ENSTİTÜSÜ

**HAFNİYUM BORÜR-ESASLI SERAMİK TOZLARININ SENTEZLENMESİ
VE KARAKTERİZASYONU**



DOKTORA TEZİ

**Nazlı AKÇAMLI
(506092425)**

Metalurji ve Malzeme Mühendisliği Anabilim Dalı

Metalurji ve Malzeme Mühendisliği Programı

Tez Danışmanı: Prof. Dr. İsmail DUMAN

MAY 2016

Nazlı AKÇAMLI, a Ph.D. student of ITU Graduate School of Science Engineering and Technology student ID 506092425, successfully defended the dissertation entitled “SYNTHESIS AND CHARACTERIZATION OF HAFNIUM BORIDE-BASED CERAMIC POWDERS”, which she prepared after fulfilling the requirements specified in the associated legislations, before the jury whose signatures are below.

Thesis Advisor : **Prof. Dr. İsmail DUMAN**
İstanbul Technical University

Jury Members : **Prof. Dr. M. Lütfi ÖVEÇOĞLU**
İstanbul Technical University

Prof. Dr. Cüneyt ARSLAN
İstanbul Technical University

Prof. Dr. Müzeyyen MARŞOĞLU
Yıldız Technical University

Prof. Dr. Ahmet EKERİM
Yıldız Technical University

Date of Submission : 05 April 2016

Date of Defense : 11 May 2016





To my mother and father,



FOREWORD

I would like to express my deepest gratitude and appreciation to my advisor Prof. Dr. İsmail Duman for his priceless mentorship, knowledge and great support throughout my doctoral researches and preparation of this dissertation. I would like to thank Prof. Dr. M. Lütfi Öveçođlu for all his priceless advices, for motivating me during my Ph.D. studies and teaching me many detailed scientific aspects.

I would also like to acknowledge Prof. Dr. Hüseyin Çimenođlu and Prof. Dr. Cüneyt Arslan for their support in characterization studies and my committee member Prof. Dr. Müzeyyen Marşođlu for her advices.

I would also express my appreciation to Prof. Dr. Deniz Uzunsoy for her guidance and great support during the last years of my doctoral studies and academic life. I also need to thank all the precious members of Bursa Technical University, Department of Metallurgical and Materials Engineering.

I would like to thank Dr. Duygu Ağaođulları for her great support all the time, guiding me in my research studies and her priceless friendship. I would also want to thank Dr. Özge Balcı for her great help and support in my research studies and her invaluable friendship. I am also thankful to Dr. Hasan Gökçe for his invaluable guidance, help and friendship.

I would also thank to all the precious members of the Particulate Materials Laboratories, particularly to Didem Ovalı, Meltem Bolluk, Veli Görkem Efe, Emre Tekođlu, Şeyma Duman, Aydın Şelte, Sultan Sönmez, Sıddıka Mertdinç, Merve Küçük, Nihan Özkan, Ceren İmer and Hadi Jahangiri for their assistance and friendship. I am also thankful to Faiz Muhaffel and Yakup Yürektürk for their help in mechanical tests, Berk Keskin for his help in using the Factsage Thermodynamical software, İnci Kol for her help in atomic absorption analyses. I am also thankful to Prof. Dr. Servet Turan and Assoc. Prof. Dr. Erhan Ayas for their help during SPS experiments.

I would like to express my deepest appreciations to my dear parents Ayşe and Recep Akçamlı for their motivation and invaluable support throughout my life. I would also like to express my appreciation and gratitude to my sister Funda and my brother Mümin and to all the family members. All the support they have provided me over the years was the greatest gift anyone has ever given to me.

This dissertation was financially supported by “The Scientific and Technological Research Council of Turkey (TÜBİTAK)” with the project title of “Synthesis of refractory metal borides via three different production methods from solid, liquid and gas raw materials for various application areas, sintering, characterization, comparison of process and final products” and with the project number of 112M470.

This dissertation was also funded by “İstanbul Technical University Scientific Research Projects” with the project title of “Synthesis and characterization of hafnium boride-based ceramic powders” and with the project number of 37544.

April 2016

Nazlı Akçamlı
M.Sc. Metallurgical and
Materials Engineer



TABLE OF CONTENTS

	<u>Page</u>
FOREWORD	ix
TABLE OF CONTENT	xi
ABBREVIATIONS	xiii
SYMBOLS	xv
LIST OF TABLES	xvii
LIST OF FIGURES	xix
SUMMARY	xxv
ÖZET	xxix
1. INTRODUCTION	1
2. LITERATURE REVIEW	7
2.1 Physical, Chemical and Structural Properties and Application Areas of Hafnium Dioxide.....	7
2.2 Production and Sintering Techniques of Hafnium Dioxide.....	18
2.2.1 Production techniques.....	18
2.2.2 Sintering techniques.....	31
2.3 Mechanochemical Synthesis and Mechanically Driven Synthesis Methods ...	36
2.3.1 Ball milling.....	37
2.3.2 The mechanism of mechanochemical synthesis.....	42
2.3.3 The effects of mechanical activation on synthesis reaction.....	45
2.4 Solvothermal Reaction Method in Autoclave.....	48
3. EXPERIMENTAL PROCEDURE	53
3.1 The Raw Materials.....	53
3.2 Synthesis of HfB ₂ -Based Powders.....	56
3.2.1 Mechanically activated borothermal reduction method.....	57
3.2.2 Mechanochemical synthesis method.....	58
3.2.3 Autoclave processing method.....	59
3.3 Consolidation of the Purified Powders.....	60
3.4 Characterization Investigations of the Powders and Sintered Product.....	61
3.4.1 Characterization investigations of the powders.....	61
3.4.2 Characterization investigations of the sintered products.....	63
3.5. Thermodynamical Calculations.....	64
4. RESULTS AND DISCUSSION	71
4.1 The Mechanically Activated Borothermal Synthesis of HfB ₂ Powders.....	71
4.1.1 Phase analyses of the as-blended, mechanically activated, annealed and purified powders.....	71
4.2 The Mechanochemical Synthesis of HfB ₂ -Based Powders from HfCl ₄ -B ₂ O ₃ -Mg and HfCl ₄ -B-Mg Blends.....	84
4.2.1 The mechanochemical synthesis of HfB ₂ -based powders from HfCl ₄ -B ₂ O ₃ -Mg blends.....	85

4.2.2 The mechanochemical synthesis of HfB ₂ powders from HfCl ₄ -B-Mg blends	100
4.3 The Synthesis of HfB ₂ -based Powders by the Mechanically Activated Autoclave Processing of HfCl ₄ -B ₂ O ₃ -Mg blends.....	104
4.3.1 Phase and thermal analyses of the as-blended and mechanically activated powders	105
4.3.2. Phase analyses of the powders after autoclave processing	108
4.4 The synthesis of HfB ₂ Powders Blends by Autoclave Processing.....	117
4.4.1 The synthesis of HfB ₂ powders from HfCl ₄ -NaBH ₄ -Mg powder blends by autoclave processing	117
4.5 The other powder blends investigated for HfB ₂ -based powder synthesis by autoclave processing	129
4.6 Consolidation and Bulk Properties of the HfB ₂ and HfB ₂ -HfO ₂ Powders.....	134
4.6.1 Microstructural characterization and density of the sintered samples	135
5. CONCLUSIONS.....	147
REFERENCES	153
APPENDICES	165
CURRICULUM VITAE	167

ABBREVIATIONS

A	: Ampere
AAS	: Atomic Absorption Spectrometer
BF	: Bright-Field
BPR	: Ball-to-Powder Weight Ratio
BSE	: Back-Scattered Electron
CP	: Cold Pressing
CVD	: Chemical Vapor Deposition
DC	: Direct Current
DSC	: Differential Scanning Calorimeter
EDS	: Energy Dispersive Spectroscopy
EDX	: Energy-Dispersive X-Ray Spectrometer
FTIR	: Fourier Transform Infrared Spectroscopy
g	: Gram
GPa	: Giga Pascal
h	: Hour
HV	: Vickers Hardness
ICDD	: International Center for Diffraction Data
Kg	: Kilogram
kJ	: Kilojoule
l	: Liter
M	: Molarity
MA	: Mechanical Alloying
min	: Minute
MO	: Metal Oxide
µm	: Micrometer
N	: Newton
nm	: Nanometer
OM	: Optical Microscope
ODS	: Oxide Dispersion Strengthened
Pa	: Pascal
PCA	: Process Control Agent
ppm	: Part per Million
R	: Reductant
PS	: Pressureless Sintering
PSA	: Particle Size Analyzer
RF	: Radio Frequency
rpm	: Rotation per minute

SADP	: Selected Area Diffraction Pattern
SEM	: Scanning Electron Microscope
SHS	: Self-Propagating High-Temperature Synthesis
SM	: Stereomicroscope
SPS	: Spark Plasma Sintering
TM	: Melting Temperature
TB	: Boiling Temperature
TM	: Trademark
TEM	: Transmission Electron Microscope
V	: Volt
VLS	: Vapor-liquid-solid
W	: Watt
WVL	: Wear volume loss
XRD	: X-Ray Diffractometer



SYMBOLS

a, b, c	: Lattice parameters
°C	: Degree Celsius
°K	: Degree Kelvin
ΔG°	: Standard Gibbs free energy change
I	: Current
λ	: Wavelength
Ω	: Ohm
T	: Temperature
θ	: Diffraction angle
~	: Approximation



LIST OF TABLES

	<u>Page</u>
Table 2.1 : Summary of some structural and physical properties of HfB ₂ , adapted from Fahrenholtz, 2007.	8
Table 2.2 : The mechanical properties of HfB ₂ and HfB ₂ composites depended on sintering techniques, conditions and composition.....	10
Table 2.3 : The mechanical properties of HfB ₂ and HfB ₂ composites depended on temperature (Rhodes et al., 1970; Ghosh and Subhash, 2013).....	10
Table 2.4 : Effect of reagent and treatment on solubility of hafnium diboride (stability of 10-15 μm), adapted from Weimer, 1997.	13
Table 2.5 : Examples of reduction reactions that can be used to synthesize hafnium diborides, adapted from Fahrenholtz et al., 2007; Guo et al., 2012; Peshev and Bliznakov, 1968; Sonber et al., 2010.	20
Table 2.6 : The summary of production techniques of hafnium diboride.....	30
Table 2.7 : Literature data on densification of the HfB ₂ ceramics, adapted from Sonber et al., 2010.	36
Table 2.8 : Important milestones in the development of mechanical alloying /milling, adapted from Suryanarayana, 2001.	38
Table 2.9 : Departure from equilibrium achieved in various processes, adapted from Sopicka-Lizer, 2010.	46
Table 3.1 : The raw materials utilized in this study.	54
Table 3.2 : The utilized synthesis methods and raw materials.....	57
Table 4.1 : SEM/EDS analysis results of different regions marked in Figure 4.10 (a) and (b).....	81
Table 4.2 : Semi-quantitative phase analyses of the HfCl ₄ -B ₂ O ₃ -Mg powders (after different treatments) obtained from the Rietveld refinement method based on their XRD patterns.....	96
Table 4.3 : Average crystallite size and lattice strain of the HfCl ₄ -B ₂ O ₃ -Mg powders after milling at different durations and purification.	97
Table 4.4 : The crystal structural information of different phases encountered in this study.	106
Table 4.5 : The sample names, synthesis methods and raw materials of sintered powders.....	135
Table 4.6 : Density values of the sintered samples.	141
Table 4.7 : Hardness values of the sintered samples.....	143
Table 4.8 : Wear volume loss and relative wear resistance of the sintered samples.	144



LIST OF FIGURES

	<u>Page</u>
Figure 2.1 : Materials with the highest reported melting temperature grouped by material family, adapted from Fahrenholtz, 2014.	8
Figure 2.2 : Evolution of structures in Zr(Hf)B ₂ -SiC composites during oxidation at: (a) 1000 °C, (b) 1200 °C, and (c) 1500 °C, adapted from Ghosh and Subhash, 2010.....	12
Figure 2.3 : The schematic representation of crystal structure and the AlB ₂ type structure of HfB ₂ adapted from Fahrenholtz et al., 2007.	15
Figure 2.4 : The Hf-B binary phase diagram, adapted from Massalski, 1990.	16
Figure 2.5 : The leading edges in the high performance hypersonic vehicles, adapted from Url-1.....	17
Figure 2.6 : A schematic of the thermal management process in the UHTC leading edge component, adapted from Ghosh and Subhash, 2013.....	17
Figure 2.7 : Flow chart for synthesis of HfB ₂ powders from solution based precursors, adapted from Wang et al., 2014b.....	23
Figure 2.8 : The Spex shaker mill, hardened steel milling vial and balls.	40
Figure 2.9 : (a) Fritsch TM Pulverisette P-5 four station ball mill and (b) Schematic depicting the ball motion inside the ball mill, adapted from Suryanarayana, 2001.	40
Figure 2.10 : (a) model 1-S attritor and (b) arrangement of rotating arms on a shaft in the attrition ball mill, adapted from Suryanarayana, 2001 and El-Eskandarany, 2001.	41
Figure 2.11 : Commercial type ball mills used for mechanical alloying by Courtesy for Inco Alloys International, adapted from Suryanarayana, 2001. ...	41
Figure 2.12 : Schematic sketches showing the reaction progress of Ti and activated carbon during mechanochemical synthesis: (a) initial stage, no TiC, (b) second stage, the refinement of Ti and carbon powders, no TiC, (c) third stage, a small amount of TiC formed on the surface of the Ti particles; (d) final stage, the as-milled products composed completely of nanocrystalline TiC, adapted from Sopicka-Lizer, 2010.	44
Figure 2.13 : The change of the conditions for chemical interaction during mechanical activation where S is specific surface area, adapted from Avvakumov et al., 2001.....	46
Figure 2.14 : Parr TM Instrument Company Pressure Vessels and Reactors, adapted from Feng and Li, 2011.....	50
Figure 2.15 : A representative and schematic view of an autoclave vessel, adapted from, Url-2.....	50
Figure 3.1. Scheme of hydrolysis of an HfCl ₄ particle, adapted from Barraud et al., 2006.	54
Figure 3.2 : The SM images of raw materials: (a) HfCl ₄ , (b) B ₂ O ₃ , (c) amorphous B, (d) NaBH ₄ and (d) Mg.....	55

Figure 3.3 : The XRD patterns of raw materials: (a) HfCl ₄ , (b) B ₂ O ₃ , (c) amorphous B and (d) Mg.....	56
Figure 3.4 : The autoclave system.....	60
Figure 3.5 : SM images of the some green bodies (a, b and c) and sintered structures (d, e and f) of hafnium diboride based products: (a),(d) HfB-B-2CoPS, (b),(e) HfBO-M-2CoPS and (c),(f) HfB-A-2CoPS.	61
Figure 3.6 : Molar amounts of the reactants and products varying according to the temperature in regard of reaction (3.2).....	64
Figure 3.7 : Standard Gibbs free energy changes of the reactions (3.2) varying according to the temperature.	65
Figure 3.8 : Standard Gibbs free energy changes of the reactions (3.3) varying according to the temperature.	65
Figure 3.9 : Standard Gibbs free energy changes of the reactions (3.4) varying according to the temperature.	66
Figure 3.10 : Molar amounts of reactants and products of the reaction (3.3) at room temperature varying according to the Mg amount.....	67
Figure 3.11 : Molar amounts of products of the reaction (3.3) varying according to the temperature.	68
Figure 3.12 : Standard Gibbs free energy changes of the reactions (3.5) varying according to the temperature.	68
Figure 3.13 : Molar amounts of the reactants and products varying according to the temperature in regard of reaction (3.5).....	69
Figure 3.14 : Molar amounts of reactants and products of the reaction (3.5) at 500 °C varying according to the NaBH ₄ amount.	70
Figure 4.1 : XRD patterns of the as-blended and mechanically activated powders: (a) as-blended, (b) 1 h and (c) 5 h.....	72
Figure 4.2 : XRD patterns of the as-blended powders with different boron amounts after annealing: (a) 0 wt.% excess boron (stoichiometric) and (b) 20 wt.% excess boron.	73
Figure 4.3 : XRD patterns of the mechanically activated powders with different boron amounts after annealing: (a) 0 wt.% excess (stoichiometric), (b) 10 wt.% excess, (c) 20 wt.% excess and (d) 50 wt.% excess.	73
Figure 4.4 : FTIR spectra of the mechanically activated and annealed powders with different wt.% excess boron amounts: (a) 0 wt.%-stoichiometric, (b) 10 wt.%, (c) 20 wt.% and (d) 50 wt.%	75
Figure 4.5 : FTIR spectra of the mechanically activated and annealed powders (with different wt.% excess boron amounts) after washing with distilled water: (a) 0 wt.%-stoichiometric, (b) 10 wt.%, (c) 20 wt.% and (d) 50 wt.%	75
Figure 4.6 : XRD pattern of the 20 wt.% excess boron containing powders after the mechanical activation, annealing and leaching treatments.....	77
Figure 4.7 : SM images of the powders containing 20 wt.% excess B: (a) as-blended, (b) mechanically activated, (c) annealed and (d) washed with distilled water.	78
Figure 4.8: SEM images of the mechanically activated powders containing 20 wt.% excess B: (a) annealed, (b) washed with distilled water, and (c) its corresponding PSA analysis.	79
Figure 4.9 : (a) SEM image of synthesized powders with 20 wt.% ex B at 20000X, EDS mapping of (b) B and (c) Hf.....	81

Figure 4.10 : SEM image of the mechanically activated powders containing 20 wt.% excess boron after: (a) annealing and (b) washing with distilled water.	81
Figure 4.11 : TEM images of the powders milled for 1 h and annealed at 1100 °C: (a), (b) bright-field (BF) images and (d) its corresponding selected area diffraction pattern (SADP) taken from the region marked in (c).	83
Figure 4.12 : XRD patterns of the as-blended HfCl ₄ -B ₂ O ₃ -Mg powder blends and those milled at different durations up to 5 h.	85
Figure 4.13 : XRD patterns of the HfCl ₄ -B ₂ O ₃ -Mg powder blends having: (a) 30 wt.% excess B ₂ O ₃ and (b) 30 wt.% B ₂ O ₃ and 20 wt.% excess Mg after 3 h of milling.	86
Figure 4.14 : XRD patterns of the HfCl ₄ -B ₂ O ₃ -Mg powder blends after milling at different durations and subsequent washing and HCl leaching treatments.	88
Figure 4.15 : FTIR spectra of (a) commercial HfOCl ₂ .8H ₂ O powders and HfCl ₄ -B ₂ O ₃ -Mg blends after (b) milling for 3 h, (c) subsequent washing with distilled water.	89
Figure 4.16 : XRD patterns of the 3 h of milled and leached HfCl ₄ -B ₂ O ₃ -Mg blends after: (a) annealing at 1000 °C for 3 h and (b) subsequent HCl leaching.	90
Figure 4.17 : SM images of the HfCl ₄ -B ₂ O ₃ -Mg powders: (a) as-blended, (b) milled for 10 min, (c) milled for 15 min, (d) milled for 3 h, (e) milled for 5 h, (f) milled for 3 h and purified (g) milled for 3 h milled, purified and annealed at 1000 °C.	91
Figure 4.18 : SEM images of the HfCl ₄ -B ₂ O ₃ -Mg powder blends subjected to milling for 3 h and subsequent purification.	93
Figure 4.19 : SEM/EDX analyses of milled (for 3 h) and purified powders: (a) SEM image and corresponding elemental maps of (b) Hf, (c) O, (d) B and (e) Mg.	94
Figure 4.20 : SEM image and corresponding general EDS analysis of the milled (for 3 h) and purified powders.	94
Figure 4.21 : SEM image and corresponding general EDS analysis of the annealed and leached powders (previously milled for 3 h and purified).	95
Figure 4.22 : Particle size distributions of the HfCl ₄ -B ₂ O ₃ -Mg powder blends after milling at different durations and subsequent purification: (a) 1 h, (b) 3 h and (c) 5 h.	96
Figure 4.23 : SEM images and particle size distribution of the powders after annealing at 1000 °C for 3 h (previously milled for 3 h and purified) and final HCl leaching.	98
Figure 4.24 : (a) and (b) Bright-field (BF) TEM images of the powders and corresponding selected area diffraction patterns (SADP): (d) SADP taken from the white-circled region in (c), revealing the presence of monoclinic HfO ₂ phase, (f) SADP taken from the white-circled region in (e), revealing the presence of hexagonal HfB ₂ phase.	99
Figure 4.25 : XRD patterns of (a) as-blended stoichiometric HfCl ₄ -B-Mg powders and those milled for (b) 1 h and (c) 5 h.	100

Figure 4.26 : XRD patterns of the HfCl ₄ -B-Mg powder blends having different stoichiometries: (a) 0 wt.% excess B and Mg (stoichiometric), (b) 30 wt.% excess B, (c) 30 wt.% excess B and 20 wt.% excess Mg and (d) 50 wt.% excess B, after milling for 1 h.	102
Figure 4.27 : XRD patterns of the HfCl ₄ -B-Mg powder blends having different excess amount of B: (a) 0 wt.%, (b) 30 wt.% and (c) 50 wt.%, after milling for 1 h and purification.....	102
Figure 4.28 : XRD patterns of the HfCl ₄ -B-Mg powder blends having different excess amount of B : (a) 0 wt.%, (b) 30 wt.% and (c) 50 wt.%, after milling for 1 h, annealing at 1100 °C for 1 h and purification.	103
Figure 4.29 : XRD patterns of the (a) as-blended HfCl ₄ -B ₂ O ₃ -Mg powders and (b) those mechanically activated for 5 min.	105
Figure 4.30 : (a) DSC scans of the as-blended HfCl ₄ -B ₂ O ₃ -Mg powders and those mechanically activated for 5 min, and (b) XRD pattern of the mechanically activated powders after DSC heating.	108
Figure 4.31 : XRD patterns of the as-blended HfCl ₄ -B ₂ O ₃ -Mg powders and those of mechanically activated for 5 min after autoclave processing at different durations: (a) as-blended powders after 6 h, (b) as-blended powders after 12 h, (c) mechanically activated powders after 6 h and (d) mechanically activated powders after 12 h.....	110
Figure 4.32 : XRD patterns of the as-blended HfCl ₄ -B ₂ O ₃ -Mg powders and those mechanically activated for 5 min after autoclave processing at different durations and subsequent purification: (a) as-blended powders after 6 h, (b) as-blended powder after 12 h, (c) mechanically activated powders after 6 h and (d) mechanically activated powders after 12 h.....	111
Figure 4.33 : FTIR spectra of the (a) B ₂ O ₃ raw material, (b) HfCl ₄ raw material, (c) as-blended HfCl ₄ -B ₂ O ₃ -Mg powders, (d) those mechanically activated for 5 min, (e) those autoclave processed for 12 h and (f) those purified with washing and leaching treatments.....	112
Figure 4.34 : SM images of the (a) as-blended HfCl ₄ -B ₂ O ₃ -Mg powders, (b) those after mechanical activation for 5 min, (c) those after reaction in the autoclave for 12 h and (d) those after purification.	113
Figure 4.35 : (a)-(b) SEM images, (c) general EDS analysis (c) and (d) PSA analysis of the powders obtained after mechanical activation (for 5 min), autoclave reaction (for 12 h) and purification treatments.....	115
Figure 4.36 : SEM/EDX analyses of the milled (for 3 h) and purified powders: (a) SEM image and corresponding elemental maps for (b) Hf, (c) O, (d) B and (e) Mg.	116
Figure 4.37 : XRD patterns of the HfCl ₄ -NaBH ₄ -Mg powder blends having different excess amounts of NaBH ₄ : (a) 0 wt.%, (b) 100 wt.% and (c) 200 wt.%, after autoclave processing at 500 °C for 12 h.....	118
Figure 4.38 : XRD patterns of the HfCl ₄ -NaBH ₄ -Mg powder blends having different excess amounts of NaBH ₄ : (a) 0 wt.%, (b) 100 wt.% and (c) 200 wt.%, after reaction in the autoclave at 500 °C for 12 h and washing with distilled water.	119
Figure 4.39 : FTIR spectra of autoclave gases evolved during the reaction of HfCl ₄ -NaBH ₄ -Mg blends having 200 wt.% excess NaBH ₄ at 500 °C for 12 h.	120

- Figure 4.40 :** XRD patterns of the $\text{HfCl}_4\text{-NaBH}_4\text{-Mg}$ powder blends having different excess amounts of NaBH_4 : (a) 0 wt.%, (b) 100 wt.% and (c) 200 wt.%, after reaction in the autoclave at 500 °C for 12 h, washing with distilled water and annealing at 750 °C for 3 h. **121**
- Figure 4.41:** XRD patterns of the $\text{HfCl}_4\text{-NaBH}_4\text{-Mg}$ powder blends having different excess amounts of NaBH_4 : (a) 0 wt.%, (b) 100 wt.% and (c) 200 wt.%, after reaction in the autoclave at 500 °C for 12 h, washing with distilled water and annealing at 1000 °C for 3 h. **122**
- Figure 4.42 :** XRD pattern of the $\text{HfCl}_4\text{-NaBH}_4\text{-Mg}$ powder blends having 200 wt.% excess amounts of NaBH_4 after reaction in the autoclave at 500 °C for 12 h, washing with distilled water, annealing at 1000 °C for 3 h and leaching with 6 M HCl. **122**
- Figure 4.43 :** XRD patterns of the $\text{HfCl}_4\text{-NaBH}_4\text{-Mg}$ powder blends having 200 wt.% excess amount of NaBH_4 after reaction in the autoclave at 500 °C for 12 h, washing with distilled water, annealing at 1700 °C for 6 h and leaching with 6 M HCl. **123**
- Figure 4.44 :** SM images of the $\text{HfCl}_4\text{-NaBH}_4\text{-Mg}$ powder blends having 200 wt.% excess NaBH_4 after: (a) processing in the autoclave at 500 °C for 12 h and subsequent, (b) washing with distilled water, (c) annealing at 1000 °C and (d) leaching with 6 M HCl..... **124**
- Figure 4.45 :** (a)-(b) SEM images of the $\text{HfCl}_4\text{-NaBH}_4\text{-Mg}$ powders having 200 wt.% excess NaBH_4 after reaction in the autoclave and washing with distilled water at different magnifications and (c) its corresponding EDS analysis..... **125**
- Figure 4.46 :** (a)-(b) SEM images of the $\text{HfCl}_4\text{-NaBH}_4\text{-Mg}$ powders having 200 wt.% excess NaBH_4 after reaction in the autoclave, washing with distilled water, annealing at 1000 °C for 3 h and leaching with 6 M HCl, corresponding (c) EDS analysis and (d) PSA analysis. **126**
- Figure 4.47 :** TEM images of the powders milled for 1 h and annealed at 1100 °C: (a), (b) bright-field (BF) images and (c) and (d) its corresponding selected area diffraction pattern (SADP)..... **129**
- Figure 4.48 :** XRD patterns of the $\text{HfCl}_4\text{-H}_3\text{BO}_3\text{-Mg}$ powder blends after autoclave process at 500 °C for 12 h, with different stoichiometries : (a) $\text{HfCl}_4\text{-H}_3\text{BO}_3$ (450 wt.% excess)-Mg (250 wt.% excess), (b) $\text{HfCl}_4\text{-H}_3\text{BO}_3$ (250 wt.% excess)-Mg (30 wt.% excess), (c) $\text{HfCl}_4\text{-H}_3\text{BO}_3\text{-Mg}$ (30 wt.% excess) and (d) $\text{HfCl}_4\text{-H}_3\text{BO}_3$ (450 wt.% excess)-Mg (250 wt.% excess)- crust layer. **130**
- Figure 4.49 :** XRD patterns of the $\text{HfCl}_4\text{-H}_3\text{BO}_3$ (250 wt.% excess)-Mg (30 wt.% excess) blends after the autoclave process at 500 °C for 12 h and 6 M HCl leaching. **131**
- Figure 4.50 :** SM images of the $\text{HfCl}_4\text{-H}_3\text{BO}_3$ (250 wt.% excess)-Mg (30 wt.% excess) blends after the autoclave process at 500 °C for 12 h: (a) powder products and (b) crust layer. **131**
- Figure 4.51 :** XRD pattern of the $\text{HfCl}_4\text{-B}$ powder blends (in the presence of NaCl-KCl-MgCl_2 molten salt) after the autoclave process at 500 °C for 12 h under the starting pressure of 5 bar and subsequent water washing with distilled water. **132**
- Figure 4.52 :** XRD pattern of the $\text{HfCl}_4\text{-B-Mg}$ powder blends after the autoclave process at 500 °C for 12 h under the starting pressure of 5 bar..... **133**

Figure 4.53 : XRD pattern of the $\text{HfOCl}_2 \cdot 8\text{H}_2\text{O} - \text{B}_2\text{O}_3 - \text{Mg}$ powder blends after the autoclave process at 500 °C for 12 h under the starting pressure of 5 bar.	134
Figure 4.54 : OM images of the sintered samples: (a) HfB-B-2CoPS, (b) HfBO-M-2CoPS, (c) HfBO-M-SPS, (d) HfBO-A-PS, (e) HfBO-A-SPS, (f) HfB-A-2CoPS and (g) HfB-A-SPS.	136
Figure 4.55 : SEM images of the sintered samples: (a) HfBO-A-PS, (b) HfBO-A-SPS and (c) HfB-A-SPS.	137
Figure 4.56 : XRD patterns of the sintered samples: (a) HfB-B-2CoPS, (b) HfBO-M-2CoPS, (c) HfBO-M-SPS, (d) HfBO-A-PS, (e) HfBO-A-SPS, (f) HfB-A-2CoPS and (g) HfB-A-SPS.	139
Figure 4.57 : SEM/EDX analysis of the HfBO-A-PS sample: (a) SEM image, and elemental maps for (b) Hf, (c) B, (d) O and (e) Mg.	140
Figure 4.58 : Worn surface SEM images of the sintered samples: a) HfBO-A-PS, b) HfBO-A-SPS and (c) their corresponding wear profiles.....	145
Figure 4.59 : Mean friction coefficients of the sintered hafnium diboride-based samples.	146

SYNTHESIS AND CHARACTERIZATION OF HAFNIUM BORIDE-BASED CERAMIC POWDERS

SUMMARY

Hafnium boride is a strategic material as one of the leading members of ultra-high temperature ceramics. In recent years, there has been an increasing research interest in transition metal diborides to meet the need for high temperature materials that can withstand extreme environments. These extreme conditions can include the effects of high temperature, oxidation, mechanical stress, radiation and wear. Hafnium and zirconium diborides are identified as the most promising candidates for high temperature applications due to their relatively good oxidation resistance compared to other refractory ceramics. Hafnium diboride has a melting point of 3380 °C, which is higher than many ceramic materials and also higher than few advanced ceramics whose melting temperatures are over 3000 °C. Additionally, it has remarkable properties including very high hardness, low thermal expansion coefficient, chemical inertness, high thermal and electrical conductivities. It exhibits a high oxidation resistance as a consequence of the stability of the HfO₂ layer formed on its surface by oxidation at high working temperatures. Some potential applications for hafnium diboride include furnace elements, plasma arc electrodes, refractory linings, molten metal containments, wear resistant coatings, control rods and heating shields in nuclear reactors. However, majority of recent research has been stimulated by unmet material needs for thermal protection systems in extreme environments especially for sharp leading edges of high velocity flights or atmospheric re-entry vehicles.

Hafnium diboride powders have been prepared by a variety of production methods. The conventional synthesis methods of hafnium diboride include high temperature borothermal/carbothermal reduction routes over 1500 °C. Apart from the conventional methods, diverse production techniques including reaction between elemental powders of Hf and B, solid-state boron carbide reduction methods, self-propagating high-temperature synthesis (SHS), sol-gel method, hydrothermal/solvothermal synthesis, chemical vapor deposition (CVD) and milling-assisted processes have been applied. The conventional borothermal and borothermal/carbothermal reduction methods of HfO₂ in which amorphous boron and B₄C are used as boron and boron/carbon sources, are generally carried out at elevated temperatures above 1500°C. Expensive equipment requirements and relatively high working temperatures are main drawbacks of these methods. In addition, large particle sizes induced by high synthesis temperature constitute some drawbacks during subsequent consolidation operations. Elemental powders have also been used to produce bulk HfB₂ ceramics by spark plasma sintering (SPS) and dynamical consolidation techniques. Although, the reaction between elemental hafnium and boron is thermodynamically more favorable, it is not a cost-effective method due to the use of expensive raw materials. Also, solution-based methods have been applied to synthesize nano-sized HfB₂ powders with low oxygen content and they offer homogeneous dispersion of different raw materials. However, high temperatures are

still needed to ensure following carbothermal reduction. Furthermore, the CVD methods are generally employed with the aim of obtaining hard surface coatings rather than powder synthesis in order to improve the surface hardness and tribological properties of desired materials. Additionally, single crystals of HfB_2 were prepared by floating zone method by means of radio frequency (RF) heating. Furthermore, some attempts were made by milling-assisted annealing processes: HfO_2 - HfB_2 composite powders were produced by high-energy ball milling of HfO_2 - B_2O_3 -Mg powder blends. In addition, preparation of HfB_2 nanorods from HfCl_4 -B and HfCl_4 -B-Mg powder mixtures by mechanical activation and isothermal annealing were suggested. The lowest synthesis temperature was reported as 600 °C in the case of utilizing a hydrothermal method in an autoclave. However, usage of relatively few amounts of reactants (in order of mmol) and small capacity equipment restrict the application of the process. In these studies, HfO_2 and HfCl_4 have been used as the most common hafnium sources depending on their properties in different synthesis methods. The HfCl_4 has been extensively utilized in recent production methods such as low temperature hydrothermal/solvothermal synthesis, sol-gel and CVD methods with the aim of benefiting from its low boiling point and higher reactivity over HfO_2 . Moreover, most commonly used boron sources in various production methods are amorphous B, B_2O_3 , H_3BO_3 , NaBH_4 powders and BCl_3 gas.

In this study, it was aimed to prepare hafnium diboride powders with novel methods provide several advantages such as usage of economical raw materials, utilization of simple equipment, reduced or low reaction temperature and scalable processes. The mechanically activated borothermal reduction route was applied to synthesize high purity and submicron size HfB_2 powders from HfCl_4 -B powder blends. In addition, HfB_2 - HfO_2 and HfB_2 powders were synthesized by mechanochemical synthesis at room temperature in nano-scale from HfCl_4 - B_2O_3 -Mg and HfCl_4 -B-Mg powder blends for the first time in the literature according to the best of our knowledge. In addition, mechanical activation was applied to HfCl_4 - B_2O_3 -Mg precursors to enable the reaction at lower temperatures during the autoclave synthesis. Mechanical activation induced by high-energy ball milling enables to reduce synthesis temperature during subsequent heat treatment by the formation of active reactant particles and their homogeneous distribution throughout the microstructure. Thus, in the borothermal reduction and autoclave synthesis routes, mechanical activation is applied to reduce the synthesis temperatures and particle size of the final powders, and to increase the process efficiency. Also, low temperature autoclave processing was utilized to synthesize high purity and nano-scale HfB_2 powders from starting powders blends of HfCl_4 - NaBH_4 -Mg. Although solvothermal autoclave synthesis methods are quite new methods for preparation of the boride compounds, they provide some advantageous which are control of size and morphology and preparing nanopowders in rod, cube or sheet morphologies. Moreover, autoclave synthesis is considered as an environmentally friendly method because the process proceeds in a closed/isolated system and it saves energy by low synthesis temperature.

In addition, the utilized powder systems were thermodynamically interpreted by the FactSageTM 6.2 thermochemical software to predict the reaction mechanisms. The detailed characterization of synthesized powders were performed using X-ray diffractometer (XRD), particle size analyzer (PSA), stereomicroscope (SM), scanning electron microscope/energy dispersive spectrometer (SEM/EDS) and transmission electron microscope (TEM). The synthesized hafnium diboride-based powders were consolidated by two different sintering techniques. The cold

pressing/pressureless sintering (without and with Co addition) and spark plasma sintering techniques were applied to selected powders which were obtained by optimum process parameters. The densification behaviour and microstructural characterization of the sintered samples were investigated using density measurement by Archimedes method and XRD, SM, SEM/EDX techniques. Mechanical properties of consolidated products were determined in terms of microhardness and wear properties.

Finally, I would be honoured if this dissertation can make a contribution to convert our boron sources into technological products with high added value.





HAFNİYUM BORÜR-ESASLI SERAMİK TOZLARIN SENTEZLENMESİ VE KARAKTERİZASYONU

ÖZET

Hafniyum diborür ultra yüksek sıcaklık seramiklerinin bir üyesi olarak stratejik bir malzemedir. Son yıllarda, zorlayıcı koşullara dayanabilecek yüksek sıcaklık malzemelerine olan ihtiyacın karşılanması amacıyla geçiş metalleri diborürleri üzerinde artan bir araştırma ilgisi gözlenmektedir. Bu zorlayıcı koşullar yüksek sıcaklık, oksidasyon, mekanik kuvvetler, radyasyon ve aşınma etkilerini içerir. Hafniyum ve zirkonyum diborürler, diğer refrakter seramiklere göre oldukça iyi oksidasyon dayanımları nedeniyle yüksek sıcaklık uygulamaları için en umut vaat eden malzemeler olarak gösterilmektedir. Hafniyum diborür 3000 °C’i aşan ve aynı zamanda ileri seramiklerden birçoğunun üzerinde olan çok yüksek bir ergime noktasına sahiptir. Bunun yanında, çok yüksek sertlik, düşük termal genleşme katsayısı, kimyasal inertlik, yüksek termal ve elektriksel iletkenlik gibi üstün özellikleri bulunmaktadır. Yüksek sıcaklıklarda yüzeyinde oluşan HfO₂ tabakasının kararlılığı sayesinde oldukça iyi bir oksidasyon direncine sahiptir. Hafniyum diborür için bazı potansiyel uygulamalar fırın elemanları, plazma ark elektrotları, refrakter astarlamalar, ergimiş metal potaları, aşınmaya dayanıklı kaplamalar, nükleer reaktörler için kontrol rodları ve ısı kalkanlarını içerir. Fakat son araştırmaların birçoğu, özellikle yüksek hızlı uçakların ya da atmosfere tekrarlı giriş araçlarının kanat ön kısımları için termal bariyerlerin geliştirilmesine yönelik bir çabayla yapılmaktadır.

Hafniyum diborür tozları çeşitli üretim yöntemleri ile hazırlanmaktadır. Hafniyum diborürün geleneksel sentez metotları 1500 °C’nin üzerindeki yüksek sıcaklıklarda gerçekleşen borotermal-karbotermal redüksiyon yollarını içermektedir. Geleneksel üretim yöntemlerinin dışında elementer Hf ve B tozları arasındaki direkt katı faz reaksiyonları, katı hal bor karbür redüksiyon metodu, kendiliğinden ilerleyen yüksek sıcaklık sentezi (SHS), sol-gel yöntemi, solvotermal sentez, kimyasal buhar biriktirme (KBB) ve öğütme destekli prosesler de uygulanmaktadır. HfO₂’in geleneksel borotermal ve borotermal-karbotermal redüksiyonları, amorf borun veya B₄C’ün bor ve bor-karbon kaynağı olarak kullanıldığı yüksek sıcaklıklarda gerçekleştirilir. Pahalı ekipman gereksinimi ve oldukça yüksek çalışma sıcaklıkları bu yöntemlerin başlıca dezavantajlarıdır. Spark plazma sinterleme (SPS) ve basınçlı sinterleme tekniklerinden yararlanılarak elementer tozlardan yığın yapıdaki HfB₂ seramiklerin üretimi de söz konusudur. Elementer hafniyum ve bor arasındaki reaksiyonun termodinamik olarak elverişli olmasına rağmen, pahalı hammaddelerin kullanımı nedeniyle uygun maliyetli bir yöntem değildir. Ayrıca, çözelti-esaslı metotlar nano boyutlu HfB₂ tozlarının düşük oksijen içeriği ile üretiminde uygulanmaktadır ve bu metotlar hammadde karışımlarının homojen olarak dağıtılmasını kolaylaştırmaktadır. Bununla birlikte, takip eden karbotermik redüksiyonun gerçekleşmesi için halen yüksek sıcaklıklara ihtiyaç duyulmaktadır. Bunun dışında, KBB metotları genel olarak malzemelerin yüzey sertliklerini ve

tribolojik özelliklerini geliştirmek amacıyla toz sentezinden ziyade sert yüzey kaplamalarının elde edilmesinde kullanılır. Araştırmacılar, hafniyum diborür tek kristallerinin hazırlanması için zon ergitme yöntemlerini de çalışmışlardır. HfB_2 - HfO_2 kompozit tozlarının üretimi için öğütme destekli tavlama prosesleri kullanılarak yüksek enerjili değirmenlerde HfO_2 - B_2O_3 -Mg toz karışımlarının öğütülmesini ve takiben tavlmasını içeren bazı çalışmalar yapılmıştır. Aynı zamanda, HfCl_4 -B ve HfCl_4 -B-Mg toz karışımlarının mekanik aktivasyonu ve takiben isothermal tavlama ile nanorod morfolojisindeki HfB_2 tozlarının üretimi önerilmiştir. Hafniyum diborür sentezi için en düşük sentezleme sıcaklığı solvotermal metot kullanılarak 600 °C olarak bildirilmiştir, fakat bu yöntemde mmol mertebelerinde oldukça az miktarda reaktanlarla çalışılması ve oldukça küçük ölçekli ekipman kullanımı prosesin uygulanmasını kısıtlayacak niteliktedir. Bu çalışmalarda kullanılan en yaygın hafniyum kaynakları HfO_2 ve HfCl_4 bileşikleridir ve bu hammaddelerin farklı sentezleme metotları için özelliklerine göre seçilmesi söz konusudur. HfCl_4 özellikle düşük sıcaklıkta gerçekleşen hidrotermal/solvotermal sentezler, sol-gel ve CVD metotları gibi güncel üretim metotlarında, düşük kaynama noktası ve HfO_2 göre daha yüksek kimyasal reaktifliğe sahip olması nedeniyle tercih edilmektedir. Çeşitli üretim yöntemlerinde en yaygın olarak kullanılan bor kaynakları ise amorf B, B_2O_3 , H_3BO_3 , NaBH_4 tozları ve BCl_3 gazı olarak sayılabilir.

Bu tez çalışmasında, yenilikçi üretim teknikleri kullanılarak hafniyum diborür tozlarının üretimi hedeflenmiştir. Bu teknikler ekonomik hammadde ve basit donanım kullanımı, oda sıcaklığında ya da düşük sıcaklıklarda gerçekleşen ve ölçeklendirilebilir prosesler olmaları gibi bazı avantajlar sağlamaktadır. Yüksek safiyette ve mikron altı boyutlarda HfB_2 tozlarının HfCl_4 -B toz karışımlarından sentezlenmesi için mekanik olarak aktive edilmiş borotermal redüksiyon yöntemi uygulanmıştır. Yapılan literatür taramalarına göre, nano boyutlu HfB_2 - HfO_2 ve HfB_2 tozlarının HfCl_4 - B_2O_3 -Mg ve HfCl_4 -B-Mg toz karışımlarından mekanokimyasal yöntemle, oda sıcaklığında üretimi ilk kez bu doktora çalışması çerçevesinde gerçekleştirilmiştir. Ayrıca, HfCl_4 - B_2O_3 -Mg toz karışımlarına mekanik aktivasyon uygulanarak otoklav sentezi sırasında reaksiyonun düşük sıcaklıkta ve daha yüksek verimle gerçekleşmesi sağlanmıştır. Yüksek enerjili bilyeli değirmende öğütme ile elde edilen mekanik aktivasyon, aktif reaktan partiküllerinin elde edilmesini ve bu partiküllerin mikroyapı içerisinde homojen dağılımını sağlayarak takip eden ısı işlemler sırasında reaksiyonun daha düşük sıcaklıklarda gerçekleşmesine olanak verir. Bu nedenle, sentezleme sıcaklığını düşürmek, toz ürünlerin partikül boyutlarını azaltmak ve proses verimliliğini arttırmak için borotermal redüksiyon ve otoklav sentezi yöntemleri öncesinde toz karışımlarına mekanik aktivasyon uygulanmıştır. Yüksek safiyette ve nanoboyutta HfB_2 tozlarının üretimi için diğer bir yöntem olarak, HfCl_4 - NaBH_4 -Mg toz karışımları kullanılarak düşük sıcaklıkta gerçekleşen otoklav prosesi uygulanmıştır. Otoklav prosesi borür tozlarının sentezlenmesinde oldukça yeni bir metot olmasına rağmen boyut ve morfoloji kontrolü ile nano tozların çubuk, küp ya da pul şeklinde hazırlanmasına imkan vermektedir. Dahası otoklav prosesleri, kapalı/izole sistemlerde gerçekleşmeleri ve düşük sıcaklıkta uygulanmaları nedeniyle çevreye duyarlı yöntemler olarak kabul edilmektedir. Farklı yöntemler için kullanılan toz sistemleri reaksiyon mekanizmalarının öngörülebilmesi amacıyla FactSageTM 6.2 termodinamik yazılımları kullanılarak yorumlanmıştır. Sentezlenen hafniyum borür tozlarının detaylı karakterizasyonu X-ışını difraktometresi (XRD), partikül boyutu analizörü (PSA), stereo mikroskop (SM), taramalı elektron mikroskobu/enerji dağılımlı spektrometre (SEM/EDS) ve geçirimli elektron mikroskobu (TEM) kullanılarak gerçekleştirilmiştir. Son olarak, üretilen

hafniyum diborür tozları iki farklı sinterleme tekniđi kullanılarak yıđın yapılar haline getirilmiřtir. Seçilen optimum üretim parametreleri ile elde edilmiş yüksek kalitedeki tozlara sođuk presleme/basınçsız sinterleme (Co katkısı ile veya katkısız) ve spark plasma sinterleme teknikleri uygulanmıştır. Sinter numunelerin yoğunlukları ve mikroyapısal özellikleri Archimed metodu ve XRD, SM, SEM/EDX teknikleri ile belirlenmiştir. Ayrıca, sinter ürünlerin mekanik özellikleri mikrosertlik ve aşınma özellikleri olarak değerlendirilmiştir.

Son olarak, bu çalışma bor madenlerimizin katma değeri yüksek ürünlere dönüřtürülmesi yolunda ilerlemeye katkı verirse bundan onur duyarım.





1. INTRODUCTION

Transition metal diborides are promising materials for a variety of high temperature structural applications and they are referred to as ultra-high temperature ceramics (UHTCs). In recent years, the UHTCs have drawn considerable attention especially by the emerging developments in the hypersonic aerospace vehicles and rocket propulsion (Monteverde et al., 2008; Simonenko et al., 2013; Upadhyaya et al., 1997). Hafnium diboride (HfB_2) is one of the leading members of this class of materials. It has a melting point of 3380 °C, which is higher than many ceramic materials and also higher than few advanced ceramics whose melting temperatures are over 3000 °C (Post et al., 1954; Upadhyaya et al., 1997). Hafnium diboride has a high oxidation resistance as a consequence of the stability of the HfO_2 layer formed on its surface by oxidation at high working temperatures (Fahrenholtz et al., 2007). Additionally, it has remarkable properties including high hardness, low thermal expansion coefficient, high thermal and electrical conductivities (Fahrenholtz et al., 2007; Post et al., 1954; Upadhyaya et al., 1997). Because of its very high melting point, corrosion resistance and thermal shock resistance, HfB_2 has been considered and investigated as a candidate for thermal protection systems in extreme environments especially for sharp leading edges of high velocity flights or atmospheric re-entry vehicles (Monteverde et al., 2008; Simonenko et al., 2013). It has found several applications as furnace elements, plasma arc electrodes, refractory linings, wear resistant coatings, control rods and heating shields in nuclear reactors owing to these superior characteristics (Cheminant et al., 1997; Fahrenholtz et al., 2007; Jayaraman et al., 2006; Monteverde and Bellosi, 2005; Opeka et al., 1999; Post et al., 1954; Savino et al., 2008; Wang et al., 2002).

Hafnium diboride has been prepared by various techniques including reaction between elemental powders of Hf and B, solid-state borothermal and boron carbide reduction methods, self-propagating high-temperature synthesis (SHS), sol-gel method, hydrothermal synthesis, chemical vapor deposition (CVD) and milling-assisted processes. Although the reaction between elemental hafnium and

boron is thermodynamically more favorable, the use of expensive raw materials cannot be considered as a commercial method. Elemental powders have also been used to produce bulk HfB₂ ceramics by spark plasma sintering (SPS) and dynamical consolidation techniques (Anselmi-Tamburini et al., 2006; Brochu et al., 2008; Musa et al., 2013). The conventional borothermal and borothermal/carbothermal reduction methods of HfO₂ in which amorphous boron and B₄C are used as boron and boron/carbon sources, is generally carried out at elevated temperatures above 1500 °C (Guo et al., 2012b; Ni et al., 2008; Ni et al., 2010; Peshev et al., 1968; Sonber et al., 2010; Zhang et al., 2009). Expensive equipment requirements and relatively high working temperatures are main drawbacks of these methods. Moreover, the lowest synthesis temperature was reported as 600 °C in the case of utilizing a hydrothermal method in an autoclave starting from HfCl₄ and NaBH₄ powders (Chen et al., 2004c). However, the usage of relatively few amounts of reactants (in order of mmol) and relatively small scale of the equipment restrict the application of process. Formerly, nano-sized HfB₂ powders with low oxygen content were synthesized by means of solution-based methods (Venugopal et al., 2013; Venugopal et al., 2014; Wang et al., 2014b). Wang et al. (2014) synthesized HfB₂ powders by boro/carbothermal reduction method using solution-based mixing route from HfCl₄, B₄C and phenolic resin in SPS apparatus between 1300-1500 °C. Venugopal et al. (2013) used sol-gel synthesis method for the preparation of HfB₂ powders: HfCl₄ and H₃BO₃ as soluble compounds and phenolic resin as a reducing carbon source were mixed in a solution medium which enhances the homogeneous dispersion of raw materials and they were annealed at 1300 °C for 25 h or at 1600 °C for 2 h. Although sol-gel method provides homogeneous dispersion of different raw materials, high temperatures are still needed to ensure the following carbothermic reduction. Furthermore, the CVD methods are generally employed with the aim of obtaining hard surface coatings rather than powder synthesis in order to improve the surface hardness and tribological properties of desired materials (Jayaraman et al., 2005; Jayaraman et al., 2006; Yang et al., 2006). Electrochemical fabrication of HfB₂ coatings with columnar structure was carried out in the NaCl–KCl–KBF₄–K₂HfF₆ molten salt at a temperature range of 700-850 °C and a cathode current density of 5-50×10⁻³A.cm⁻² (Kuznetsov, 2012). Additionally, single crystals of HfB₂ were prepared by floating zone method by means of radio frequency (RF) heating (Otani et al., 1998). Furthermore, some attempts were made by milling-assisted annealing

processes: HfO₂-HfB₂ composite powders were produced by high-energy ball milling (5, 7, 11 and 30 h) and annealing (at 900, 1100 and 1300 °C for 6, 12 and 18 h) of HfO₂-B₂O₃-Mg powder blends (Balci et al., 2010). Barraud et al. (2005) synthesized HfB₂ nanorods from HfCl₄-B and HfCl₄-B-Mg powder mixtures by mechanical activation and isothermal annealing.

On the other hand, there are intense research efforts to develop efficient methods for preparing these transition diborides in high purity, small particle size and various morphologies. Also, new synthesis methods utilizing low energy consumption, simple precursors with low-cost and environment-friendly production have gained importance in recent years.

In this study, it was aimed to prepare hafnium diboride powders with novel methods which provide several advantages such as usage of economical raw materials, utilization of simple equipment, reduced or low reaction temperature and scalable processes. Apart from the above mentioned methods, mechanochemical synthesis, mechanically activated synthesis and low-temperature autoclave synthesis routes were investigated using hafnium tetrachloride as hafnium source and using different boron compounds which are B₂O₃, amorphous B and NaBH₄ as boron sources. In this dissertation, mechanochemical synthesis of hafnium diboride powders from HfCl₄-B₂O₃-Mg and HfCl₄-B-Mg powder blends were applied for the first time in the literature according to the best of our knowledge. In addition, mechanical activation was applied to some precursors to enable the reaction at lower temperatures during the autoclave synthesis and the borothermal synthesis routes. Also, low temperature autoclave synthesis was investigated as an alternative method to the conventional high temperatures methods.

Mechanical activation induced by high-energy ball milling enables to reduce the synthesis temperature during subsequent heat treatment due to the formation of active reactant particles and their homogeneous distribution throughout the microstructure. During the activation process, high amount of energy evolved by ball to ball or ball to wall collisions can be accumulated in the particles in the form of structural defects (such as stacking faults, dislocations, vacancies in crystalline lattice, etc.) (Balaz, 2008; Boldyrev and Tkacova, 2000; Butyagin, 1984; McCormick and Froes, 1998; Murty and Ranganathan; 1998; Sopicka-Lizer, 2010; Suryanarayana, 2001). Thus, in the borothermal reduction and autoclave synthesis

routes, mechanical activation is expected to create active particle surfaces, to distribute these particles homogeneously throughout the microstructure, to reduce the synthesis temperature and particle size of the final powders, and to increase the process efficiency.

Although autoclave or solvothermal synthesis methods are quite new applications for preparation of boride compounds, they have been attracting great research interest owing to some their advantages. These methods enable to control size and morphology and to obtain the nanopowders in rod, cube or sheet morphologies (Chen et al., 2012; Ma et al., 2003). Moreover, autoclave synthesis is considered as an environmentally friendly method because the process proceeds in a closed/isolated system and it saves energy by using low synthesis temperatures (Feng and Li, 2011; Feng and Xu, 2001). It was stated that the usage of relatively mild temperatures which are high enough to trigger crystallization but still low enough to avoid excessive grain growth, ideally in the range of 500-900 °C, enables to obtain nanostructures (Portehault et al., 2011). In a previous study, HfB₂ powders were prepared by a reaction of HfCl₄ with NaBH₄ at 600 °C in an autoclave and it was stated that the powders had small particle morphology with a particle size in the range of 20-30 nm in diameter (Chen et al., 2004c). Also, in some studies, it was shown that various boride compounds such as ZrB₂, TiB₂ and LaB₆ could be produced by autoclave synthesis route in different morphologies like rods, cubes or flakes (Chen et al., 2012; Ma et al., 2003; Zhang et al., 2008).

Densification of monolithic HfB₂ powders is fairly difficult and requires harsh conditions due to the strong covalent character of bonding and low self-diffusion rates (Sonber et al., 2010; Sonber and Suri, 2011; Telle et al., 2000). In earlier studies (1970s or earlier) hot-pressing was the most common densification method for the HfB₂-based ceramics (Fahrenholtz et al., 2007; Fahrenholtz et al., 2014; Zhang et al., 2009). However, researches have been focused on activated sintering and modern sintering techniques such as spark plasma sintering in recent years. Metallic additives and liquid-phase sintering aids are applied to promote densification so that larger components with more complex shapes can be produced rather than hot-pressing (Fahrenholtz et al., 2007). Various additives have been added to enhance the densification rates of hafnium diboride such as SiC, HfN, HfC and MoSi₂ (Fahrenholtz et al., 2007). As an example, Monteverde et al. (2005)

reached full density for HfB₂-30 vol.% SiC by SPS technique applying at 2100 °C with 2 min hold time under 30 MPa. On the other hand, there is limited number of studies on the consolidation of HfB₂-HfO₂ ceramics. Li et al. (2009) investigated the preparation of ZrB₂-ZrO₂ ceramics by hot pressing and it has been stated that the ZrO₂ content is beneficial for the densification of ZrB₂.

In this dissertation, novel synthesis methods and simple raw materials were employed for the synthesis of hafnium diboride-based powders. HfCl₄ powders were used as hafnium source while B/B₂O₃/NaBH₄ and Mg were used respectively as boron sources and metallic reducing agent. The mechanically activated borothermal reduction, mechanochemical synthesis and low-temperature autoclave synthesis (without and with mechanochemical activation) routes were applied to different reactant blends. Hafnium diboride (HfB₂) powders were synthesized by mechanically activated borothermal synthesis from HfCl₄-B blends. In addition, mechanochemical synthesis route was applied to HfCl₄-B₂O₃-Mg and HfCl₄-B-Mg blends for preparing HfB₂-HfO₂ and HfB₂ powders. Moreover, mechanically activated autoclave synthesis was investigated to synthesis of HfB₂-HfO₂ powders starting from HfCl₄-B₂O₃-Mg blends. Furthermore, HfCl₄-NaBH₄-Mg blends were utilized for production of HfB₂ powders by low-temperature autoclave process. The applied powder systems were thermodynamically interpreted by utilizing the FactSageTM 6.2 thermochemical software to predict the reaction mechanisms. The detailed characterization investigations of synthesized powders were performed using X-ray diffractometer (XRD), particle size analyzer (PSA), stereomicroscope (SM), scanning electron microscope/energy dispersive spectrometer (SEM/EDS) and transmission electron microscope (TEM). The synthesized HfB₂-based powders were consolidated by two different sintering techniques. The cold pressing/pressureless sintering (with and without Co addition) and spark plasma sintering techniques were applied to selected high quality powders which were obtained by optimum process parameters. The densification behaviour and microstructural characterization of the sintered samples were investigated using density measurement by Archimedes method and XRD, SM, SEM/EDX techniques. Mechanical properties of consolidated products were determined in terms of microhardness, wear properties, elastic modulus, indentation behaviour and fracture toughness.

2. LITERATURE REVIEW

The refractory borides have several distinct properties and many of these properties are of great interest for technical applications. Diborides of IV-B group transition metals (TiB_2 , ZrB_2 and HfB_2) are referred as ultra-high temperature ceramics (UHTCs) (Fahrenholtz et al., 2007; Simonenko et al., 2013). They are characterized by relatively high melting point, great hardness and most of them, good electrical and thermal conductivity. They also exhibit further characteristics such as good corrosion and wear resistance and a thermal shock resistance much better than that of oxide ceramics (Fahrenholtz et al., 2007; Mallik et al., 2012; Monteverde et al., 2008). Among all refractory metal borides, ZrB_2 and HfB_2 are considered as potential candidates to withstand temperatures in the 1900-2500 °C range, by means of their very high melting point and superior oxidation resistance which is attributed to the stability of the ZrO_2 and HfO_2 scales. The leading features of these materials make them candidates for use in various high temperature applications, such as hypersonic vehicles, and high temperature shielding (Fahrenholtz et al., 2007; Telle et al., 2000; Wang et al., 2002; Upadhyaya et al., 1997)

2.1 Physical, Chemical and Structural Properties and Application Areas of Hafnium Diboride

Hafnium diboride (HfB_2) is one of the leading members of UHTCs family. The most common definition for UHTCs is a material has a melting point over 3000 °C. Very few materials meet this criterion (Fahrenholtz, 2014) as shown in Figure 2.1. Along with zirconium and hafnium diborides, several carbides and nitrides of the IVB and VB transition metals are also considered as UHTCs, based on melting temperature over 3000 °C and other properties (Fahrenholtz, 2014; Telle et al., 2000). HfB_2 has leading properties including very high melting point (3380 °C) which is higher than many ceramic materials and also higher than few advanced ceramics

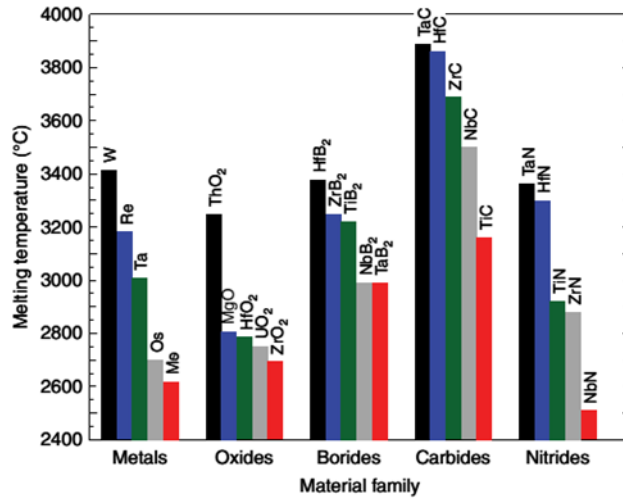


Figure 2.1 : Materials with the highest reported melting temperature grouped by material family, adapted from Fahrenholtz, 2014.

whose melting temperatures are over 3000 °C (Monteverde et al., 2008; Post et al., 1954; Upadhyaya et al., 1997;). It has a high oxidation resistance as a consequence of the stability of the HfO₂ layer formed on its surface by oxidation at high working temperatures (Fahrenholtz et al., 2007). Of the known diborides, HfB₂ has the highest bulk hardness (29 GPa) (Fuller and Sacks, 2004; Jayaraman et al., 2006). Additionally, it has low thermal expansion coefficient, high thermal and electrical conductivities (Ghosh and Subhash, 2013; Telle et al., 2000). The summary of

Table 2.1 : Summary of some structural and physical properties of HfB₂, adapted from Fahrenholtz, 2007.

Property	
Crystal System	Hexagonal
Lattice parameters (nm)	a=b=0.314, c=0.347
Density (g/cm ³)	11.212
Melting point (°C)	3380
Young's modulus (GPa)	480
Bulk modulus (GPa)	212
Hardness (GPa)	28
Coefficient of thermal expansion (K ⁻¹)	6.3x10 ⁻⁶
Heat Capacity at 25°C (J.(mol.K) ⁻¹)	49.5
Electrical conductivity (S/m)	9.1x 10 ⁶
Thermal conductivity (W.(m.K) ⁻¹)	104

structural and physical properties of HfB_2 is presented in Table 2.1. The effect of mainly covalent character of chemical bonds in HfB_2 shows itself in the properties such as high elastic modulus, chemical stability at room and high temperatures (Ghosh and Subhash, 2013). On the other hand, HfB_2 has a good combination of properties which observed both in metals and ceramics (Ghosh and Subhash, 2013; Fahrenholtz et al., 2007). The high melting point, high elastic modulus (>400 GPa), and thermo-chemical stability are in accordance with ceramic character. Additionally, it surprisingly has high electrical and thermal conductivity in contrast to typical structural ceramics. The exact mechanism of high electrical conductivity in $\text{Hf}(\text{Zr})\text{B}_2$ ceramics is not known, but it was proposed that it originates from $\text{Hf}(\text{Zr})$ - $\text{Hf}(\text{Zr})$ metallic bonding (Ghosh and Subhash, 2013; Zhang et al., 2008).

Although there exists a mature literature information on processing of these composites, further investigations are still needed to be carried out on the mechanical properties of these advanced ceramics both on room and elevated temperatures (Ghosh and Subhash, 2013).

The wide scattered data in the mechanical properties such as hardness, elastic modulus and fracture strength of HfB_2 is probably due to differences in consolidation techniques, consolidation parameters, purity and grain size of starting powders (Fahrenholtz et al., 2007). The evaluated values for some mechanical properties of HfB_2 determined in different studies are given in the Table 2.2. It was stated that large grain size are detrimental to mechanical strength due to residual thermal stresses that is caused by thermal expansion anisotropy.

Young's modulus of HfB_2 was evaluated in the range of 480-510 GPa (Fahrenholtz et al., 2007; Ghosh and Subhash, 2013). It was reported in the former studies that the elastic modulus was affected by the dispersed particulates (Ghosh and Subhash, 2013). Hardness values of HfB_2 ceramics and their composites are mainly reported as Vickers. Hardness values are generally relatively high because of the covalent character of chemical bonds. For the monolithic HfB_2 ceramics, the maximum hardness value was reported as 28 GPa (Telle et al., 2000). However, hardness values were generally determined in the range of 8.7-16 GPa in the literature, as a result of relative density, grain size, load and porosity (Ghosh and Subhash, 2013; Fahrenholtz et al., 2007). Because of relatively high melting temperature of HfB_2 , it is very hard to reach full density even after utilizing modern sintering techniques.

Thus sintering aids such as SiC, B₄C, HfN HfC, WC, etc. are generally used as secondary phases (Ni et al., 2012a; Ni et al., 2012b; Sciti et al., 2008; Wang et al., 2012; Wang et al., 2014a; Zou et al., 2010;). These phases affect the hardnesses of HfB₂ composites and generally higher hardness values were observed mainly due to higher relative density and restricted grain growth (Ghosh and Subhash, 2013).

The Young's moduli of HfB₂ are high similarly due to the highly covalent character of bonding and are at around 500 GPa with and without SiC addition. However, they decrease gradually above the temperature of 800 °C, as can be seen in Table 2.3 (Rhodes et al., 1970; Ghosh and Subhash, 2013).

Table 2.2 : The mechanical properties of HfB₂ and HfB₂ composites depended on sintering techniques, conditions and composition.

Composition	Tech.	Operating Conditions	Density, %	Hardness (GPa)	Modulus (GPa)	Reference
HfB ₂	HP	2160°C, 3sa, 27.3 MPa	-	-	445	Opeka et al., 1999.
HfB ₂	PS	2350 °C, 2 h	85.6	-	-	Zou et al., 2010.
HfB ₂ -2w.1% B ₄ C	PS	2200 °C, 2 h	98	19.5	529	Zou et al., 2010.
HfB ₂ -15vol.%MoSi ₂	SPS	1700 °C	94.7	15.7	519	Sciti et al., 2008.
HfB ₂ -20vol.%SiC	HP	2000 °C, 1h, 30 MPa	93.8	18.3	-	Weng et al., 2009.
HfB ₂ -22vol.%SiC-6vol.%HfC	HP	1900 °C	99.2	19	520	Monteverde and Bellosi, 2005.

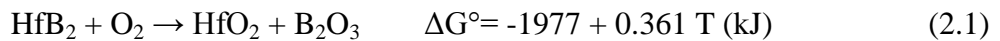
The flexural strength of HfB₂ can also show variations because of differences in process conditions, grain size and impurities. Higher strength values are generally obtained with finer grain size. The residual impurities can be points of stress in the material and limits the strength of HfB₂. According to Table 2.3, strength decreases above 800 °C, however these results have not been confirmed (Ghosh and Subhash, 2013).

Table 2.3 : The mechanical properties of HfB₂ and HfB₂ composites depended on temperature (Rhodes et al., 1970; Ghosh and Subhash, 2013)

Material	Temp. (°C)	Young's Modulus (GPa)	Flexural Strength (MPa)	Poisson's Ratio	Hardness (GPa)
HfB ₂	23	530	480	0.12	21.2- 28.4
	800	485	570	-	-
	1400	300	170	-	-
	1800	-	280	-	-
HfB ₂ -20vol.%SiC	23	540	420	-	-
	800	530	380	-	-
	1400	410	180	-	-
	1800	-	280	-	-

There exist different values for the electrical resistivity of HfB₂ in literature which vary between 6.3–16.6 μΩ.cm (Samsonov et al., 1971). The different values reported in the literature are based on the strong influence of production parameters, purity of product and grain size of the constituent phases and relative density of composite. The thermal conductivity of HfB₂ at 25 and 1027 °C were reported as 105 and 60 W/mK, respectively (Cutler, 1991; Opeka et al., 1999). The high thermal conductivity can cause good thermal shock resistance at the same time, as a result of fast removal of heat from a local area so that thermal gradients can be kept minimum (Mallik et al., 2012). In addition, the thermal shock resistance is partially depends on coefficient of thermal expansion (CTE) which related with thermal stress introduced in to material during a high temperature application (Mallik et al., 2012). The thermal expansion coefficient for the monolithic HfB₂ was reported as 6.3×10⁻⁶ K⁻¹ (Cutler, 1991). Addition of SiC with lower CTE is shown to reduce the thermal expansion of HfB₂, which is expected to improve the dimensional stability (Mallik et al., 2012).

HfB₂ and ZrB₂ encountered oxidizing conditions (at elevated temperatures), reactive environments (e.g., molten slags) and erosive conditions in many proposed applications. Thus, the oxidation properties of these materials have been investigated extensively. These diborides are capable in withstanding high temperatures in the range of 1900-2500 °C as a result of their high melting point and their ability to form refractory oxide scales. It was shown that HfB₂ undergoes an oxidation reaction when it is contacted with air at elevated temperatures, where HfO₂ and B₂O₃ form on the surface according to (2.1).



Berkowitz-Mattuck (1966) investigated the oxidation of zone melted HfB₂ between 927 and 1727 °C with the oxygen partial pressure of 1-700 Torr in helium. Pertinent TGA analyses have shown that negligible amounts of mass gain up to 700 °C, whereas below 1100 °C, HfO₂ and B₂O₃ formed and a passive oxidation protection was provided (Bargeron et al., 1993; Fahrenholtz, 2014). It was concluded that the rate limiting step for oxidation was the oxygen transport through B₂O₃ which resulted in mass gain or reaction layer thickness (Fahrenholtz et al., 2007; Savino et al., 2008). In the temperature range between 1100 and 1400 °C, a combined effect of

mass gain and loss due to the evaporation of B_2O_3 and the formation of condensed oxides were observed (Fahrenholtz et al., 2007; Savino et al., 2008). A porous layer of HfO_2 forms by B_2O_3 evaporation under the small amount of remained B_2O_3 and mass gain was generally dominant. Moreover, at the exceeding temperatures over $1400\text{ }^\circ\text{C}$, oxide layer was not protective anymore and rapid mass gain kinetics were recorded. Additionally, an increase in the rate of oxidation was reported at around $1700\text{ }^\circ\text{C}$, with monoclinic to tetragonal phase transformation of HfO_2 (Berkowitz-Mattuck, 1966, Carney et al., 2014; Fahrenholtz, 2007; Levine et al., 2002; Monteverde and Bellosi, 2005).

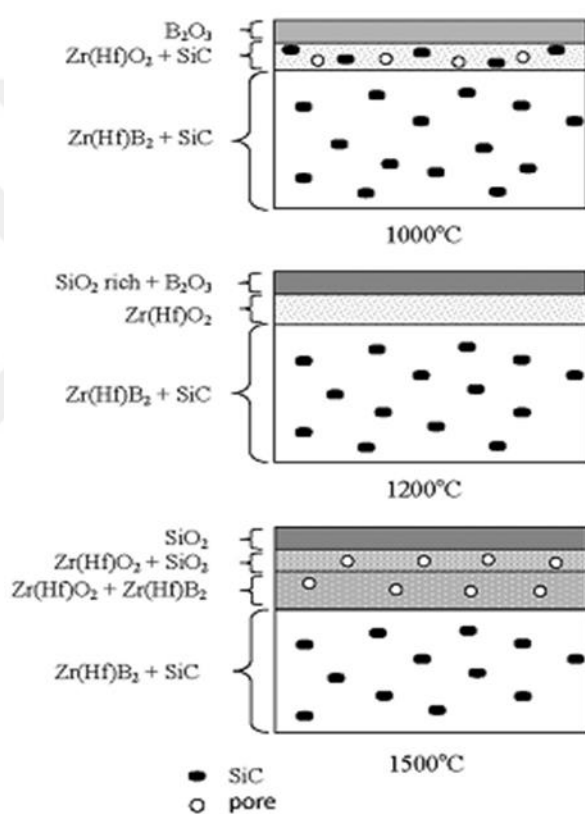


Figure 2.2 : Evolution of structures in $Zr(Hf)B_2$ -SiC composites during oxidation at: (a) $1000\text{ }^\circ\text{C}$, (b) $1200\text{ }^\circ\text{C}$, and (c) $1500\text{ }^\circ\text{C}$, adapted from Ghosh and Subhash, 2010.

The sintering additives give rise to differences in the oxidation behavior of HfB_2 . It was stated that SiC which is most common additive reduces the oxidation rate by forming a silica-rich scale (Nguyen et al., 2004; Monteverde and Bellosi, 2005; Tripp and Graham, 1971). The addition of SiC does not change the oxidation behavior of HfB_2 and ZrB_2 below $1100\text{ }^\circ\text{C}$ since the oxidation rate of SiC is much lower than those of diborides up to this temperature (Nguyen et al., 2004). Over this temperature, there exist two factors that affect the oxidation behavior: SiC oxidation

becomes faster and SiO₂ particles and CO and CO₂ gases form, at the same time, the rate of B₂O₃ evaporation increases significantly. The weight change of ZrB₂ and ZrB₂-20 vol.% SiC during heating to 1500 °C was measured by thermal gravimetric analysis (TGA) by Opeka et al. (2004). According to Figure 2.2., HfB₂-SiC shows a mass loss between 1200 and 1300 °C due to B₂O₃ evaporation and then mass gain is observed by protective behavior of silica-rich layer up to 1600 °C.

In terms of chemical properties, hafnium diboride is attacked by different acids at room temperature such as HNO₃ and H₂SO₄ and it is soluble in some boiling acids (Weimer, 1977). The solubility of hafnium diboride in water and different acids is given in Table 2.4.

Table 2.4 : Effect of reagent and treatment on solubility of hafnium diboride (stability of 10-15 µm), adapted from Weimer, 1997.

Reagent	Treatment	Solubility, %	Degree of oxidation with gases weight gain (g/m ²)
H ₂ O	100 °C	0	-
HCl	20 °C, 2 h	20-40	-
	100 °C, 2 h	100	-
H ₂ SO ₄	2 h	100	-
HNO ₃	Boiling, 30 min	100	-
H ₃ PO ₄	Boiling, 2 h	100	-
NH ₄ OH	2 h	0	-
H ₂ O ₂	2 h	0	-
Air	500-600 °C	-	None

HfB₂ is considered as a radiation shielding, control rod in fission reactor power plants (pressurized water reactors (PWR)) and it has potential usage in fusion facilities, e.g. first wall of fusion reactors due to the existence of boron which has a high thermal neutron cross section and its good thermal and mechanical properties (Cheminant-Coatanlem et al., 1998; Nasser, 2015). Moreover, its relatively low cost of fabrication, high melting point and low neutron activity after irradiation, make it attractive for such applications (Cheminant et al., 1997). However, the behavior of these materials under irradiation has not been thoroughly understood yet (Simeone et al., 1997). Of the HfB₂ elements, boron (B) has two naturally stable isotopes ¹¹B (80.1% isotopic abundance) and ¹⁰B (19.9% isotopic abundance), at that ¹⁰B isotope has a larger neutron cross-section than ¹¹B isotope with 3980 barn. The ¹⁷⁴Hf and

^{180}Hf (with 0.0006% isotopic abundance) isotopes have neutron cross-section of 14 and 1500 barn, respectively (Nasseri, 2015). In a former study, the behaviors of different high density boride pellets under neutron irradiation were investigated by irradiating them in the temperature range between 350-500 °C in a reactor. The results showed that especially HfB_2 has low swelling rate and lowest helium release during the subsequent annealing (Gösset and Kryger, 1993). In addition, $\text{HfB}_2\text{-B}_4\text{C}$ composites illustrated better thermo-mechanical properties as compared to pure B_4C such as the thermal gradients for crack initiation by thermal shocks were higher (Gösset and Kryger, 1993). It was also asserted that the higher melting point, chemical inertness and good mechanical properties of HfB_2 provide some advantageous in regard of safety point. As a result, neutron absorption properties of boron coupled with the high temperature properties of HfB_2 makes these borides the ideal candidates for control/shutoff rod material for high temperature in compact type nuclear reactors (Gösset and Kryger, 1993; Nasseri, 2015).

HfB_2 has a primitive hexagonal Bravais Lattice and AlB_2 -type crystal structure (space group $P6/mmm$) and consists in a repeated stacking of a graphite-like boron layers separated by hexagonal closed-packed transition metal layers (Barraud et al., 2005; Fahrenholtz et al., 2007). The unit cell contains one MB_2 formula unit. The structure consists of layers of B atoms in graphite-like 2D nets and hexagonal close-packed M layers. Each hafnium atom belongs to 12 trigonal prisms and the composition is simply $\text{M}_6/12\text{B}$. A schematic representation of the crystal structure of HfB_2 is illustrated in Figure 2.3 (a) and (b), adapted from Sichkar and Antonov (2013) and Fahrenholtz et al., 2007. The inter-layer interaction is strong in this structure despite the Hf layers alternate with the B layers in their crystal structure. The hafnium atoms are located at the centers of boron hexagons with the three nearest neighbor boron atoms in each plane. The boron atoms sit at the corner of hexagons with the three nearest neighbor boron atoms on each plane (Barraud et al., 2005; Sichkar and Antonov, 2013; Zhou et al., 2014). In addition, it was stated that it can be expected that the physical properties of diborides are highly anisotropic because of their layered structure and the extent of the anisotropy varies depending on c/a axial ratios. On the other hand, due to the difficulties in growing monocrystals of transition metal diborides mainly as a result of their high melting point, very little

is known about how their physical properties change with crystallographic directions (Okamoto et al., 2010).

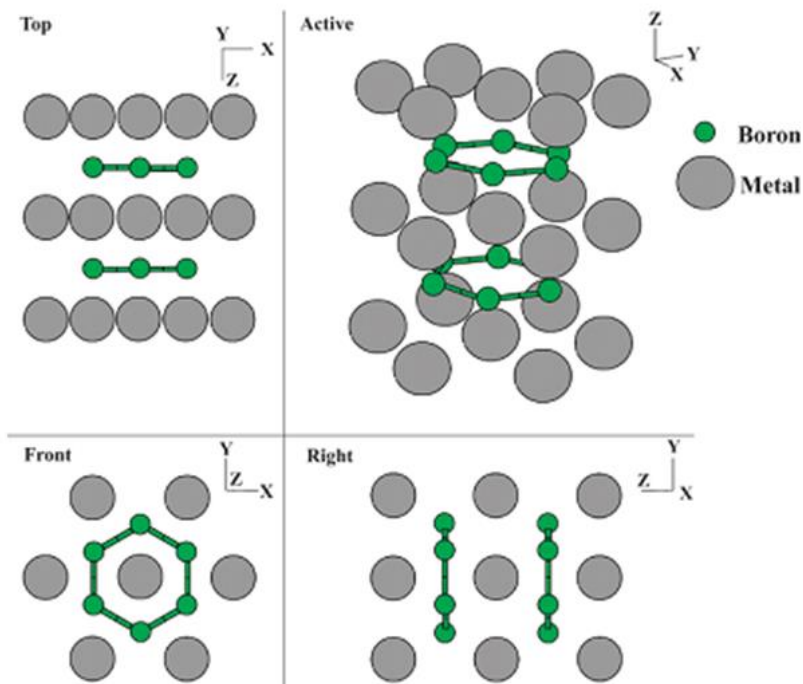


Figure 2.3 : The schematic representation of crystal structure and the AlB_2 type structure of HfB_2 adapted from Fahrenholtz et al., 2007.

The Hf-B binary phase diagram is given in Figure 2.4 (Massalski, 1990). The experimental data for Hf-B phase diagram was published by Rudy and Portnoi (1972) and critically assessed by Okamoto et al. (2010) (Cacciamani et al., 2011). The accepted melting points of zirconium free hafnium and boron are given as 2231 and 2092 °C, respectively. The α/β transformation temperature for hafnium is stated as 1743 °C. The solubility of B in α Hf is limited (< 0.5 at.% B) at lower temperatures although it increases with increasing temperature and lead to peritectoid decomposition of the α -Hf solid solution into β -Hf and HfB at around 1800 °C. An interstitial solution is suggested for B in the α -Hf and B amount in β -Hf at the eutectic temperature was reported as less than 2 at.%. In addition, HfB_2 melts congruently at 3380 °C, the highest among the refractory borides and HfB forms by a peritectic reaction at around 2100 °C (Bittermann and Rogl, 1997; Cacciamani et al., 2011; Massalski, 1990).

Making use of the advantages of above mentioned properties such as high melting point, high hardness, chemical and thermal stability, high thermal and electrical

conductivity, the application areas of HfB_2 are those which endure extreme chemical and thermal environments.

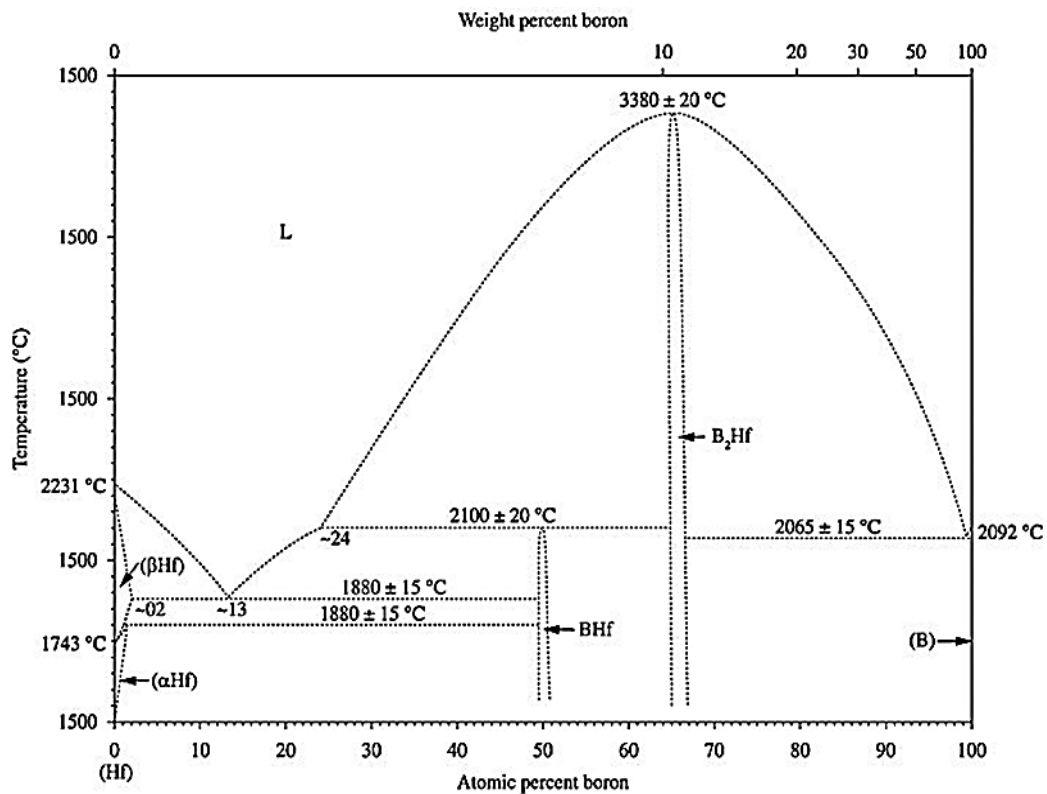


Figure 2.4 : The Hf-B binary phase diagram, adapted from Massalski, 1990.

Owing to chemical inertness with molten metals, potential industrial usage areas for HfB_2 are foundry or refractory processing of materials such as electrodes in arc furnace, refractory lining, metal crucibles and wear resisting coatings and as parts for electrical devices such as heaters and igniters (Gasch et al., 2004; Upadhyya et al., 1997). Similarly, they are used as cathode materials in Hall-Heroult cell cathodes and thermowell tubes for steel refining (Bellosi et al., 2006).

Because of recent efforts to develop hypersonic aerospace vehicles and re-usable atmospheric re-entry vehicles, interest in UHTCs has increased significantly in the past few years (Gasch et al., 2004; Levine et al., 2002). HfB_2 and ZrB_2 are potential materials for used as thermal protection systems in extreme conditions especially for scramjet propulsion, rocket propulsion, atmospheric re-entry vehicles, and sharp leading edges of hypersonic aircraft (Levine et al., 2002; Upadhyya et al., 1997). The UHTCs have recently gained importance by their combined properties as enduring materials in the ultrahigh temperature regime (considered to begin at 1600 °C) and in highly oxidizing environments (Fahrenholtz et al., 2007; Monteverde et al., 2008).

Thus, they are in high demand for thermal shields parts of hypersonic aerospace vehicles and re-usable atmospheric re-entry vehicles. The sharp nose tips and wing leading edges (WLEs) shown in Figure 2.5, in the high-performance hypersonic vehicles provide reduced drag of vehicle and enhance maneuverability and performance (Ghosh and Subhash, 2013). Due to the convective heating of sharp WLEs, surface temperature on the stagnation region has the potential of heating over 2000 °C. The dimensional and structural integrity and mechanical strength at these high temperatures are the main challenges in such a design. The thermal conductivity plays an important role on the conduction of heat away to the cooler region of leading edge (Figure 2.6.) (Cheminant et al., 1997; Jayaraman et al., 2006; Fahrenholtz et al., 2007; Monteverde and Bellosi, 2005; Savino et al., 2008; Opeka et al., 1999; Post et al., 1954; Wang et al., 2002).

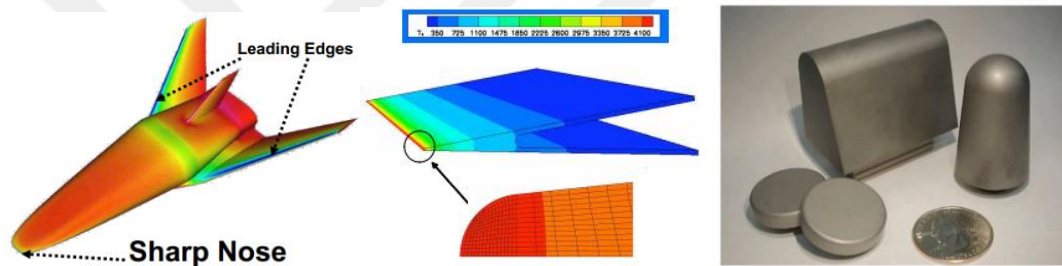


Figure 2.5 : The leading edges in the high performance hypersonic vehicles, adapted from Url-1.

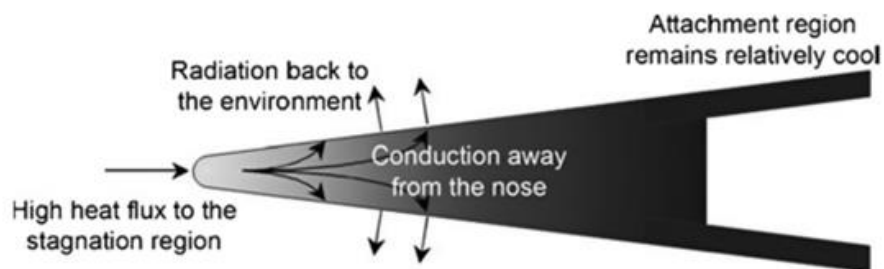


Figure 2.6 : A schematic of the thermal management process in the UHTC leading edge component, adapted from Ghosh and Subhash, 2013.

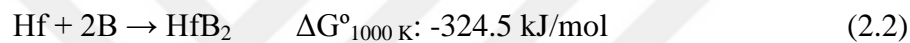
Indeed, the investigations of dense diboride ceramics were initially motivated by nuclear field that high neutron absorption cross sections were needed. Afterwards, researches shifted to aerospace applications. HfB_2 is a potential material as a neutron absorber in nuclear reactor control rods and heating shields in nuclear reactors (Cheminant et al., 1997; Opeka et al., 1999; Post et al., 1954; Wang et al., 2002).

2.2 Production and Sintering Techniques of Hafnium Diboride

2.2.1 Production techniques

Hafnium diboride has been synthesized by various production techniques such as borothermal reduction, carbothermal/borothermal reduction, self-propagating high-temperature synthesis (SHS), sol-gel method, mechanochemical synthesis, reactive spark plasma sintering, solvothermal processes and chemical vapor deposition routes. Synthesis of hafnium diboride from elemental powders of Hf and B was investigated by various researchers. In general, self-propagating high temperature synthesis, reactive spark plasma sintering and mechanochemical synthesis routes were applied for this purpose.

Brochu et al. (2008) used shock consolidation process to produce HfB_2 powders according to the reaction 2.2:



The elemental powders of hafnium and crystalline boron were mixed in a mortar with isopropyl alcohol medium, then the powder mixture was cold pressed in seamless steel tubing (65% theoretical density was reached) and the end plugs were welded. In the shock consolidation process, a single tube cylindrical implosion system was used to consolidate the powder mixtures. The test tubes were centered in a cardboard tube and filled with ammonium nitrate/fuel oil explosive. After the compaction, consolidated samples were removed by machining. Then a heat treatment was applied to samples at 1600, 1800 and 2000 °C for 1 h in a controlled atmosphere furnace equipped with tungsten heating element. A relative density of 62% was obtained and it was stated that the heat treatment temperature did not have any particular effect on the final density. This low densification value was attributed to the covalent character of Hf-B bonds and low volume and grain boundary diffusion rates in diborides. The angular shape pores were still observed after the heat treatment at 2000 °C, so the temperature range of the heat treatment was thought to be too low to promote the any change in pore morphology (Brochu et al.; 2008).

Musa et al. (2013) synthesized hafnium diboride powders via self-propagating combustion and reactive spark plasma sintering techniques. Hf and amorphous B as starting powders were mixed for 20 min using a SPEX 8000 shaker mill in plastic

bottle with zirconia balls. The powder mixture was pressed into cylindrical pellets and then reacted by SHS to fabricate HfB₂ powders according to reaction 2.3:



X-ray diffraction (XRD) spectra of the SHS products having different B/Hf atomic ratios indicated the presence of residual elemental Hf when started from stoichiometric ratios. B deficiency because of volatile B₂O₃ formation caused by this situation. To compensate this loss, molar ratio of x was utilized as 0.1 in reaction (2.3). In addition, spark plasma sintering was applied to synthesized HfB₂ powders although maximum relative density achieved was only 93%. Due to the unsatisfactory densification obtained by SHS technique, simultaneous synthesis and densification by reactive spark plasma sintering (RSPS) of Hf and B powders was alternatively applied. In this method, HfB₂ formation occurs simultaneously for the duration of consolidation. A combustion synthesis reaction was stated to take place at temperatures between 500 and 600 °C during the RSPS process. Relatively high densification rate (almost 99% relative density) was obtained in 30 min with 1350 A under 20 to 50 MPa just after the formation of the synthesis reaction. On the other hand, composites reinforced with SiC whiskers could not be produced by RSPS due to the heat created by reaction which gave rise to whiskers degradation (Musa et al.; 2013).

Anselmi-Tamburini et al. (2006) utilized a similar reactive spark plasma sintering route to synthesize HfB₂ from elemental powders. The simultaneous synthesis and consolidation of diboride (reactive sintering) from stoichiometric amounts of Hf and B were conducted at 1700 °C with a holding time of 10 min and an applied uniaxial pressure of 95 MPa. The reaction between the elements was recorded at temperatures as low as 1100 °C and was completed relatively at a wide temperature range. In addition, the densification was observed after diboride formation completed (Anselmi-Tamburini et al.; 2006).

As an another example for HfB₂ synthesis from elemental powders, HfB₂ powders were prepared through mechanochemical synthesis route from elemental Hf and B powder mixtures in a planetary ball mill (Makarenko et al., 2015). The ball-to-powder weight ratio was 20:1 and steel balls with diameter of 9.5 mm were used. It was stated that the HfB₂ formation started after 10 min of milling in the presence of

metastable HfB phase. The single-phase HfB₂ composition was obtained after 60 min of milling (Makarenko et al., 2015).

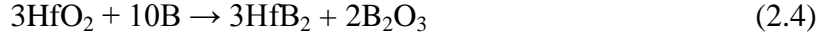
Additionally, ZrB₂ powders were synthesized from elemental Zr and B powders by mechanical alloying in a planetary ball mill at 250 rpm for 10-20 h. Tungsten carbide vial and balls were utilized and the ball to powder weight ratio was 10:1. The mechanism of formation was explained as mechanically induced combustion synthesis which starts when the temperature during the milling exceeds the ignition temperature of reaction (Wu et al., 2013).

Several reduction processes are applied to prepare diborides. The most common reducing agents are boron and carbon, but boron carbide (B₄C) and aluminum (Al) are also utilized. In addition, combinations of these reducing agents such as B₄C-C are utilized. The general reduction reactions can be used in diboride synthesis are summarized in Table 2.5 (Fahrenholtz et al., 2007; Guo et al., 2012; Peshev and Bliznakov, 1968; Sonber et al., 2010).

Table 2.5 : Examples of reduction reactions that can be used to synthesize hafnium diborides, adapted from Fahrenholtz et al., 2007; Guo et al., 2012b; Peshev and Bliznakov, 1968; Sonber et al., 2010.

Category	Example
Carbothermal	$\text{HfO}_2(\text{s}) + \text{B}_2\text{O}_3(\text{l}) + 5\text{C}(\text{s}) \rightarrow \text{HfB}_2(\text{s}) + 5\text{CO}(\text{g})$
Borochemical	$\text{HfO}_2(\text{s}) + 4\text{B}(\text{s}) \rightarrow \text{HfB}_2(\text{s}) + \text{B}_2\text{O}_2(\text{s})$
Aluminothermal	$\text{HfO}_2(\text{s}) + \text{B}_2\text{O}_3(\text{l}) + 10\text{Al}(\text{l}) \rightarrow 3\text{HfB}_2(\text{s}) + 5\text{Al}_2\text{O}_3(\text{s})$
Boron Carbide	$7\text{HfO}_2(\text{s}) + 5\text{B}_4\text{C}(\text{s}) \rightarrow 7\text{HfB}_2(\text{s}) + 3\text{B}_2\text{O}_3(\text{l}) + 5\text{CO}(\text{g})$
Combined	$2\text{HfO}_2(\text{s}) + \text{B}_4\text{C}(\text{s}) + 3\text{C}(\text{s}) \rightarrow 2\text{HfB}_2(\text{s}) + 4\text{CO}(\text{g})$

Borochemical reduction is a commonly applied conventional method for hafnium diboride synthesis. Borochemical reduction of hafnium oxide involves use of amorphous B according to reaction (2.4) and requires temperatures higher than 1500 °C. The excess boron addition is needed to compensate the boron loss due to sublimation of boron suboxides. Boron does not sublimate only in the form of B₂O₃, but also boron suboxides such as B₂O and B₂O₂ form according to reaction (2.5) and the lack of boron causes to unreacted hafnium oxide impurity (Fahrenholtz et al., 2007).



Zhang et al. (2009) used HfO_2 and amorphous B as raw materials to fabricate HfB_2 powders. The HfO_2 -B starting mixtures were prepared by milling for 24 h in a polythene bottle using ethanol and Si_3N_4 balls. After drying, powder mixtures were heated in the temperature range between 1400 and 1600 °C for 1 h in a resistance-heated graphite element crucible. In the XRD patterns of powders synthesized at 1600 °C with stoichiometric amount boron, HfO_2 phase was identified together with HfB_2 . However with 10 wt.% excess amount of B, only the HfB_2 phase was observed in the XRD analyses. The excess boron need depended on boron sublimation not only in the form of B_2O_3 , but also boron suboxides such as B_2O_2 and B_2O form according to reaction (2.5) (Zhang et al., 2009).

Ni et al. (2010) synthesized HfB_2 powders by borothermal reduction of HfO_2 with amorphous B at 1600 °C according to reaction (2.4). Stoichiometric and 10 wt.% excess amounts of boron were utilized in the experiments. The starting powders were mixed in a polythene bottle with Si_3N_4 balls and ethanol for 10 h. The dried and pressed powders were heat-treated at 1600 °C for 1 h in a graphite resistance furnace under vacuum. The presence of the HfO_2 phase in addition to the major HfB_2 phase was determined in the synthesized powders when stoichiometric amount of B was used due to the boron loss according to the reaction (2.5). The oxygen content of powders synthesized at 1600 °C with excess amount of boron was determined as 0.79%. The HfB_2 powders had mean grain size of 1.37 μm and equiaxial morphology (Ni et al., 2010).

Guo et al. (2012b) suggested a borothermal reduction route to obtain submicron HfB_2 powders according to reaction (2.4). The HfB_2 formation was completed at 1100 °C after 2 h. On the other hand, the complete removal of B_2O_3 required a thermal treatment above 1500 °C. HfO_2 and amorphous B were mixed and dry pressed into disks through a similar method mentioned in other methods and heated to 1100 °C for 2 h in a graphite element furnace. The heat treated disks were immersed into hot water to remove boron oxides. After water washing, a second heat treatment was applied to powders at 1550 °C for 1 h with the aim of further elimination of B_2O_3 . The oxygen content of powders synthesized at 1100 °C was stated as 7.55% in spite

of only HfB₂ phase was detected in the XRD analysis. This situation was attributed to existence of B₂O₃ in the synthesized powders which could not be determined due to the low intensity of B₂O₃ phase. After water washing with distilled water, the oxygen content of powders was decreased to 2.46%. In addition, after the second heat treatment at higher temperatures, the oxygen content of powders was only 0.56%. It was asserted that HfO₂/B molar ratio should be lower than 0.3 in order to remove the remained B₂O₃ based on reaction (2.5). The average particle size of powders was reported as 0.8 μm (Guo et al., 2012b).

Another conventional method for preparing the HfB₂ powders is borothermal/carbothermal or namely boron carbide reduction route. The general reaction for the boron carbide reduction of HfO₂ is given in the reaction (2.6):



Wang et al. (2014b) prepared HfB₂ powders according to reaction (2.6) by the boron carbide reduction route. It was stated that hafnium oxychloride (HfOCl₂), phenolic resin and B₄C were used as hafnium, carbon and boron sources, respectively. HfOCl₂.8H₂O was dissolved in distilled water and B₄C powders were dispersed in the solution by stirring. The phenolic resin dissolved in ethanol was added to the slurry. Then, the resultant precipitate was dried and compacted at 700 °C as a precursor powder mixture for the heat treatment in spark plasma sintering apparatus between 1300 and 1500 °C under vacuum (Figure 2.7). The XRD analysis showed that HfO₂ was the dominant phase at 1300 °C whereas the major phase changed to the HfB₂ over 1350 °C and the pure HfB₂ were obtained only after 1400 °C. The crystallite sizes of the synthesized powders were reported as <500 nm and they had rather spherical morphology. Also, the oxygen and carbon content of resultant HfB₂ powders synthesized at 1450 °C were determined by an oxygen/nitrogen determinator as 0.85% and 0.05%, respectively.

Ni et al. (2008) used the boron carbide reduction technique for preparing HfB₂ powders according to reaction equation (2.7). HfO₂, B₄C and graphite (C) in different stoichiometric amounts were mixed in a polythene bottle with ethanol and Si₃N₄

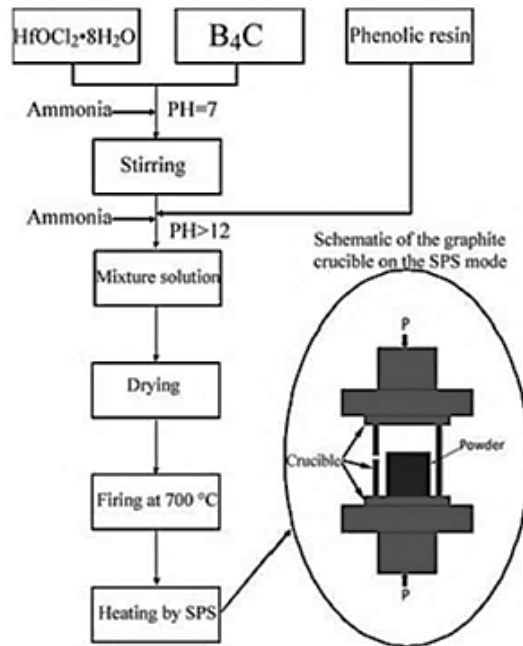
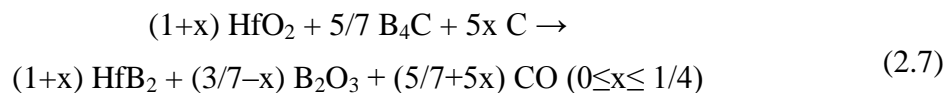


Figure 2.7 : Flow chart for synthesis of HfB₂ powders from solution based precursors, adapted from Wang et al., 2014b.

balls for 10 h, then the dried powder mixture was pressed in the form of disks and placed into a graphite resistance furnace and heat treated between 1400 and 1600 °C for 60-120 min under vacuum.



It is stated that a sublimated B₂O₃ phase was seen on the walls of crucible, so the boron was lost by the sublimation. Besides, HfC phase was identified in the XRD analysis. The high purity HfB₂ powders were achieved to obtain with excess B₄C (0-10%) and C (0-15%). The oxygen content of powders was evaluated between 0.18 and 0.29 % for different x values in reaction (2.7). At the same time, heat treatments were carried out at 1500 °C for 2 h or at 1600 °C for 1 h. However, the prolonged durations of heat treatment at high temperatures gave rise to the grain growth (Ni et al., 2008).

Wang et al. (2012) synthesized HfB₂ powders via borothermal/carbothermal reduction technique using spark plasma sintering (SPS). HfO₂, B₄C and phenolic resin were used as raw materials and experiments were conducted with different molar ratios of reactants. The raw materials were mixed using a ball mill in a polythene bottle with ethanol and zirconia balls. The dried and compacted powder

mixtures were subjected to SPS between 1400 and 1550 °C. Small amounts of HfC were also detected in the synthesized powders when stoichiometric ratio of HfO₂/B₄C/C was used. The formation of HfC and HfO₂ could be suppressed by adding excess B₄C and carbon (15 and 10 wt.%, respectively). The crystallite size of the powders was reported as between 100 and 200 nm. The oxygen and carbon content of the HfB₂ powders sintered at 1500 °C were 0.62% and 0.66%, respectively (Wang et al., 2012).

Sonber et al. (2010) used HfO₂, B₄C and petroleum coke as raw materials to synthesize HfB₂. The powders were mixed in a motorized mortar for 30 min and pelletized under pressure of 220 MPa. The pellets were heat treated between 1200 and 1875 °C for 2 h in an induction furnace. It was stated that the boride formation started at 1200 °C, however HfB₂ powders with low oxygen and carbon content (each <0.5%) were obtained at 1875 °C under a vacuum of 10⁻⁵ mbar (Sonber et al., 2010).

The reaction (2.2) can be used to synthesize HfB₂ by self-propagating high-temperature synthesis (SHS), which is also known as combustion synthesis, as mentioned above. The SHS method also applied to preparation for composites of diborides or diborides doped with additives such as sintering aids (Fahrenholtz et al., 2007).

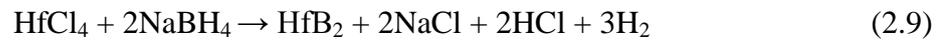
HfB₂-SiC products were produced by self-propagating synthesis according to the following reaction (2.8) (Licheri et al., 2009):



The raw materials powders were mixed in a Spex shaker mill for 30 min and pressed into cylindrical pellets having diameter of 16 mm and height of 30 mm. By using a tungsten coil, combustion front reaction was started at one end of sample and the reaction self propagated until it reached the opposite end. The synthesized powders consisted of HfB₂ and SiC phases and did not include any other secondary phases or impurities according to the XRD results. The particle size of prepared HfB₂ powders was reported as less than 30 μm. The synthesized powders were subsequently consolidated without the addition of any sintering aid via the SPS technique. A fully densified HfB₂ (relative density of 99.5%) was obtained at 1800 °C for 30 min under the applied pressure of 20 MPa (Licheri et al., 2009).

Chemical routes used to synthesize hafnium and zirconium diborides include solution-based methods, reactions with boron-containing polymers, and pre-ceramic polymers. Nanocrystalline HfB₂ and ZrB₂ were synthesized by a chemical reaction between anhydrous chlorides and sodium borohydride (NaBH₄) above 500 °C under pressure in an autoclave (Chen et al., 2004b; Chen et al. 2004c).

Chen et al. (2004c) synthesized HfB₂ powders from HfCl₄ and NaBH₄ powders in a stainless steel autoclave at 600 °C for 12 h. For the possible formation mechanism, the overall reaction between the HfCl₄ and NaBH₄ was stated as follows in reaction (2.9):



But the reaction may proceed via a vapor phase mechanism depending on the decomposition of NaBH₄ to borane gas (BH₃) and its subsequent reaction with gaseous chlorides. The NaBH₄ begins to decompose with increasing temperature (above 500 °C) according to reaction (2.10) and the resultant BH₃ reacts further with HfCl₄ to produce HfB₂. Also, the HCl reacts with NaH to give NaCl and H₂ according to reaction (2.11):



The reaction temperature and time were stated as important process parameters for the formation of the hexagonal HfB₂. The HfB₂ could not be obtained when the temperature was lower than 450 °C. The crystallinity of HfB₂ phase increased by increasing temperature up to 600 °C. Also, the holding times between 12 and 24 h did not significantly influence the crystallinity and particle size. The hafnium diboride prepared by this method had an average crystallite size of 30 nm (Chen et al., 2004c).

Kravchenko et al. (2015) investigated the reactions between Hf powders and microcrystalline B in a Na₂B₄O₇ ionic melt have at temperature range of 600 and 850 °C in an autoclave. The Hf and B powders in stoichiometric amounts were mixed with an excess of anhydrous borax (Na₂B₄O₇) in a vibratory mill for homogenization. The powder mixture was placed in a autoclave (30 mm in diameter and 200 mm in length) and maintained at the temperatures between 600 and 850 °C. The

nanoparticulate HfB₂ formation was observed to start at 750 °C. The HfB₂ powders prepared at 850 °C consisted of nearly spherical particles with 50–55 nm in diameter.

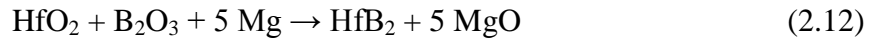
Additionally, ZrB₂, TiB₂ and a series of borides were prepared from related oxides and amorphous boron in the presence of elemental Na and S in an autoclave with a capacity of 20 ml at 150 °C for 2 h. In the TiB₂ synthesis, the molar amounts of TiO₂, amorphous B, metallic Na and sublimed S were given as 0.01, 0.04, 0.04 and 0.02 moles, respectively. After the chemical reaction in the autoclave, the raw product was washed with ethanol, distilled water and HCl (0.5 M) and dried in a vacuum oven. ZrB₂ and TiB₂ particles with average particles size of 500 and 100 nm were obtained, respectively (Chen et al., 2012).

Venugopal et al. (2014) used the sol-gel method in the synthesis of HfB₂ powders using phenolic resin, HfCl₄ and H₃BO₃ as source of carbon, hafnium and boron sources, respectively. The H₃BO₃ dissolved in ethanol at 120 °C in an oil bath and the HfCl₄ and phenolic resin were added. The obtained solution was stirred for 24 h at 120 °C with continuous refluxing. This sol-gel was dried at 250 °C for 2 h in air to obtain the precursor. The precursor powders were annealed at the temperature range of 1300-1600 °C. Different products were obtained according to the molar ratios of raw materials. By the annealing of mixture include the exact stoichiometric amounts of reactants at 1600 °C, a small amount of HfC was detected. The single phase HfB₂ was obtained with adding the slight excess of boron sources and annealing the precursor powders at 1600 °C for 2 h or 1300°C for 25 h.

In an another study, in which pre-ceramic method was applied, the ceramic precursor for HfB₂/HfC/SiC/C was prepared via solution-based processing of polyhafnoxanesal, linear phenolic resin, boric acid and poly [(methylsilylene) acetylene]. The obtained precursor was cured at 250 °C and was subsequently annealed at 1500 °C to form HfB₂/HfC/SiC/C ceramic powders. The effect of carbon sources on size and morphology of the resultant HfB₂ powders was investigated. It was stated that the structure and level of agglomeration of carbon sources played an important role on the particles size of HfB₂ powders. The finest HfB₂ powders were obtained when powder phenolic resin was utilized as the carbon source (Cai et al., 2013).

The mechanically activated annealing synthesis of hafnium diboride involves the reduction of oxides and chlorides raw materials. Barraud et al. (2005) synthesized HfB₂ nanorods from HfCl₄-B and HfCl₄-B-Mg powder mixtures by mechanical activation and isothermal annealing. In the XRD patterns of HfCl₄-B-Mg powder mixtures milled for 2 h in a planetary ball mill, a few amount of HfB₂ phase was determined together with hafnium hydride (HfH_x) phase. However, the HfH_x phase was converted to the HfB₂ during the high temperature annealing. The mechanically activated (for 1 h) powder mixtures of HfCl₄-B and HfCl₄-B-Mg were annealed at the temperature range of 700-1100 °C. The mechanically activated powders after annealing at 1000 and 1100°C had the HfO₂ phase in the amounts of 21 and 8 wt.%, respectively. Also, the FeB phase was identified in the XRD patterns of synthesized powders and the necessity of these iron borides and boron oxide for the growth of nanorod-shaped particles during annealing was stressed (Barraud et al., 2005).

Some other attempts were made for the metallothermic reduction of HfO₂ via milling-assisted annealing processes (Balci et al., 2010). The HfO₂-HfB₂ composite powders were fabricated by a two-step process which includes the mechanical activation and isothermal annealing at high temperatures according to the reaction (2.12):

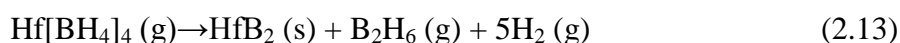


The HfO₂-B₂O₃-Mg powder blends were milled in a high-energy ball mill for 5, 7, 11 and 30 h. The mechanically activated powder blends were subsequently annealed at different temperatures between 900 and 1300 °C for 6, 12 and 18 h. The HfB₂, HfO₂ and MgO (as a by-product) phases were identified in the XRD analyses of the synthesized powders. However, complete conversion of the HfO₂ phase to HfB₂ could not be provided at these conditions (Balci et al., 2010).

In addition, HfB₂ powders were prepared by annealing the powder mixtures of HfO₂, amorphous B and Mg at 800 °C. It was stated that for the preparation of single phase HfB₂, the formation of MgB₄ should be controlled by keeping the reaction temperature below 850 °C (Kobayashi et al., 1993).

Furthermore, the CVD methods are generally employed with the aim of obtaining hard surface coatings rather than powder synthesis in order to improve the surface hardness and tribological properties of desired materials (Brochu et al., 2008;

Cheminant et al., 1997; Jayaraman et al., 2006). The HfB₂ thin films were grown by CVD from the Hf[BH₄]₄ precursor. The films were deposited on various substrates including Si (100) and Mo discs at various temperature less than 350 °C. The precursor pressure of 1.3×10⁻² Pa (0.1 mTorr) was utilized and an argon–nitrogen mixture was dissociated in a remote plasma source. The idealized growth reaction for the CVD growth process was given as reaction (2.13) (Jayaraman et al., 2006):



In addition, chemical vapor deposition (CVD) of various diborides was applied (Sonber and Suri, 2011). Such as for production of ZrB₂ by CVD method, ZrCl₄ and BCl₃ are the most commonly used precursors and H₂ is generally utilized as reducing gas. This technique provides some advantages like low synthesis temperature and high purity. The major process parameters are temperature, pressure and flowrate of reactants and deposition rate generally increases with increasing temperature and hydrogen concentration. The general reaction used by the researchers is:



Various substrates used for the deposition of ZrB₂ such as copper, zircalloy, graphite and quartz (Motojima et al., 1990; Sonber and Suri, 2011). Motojima et al. (1990) deposited ZrB₂ on Cu substrate at 700-900 °C according to the reaction (2.14) as adherent coating. The reaction (2.14) was written according to ZrB₂, but it is an analogous process for the HfB₂ synthesis.

Furthermore, single crystals of HfB₂ were prepared by floating zone method by means of radio frequency (RF) heating (Otani et al., 1998). Commercial HfB₂ powders and amorphous B powders were mixed in fixed ratios and isostatically pressed into a rod shape. The rod was heated in vacuum at 1700 °C for 30 min under the 0.8 MPa of ambient helium or argon gas. Boron is known as a good flux for preparing refractory crystals. The best growth rate and composition were reported as 2.5-3 cm/h and B/Hf=2.1-2.15, respectively. Carbon and oxygen were determined in level of 40 and 120 ppm in the crystal, respectively (Otani et al., 1998).

It is also known that borides of various metals (Ti, Zr, Mg, Mo, W) can be produced by molten salt electrolysis method (Sonber and Suri, 2011). Electrochemical fabrication of HfB₂ coatings was carried out in the NaCl–KCl–KBF₄–K₂HfF₆ molten

salt at a temperature range of 700-850 °C and a cathode current density of $5-50 \times 10^{-3} \text{ A.cm}^{-2}$. The HfB_2 coatings presented a columnar structure on the graphite substrate and the microhardness of coatings was determined as $3200 \pm 250 \text{ kg/mm}^{-2}$ (Kuznetsov, 2012).

Schwab et al. (2004), proposed a polymeric precursors route to synthesize ZrB_2 and HfB_2 . It was stated that improved results were obtained from oxide free-precursors prepared from the metal borohydride and borazine compared to the initial studies which concentrated on carbothermal/borothermal reduction of metal alkoxides. ZrB_2 and HfB_2 were prepared by subsequent pyrolysis of polymeric precursors obtained through a reaction of borazine ($\text{H}_6\text{B}_3\text{N}_3$) with a metal borohydride ($\text{Hf}(\text{BH}_4)_4$). On the other hand, the polymeric precursors was proposed as a binder for processing of commercial ZrB_2 and HfB_2 powders, rather than a stand-alone coating or a monolithic ceramic.

A summary of applied methods with utilized raw materials for synthesis of hafnium diboride is given in Table 2.6.

Table 2.6 : The summary of production techniques of hafnium diboride.

Production Techniques	Raw Materials	References
• Direct solid-state reaction of elemental powders	Hf, B	Brochu et al., 2008. Musa et al., 2013. Makarenko et al., 2015. Blum et al., 2008. Anselmi-Tamburini et al., 2006.
• Carbothermal reduction	HfO ₂ , B ₂ O ₃ , C	Fahrenholtz et al., 2007.
• Borothermal reduction	HfO ₂ , B	Ni et al., 2010. Peshev and Bliznakov, 1968.
• Boron carbide reduction	HfO ₂ , B ₄ C, C	Sonber et al., 2010. Ni et al., 2008.
• Chemical reaction at low temperatures in an autoclave	HfCl ₄ , NaBH ₄ Hf, B, Na ₂ B ₄ O ₇	Chen et al., 2004c. Kravchenko et al., 2015.
• Sol-gel method	HfCl ₄ , H ₃ BO ₃ , phenolic resin HfOCl ₂ .8H ₂ O, B ₄ C, phenolic resin	Venugopal et al., 2014. Wang et al., 2014b.
• Mechanically activated annealing methods	HfO ₂ , B ₂ O ₃ , Mg HfCl ₄ , B and HfCl ₄ , B, Mg	Balcı et al., 2001. Barraud et. al., 2005.
• Self-propagating high-temperature synthesis (SHS)	Hf, B ₄ C, Si	Licheri et al., 2009.
• Floating zone method	HfB ₂ , B	Otani et al., 1998.
• Molten salt electrolysis	NaCl–KCl–KBF ₄ –K ₂ HfF ₆	Kuznetsov, 2012.
• Chemical vapor deposition method (CVD)	Hf[BH ₄] ₄	Jayaraman et al., 2006.
• Polymeric precursor	Borazine (H ₆ B ₃ N ₃), Hf(BH ₄) ₄	Schwab et al., 2004.

2.2.2 Sintering techniques

Hafnium diboride (HfB_2) is a well known member of ultra-high temperature ceramics (UHTCs) family. It has a very high melting point of 3380 °C. Several carbides and nitrides are also considered as members of this family because of their melting temperatures over 3000 °C and some other properties (Cacciamani et al., 2011; Fahrenholtz et al., 2014). On the other hand, hafnium and zirconium diborides are the most prominent and commonly studied compounds in this class of ceramic materials (Levine et al., 2002; Rhodes et al., 1970; Upadhyaya et al., 1997). Due to the relatively high melting temperature, highly covalent character of Hf-B bond and low self-grain boundary and volume diffusion rates of HfB_2 , it is very difficult to obtain near full density compacts (Fahrenholtz et al., 2007; Telle et al., 2000). Generally, very high temperatures and external pressure are needed to densify the monolithic HfB_2 structures (Cutler, 1991; Zou et al., 2010). The properties of powders such as particle size and morphology have a dramatic effect on the sinterability and sintering conditions (Cutler, 1991; Jung et al., 2013). The advanced sintering techniques such as hot pressing and spark plasma sintering have been used in the densification of these ceramics as well as conventional sintering techniques. In addition, the use of sintering aids to enhance the densification of diborides has been subjected to intense research interests (Fahrenholtz et al., 2007; Monteverde, 2007; Pastor, 1977).

Pressureless sintering (PS) technique has important advantages as it is cost effectiveness and giving opportunity to produce near-net shape components. On the other hand, to reach a reasonable densification, a high sintering temperature is often needed due to the lack of external holding pressure. The reduced particle size and sintering additives are generally provided to compensate this limitation. The densification rate of diborides has been appreciably increased with various additives such as refractory metals (Fe, Cr, Ni), refractory metal silicides (MoSi_2 , TiSi_2) and HfSi_2 and ceramic additives (SiC , Si_3N_4) (Fahrenholtz et al., 2007; Sonber et al., 2010; Saito et al., 2012; Mishra et al., 2002; Monteverde, 2007; Zou et al., 2010).

Additionally, it was shown that the mechanical milling can be applied to powders prior to the densification (Wang et al., 2014a). The mechanical milling facilitates the densification by both providing particle refinement and increasing the number of

point defects which enhance the grain boundary diffusion. However, milling can give rise to increased oxygen content due to the rising surface area (Fahrenholtz et al., 2007; Wang et al., 2014a).

In former studies, full densification of UHTCs without sintering additives were achieved only by hot pressing (HP). However, due to limitations of HP related to both size and geometry, further investigations have concentrated on the reactive sintering and different sintering aids. Recently, sintering studies has been focused on some modern sintering techniques and sintering additives. The sintering aids such as SiC, MoSi₂, La₂O₃, B₄C, WC, etc. are investigated for the liquid-phase sintering of hafnium diboride (Ni et al., 2012a; Silvestroni and Sciti, 2007; Zapata-Solvas et al., 2013; Zou et al., 2010).

Apart from the conventional techniques, spark plasma sintering (SPS) and plasma pressure compaction (P2S) which involve plasma activation and localized heating have been applied to UHTCs (Fahrenholtz et al., 2007; Sonber et al., 2010). During SPS a direct or pulsed electric current is applied to the powder compact under a uniaxial holding pressure. Unlike the traditional sintering techniques, relatively high heating rates can be reached and consolidation times decrease from hours to few minutes (Bellosi et al., 2006; Golla and Basu, 2014). Thus, formation of grain growth which adversely affects the mechanical properties is kept at minimum level and homogenous grain microstructure can be retained. Additionally, the in-situ elimination of surface oxides (or contaminants) by applied DC voltage helps bonding of particles. However the underlying mechanisms that allowed enhanced sintering within a limited time are still needed for further elucidations (Bellosi et al., 2006; Golla and Basu, 2014; Monteverde, 2007; Sciti et al., 2008; Wang et al., 2012; Wang et al., 2014a).

Silvestroni (2007) reported the fabrication of HfB₂-MoSi₂ composites with different amount of MoSi₂ between 5-20 wt.% by pressureless sintering at 1950 °C for 1 h. Sintered samples including 0 and 20 wt.% of MoSi₂ reached to relative density values of 89 and 98 %, respectively. The hardness of HfB₂-5MoSi₂ and HfB₂-20MoSi₂ composites were reported as 18.2 GPa. Also, the fracture toughness values of these two samples were reported as 4 and 4.1 MPa/m².

Another pressureless sintering study on the HfB₂-20 vol.% SiC ceramics was conducted with using WC as sintering aid at 2200 °C for 2 h and 99% of relative density was reported (Ni et al., 2012b). It was shown that the complex reactions between WC and HfB₂-SiC system enabled high densification rates. The mechanical properties such as Young's modulus, fracture toughness and three point bending strength of HfB₂-20 vol.% SiC having 10 wt.% WC were given as 511 GPa, 4.85 MPa.m⁻² and 563 MPa, respectively (Ni et al., 2012b).

The HfB₂ ceramics were sintered at a temperature range of 2100-2350 °C with B₄C (between 0 and 2 wt.%) as sintering aid without external pressure (Zou et al., 2010). It was stated that the sintering mechanism changed to liquid phase sintering at the temperatures above 2300 °C. The role of B₄C on the improved densification was explained by its effect on the removal of oxide impurities during solid-state sintering. In addition, formation of a liquid phase which wetted the hafnium diboride grains very well during liquid phase sintering process improved the densification. However, a sharp decrease in the mechanical properties (except modulus) was observed in the samples subjected to liquid phase sintering. The best results were recorded for the HfB₂-2 wt.% B₄C sample sintered at 2150 °C as relative density of 98.3%, 20.1 GPa, 532 GPa and 492 MPa for Vickers hardness, elastic modulus and flexure strength, respectively (Zou et al., 2010).

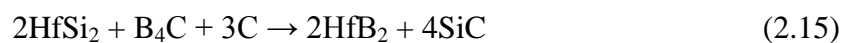
The HfB₂-SiC composites with B₄C addition were hot-pressed at 1850 °C under 35 MPa (Weng et al., 2009). When the B₄C free, HfB₂-20 vol.% of SiC composites were hot-pressed at 2000 °C for 60 min, grain growth rather than densification was observed. The density and average grain size of this composite reported as 97.4% and 7 μm, respectively. By the addition 5 vol.% of B₄C, the grain size reduced to 4 μm, which indicated that B₄C inhibited the abnormal grain growth. It was stated previously that the oxide-rich layer on the surface of diborides can be deteriorative for densification (Monteverde et al., 2005; Weng et al., 2009). It was suggested in this study that a chemical reaction between this HfO₂ and B₄C to form HfB₂, CO and BO gas when temperature was above 1200 °C enhanced the densification of HfB₂ by lowering the diffusion barrier. The hardness of HfB₂-20 vol.% SiC-20 vol.% B₄C sample increased to 20.9 GPa from 17.3 GPa (for HfB₂-20 vol.% of SiC).

In another study, hot pressing of HfB₂-based ceramics with B₄C and HfSi₂ addition were investigated (Monteverde, 2008). The positive effect of B₄C addition on

sinterability explained by the similar mechanism: B_4C contributed to the densification by promoting the removal of surface oxide contamination, thus it enhanced the reactivity at the high temperatures. Additionally, the effect of $HfSi_2$ addition was explained by its low melting point (close to $1700\text{ }^\circ\text{C}$) under the pressing temperature and strengthening effect of the partial dissolution of HfB_2 in the Si-based liquid phase. Also, it was postulated that the Si-based liquid phase allowed the high densification rate by the controlled removal of the surface oxide impurities.

Monteverde (2007) consolidated HfB_2 -SiC ceramics with addition of 2 vol.% $TaSi_2$ as sintering aid by hot-pressing (HP) at $1900\text{ }^\circ\text{C}$ for 35 min and spark plasma sintering (SPS) techniques at $2100\text{ }^\circ\text{C}$ for 3 min. The complete densification was achieved for powder mixture of HfB_2 + 30 vol.% SiC with the addition of 2 vol.% $TaSi_2$ as sintering aid, and applying the following conditions: $2100\text{ }^\circ\text{C}$ for 3 min (SPS), or 1900°C for 35 min (HP). Both the SiC and $TaSi_2$ were suggested as the activators to enhance the sinterability. The positive effect of silicides on the densification behavior was explained by the formation of a liquid phase in the temperature range of $1400\text{-}1800\text{ }^\circ\text{C}$, which enhanced the diffusion and rearrangement of loose particles. During the hot pressing, the HfB_2 -SiC mixtures exhibited considerably lower densification compared to $TaSi_2$ doped mixtures. The elastic moduli of samples were above 490 GPa. The flexural strengths of the hot-pressed composites at room temperature and $1500\text{ }^\circ\text{C}$ (in air) were 665 and 480 MPa, respectively. Additionally, HfO_2 and (Hf, Ta)-carbides were determined as the second phases. Also, it was claimed that the endurance of both ceramics to air oxidizing conditions between 1450 and $1650\text{ }^\circ\text{C}$ improved. This was due to the positive effect of SiC which produces the SiO_2 layer during oxidizing and forms protective borosilicate glass with B_2O_3 (evolved by the degradation of HfB_2) on the top surface (Monteverde, 2007).

In addition, HfB_2 -SiC composites were prepared by the reactive spark plasma sintering (RSPS) technique (Wang et al., 2014a). $HfSi_2$, B_4C and carbon black powders were mixed in stoichiometric composition based on reaction (2.15) and sintered in a spark plasma sintering apparatus at $1600\text{ }^\circ\text{C}$ under a pressure of 40 MPa for 10 min.



It was claimed that the HfB₂ and SiC phases distributed homogeneously in the structure and their particle size were 2 and 1 μm, respectively. The relative density of products was reported as 98.7%, and the hardness and fracture toughness of composites were reported as 20.4 GPa and 4.7 MPa.m^{1/2}, respectively. The particle size reduction (obtained by ball milling of the starting powders) and the enhanced mass transfer rates were stated as critical factors for reaching the high densification rates during the reactive SPS (Wang et al., 2014a).

Sciti et al. (2008) produced HfB₂-based ceramics with additions of 1, 3, and 9 vol.% MoSi₂ as sintering aids by the spark plasma sintering at temperatures between 1700 and 1950 °C under a pressure of 100 MPa. Complete densification was achieved with silicide additions between 1750 and 1850 °C. Extra phases like HfO₂, SiC and SiO₂ were detected in the microstructure of composites. The relative density value of the monolithic HfB₂ sintered by SPS under conditions of 2200 °C, 65 MPa and 5 min was reported as 80%. Additionally, hardness values of the samples including 1, 3 and 9 vol.% MoSi₂ were 21.2, 22.0 and 21.1 GPa, respectively.

A summary of literature data on the examples of densification of the HfB₂ ceramics are listed in Table 2.7.

Table 2.7 : Literature data on densification of the HfB₂ ceramics, adapted from Sonber et al., 2010.

Densification Method	Sinter additive	Temp. (°C), Press. (MPa), Time (min)	Relative Density (%)
Pressureless sintering	-	1950, -, 60	89
	5% MoSi ₂	1950, -, 60	97
Hot Pressing	-	1840, 793, 10	90-95
	20% SiC	2200, 25, 60	100
	20% SiC	2000, 35, 60	97.4
	20% SiC	2200, 30, 120	97
	20% SiC	2200, 30, 60	93.8
	20% SiC + 10% B ₄ C	1850, 35, 40	98.9
	20% SiC + 18% AlN	1800, 30, 30	99.6
	15% TaSi ₂	1900, 30, 15	99
	5% HfSi ₂	1600, 30, 15	99
	7% B ₄ C	1900, 30, 40	94
	30% SiC + 2% TaSi ₂	1900, 42, 35	100
2.5% Si ₃ N ₄	1800, 30, 30	100	
Spark plasma sintering	-	1900, 95, 10	86.8
	-	1850, 50, 15	86
	0.1% C	1850, 50, 15	95
	30% SiC	2100, 30, 2	100
	26.5% SiC	1800, 20, 30	99.9
	30% SiC + 2% TaSi ₂	2100, 30, 3	100
	20% SiC	1800, 80, 8	100
	-	2200, 65, 5	80
3% MoSi ₂	1750, 100, 3	98.8	

2.3 Mechanochemical Synthesis and Mechanically Driven Synthesis Methods

Advanced materials can be described as those have a systematic synthesis route and controlled structure with the aim of providing a tailored set of properties for demanding applications. The structure and the constitution of advanced materials can be achieved by synthesizing them in a non-equilibrium state for example as rapid solidification by quenching and mechanical alloying techniques. These methods can be energize materials and bring them into a highly non-equilibrium (metastable) state by some external dynamical forcing, e.g. application of pressure, or storing of

mechanical energy by severe plastic deformation. Materials processed with such a technique have improved physical and mechanical properties comparing to the conventionally processed materials (Sopicka-Lizer, 2010; Suryanarayana, 2001).

2.3.1 Ball milling

El-Eskandarany (2001) described mechanical alloying as a “unique process for fabrication of several alloys and advanced materials at room temperature”. That same year, another definition was suggested by Suryanarayana (2001): “a solid-state powder processing technique involving repeated welding, fracturing, and rewelding of powder particles in a high-energy ball mill”.

The mechanical alloying (MA) process was developed in 1966 at The International Nickel Company (INCO) in scope of a project about gas turbine applications. The method was investigated to fabricate a nickel-based super alloy combining oxide dispersion strengthening with gamma prime precipitation hardening. Then, some researches were conducted for coating of oxides or carbides particles (hard phases) with metals (a soft phase) such as coating of tungsten carbide with cobalt. In mid-1966, attention was directed to the ball-milling process to make metal powders for production of some alloys itself by powder metallurgy. In 1970, a pioneering development was introduced by production of oxide-dispersion-strengthened (ODS) alloys for high temperature structural applications, such as jet engine parts (Gilman and Benjamin, 1983). The method was used for dispersing oxide particles (Al_2O_3 , Y_2O_3 , Th_2O_3) in nickel-base super alloys. Apart from the fabrication of ODS alloys, the ball-milling technique was used to produce amorphous phases such as Ni60Nb40 alloy (El-Eskandarany, 2001). Thus, several alloys that cannot be produced by liquid metallurgy were prepared through this technique. By the contribution of following studies on the nature and mechanism of the MA and design of special equipment for carrying out the process throughout four decades, MA has become a well known process. Table 2.8 shows the important attributes of mechanical alloying (El-Eskandarany, 2001; Suryanarayana, 2001).

Over the past three decades, ball milling has evolved to an important method for the preparation of advanced materials including equilibrium, nonequilibrium (e.g., amorphous, quasicrystalline, nanocrystalline, etc.) and composite materials having improved physical and mechanical properties, also new phases or new

Table 2.8 : Important milestones in the development of mechanical alloying /milling, adapted from Suryanarayana, 2001.

Year	Important developments
1966	Development of ODS nickel-base superalloys
1981	Amorphization of intermetallics
1983	Amorphization of blended elemental powder mixtures
1988	Synthesis of nanostructures
1989	Occurrence of displacement reactions
1900	Observation of disordering of intermetallics

engineering materials. Furthermore, it has been applied as a room temperature method for reduction of some oxide compounds with a reducing agent. These solid-state reactions that take place between the fresh powder surfaces of the reactants are enabled by means of MA at room temperature. Consequently, MA can be employed to fabricate some advanced alloys and to synthesize some compounds which are hard or unmanageable to be produced by conventional melting and casting techniques (El-Eskandarany, 2001; Öveçoğlu, 1987; Soni, 2001; Suryanarayana, 2001).

As a complex process, mechanical milling involves numbers of parameters that should be arranged properly to obtain desired materials and properties, which can be summarized as (Suryanarayana, 2001):

- type of mill,
- milling container,
- milling speed,
- milling time,
- type, size and size distribution of the grinding medium,
- ball-to-powder weight ratio,
- extent of filling the vial,
- milling atmosphere,
- process control agent (PCA) and
- temperature of milling.

Different types of high-energy ball mills are utilized for mechanical alloying, milling and activation processes according to their rotation type, rotational speed, milling capacity, efficiency, milling medium and contamination of powders (Suryanarayana, 2004; Takacs, 2002). Most suitable mill can be chosen according to type of powder, quantity and desired mechanism. However, the multi-axial and vibratory mills (shaker mills) are the most commonly preferred ones for mechanochemical synthesis and mechanical alloying applications whereas the planetary ball mills or the attritors are suitable for large quantities of powder batches (El-Eskandarany, 2001; Suryanarayana, 2004; Takacs, 2002).

The most common types of materials for milling vials are hardened steel, hardened chromium steel, stainless steel and WC-Co. Also, it is desirable to use balls made from same materials with milling vial for reduce the contamination amount. The impact energy evolved by balls is related to the size of balls. In general, large sized and high density balls transfer more impact energy to the powder particles. On the other hand, it was also stated that soft milling conditions like small ball size, lower energies and lower ball-to-weight ratio are thought to promote metastable phase formation (Balaz, 2008; El-Eskandarany, 2001; Suryanarayana, 2001).

Shaker mills such as Spex mills make a back and forth motion which is combined with lateral movements of the ends of the vial. The vials swing energetically several thousand times in a minute. With these swing motion, the balls impact on powder samples, upon each other and the end of the vial and provide mixing and milling of sample. Two vials in which sample and grinding balls inserted are used. Generally, 10-20 g of powder batches are loaded to the vial for one run and the second vial is used as a balance. The ball velocities are relatively high (on the order of 5 m/s) due to the amplitude (about 5 cm) and speed (about 1200 rpm) of the clamp motion. Thus, the force applied by balls is unusually great and system can be identified as high-energy variety (Suryanarayana, 2001) A typical Spex mill, milling vial and balls which are also used in our laboratories are shown in the Figure 2.8.



Figure 2.8 : The Spex shaker mill, hardened steel milling vial and balls.

Planetary ball mills are other widely used mills for mechanical alloying and milling (Figure 2.9). They are also referred to as Pulverisette and they utilize the centrifugal acceleration to obtain an increased effective acceleration of gravity. They include usually up to four jars (1, 2, 3 or 4). The planetary ball mills make a planet-like movement in two directions which are around the central axes and simultaneously around their own axes in opposite direction. Milling balls and sample (generally a few hundred grams of the powder at a time) are loaded into the milling vials. The powders to be milled are subjected to collisions both with grinding balls and the jar walls. In addition, centrifugal force and force produced by rotating support disk act on the powder. The vials and the supporting disk rotate in opposite directions and as a consequence the friction and impact effects are obtained (Avvakumov et al., 2001; Balaz, 2008; Suryanarayana, 2001).

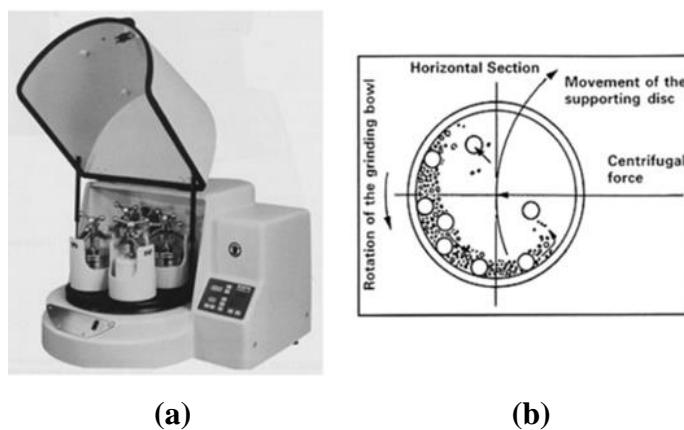


Figure 2.9 : (a) Fritsch™ Pulverisette P-5 four station ball mill and (b) Schematic depicting the ball motion inside the ball mill, adapted from Suryanarayana, 2001.

Additionally, other mills such as vibratory and attritor mills are utilized for mechanical alloying and milling (Figure 2.10). In the vibratory mills, a grinding

mortar and a single ball are used. The mortar is vibrated in low amplitudes, the milling intensity is accordingly low. An attritor (stirred ball) mill is a conventional ball mill consists of a rotating horizontal drum half-filled with small steel balls. Attritors are mainly designed for wet grinding of large amounts samples and they are also suitable for mechanochemical synthesis experiments (El-Eskandarany, 2001; Suryanarayana, 2001).

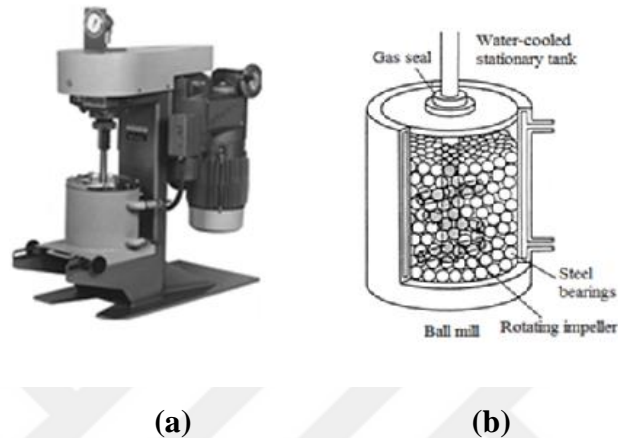


Figure 2.10 : (a) model 1-S attritor and (b) arrangement of rotating arms on a shaft in the attrition ball mill, adapted from Suryanarayana, 2001 and El-Eskandarany, 2001.

Mechanical alloying and mechanochemical synthesis are not only confined to laboratory practice and there exist some applications of mechanical alloying in commercial scale in the industry. Commercial mills have a capacity of several hundred kilograms at a time. In ball mills, mechanical alloying is performed with a maximum capacity of 1250 kg (Figure 2.11) (Suryanarayana, 2001).

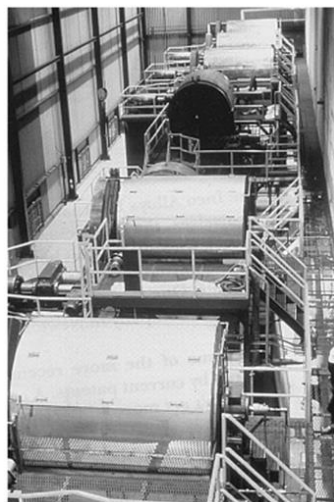


Figure 2.11 : Commercial type ball mills used for mechanical alloying by Courtesy for Inco Alloys International, adapted from Suryanarayana, 2001.

One of the most important parameters for mechanical alloying and mechanochemical synthesis is the speed of milling. With the increase of milling speed, the energy induced into the powders at a certain time increases. The milling time decreases with increasing milling speed and energy. As an example, it was reported that to obtain milling effect of 20 min Spex milling, 20 h milling in a low-energy type mill of Invicta BX 920/2 was needed (Suryanarayana, 2001).

The ball to powder weight ratio (BPR) is another important parameter for the ball milling experiments. The most commonly used BPR for a Spex and large capacity mill like attritor are given as 10:1 and 50:1 or 100:1, respectively (Suryanarayana, 2001). In general, the time required for formation of a desired phase can be shortened by the higher BPRs. However, it was asserted that by soft milling conditions (low BPR values, low speeds of rotation, etc.) of mechanical alloying, metastable phases are formed whereas with hard conditions the equilibrium phases might be obtained (Soni, 2001; Suryanarayana, 2001).

The times required for a particular powder system show differences according to the type of mill, energy of mill, ball-to-powder weight ratio and the temperature of milling (Murty and Ranganathan, 1998). The time is normally chosen to obtain a steady-state between fracturing and cold welding of the particles. Also, the contamination level increases after an unnecessarily prolonged milling duration. Another factor that affects milling is the extent of filling the vial with powder and balls. It is necessary to give enough space to balls for high energy collisions (Balaz, 2008; Suryanarayana, 2001).

Moreover, the milling atmosphere must be controlled for preventing contaminations especially formed by oxidation from atmospheric conditions. Since, generally a controlled inert atmosphere is utilized during milling experiments (Balaz et al., 2013; El-Eskandarany, 2001; Suryanarayana, 2001; Suryanarayana et al., 2001).

2.3.2 The mechanism of mechanochemical synthesis

Mechanochemical synthesis is a very old process with the first publication dating back to 1894 (Suryanarayana, 2001; Boldyrev, 1986). After that, in late 1980 it was shown that the chemical reaction between Ca and CuO induced by the high-energy mechanical milling. This study opened up another exciting area which is a combination of mechanical milling and chemical reactions. Mechanochemical

synthesis or mechanochemistry can be applied to different types of reactions, like exchange, reduction/oxidation, decomposition reactions and phase transformations (Gilman and Benjamin, 1983; Gutman, 1998; Suryanarayana, 2001).

The exchange reactions can be shown by a general reaction given in (2.16):



where R is a reducing agent (Mg, Ca or C, etc.) which reduces a metal oxide (MO) to a pure metal (M) (Suryanarayana, 2001). Metal chlorides and sulfides can also be reduced to the metallic phase by a similar reaction. These reactions have a large negative free energy and are thermodynamically feasible at room temperature. During the solid-state reactions, the product forms at the interfaces of reactants and further growth takes place by diffusion of reactant atoms to interface through product phase, which constitutes a barrier layer and rate limiting step (El-Eskandarany, 2001; Murty and Ranganathan, 1998). In such a reaction, heat treatment is essential for the reaction to occur at reasonable speeds. Mechanical milling enhances the reaction kinetics by means of clean and fresh surfaces (a result of fracturing), increased defect density and reduction of particle sizes. Pure metals, alloys and compounds at room temperature both at the laboratory and commercial scales can be produced by means of these mechanochemical reactions (El-Eskandarany, 2001; Murty and Ranganathan, 1998; Suryanarayana, 2001; Takacs, 2002).

As an example for a mechanochemical reaction, TiC forms after a series of reaction induced by ball milling, as schematically illustrated in Figure 2.12. Non-stoichiometric Ti(C) forms as result of diffusion of carbon atoms into the Ti lattice. Due to extensive mechanical deformation, ductile Ti particles are flattened and fragmented and graphite particles are dispersed among them. The Ti(C) particles are then gradually refined and after accumulation of more defects by reaching threshold energy level, TiC forms (Sopicka-Lizer, 2010). It was also stated that the reactant layers disappear after the formation of the new phase (El-Eskandarany, 2001; Sopicka-Lizer, 2010).

In mechanochemistry, chemical reactions and phase transformations are triggered by inducement of mechanical stresses (Levitas, 2004). In general terms, it takes place by mechanical deformation of solid phases obtained by mechanical forces (Butyagin, 1984; Gutman, 1998; Suryanarayana, 2001; Levitas, 2004). The mechanical

deformation of crystalline structure causes the distortion of the coordination shells of individual atoms at the atomic level, which can be basically described as local structural excitations (Butyagin, 1984; Gutman, 1998; Suryanarayana, 2001; Levitas, 2004). The system is pushed away from thermodynamic equilibrium by these excitations, since the chemical reactivity of reactants increase significantly (Gutman, 1998; Levitas, 2004; Mulas and Delogu, 2010). Locally excited states are generally have characteristic nature and lifetimes. Resulting from the fast dynamics of relaxation processes in the local solid phase, they have quite short lifetimes roughly on the order of nanoseconds (Butyagin, 1984; Delogu and Mulas, 2010). Nevertheless, chemical reactivity can be promoted whenever excited atoms interact directly with other chemical species (Butyagin, 1984; Sopicka-Lizer, 2010).

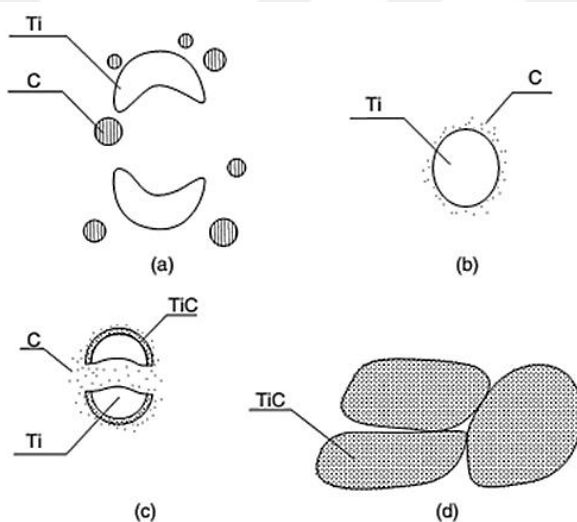


Figure 2.12 : Schematic sketches showing the reaction progress of Ti and activated carbon during mechanochemical synthesis: (a) initial stage, no TiC, (b) second stage, the refinement of Ti and carbon powders, no TiC, (c) third stage, a small amount of TiC formed on the surface of the Ti particles; (d) final stage, the as-milled products composed completely of nanocrystalline TiC, adapted from Sopicka-Lizer, 2010.

Mechanical deformation of solid phases is generally induced by ball milling process. During the mechanical milling, relatively intense impulsive forces act on the particles, including severe plastic deformation and a variety of associated processes (Butyagin, 1984; Suryanarayana, 2001; Delogu and Mulas, 2010). Consequently, point, line and planar defects induced by plastic deformations are accumulated in the solid phase crystalline lattice (Sopicka-Lizer, 2010). Distorted local structures are characterized by an intrinsic enhancement of chemical reactivity (form by the effect of structural defects) (Suryanarayana, 2001). The local excited states associated with

continuing deformation processes are expected to trigger chemical transformations. The atoms participating in local excitations interact with chemical species in the surroundings (Delogu and Mulas, 2010). The application of mechanical activation to enhance chemical reactivity has been applied in different areas such as powder metallurgy (Suryanarayana, 2001), mineral processing (Balaz, 2008) and organic synthesis. Mechanical processing technique has a special importance in the production of metastable phases like amorphous alloys and nanostructured phases (Sopicka-Lizer, 2010; Suryanarayana, 2001).

In spite of the above-mentioned special advantages of mechanical alloying (MA) and mechanochemical synthesis, some problems are inevitable. The most common drawbacks can be summarized as powder contamination, limited science content and limited applications (Suryanarayana et al., 2001). The industrial applications of MA are limited in number, although it has now become an established commercial technique especially for oxide dispersion strengthened (ODS) nickel- and iron-based materials. The most significant applications are in the areas of ODS (oxide dispersion strengthened) materials (350 t), solder alloy (200 t) and PVD target (Cr-V) (5 t) alloys per year. The use of mechanochemistry for fabrication of pure metals, alloys and compounds, dental filling alloys, catalyst materials and inorganic pigments has been known for some time but needs to be exploited further (Boldyrev and Tkacova, 2000; Suryanarayana et al., 2001).

2.3.3 The effects of mechanical activation on synthesis reaction

Mechanochemical process (MCP) utilize mechanical energy and structural changes for activation chemical reactions and inducing structural changes as well as particle size reduction (Sopicka-Lizer, 2010). Under the action of cyclic loading, breaking of crystal bonds comes about and subsequently powder particles move into a non-equilibrium state with a relaxation time of 10^{-7} - 10^{-3} s (Sopicka-Lizer, 2010). The first result of mechanical action is the creation of a stress field in the solid being worked. Subsequent relaxation can occur by several ways: evolution of heat, formation of various kinds of defects in crystal lattice, initiation of chemical reactions and so on (Boldyrev, 2006). As seen from Table 2.9, comparison with other far from equilibrium processes illustrates that departure from equilibrium in MCP is faster than in rapid solidification (Sopicka-Lizer, 2010).

Table 2.9 : Departure from equilibrium achieved in various processes, adapted from Sopicka-Lizer, 2010.

Process	Maximum departure from Equilibrium (kJ/N _a)*
Solid-state quench	16
Quench from liquid (rapid solidification)	24
Condensation from vapor	169
Irradiation/ion implantation	30
Mechanical cold work	11
Mechanical alloying	30

* Assuming relaxation owing to kinetic effects.

During mechanical activation, the conditions for chemical interaction of powder particles change as shown in Figure 2.13. The first stage of interaction is related with the progressive growth of surface area of the powders. The destruction of polycrystalline powders takes place by means of separation into crystallites and reduction of particle size, so the process becomes more efficient. As a result, the chemical reactions only form at the contact points of particles. At the second and third stages, the plastic deformation of particles occurs by the effect of mechanical forces. At the same time, dispersion process is overlapped by the formation of secondary phases and the rate of this formation is comparable with dispersing rate so that the surface area remains constant. During the third stage, the crystallization of the products may occur as well as their repeated amorphization until a steady-state

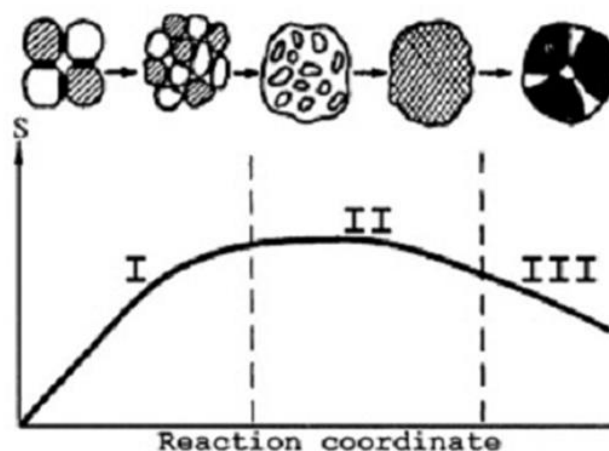


Figure 2.13 : The change of the conditions for chemical interaction during mechanical activation where S is specific surface area, adapted from Avvakumov et al., 2001.

between these two mechanisms are obtained. The duration for each step varies depending on the amount of mechanical energy loading. Even, if it is too low the process can be interrupted. (Avvakumov et al., 2001; Boldyrev. and Tkacova, 2000; Morris and Morris; 1991).

One of the most frequently occurred phenomena during the mechanical activation is amorphization(Avvakumov et al., 2001). It has been shown that most of an alloy can be made amorphous under the proper milling conditions. The mechanism of amorphization during mechanical alloying has not been fully understood. Nevertheless, during mechanical milling, destabilization of the crystalline phases is thought to take place by the accumulation of structural defects such as vacancies, dislocations, grain boundaries, and anti-phase boundaries. The continuous grain size reduction (and consequent increase in grain boundary area) and a lattice expansion would also increase free energy of the system (Avvakumov, 2001; Sopicka-Lizer, 2010).

By the change of relaxation type from fracture to plastic deformation, a drastic escalation in the strain which is followed by an extreme dislocation flow occurs. Elastic strain energy transforms into lattice defects, structural disordering or is relaxed through fracturing of brittle phases or crystallographic lattice rearrangement. During mechanical alloying, relaxation can take place by decomposition or synthesis of a new chemical phase. These changes form as a function of material's properties (chemical bonds, crystal structure, elastic modulus, etc.) and degree of applied mechanical force (the magnitude, direction, stress rate and frequency). The energy of the milled powders increases as a result of increased volume fraction of grain boundaries and lattice disordering raises the free energy above the level of the amorphous state (McCormick and Froes,1998; Sopicka-Lizer, 2010).

One of the most important results of mechanical activation is the formation of numerous reaction sites which increase with decreasing particle size. Furthermore, more importantly the reactants are not present in separate positions as generally happens in an ordinary chemical reaction. The close contact between the reactants and formation of various defects (acts as the fast diffusion paths) solve the diffusion barrier problem which control the rate. As a result, some solid-state reactions or alloying reactions come about at ambient temperatures during

mechanochemical synthesis or they could easily proceed during the subsequent heat treatment (Sopicka-Lizer, 2010).

2.4 Solvothermal Reaction Method in Autoclave

Demazeau (2010) defined the solvothermal processes as “A solvothermal process can be defined as a process in a closed reaction vessel inducing a decomposition or a chemical reaction(s) between precursor(s) in the presence of a solvent at a temperature higher than the boiling temperature of this solvent.” The pressure in the autoclave can be autogeneous and in that case, it changes depending on the boiling points of reactants and solvent and the filling degree of the reaction vessel. In other case, pressure can be imposed into the reactor at the start point of the experiments. A high initial pressure is commonly applied in order to enhance the solubility of reactants. The system can be homogenous or heterogeneous according to the properties of reactants and solvent: whether or not the reactants are soluble or partially soluble in the solvent at related temperature and pressure conditions (Demazeau, 2010). The system exists in subcritical or supercritical conditions depending on the applied temperature and pressure. Solvothermal synthesis are used in different hydrothermal processes such as recovering ores in hydrometallurgical applications, synthesize novel materials- lots of time metastable phases when the kinetic effects are dominant, preparing single crystals of oxides- particularly low-temperature structural varieties and synthesis of fine particles. The most common reaction types involved in the solvothermal processes are hydrolysis, complex-formation, metathesis and oxidation-reduction reactions of nanocrystallites (Demazeau, 2008a; Guo et al., 2011; Portehault et al., 2011).

High pressure-vessels which are generally known as autoclaves are the main equipment of hydrothermal and solvothermal synthesis. The high pressure vessels used in crystal growth or materials processing under hydrothermal and solvothermal conditions must have special properties for extreme conditions (Feng and Li, 2011).

The main characteristics for an ideal autoclave are:

- Mechanical strength for enduring high temperature and pressure for long duration.
- Resistance for acidic, alkali, and oxidant environments.

- Good sealing performance in order to obtain and maintain the required pressure.
- Suitable size and shape to provide a suitable temperature gradient (Feng and Li, 2011).

A closed reactor/autoclave should include certain safety control components comprising temperature and pressure control systems and closed system control. The pressure level of a closed reactor is crucial to the safety of hydrothermal experiments. For an internally pressurized autoclave, the pressure evolved during synthesis depends on the degree of filling and the properties of reaction reactants and solvents (most importantly, their boiling point). The internal pressure of a closed vessel can be calculated from the ideal gas law ($PV=nRT$). The degree of filling is an important element and should not exceed the level of 50% for safety reasons (Feng and Li, 2011).

There is no exact standard for the classification of hydrothermal autoclaves in the literature. The hydrothermal autoclaves can be classified according to their sealing methods, mechanical structure, pressure formation method and heating methods. In general, classification can be made as externally heated and internally pressurized autoclave, and externally heated and externally pressurized autoclave (Feng and Li, 2011). First type autoclave generally has 10-20 cm length and 2.5 cm inner diameter. An autogenous pressure forms in the autoclave depending on the degree of filling, types of reactants and the temperature. This autoclave can be used under the conditions of 600 °C and 0.04 GPa for long reaction durations, whereas for a short time reaction it is durable up to 700 °C and a high working pressure of up to 0.07 GPa. The autoclave is sealed by an internally pressurized seal gasket if the working pressure is very high. Nonetheless, it has disadvantages as it is prone to leakage and difficult to open the autoclave. The most autoclave used for hydrothermal or solvothermal synthesis in laboratory scale are generally improved versions of this type of autoclave (Morey autoclave) (Feng and Li, 2011; Guo et al., 2011). The second type, externally heated and externally pressurized autoclave, is generally known as a Tuttle autoclave. The closing of working chamber is made by a cone-in-cone seal. The entire autoclave is kept inside a furnace and high temperature can be applied providing a well pressure control. This system is robust under higher working temperatures up to 750 °C and a high working pressure of up to 1.2 GPa. Owing to the features like simplicity, convenient operation and low cost,

these type of apparatus are widely used for hydrothermal synthesis and materials processing. Moreover, there exists another type of autoclave which is internally heated and externally pressurized autoclave. Figure 2.14 shows the photographs of commercial hydrothermal autoclaves produced by a commercial company (Feng and Li, 2011; Guo et al., 2011).



Figure 2.14 : ParrTM Instrument Company Pressure Vessels and Reactors, adapted from Feng and Li, 2011.

In the hydrothermal and solvothermal synthesis methods, synthesis reactions are generally conducted in a closed vessel like autoclave, so the temperature, pressure and volume parameters are important. A schematic view for autoclave vessel is given in Figure 2.15. Hydrothermal/solvothermal routes have been attracted great research interest for the fabrication of nanopowders with controllable size and morphology like rods, cubes or flakes in recent years (Feng and Li, 2011).

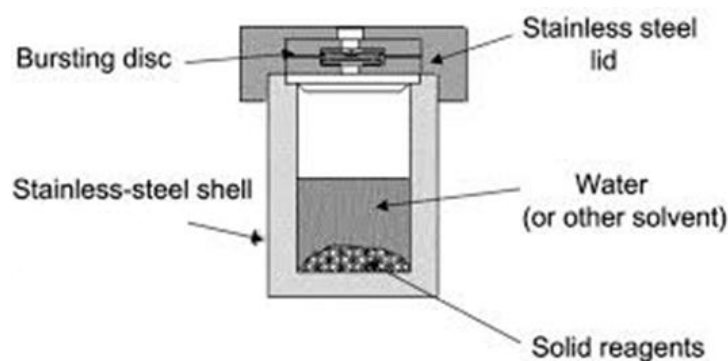


Figure 2.15 : A representative and schematic view of an autoclave vessel, adapted from, Uri-2.

In a typical solvothermal route, reactants of an intended reaction are mixed with an organic or aqueous solvent, a reducing agent and assistive reagents. The mixture is

then placed in a sealed autoclave and heated to a desired temperature and high pressure above the critical point of solvent to produce nanopowders (Feng and Li, 2011). Hydrothermal synthesis routes are environmentally friendly methods because of reduced energy consumption (low temperature synthesis) and taking place in the closed/isolated conditions (Feng and Li, 2011).

The main factors that are involved in the solvothermal reactions are chemical factors and thermodynamical factors (Demazeau, 2008b). The most important chemical factors are the nature of reagents and the solvent. The properties of used solvent affects significantly chemical mechanism involved in the solvothermal reactions. The chemical composition of precursor materials must be arranged to obtain desired materials. Additionally, it was shown that the chemical composition of starting materials plays an important role on the shape and morphology of products (Demazeau, 2008b). Wang et al. (2006) synthesized CdSe and CeTe nanocrystals in different shapes like nanorods and nanodots by the solvothermal synthesis which was controlled by concentration of the precursors. Chen et al. (2012) prepared a series of borides (TiB_2 , ZrB_2 , CeB_6 , LaB_6), carbides and nitrides in a stainless steel autoclave with 20 ml capacity from related oxides and amorphous boron/active carbon/ NaN_3 with the assistance of metallic Na elemental S. They reported that products have different morphologies like particles, nanosheets and cubes.

On the other hand, thermochemical parameters can be summarized as temperature, pressure and the reaction time. These reactions are generally performed at mild temperature conditions (up to 600 °C). Temperature and pressure generally enhance the solubility of reactants into the solvent and favor the proceeding of reaction (in particular during the preparation of micro- or nanocrystallites) since the diffusion and reactivity of chemical species are drastically affected (Demazeau, 2008b). In addition, pressure and temperature can have strong effects on the physicochemical properties of the solvent such as density and viscosity which change considerably with these parameters.

The role of pressure in solvothermal processes were described as (Demazeau, 2010):

- stabilization of more dense structures, if the pressure is high enough,
- increase of the thermal stability range of the reactants,
- enhancement of the chemical reactivity and reaction kinetics.

The solvothermal synthesis of Sb_2S_3 from SbCl_3 and thiourea mixtures in methanol medium as a solvent was given as an example for the pressure formation of nanorods (Yang et al., 2000). As an another example, the effect of imposed pressure values on the formation CuO and Cu_2O nanocrystallites from $\text{Cu}(\text{CH}_3\text{COO})_2$ and water (as the solvent) by the solvothermal route was investigated (Ma et al., 2009). It was stated that the increase of pressure led to hindering the reduction of CH_3COOH (with the partial formation of CuO) and affects the morphology of the crystallites (Ma et al., 2009; Demazeau, 2010).

According to recently published papers, different research areas have been contributed for the development of solvothermal processes (Demazeau, 2010). Synthesis of novel materials, nanocrystallites, biomaterials, hydro/solvothermal crystal growth and preparation of thin films are examples of recent topics of solvothermal processes. During the last twenty years, mainly nanophosphors, nanotubes and nanocomposites well defined in size but with specific morphologies, have been prepared through solvothermal routes. Also, solvothermal synthesis of carbon, in particular carbon sheets, carbon nanotubes and graphene has drawn great interest in recent years (Demazeau, 2010; Guo et al., 2011; Portehault et al., 2011; Xie and Shang, 2007).

3. EXPERIMENTAL PROCEDURE

In this dissertation, hafnium diboride-based powders were synthesized by utilizing mechanically activated borothermal reduction synthesis, mechanochemical synthesis, and autoclave processing methods. Hafnium tetrachloride (HfCl_4) powders were used as the hafnium source. Boron oxide (B_2O_3), amorphous boron (B) and sodium boron hydride (NaBH_4) powders were utilized as boron sources in different synthesis methods. In addition, Mg powders were used as metallic reduction agent. The synthesized HfB_2 -based powders were purified after each process step by eliminating the by-products and impurities with appropriate leaching treatments. Finally, the HfB_2 -based powders prepared by optimum process parameters were consolidated by cold pressing/pressureless sintering and spark plasma sintering techniques. The details of each production and sintering technique are explained below.

3.1 The Raw Materials

The list of the raw materials utilized in this study and their average particle size and purity values are listed in the Table 3.1. Hafnium tetrachloride (HfCl_4) powders were used as an economical hafnium source. In the literature, generally oxide and chloride compounds of hafnium are used for production of hafnium diboride. Hafnium dioxide is known as a highly stable refractory material. Also, it was seen in previous studies conducted in our Particulate Materials Laboratories (PML) that the fabrication of a single phase hafnium diboride by mechanochemical synthesis and mechanically activated annealing synthesis routes starting from HfO_2 is fairly difficult because of its high chemical stability (Balci et al., 2010). In addition, HfCl_4 provides some advantageous over HfO_2 such as its higher reactivity and relatively low boiling point. Thus, HfCl_4 was selected as an alternative and economical hafnium source in this study. On the other hand, there exist some difficulties in handling HfCl_4 , due to its very hygroscopic behavior. Since HfCl_4 is highly

hygroscopic, it is immediately hydrated when it contacts with air. Therefore hafnium oxychloride forms as a result of interaction with moisture in regard of reaction (3.1):



Table 3.1 : The raw materials utilized in this study.

Raw material	Company	Purity, %	Particle Size (μm)
HfCl ₄	Alfa Aesar TM	+98	-
B ₂ O ₃	Eti Mine TM	+98	470
B	ABCR TM	95-97	50
NaBH ₄	ABCR TM	+98	-
Mg	MME TM	99.7	145

HfOCl₂ particles can be further hydrated up to a maximum hydration level of HfOCl₂.8H₂O. Barraud et al. (2006) stated that partially hydrated HfOCl₂.nH₂O powders consist of a HfCl₄ core surrounded by hydrated outer layers having different hydration rates as shown in Figure 3.1.

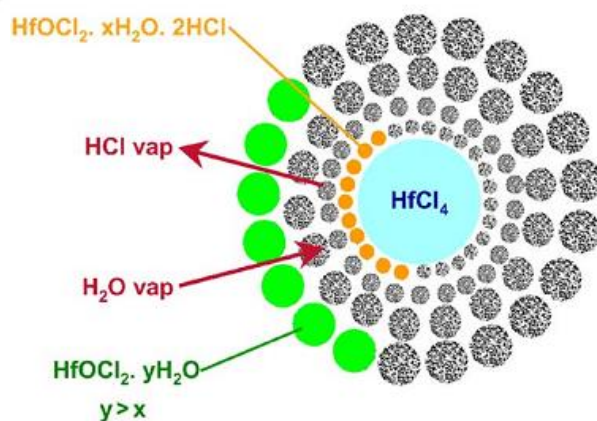


Figure 3.1: Scheme of hydrolysis of an HfCl₄ particle, adapted from Barraud et al., 2006.

In addition, different boron compounds were utilized as boron sources for the different synthesis routes with the intention of exploiting their different chemical and physical properties. And follow-on effects of these boron sources on the synthesis routes and products were investigated.

The stereomicroscope images of raw materials were captured using a ZeissTM Discovery.V12 Stereomicroscope (SM) coupled with a ZeissTM Axiocam ERc5s high resolution digital camera and they are given in the Figure 3.2 (a)-(e).

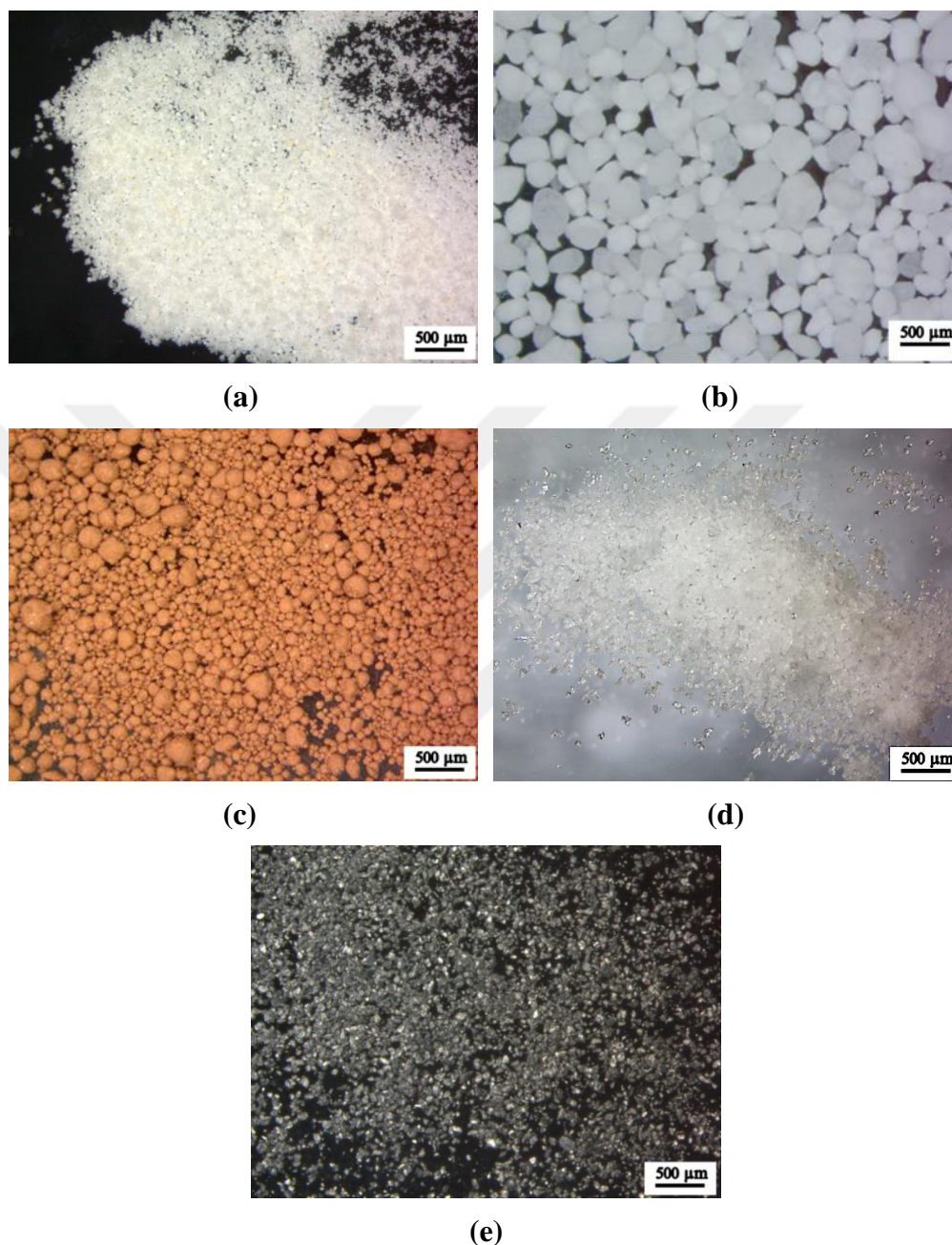


Figure 3.2 : The SM images of raw materials: (a) HfCl_4 , (b) B_2O_3 , (c) amorphous B, (d) NaBH_4 and (e) Mg.

The XRD patterns of HfCl_4 , B_2O_3 , B and Mg powders are respectively illustrated in Figure 3.3 (a)-(d), which reveal the pure materials without any trace of impurities. However, the HfCl_4 powders were oxidized to $\text{HfOCl}_2 \cdot x\text{H}_2\text{O}$ compounds resulting from the handling of the powders during the XRD analysis in a laboratory

atmosphere. Thus, the only phases identified in the XRD pattern of HfCl_4 belong to the $\text{HfOCl}_2 \cdot 4\text{H}_2\text{O}$ (ICDD Card No: 015-0380) and $\text{HfOCl}_2 \cdot 6\text{H}_2\text{O}$ (ICDD Card No: 047-0816) compounds. Additionally, there is a small presence of H_3BO_3 phase (ICDD Card No: 01-072-3608) in the structure of B_2O_3 (Figure 3.3(b)).

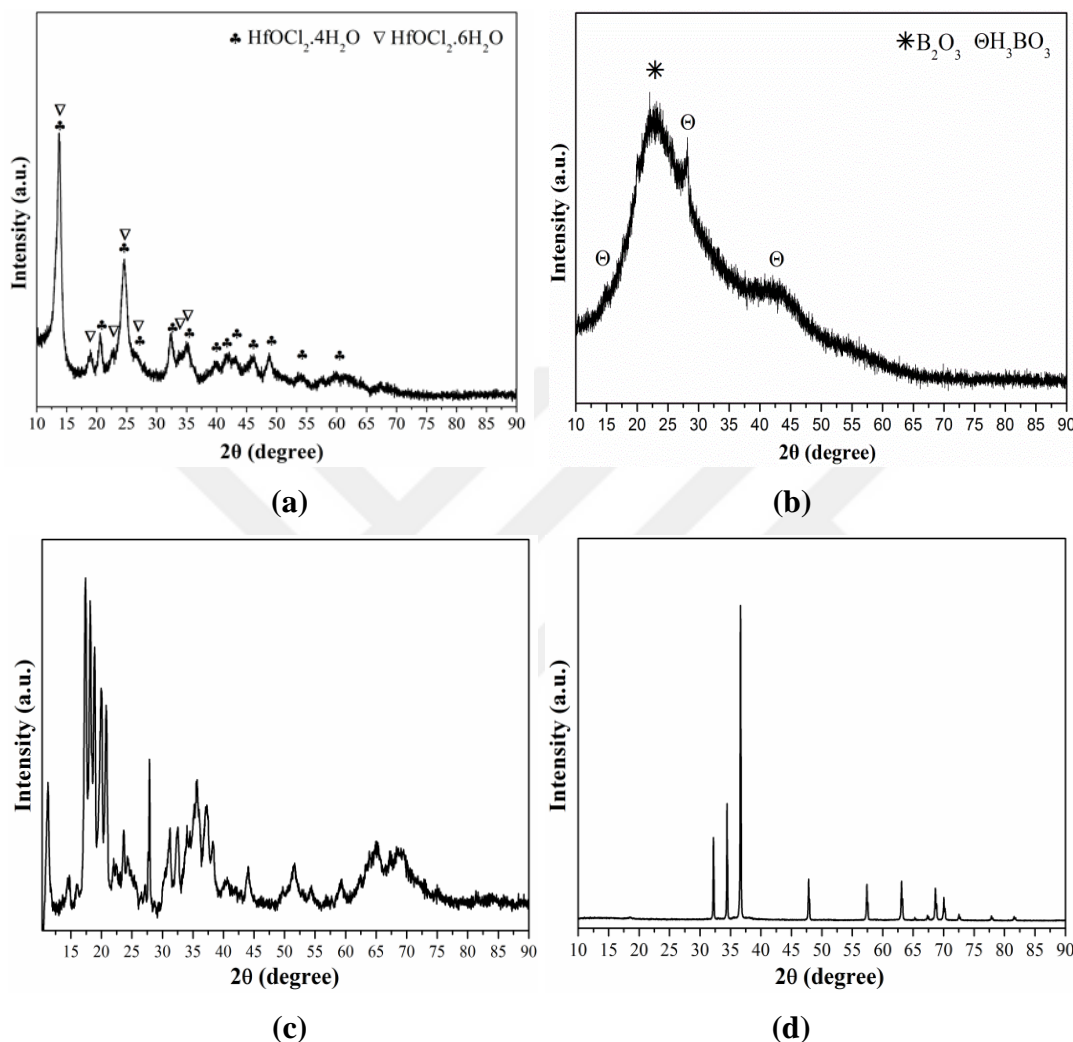


Figure 3.3 : The XRD patterns of raw materials: (a) HfCl_4 , (b) B_2O_3 , (c) amorphous B and (d) Mg.

Furthermore, Co powders (Eurotungstene® with 99.7% purity and particle size of 28 μm) were used as sintering agent during the sintering experiments.

3.2 Synthesis of HfB_2 -Based Powders

The synthesis experiments were conducted using three different methods which are mechanically-activated borothermal reduction, mechanochemical synthesis, and autoclave processing synthesis routes. The powder systems utilized in the each synthesis route are given in the Table 3.2.

Table 3.2 : The utilized synthesis methods and raw materials.

Synthesis Method	Raw Materials
Mechanically-activated borothermal reduction	HfCl ₄ -B
Mechanochemical Synthesis	HfCl ₄ -B ₂ O ₃ -Mg, HfCl ₄ -B-Mg
Mechanically-activated Autoclave Process	HfCl ₄ -B ₂ O ₃ -Mg
Autoclave Process	HfCl ₄ -NaBH ₄ -Mg

3.2.1 Mechanically-activated borothermal reduction method

In the mechanically-activated borothermal reduction route, HfCl₄ and amorphous B powders were used as starting materials. The powder blends containing stoichiometric and stoichiometric excess amounts of the reactants were prepared according to the ideal reduction reaction given in (3.2):



The stoichiometric excess amounts (10-50 wt.% excess) of B were used in order to reveal the effect of the boron content on the final products. The prepared powders were initially blended in an agate mortar under ambient air conditions and they are referred to as as-blended HfCl₄-B powders. All the as-blended HfCl₄-B powders were mechanically activated by milling for 1 h prior to annealing, in a multi-axial vibratory high-energy ball mill (SpexTM 8000D Mixer/Mill) with a rate of 1200 rpm. Milling was performed with a ball-to-powder weight ratio (BPR) of 10:1 using hardened steel balls (in diameter of 6 mm) in a hardened steel vial (with capacity of 50 ml). Powder blends loaded into the vials were sealed in a glove box (PlaslabsTM) under Ar atmosphere (LindeTM, in purity of 99.999 %) to prevent contamination of powder blends from atmospheric conditions during milling process. After mechanically activated powders were unloaded from the vials in the same glove box, they were annealed in alumina boats using a tube furnace (ThermoscientificTM F21130) at 1100 °C for 1 h with a heating and cooling rate of 10 °C/min and under Ar gas flow at a rate of 500 ml/min.

The annealed powders were subsequently washed with distilled water for several times in order to remove the unwanted B₂O₃ phase emerged during the annealing as an impurity. Then, they were subjected to HCl (Merck™, 4 M) leaching under the effect of ultrasonic stirring and heating (Bandelin™ Sonorex), for the elimination of Fe impurity which might have formed as a result of the wear from the milling media during mechanical activation. Leaching parameters such as solid-to-liquid ratio of the solution and duration were fixed respectively at 1 g/10 ml and 15 min, respectively. The supernatant liquids were separated from the insoluble solids by repeated centrifugation (Hettich™ Rotofix 32A, 3500 rpm, 20 min) and decantation steps. All the insoluble solids were dried in a vacuum furnace (Jingke™) at 105 °C for 24 h and the pure resultant powders were obtained.

3.2.2 Mechanochemical synthesis method

The mechanochemical synthesis of HfB₂-HfO₂ and HfB₂ powders was conducted starting from HfCl₄-B₂O₃-Mg and HfCl₄-B-Mg powder blends, respectively. All the prepared powder blends were homogenized in a WAB™ T2C Turbula blender for 1 h prior to the mechanochemical synthesis experiments (the powder mixture was previously prepared and sealed under Ar atmosphere in the glove box). The powder blends containing stoichiometric and stoichiometric excess amounts of the reactants were prepared according to the ideal reduction reactions given in (3.3) and (3.4):



Powder blends loaded into the vials which were sealed in the glove box under Ar atmosphere. The HfCl₄-B₂O₃-Mg and HfCl₄-B-Mg powder blends were milled in the multi-axial vibratory high energy ball mill (Spex™ 8000D Mixer/Mill) operated at 1200 rpm for different durations up to 5 h. The milling experiments were conducted with the same conditions used in the mechanically-activated borothermal reduction method as explained in the section 3.2.1.

After the mechanochemical synthesis, the resultant powders were washed with distilled water for removal of MgCl₂ by-products. Then, they were subjected to HCl (4 M) leaching for the elimination of MgO by-product and the probable Fe impurity. The same leaching and drying parameters which are used

in the mechanically-activated borothermal reduction method were utilized as described in the section 3.2.1.

In addition, some annealing experiments were conducted on the mechanochemically synthesized and purified powders with the aim of observing the any possible phase transformation. The leached powders were annealed in alumina boats using the tube furnace with a heating and cooling rate of 10 °C/min and under Ar gas flow at a rate of 500 ml/min.

3.2.3 Autoclave processing method

In the autoclave processing method, different powder systems which are HfCl₄-B₂O₃-Mg; HfCl₄-NaBH₄-Mg; HfCl₄-H₃BO₃-Mg; HfCl₄-B; HfCl₄-B-Mg and HfOCl₂.8H₂O-B-Mg were utilized. The overall formation reactions for HfCl₄-B₂O₃-Mg and HfCl₄-NaBH₄-Mg powder systems can be written as given in (3.2) and (3.5):



Stoichiometric and stoichiometric excess amounts of reactants were weighed according to the related theoretical formation reactions in order to constitute powder batches of 12 g. The related powder batches were homogenized in the Turbula blender for 1 h (the reactants were previously weighed and sealed under Ar atmosphere in the glove box). Mechanical activation was applied to the HfCl₄-B₂O₃-Mg powder blends by milling in the Spex Mixer/Mill for a short duration using the same milling conditions described in the sections 3.2.1. The powder blends (as-blended or mechanically-activated) transferred into the autoclave vessel in the glove-box under Ar atmosphere. The chemical reactions were took place in a hastelloy autoclave (AmarTM) with 400 ml capacity (Figure 3.4.). The autoclave was purged and sealed under Ar atmosphere and heated to 500 °C at different durations up to 12 h. An initial Ar pressure of 1 or 5 bar was applied during the different experiments. After chemical reaction in the autoclave, water washing and leaching with HCl (4 or 6 M) were applied for removal of MgCl₂ and MgO by-products, respectively. The same leaching and drying parameters which is described in the mechanically-activated borothermal reduction method were utilized.

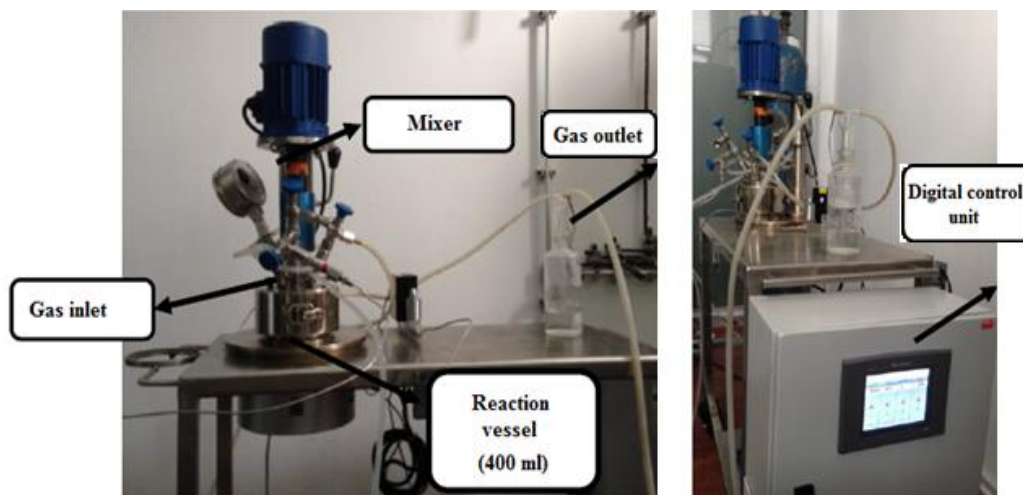


Figure 3.4 : The autoclave system.

The $\text{HfCl}_4\text{-NaBH}_4\text{-Mg}$ blends were annealed at different temperatures after the autoclave processing at $500\text{ }^\circ\text{C}$ for 12 h and washing with distilled water to observe the any possible phase transformation. The annealing treatments were conducted at 750 , $1000\text{ }^\circ\text{C}$ for 3 h and $1700\text{ }^\circ\text{C}$ for 6 h in alumina boats with a heating and cooling rate of $10\text{ }^\circ\text{C}/\text{min}$ and under Ar gas flow.

3.3 Consolidation of the Purified Powders

The HfB_2 and $\text{HfB}_2\text{-HfO}_2$ powders obtained using optimum process parameters through different synthesis methods were consolidated by cold pressing/pressureless sintering (PS) and spark plasma sintering (SPS) techniques.

For the cold pressing/pressureless sintering experiments, the powders were compacted by cold pressing (CP) in a 10 ton capacity MSETM MP-0710 uni-axial hydraulic press under a pressure of 800 MPa to obtain a cylindrical preform with a diameter of about 6.3 mm. The green bodies were sintered at $1700\text{ }^\circ\text{C}$ for 6 h in a LinnTM HT-1800 high temperature controlled atmosphere furnace with a heating and cooling rate of $10\text{ }^\circ\text{C}/\text{min}$ under Ar atmosphere. The images of the green bodies and sintered samples were captured by using a ZeissTM Discovery.V12 Stereomicroscope (SM) coupled with a ZeissTM Axiocam ERc5s high resolution digital camera and illustrated in Figure 3.5. As can be seen from the Figure 3.5, considerable amount of decrease in the diameter sizes of green bodies were observed after sintering which indicates occurring significant amount of shrinkage in the sample volumes and densification during PS.

Spark plasma sintering (SPS) of powders was performed in a FCT Systeme™ HP D 25 SPS equipment. Powders were loaded in a graphite die with an inner diameter of 20 mm and sintered at 1700 °C and 1900 °C for 15 min with heating and cooling rates of 100 °C/min under an applied pressure of 60 MPa.

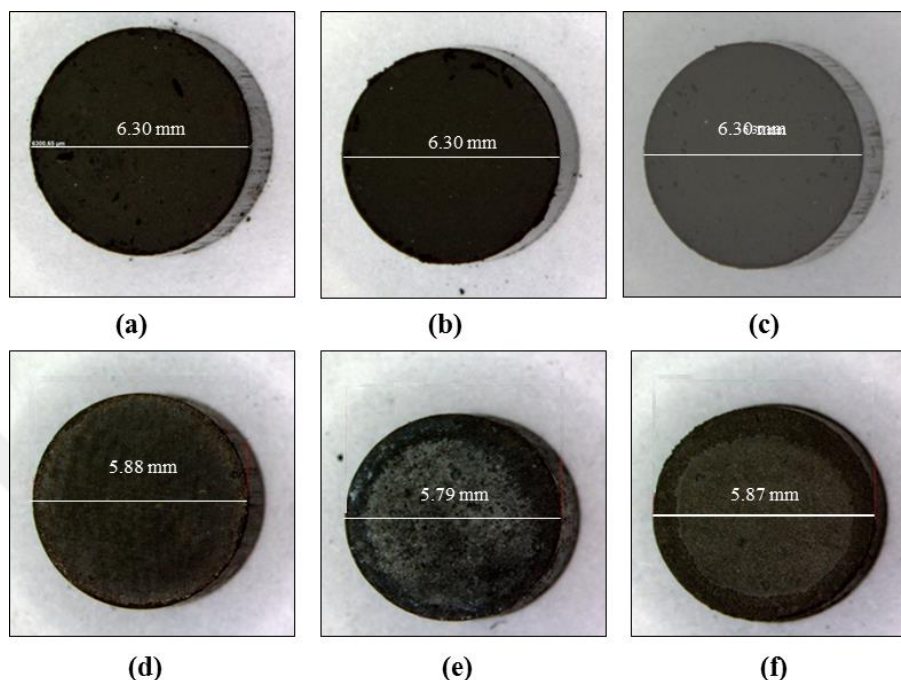


Figure 3.5 : SM images of the some green bodies (a, b and c) and sintered structures (d, e and f) of HfB₂-based products: (a),(d) HfB-B-2CoPS, (b),(e) HfBO-M-2CoPS and (c),(f) HfB-A-2CoPS.

3.4 Characterization Investigations of the Powders and Sintered Product

3.4.1 Characterization investigations of the powders

Phase analyses of the as-blended, mechanically activated, annealed and purified powders were performed by using a Bruker™ D8 Advanced Series X-ray diffractometer (XRD) with CuK α radiation ($\lambda=0.154$ nm, 40 kV and 40 mA) in the 2θ range of 10-90° with a scan rate of 2°/min and a step size of 0.02°. Crystalline phases were identified by utilizing The International Center for Diffraction Data® (ICDD) powder diffraction files. Average crystallite sizes and lattice strains of the powders obtained via the mechanochemical processing of the HfCl₄-B₂O₃-Mg blends were examined using Bruker-AXS™ TOPAS V3.0 software according to the modified Scherrer's formula (Suryanarayana and Norton, 1998). The amounts of different phases in the powders obtained through the mechanochemical processing

and autoclave processing of the $\text{HfCl}_4\text{-B}_2\text{O}_3\text{-Mg}$ blends determined by the semi-quantitative Rietveld method. The Fourier transform infrared (FTIR) spectra of some powders after borothermal reduction and mechanochemical synthesis routes were examined at the wavenumbers between 1000 and 3500 cm^{-1} using a BrukerTM Alpha-T spectrometer equipped with a DRIFT module via KBr pellet technique in the resolution of 4 cm^{-1} with sample and background scan time of 24 scans/min. The gaseous reaction products of the $\text{HfCl}_4\text{-NaBH}_4\text{-Mg}$ system formed during the autoclave processing were analyzed by Fourier transform infrared (FTIR) at the wavenumbers between 1000 and 3500 cm^{-1} in by using a BrukerTM. Alpha-T spectrometer equipped with a gas cell in the resolution of 4 cm^{-1} with sample scan time of 24 scans/min. The reaction gasses formed during the reaction at 500 °C for 12 h in the autoclave were cooled down to the room temperature and they were fed into the gas cell of FTIR unit which was heated to 220 °C for preventing condensation. The thermal properties of the HfCl_4 , as-blended, milled and purified powders were determined via a TATM Instruments SDT Q600 Differential Scanning Calorimeter (DSC)/Thermogravimetric Analyser (TGA). DSC experiments were performed in an alumina crucible up to a heating temperature of 1200 °C with a heating rate of 10°C/min under Ar atmosphere. After DSC analyses, heated powders were subjected to XRD analyses to determine the evolved phases.

The general images of the powders (such as as-received, as-blended, mechanically activated, annealed or purified) were determined by using a ZeissTM DiscoveryV12 stereomicroscope (SM) coupled with a ZeissTM Axiocam ERc5s high resolution digital camera. The microstructures of powders were investigated by using a FEI-Quanta FEG 250 scanning electron microscope (SEM) and a JEOLTM JC-6000 Neoscope SEM both equipped with an energy-dispersive X-ray spectrometer (EDX) and a JEOL JEM-ARM200CFEG UHR transmission electron microscope (TEM). Specimens for SEM investigation were prepared by dispersing the powder in ethanol ($\text{C}_2\text{H}_5\text{OH}$, MerckTM, 99.9 % purity) and drying the suspensions on appropriate SEM plate in air and coating their surfaces with a thin layer of gold using a PolaronTM SC7620 sputter coater to enhance their conductivities. For TEM analysis, the particles were dispersed in the ethanol and a drop of it was taken on a porous carbon film supported on a copper grid and dried in a vacuum oven.

Particle size measurements were conducted on the annealed powders using a MicrotracTM Nano-flex particle size analyzer (PSA) in conjunction with a Bandelin SonopulsTM ultrasonic homogenizer. Supernatant liquids decanted from the water and HCl leaching treatments were also analyzed by a Perkin ElmerTM 1100B atomic absorption spectrometer (AAS) with the aim of determining the boron and iron concentrations.

3.4.2 Characterization investigations of the sintered products

The XRD technique (operating at the same conditions as those of powders), the HitachiTM TM-1000 SEM and FEI-Quanta FEG 250 SEM operating at 15 kV and the optical microscope (OM, Nikon, Eclipse) were used for microstructural characterization studies of the sintered samples. The densities of sintered samples were determined according to the Archimedes method in the ethanol medium and the results were calculated as the arithmetic means of three different measurements for each sample. To obtain scratch-free finished samples, a typical metallographic preparation procedure was applied to the sintered samples before the SEM analyses; microhardness measurements and reciprocating sliding wear test. The sintered samples were hot mounted using StruersTM LaboPress-1 and then they were polished in a StruersTM Tegrapol-15 polishing instrument. Microhardness values of the sintered samples were determined by a ShimadzuTM HMV Microhardness Tester under a load of 200 g for 15 s. Vickers microhardness of each sample include the arithmetic mean of twenty indentation and standard deviations. Reciprocating sliding wear tests of samples were conducted by a TribotechTM Oscillating Tribotester with a 6 mm alumina ball under an applied force of 4 N and a sliding speed of 6 mm/s and a stroke length of 2 mm for a total sliding distance of 20 m at room temperature. A HitachiTM TM-1000 SEM and a VeecoTM Dektak 6M Stylus Profilometer were utilized for imaging the wear tracks after the wear tests. Wear test results of sintered samples are reported as wear volume loss ($WVL = (\pi/4) * \text{width} * \text{depth} * \text{length}$) values which are the arithmetic mean of three different measurements. Relative wear resistance values were calculated as the ratio of highest wear volume loss to the wear volume loss of each sample.

3.5. Thermodynamical Calculations

Thermodynamical interpretations were theoretically conducted by utilizing the FactSage™ 6.2 thermochemical software. The possible reaction mechanisms for the $\text{HfCl}_4\text{-B}$, $\text{HfCl}_4\text{-B}_2\text{O}_3\text{-Mg}$, $\text{HfCl}_4\text{-B-Mg}$ and $\text{HfCl}_4\text{-NaBH}_4\text{-Mg}$ systems were theoretically investigated in some aspects.

Figure 3.6 illustrates the FactSage™ graph of the molar amount variations of the reactants and products with respect to temperature up to 2000 °C in regard of reaction (3.2). According to the thermodynamical predictions, the reaction between the HfCl_4 and B starts approximately at 200 °C with a linear decrease in the mole amounts of the HfCl_4 and B phases and with the emergence of HfB_2 and BCl_3 products. Besides, the formation of HfB_2 and BCl_3 phases reaches their maximum amounts between 1000 and 1200 °C. Also, B sharply diminishes after 1100 °C and is completely consumed at 1200 °C, indicating that the borothermal reduction reaction is completed at this temperature. On the other hand, significant amount of HfCl_3 gas yields especially after 1100 °C and increases gradually with increasing temperatures. This causes to the loss of hafnium source without contributing to the HfB_2 formation and to the decrease in the reaction efficiency. Thus, the results of the thermodynamical evaluations indicate that the temperature range of 1100-1200 °C

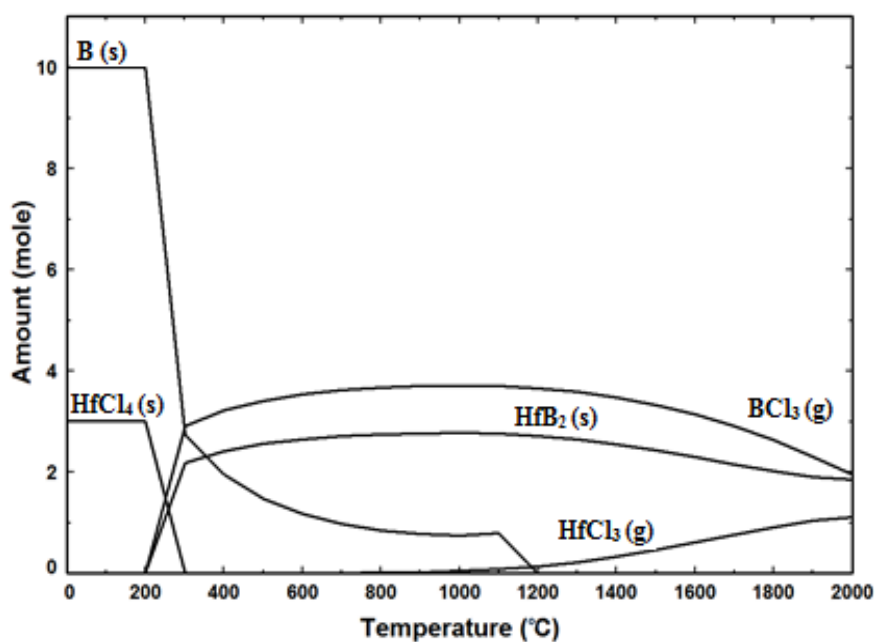


Figure 3.6 : Molar amounts of the reactants and products varying according to the temperature in regard of reaction (3.2).

would be the optimum reaction temperatures to yield the maximum amounts of HfB_2 and BCl_3 and the minimum amount of HfCl_3 .

Figure 3.7 gives the standard Gibbs free energy changes (ΔG°) of the reactions (3.2). The reaction (3.2) has a positive standard free energy change of ~ 150 kJ at room temperature, and it has negative free energy changes at temperatures above ~ 300 °C.

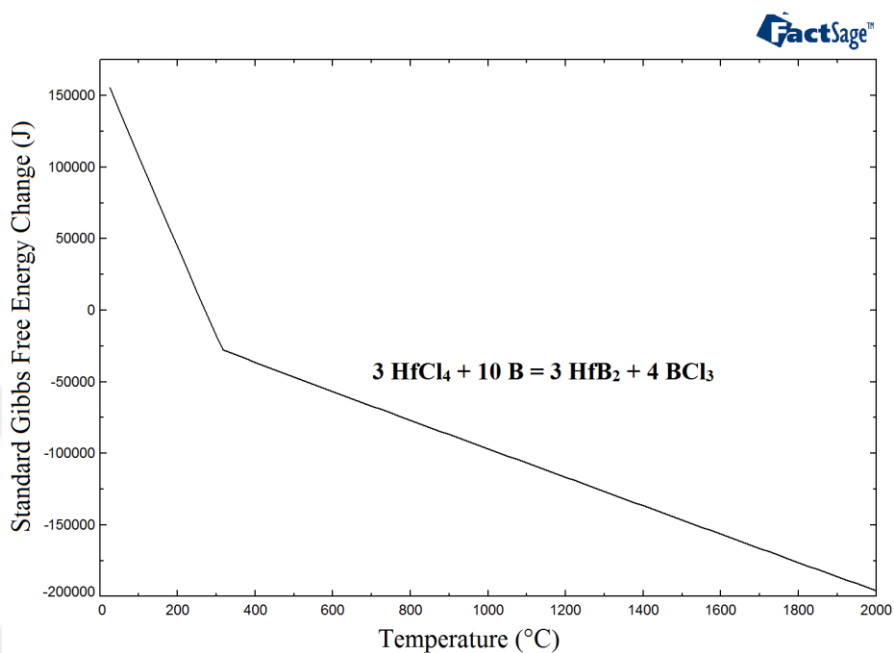


Figure 3.7 : Standard Gibbs free energy changes of the reactions (3.2) varying according to the temperature.

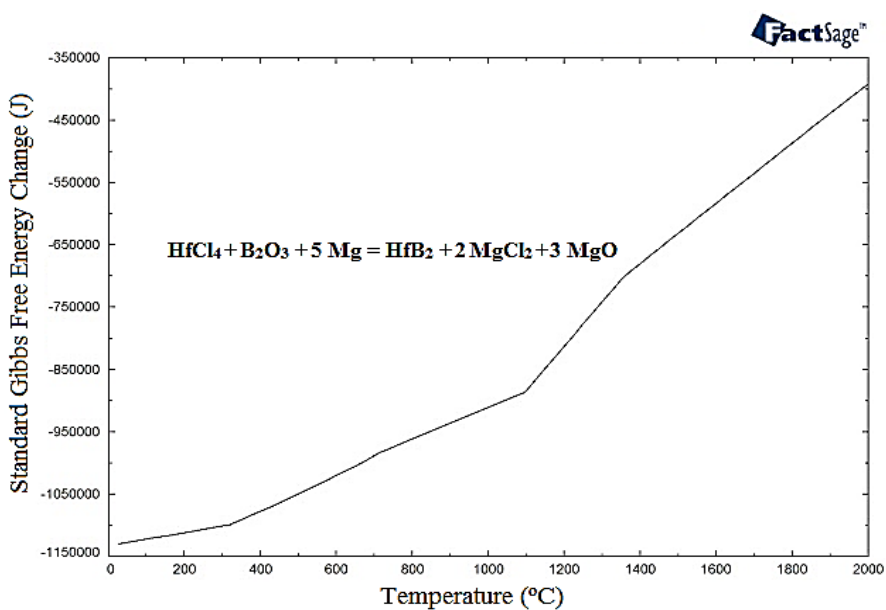


Figure 3.8 : Standard Gibbs free energy changes of the reactions (3.3) varying according to the temperature.

The value of the Gibbs free energy change decreases from -35 to -110 kJ as the temperature increases from 300 to 1100 °C. The mentioned reaction is thermodynamically not feasible at temperatures between 25 and 300 °C, and hence it takes place spontaneously if the temperature is increased over 300 °C.

Figure 3.8 illustrates the standard Gibbs free energy change (ΔG°) versus temperature curve of the reaction given in Eq. (1) up to 2000 °C. The reaction has large negative standard free energy change between -400 and -1125 kJ in the temperature range of 0-2000 °C. This means that the reduction reaction in the HfCl₄-B₂O₃-Mg system is thermodynamically feasible and takes place spontaneously at room temperature and above. Moreover, a large negative enthalpy change of the reaction implies that it is extremely exothermic and a large amount of heat will be released during synthesis procedure. The difference between Figure 3.7 and 3.8 regarding ΔG° of related reactions according to temperature emphasizes the difference between the borothermal and the magnesiothermal reactions. Figure 3.9 gives the standard Gibbs free energy changes (ΔG°) of the reactions (3.4). As seen from Figure 3.9, the reaction (3.4) has large negative standard free energy changes (between -625 and -325 kJ) in the temperature range of 0-2000 °C. This means that reaction (3.4) takes place spontaneously and therefore it is thermodynamically feasible at room temperature and above.

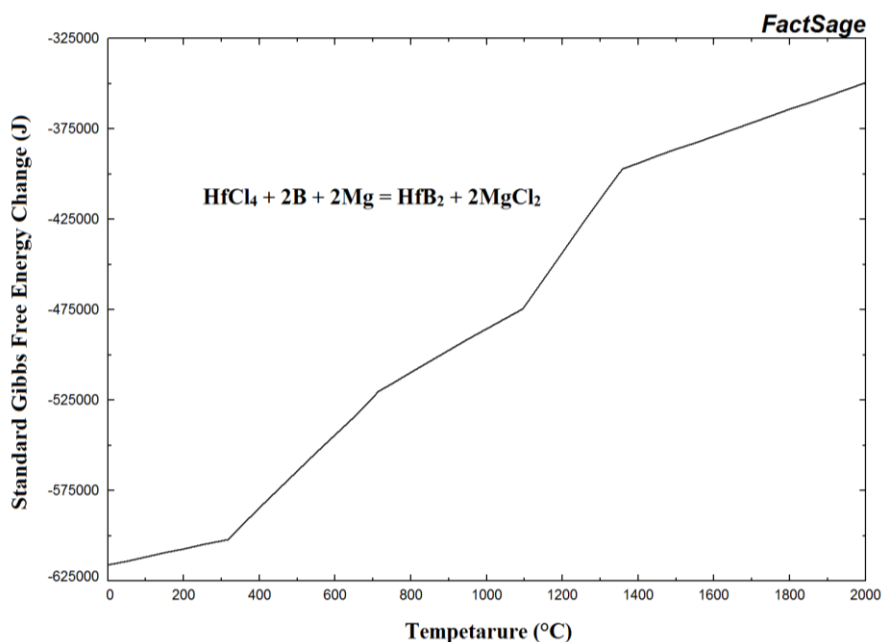


Figure 3.9 : Standard Gibbs free energy changes of the reactions (3.4) varying according to the temperature.

Molar amounts of the reactants and products of the reaction (3.3) varying according to the Mg amount were calculated for room temperature and given in Figure 3.10. According to the Figure 3.10, almost all amount of HfCl_4 is consumed when 5 moles of Mg (stoichiometric amount) is used and the amounts of reaction products (HfB_2 , MgCl_2 and MgO) remain unchanged after this amount. Therefore, experiments on the $\text{HfCl}_4\text{-B}_2\text{O}_3\text{-Mg}$ system were mainly conducted with stoichiometric amount of Mg.

The reaction products for the $\text{HfCl}_4\text{-B}_2\text{O}_3\text{-Mg}$ system were thermodynamically predicted by varying the temperature up to 2000 °C for the autoclave processing route and given in Figure 3.11. The amounts of reaction products such as HfB_2 (1 mol) and MgO (3 moles) are constant approximately up to 1500 °C and start to decrease after this temperature. Meanwhile, MgCl_2 starts to convert into gas phase after reaction temperature reaches to 1125 °C. In addition, at higher temperatures especially over 1500 °C, HfO_2 and magnesium borate ($\text{Mg}_3\text{B}_2\text{O}_6$) phases appear probably due to the interaction of HfB_2 with MgO .

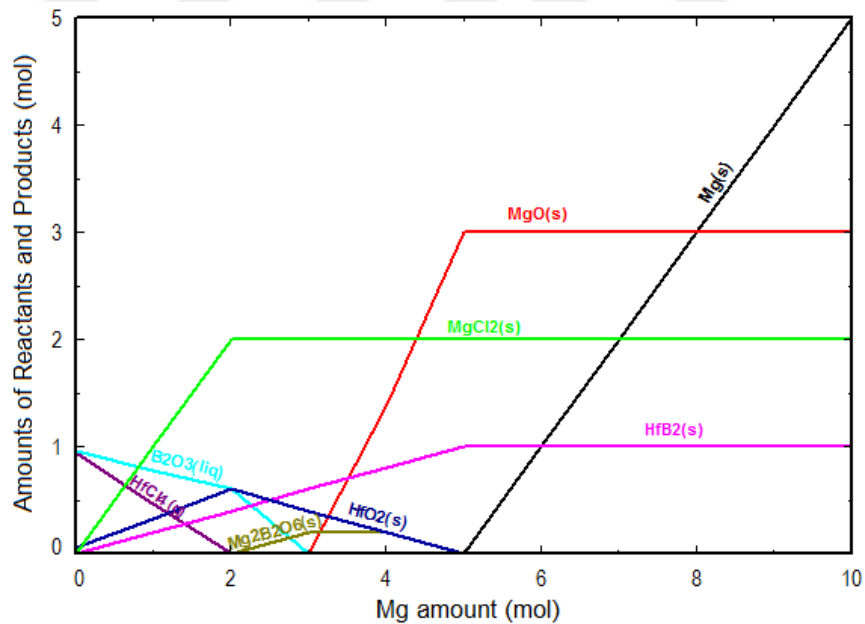


Figure 3.10 : Molar amounts of reactants and products of the reaction (3.3) at room temperature varying according to the Mg amount.

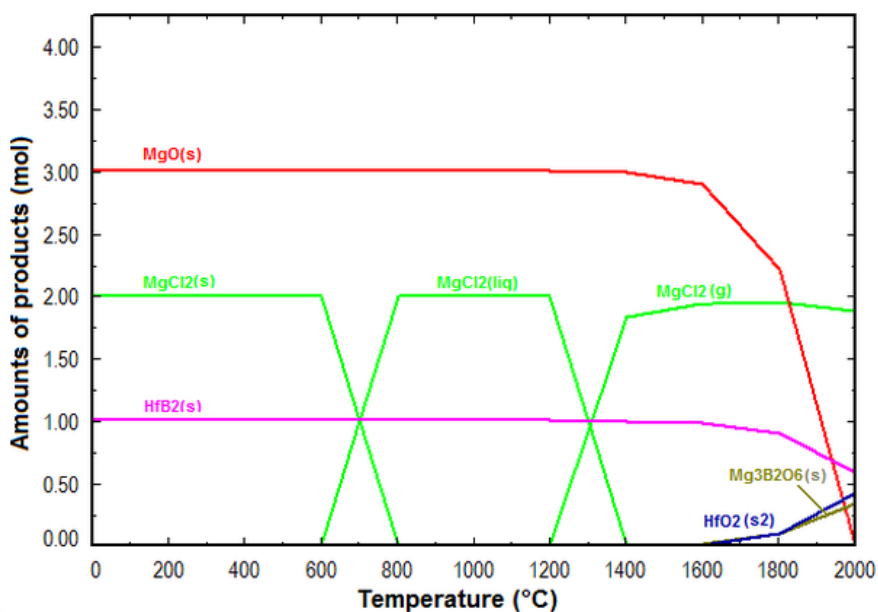


Figure 3.11 : Molar amounts of products of the reaction (3.3) varying according to the temperature.

Figure 3.12 gives the standard Gibbs free energy changes (ΔG°) of the reactions (3.5). The reaction (3.5) has large negative free energy changes (between -600 and -2400 kJ) in the temperature range of 0 - 2000 °C according to the Figure 3.12. In addition, the standard Gibbs free energy of the system reduces further by increasing temperature and formation of the reaction become more feasible. The reaction (3.5) has a ΔG° value of about -1100 kJ at 500 °C.

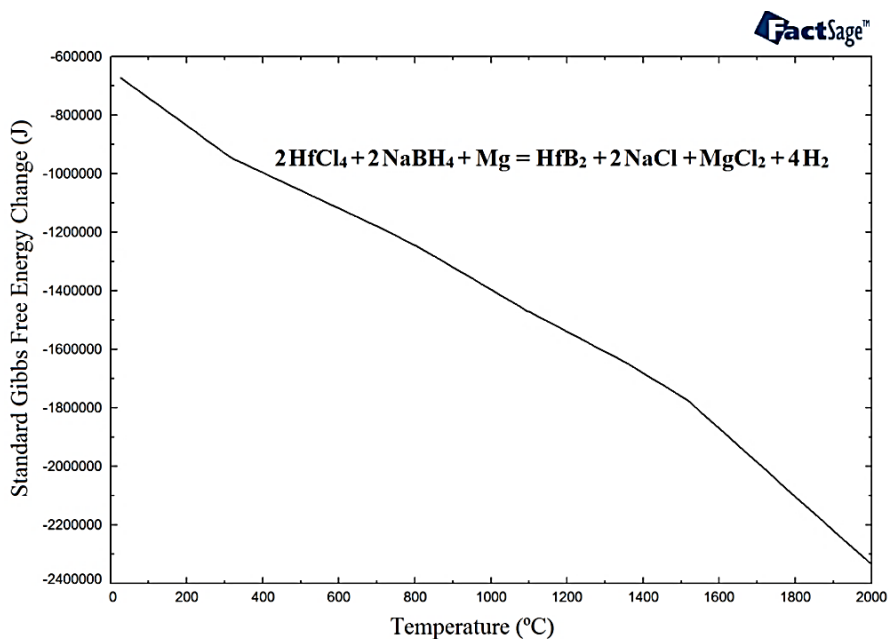


Figure 3.12 : Standard Gibbs free energy changes of the reactions (3.5) varying according to the temperature.

For the autoclave processing of HfCl_4 - NaBH_4 - Mg system, the reaction products were thermodynamically predicted by varying the temperature up to 2000 °C and given in Figure 3.13. HfB_2 , Na_2MgCl_4 and H_2 are determined as main products of the reaction approximately up to 800 °C and over this temperature NaCl , MgCl_2 and HCl form by decomposition of Na_2MgCl_4 . On the other hand, the amount of the HfB_2 phase remains almost constant by rising temperature from room temperature to 2000 °C.

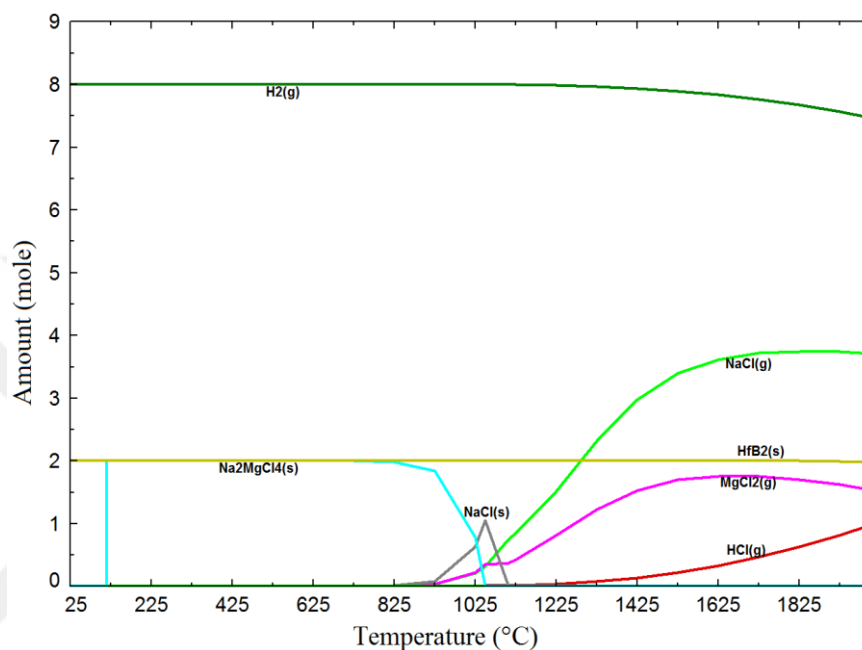


Figure 3.13 : Molar amounts of the reactants and products varying according to the temperature in regard of reaction (3.5).

Molar amounts of the reactants and products of the reaction (3.5) varying according to the NaBH_4 amount were calculated at 500 °C and given in Figure 3.14. In the Figure 3.14, the HfB_2 amount increases by increasing NaBH_4 amount and reach its maximum amount at 5 moles of NaBH_4 . This indicates the stoichiometric excess amounts of NaBH_4 are needed to complete reduction of the HfCl_4 at this temperature. Therefore, NaBH_4 were utilized in 100% and 200% excess amounts during the autoclave processing experiments to investigate the effect of NaBH_4 amount on the reaction products.

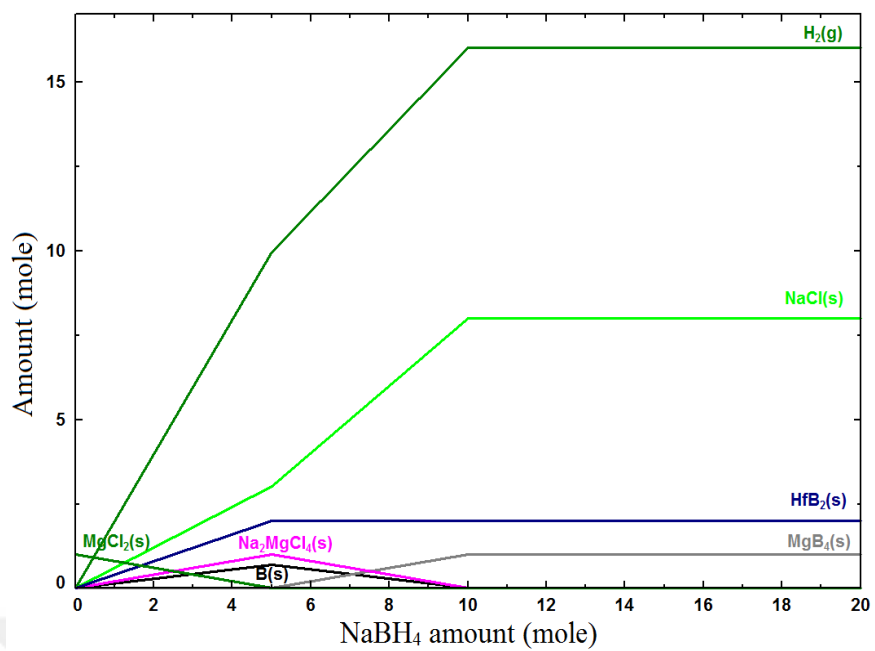


Figure 3.14 : Molar amounts of reactants and products of the reaction (3.5) at 500 °C varying according to the NaBH₄ amount.

4. RESULTS AND DISSCUSION

4.1 The Mechanically Activated Borothermal Synthesis of HfB₂ Powders

HfB₂ powders were synthesized via a borothermal reduction route from mechanically activated HfCl₄ and B powder blends. Mechanical activation of the powder blends was carried out for 1 h in a high-energy ball mill using hardened steel vial and balls. Mechanically activated powders were subsequently annealed at 1100 °C for 1 h under Ar atmosphere. Then, purification treatments such as washing with distilled water and leaching in HCl solution were applied for the elimination of the undesired boron oxide (B₂O₃) phase and the probable Fe impurity. The effect of boron amount on the microstructure of the resultant powders was investigated.

4.1.1 Phase analyses of the as-blended, mechanically activated, annealed and purified powders

Figure 4.1 (a) through (c) show the XRD patterns of the as-blended stoichiometric HfCl₄-B powders and those mechanically activated for 1 and 5 h. As clearly seen from Figure 4.1, there was no reaction between the HfCl₄ and B particles even after milling for 5 h. The only phases identified in the XRD patterns (Figure 4.1 (a) through (c)) belong to the HfOCl₂.4H₂O (ICDD Card No: 015-0380) and HfOCl₂.6H₂O (ICDD Card No: 047-0816). The B phase could not be detected in the XRD patterns of the as-blended and those milled for 1 and 5 h due to its amorphous nature. It is clear that HfOCl₂.xH₂O peaks broaden and their intensities gradually decrease upon increasing the milling

Since HfCl₄ is highly hygroscopic, it is immediately hydrated when it contacts with air, therefore hafnium oxychloride forms as a result of interaction with moisture in regard of reaction given in (3.1).

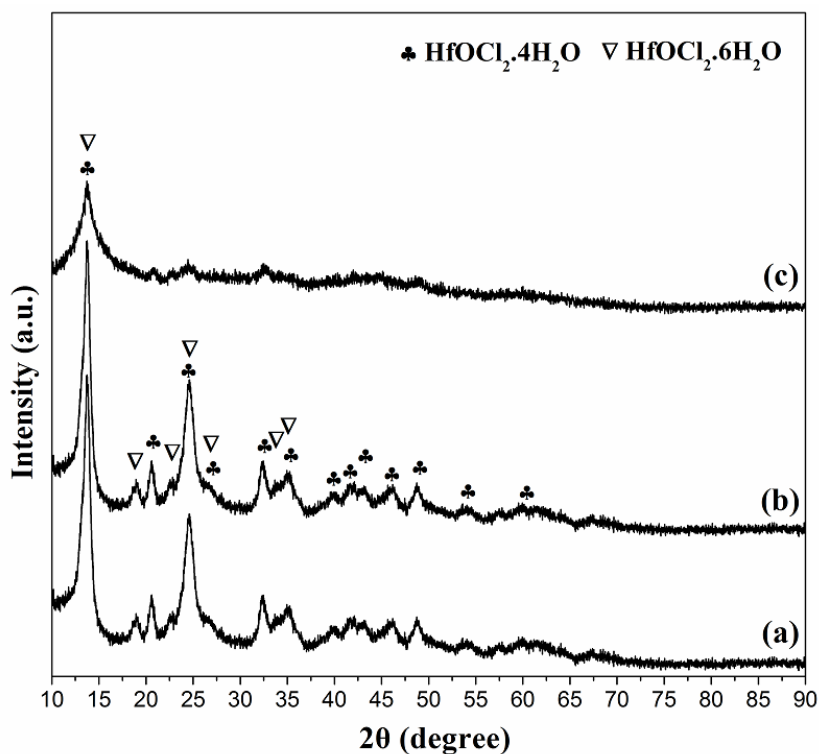


Figure 4.1 : XRD patterns of the as-blended and mechanically activated powders: (a) as-blended, (b) 1 h and (c) 5 h.

HfOCl₂ particles can be further hydrated up to a maximum hydration level of HfOCl₂.8H₂O. Barraud et al. (2006) stated that partially hydrated HfOCl₂.nH₂O powders consist of a HfCl₄ core surrounded by hydrated outer layers having different hydration rates.

On the basis of Figure 4.2., the mechanical activation time was selected as 1 h considering that a short duration is generally required for the activation of the reactant particles without resulting in any microstructural change in the overall powder. Thus, further annealing was conducted only on the powders mechanically activated for 1 h.

In order to reveal the effect of mechanical activation, XRD investigations were carried out on the as-blended and annealed powders with addition of stoichiometric and 20 wt.% stoichiometric excess boron (Figure 4.2). Furthermore, Figure 4.3 displays the XRD patterns of the mechanically activated and subsequently annealed powders with different excess amounts of boron (0, 10, 20 and 50 wt.%). As obviously seen from Figures 4.2 and 4.3, the HfB₂ (ICDD Card No: 038–1398, Bravais lattice: primitive hexagonal, a=b=0.314, c=0.347 nm) as a primary phase was detected in the microstructure of all powders after annealing.

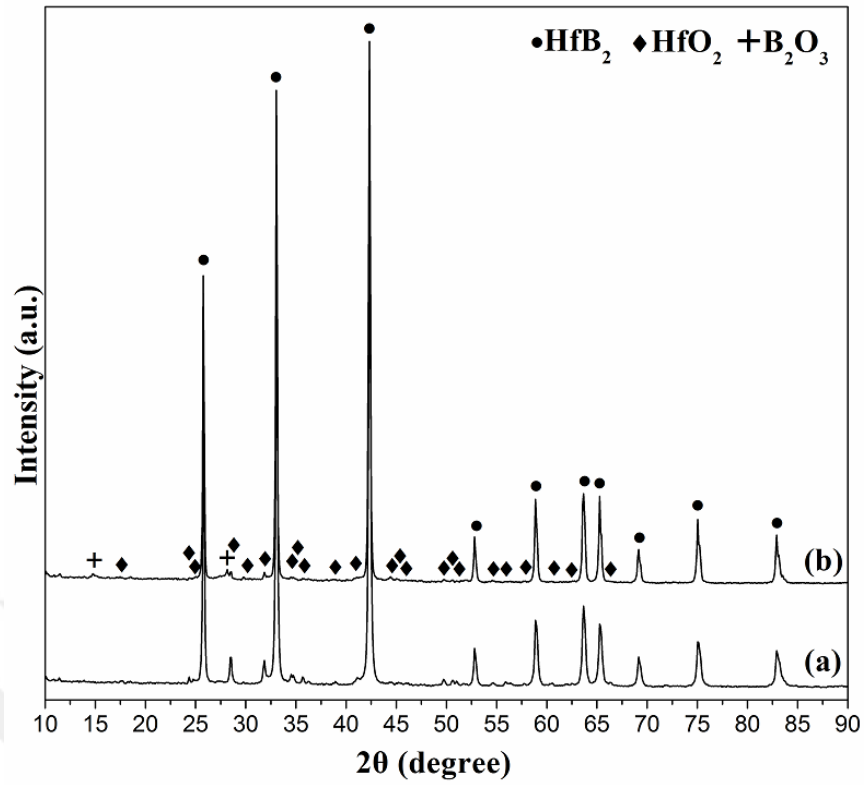


Figure 4.2 : XRD patterns of the as-blended powders with different boron amounts after annealing: (a) 0 wt.% excess boron (stoichiometric) and (b) 20 wt.% excess boron.

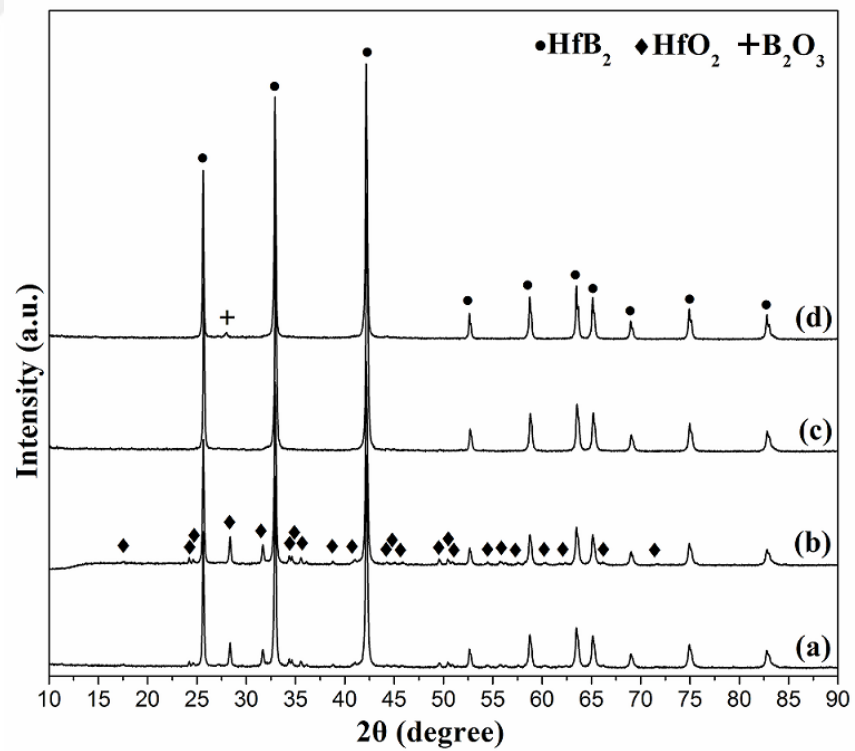


Figure 4.3 : XRD patterns of the mechanically activated powders with different boron amounts after annealing: (a) 0 wt.% excess (stoichiometric), (b) 10 wt.% excess, (c) 20 wt.% excess and (d) 50 wt.% excess.

X-ray reflections for the HfB_2 phase contain ten peaks at values of 25.606, 32.887, 42.135, 52.611, 58.714, 63.447, 65.093, 68.954, 74.877 and 82.735° which are respectively indexed as {001}, {100}, {101}, {002}, {110}, {102}, {111}, {200}, {201} and {112} families of planes. On the other hand, it can be seen by comparison of the XRD patterns in the Figures 4.2 (b) and 4.3 (c) that a small amount of HfO_2 (ICDD Card No: 034–0104, Bravais lattice: primitive monoclinic, $a=0.528$, $b=0.518$, $c=0.511$ nm, $\beta=99.259^\circ$) phase was observed in the XRD patterns of the as-blended powders with the addition of 20 wt.% excess of boron after annealing while mechanically activated ones with the same boron content have only HfB_2 phase without any detectable HfO_2 . High-energy ball milling enables to obtain intimate mixing at chemical level by particle size reduction and impact, which affects the reactivity of the powder particles. Additionally, accumulation of structural defects such as stacking faults, dislocations and vacancies in crystalline lattice during milling could enhance the mass transport during the annealing step (Suryanarayana, 2001). Also, the XRD patterns in Figure 4.3 reveal that the utilized boron amount has a considerable effect on the formation of the HfO_2 phase. In the XRD patterns of the mechanically activated and annealed powders having stoichiometric and 10 wt.% excess amounts of boron, HfO_2 phase was detected as a secondary phase together with the major HfB_2 phase. The existence of the HfO_2 phase is due to the decomposition of hydrated HfCl_4 powders (conversion of HfOCl_2 to HfO_2) by the effect of temperature during annealing. Barraud et al. (2006) investigated the thermal gravimetric analysis of weakly hydrated $\text{HfOCl}_2 \cdot n\text{H}_2\text{O}$ with $n \leq 4$ and stated that after initial sublimation of HfCl_4 occurring from 240 to 300 °C, transformation into HfO_2 takes place at higher temperatures. Fang and Dixon (2013) reported reaction paths for the HfCl_4 and ZrCl_4 reacting with H_2O . They stated that the hydrolysis of $\text{ZrCl}_4/\text{HfCl}_4$ begins with the formation of oxychlorohydroxides followed by the gradual elimination of HCl instead of the direct production of $\text{ZrOCl}_2/\text{HfOCl}_2$ and HCl. During the annealing at 1100 °C, the HfO_2 phase formed upon heating and was reduced by boron to form HfB_2 . Guo et al. (2012b) reported on the borothermal reduction of HfO_2 with amorphous B at the temperatures between 900 and 1100 °C. Their results indicated that borothermal reduction of HfO_2 by B could be completed at 1100 °C, however below this temperature HfO_2 phase still existed. Additionally, B_2O_3 phase (ICDD Card No: 013–057) at $2\theta=27.77^\circ$ was identified in the microstructure of some of the annealed samples originating from the as-blended

powders with 20 wt.% excess boron (Figure 4.2(b)) and mechanically activated powders with 50 wt.% excess boron (Figure 4.3 (d)), indicating that the effect of activation by providing homogeneous distribution of the reactants.

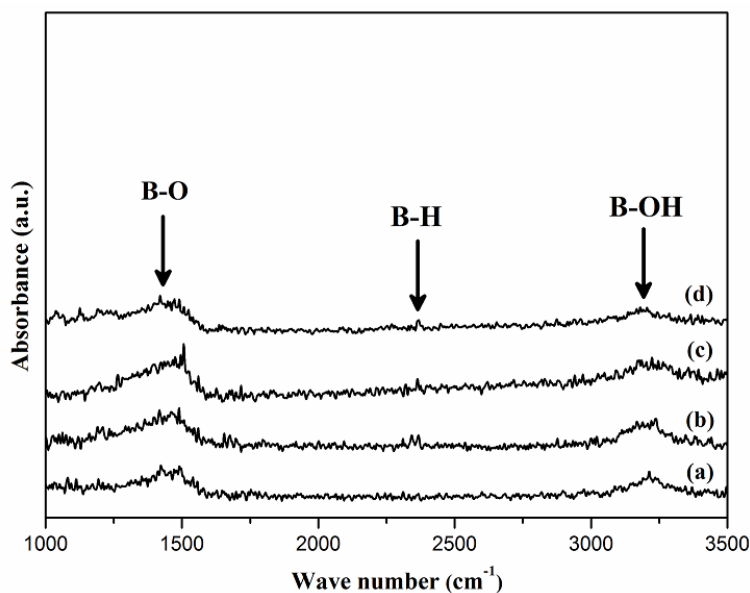


Figure 4.4 : FTIR spectra of the mechanically activated and annealed powders with different wt.% excess boron amounts: (a) 0 wt.%-stoichiometric, (b) 10 wt.%, (c) 20 wt.% and (d) 50 wt.% .

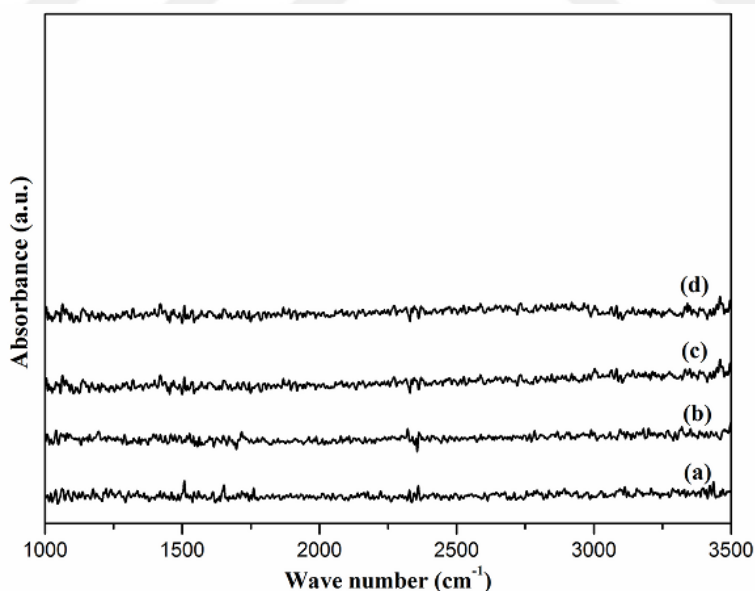


Figure 4.5 : FTIR spectra of the mechanically activated and annealed powders (with different wt.% excess boron amounts) after washing with distilled water: (a) 0 wt.%-stoichiometric, (b) 10 wt.%, (c) 20 wt.% and (d) 50 wt.% .

Excess boron amounts in the overall powders cannot completely contribute to the reduction reaction and some amount of unreacted B might be converted into the B_2O_3 phase during annealing. If there is some B_2O_3 in the structure of the annealed

samples originating from stoichiometric as-blended powders and mechanically activated powders with 0, 10 and 20 wt.% excess B amounts, it is not possible to detect it using XRD due to the dominant peaks of HfB_2 with high intensities. Ran et al. (2010) reported the existence of the B_2O_3 phase in the XRD analyses of ZrB_2 powders prepared by borothermal reduction of ZrO_2 . As another evidence to demonstrate the presence of the B_2O_3 phase, the FTIR analyses were conducted on the annealed powders.

Figures 4.4 and 4.5 represent the respective FTIR analyses of the mechanically activated powders both after annealing and washing with distilled water, which were conducted to demonstrate the presence and the removal of B_2O_3 after respective annealing and washing treatments. Broad absorption peaks at about 1500 cm^{-1} (B-O stretching mode) and 3213 cm^{-1} (OH stretch of hydroxyl group) were observed in the annealed powders. As expected, the peak intensities of the IR absorptions at 1500 cm^{-1} increase as the boron content increases from 0 to 50 wt.% (Figure 4.4 (a) through (d)). Additionally, annealed powders have a weaker IR absorption peak at about 2300 cm^{-1} (B-H mode) (Moon et al., 2004; Putkonen and Niinisto, 2006). This proves that the HfO_2 phase was reduced by B and the B_2O_3 phase was emerged by the effect of temperature during the annealing process. The formation of B-H and B-OH bonds in addition the B-O bonds can be attributed to the humidity physically or chemically adsorbed onto the B_2O_3 structure resulting from the handling of the powders during the FTIR analyses in a laboratory atmosphere. On the other hand, in the FTIR spectra of the same powders after washing (Figure 4.5 (a)-(d)), no absorption belongs to B-O, B-OH and B-H bands were detected because complete elimination of the undesired B_2O_3 phase was succeeded.

For a quantitative evidence of the presence of B_2O_3 in the annealed powders, AAS analyses were conducted on the supernatant liquids. AAS results showed that the supernatant liquids obtained from the leaching treatment of the stoichiometric powders and the powders containing 20 wt.% stoichiometric excess of B consist of 167 and 257 ppm B, respectively.

The XRD pattern of the powders containing 20 wt.% excess boron after washing with distilled water is given in Figure 4.6. Comparing this with the XRD pattern in Figure 4.3 (c), no remarkable changes were observed in the XRD pattern of the washed powders (Figure 4.6) after removal of B_2O_3 . Additionally, these powders

were leached in 4 M HCl in order to remove any possible Fe impurities which could be released from hardened steel milling vial/balls and hence incorporated into the particles.

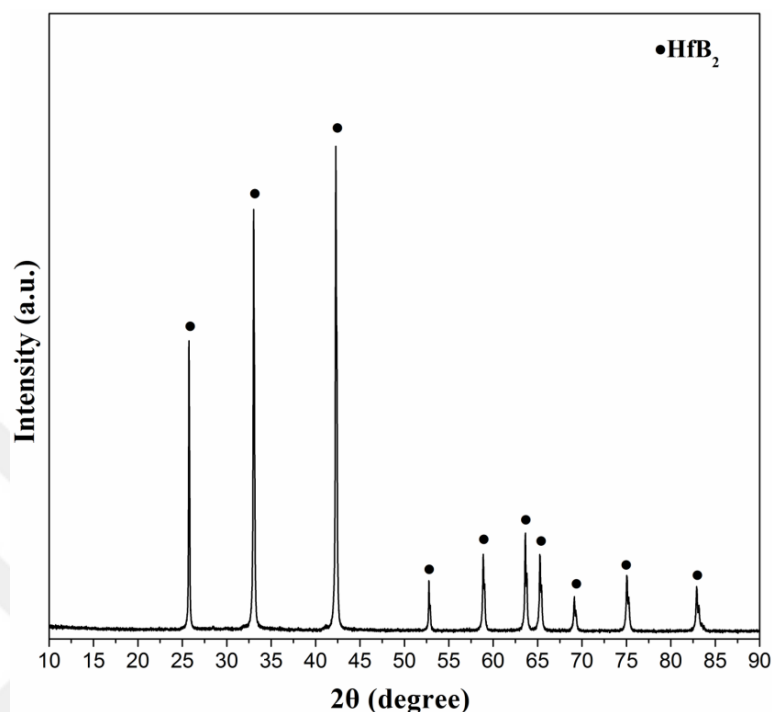


Figure 4.6 : XRD pattern of the 20 wt.% excess boron containing powders after the mechanical activation, annealing and leaching treatments.

AAS analysis showed that there was 4.37 ppm Fe in the solution of the leached powders. In some studies about the synthesis of LaB₆ and SmB₆ powders from La₂O₃-B₂O₃-Mg and Sm₂O₃-B₂O₃-Mg blends by mechanochemical reactions in the SPEXTM 8000D Mixer/Mill for 5 h (using the same conditions such as BPR, milling container, media and atmosphere), the supernatant liquids respectively comprised about 11 and 7.81 ppm Fe after leaching with 3.6 and 4 M HCl (Ağaoğulları et al., 2012a, 2015). As expected, the amount of Fe impurity released from the purified HfB₂ powders is lower than those released from the leached LaB₆ and SmB₆ powders due to the lower duration of milling. Thus, as shown by the XRD pattern in Figure 4.6 and as mentioned by the AAS results, HfB₂ powders were prepared by the borothermal reduction of HfO₂ evolved by the dehydration of hafnium oxide halides upon heating without the presence of any detectable HfO₂ and undesired B₂O₃ and Fe impurities.

The stereo-microscope (SM) images of the as-blended, mechanically activated, annealed and purified powders containing 20 wt.% excess boron are given in Figure

4.7. As clearly observed from the images, the mechanically activated powders (Figure. 4.7 (b)) have a rather homogenized structure compared to the as-blended ones (Figure 4.7 (a)). The high-energy ball milling process provides a homogeneous distribution of the particles throughout the microstructure, which accelerate the synthesis reaction. During the annealing, color of the powders turned to dark gray as a result of the HfB_2 phase formation (Figure 4.7 (c)). After the purification, a morphological difference was observed due to the agglomeration of the particles (Figure 4.7 (d)).

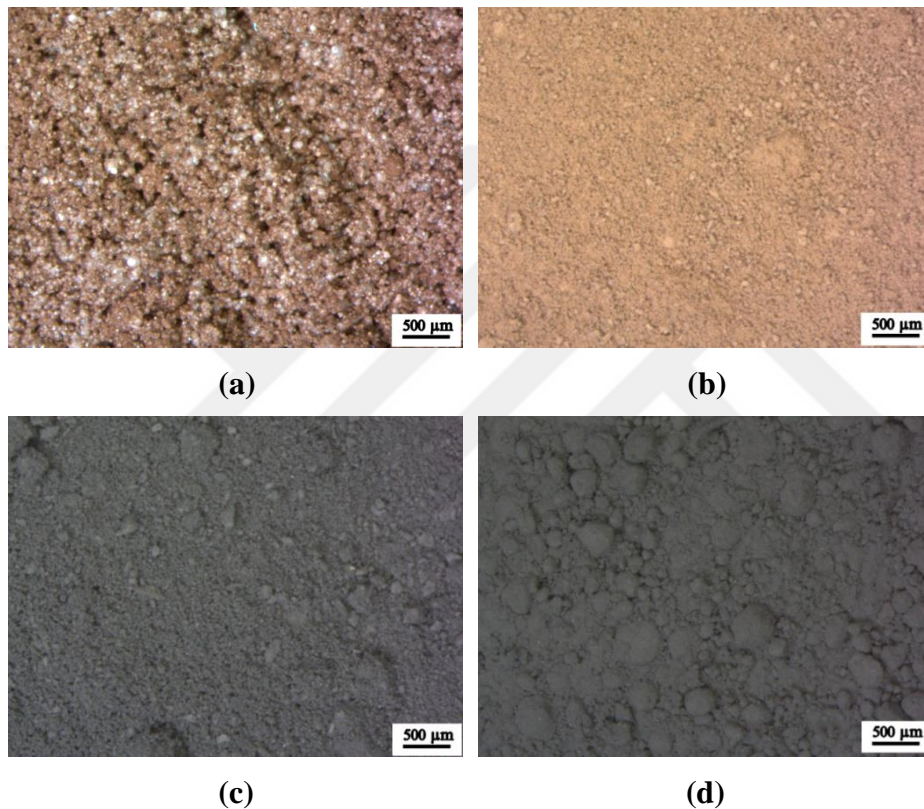


Figure 4.7 : SM images of the powders containing 20 wt.% excess B: (a) as-blended, (b) mechanically activated, (c) annealed and (d) washed with distilled water.

Figure 4.8 (a) and (b) display the secondary electron SEM images of the mechanically activated HfCl_4 -B powders with the addition of 20 wt.% excess boron which are subjected to annealing and purification, respectively. In Figure 4.8 (a), the heat treated powders show irregular and faceted particles having sizes in the range of 500 nm and 2 μm . After washing and HCl leaching (Figure 4.8 (b)), the particles with sizes ranging between 300 nm and 1.5 μm have rather uniform appearance with different faceted (rectangular or elongated) rod-like and irregular morphologies. In a current study, ZrB_2 powders obtained by borothermal reduction of ZrO_2 also

showed a very similar faceted morphology after washing the prepared powders by hot distilled water (Ran et al., 2010). Guo et al. (2012a) synthesized ZrB_2 powders from mechanically activated $ZrCl_4$ and B blends; they reported the powders consist of platelet-like particles and whiskers. Moreover, Barraud et al. (2005) prepared HfB_2 powders from mechanically activated $HfCl_4$ and B powders with nanorod morphology and the necessity of presence of iron borides and boron oxide for the growth of nanorods during annealing was stressed. The effect of B_2O_3 phase on the growth mechanism of nanorods has been well discussed in the literature (Barraud et al., 2005; Guo et al., 2012a; Liu et al., 2003; Wang et al., 2015). The B_2O_3 phase melts (T_M : 450 °C) during the annealing and HfO_2 particles may be dispersed in the liquid B_2O_3 which enhances the diffusion and facilitates the nucleation at the solid-liquid interface. Additionally, mechanical activation of reactants helps to improve diffusion by homogeneous mixing and intimate contact between the particles (Barraud et al., 2005; Guo et al., 2012a; Suryanarayana, 2001).

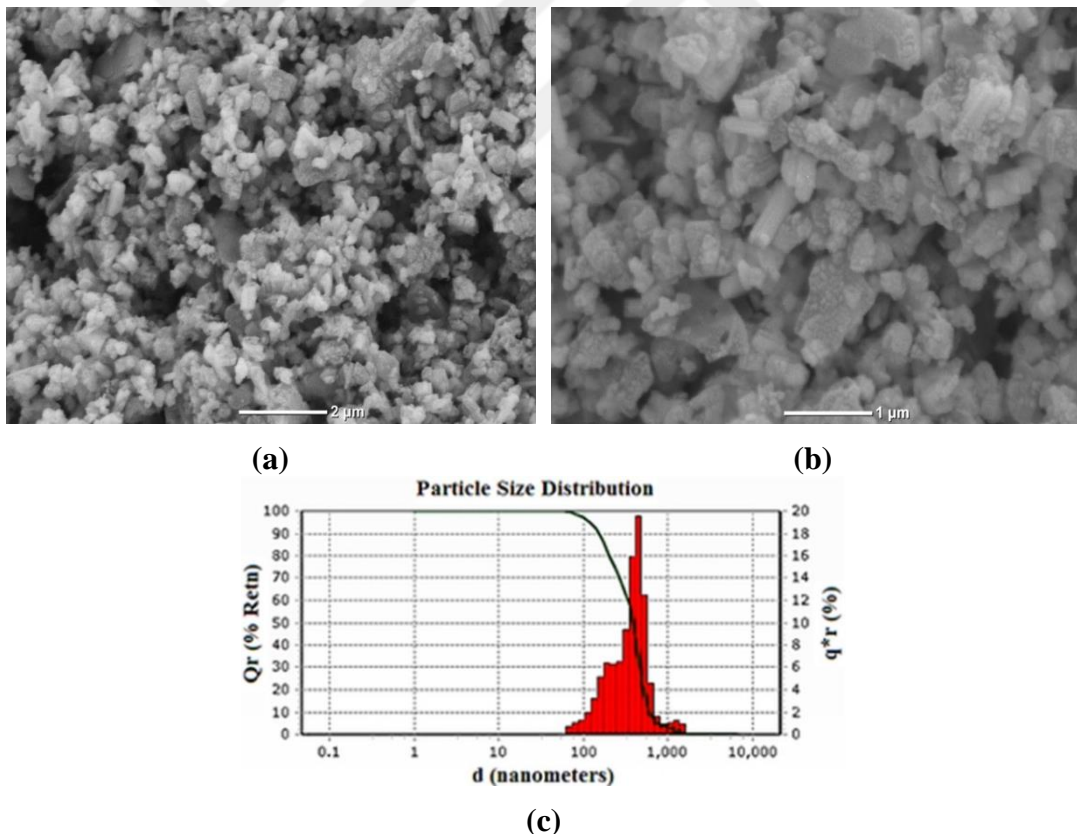


Figure 4.8: SEM images of the mechanically activated powders containing 20 wt.% excess B: (a) annealed, (b) washed with distilled water, and (c) its corresponding PSA analysis.

PSA graph of the powders in Figure 4.8 (c) represents the particle size distribution almost between 100 nm and 1 μm which is in good accordance with the SEM result in Figure 4.8 (b). As well as, the average particle size of the resultant powders was measured as 391 nm, which is an expected result of the short mechanical activation derived by high-energy ball milling and subsequent heat and purification treatments. In their study, Barraud et al. (2005) obtained faceted HfB_2 grains with a size range of 100-300 nm by annealing the mechanically activated HfCl_4 -B-Mg mixtures at 1100 $^\circ\text{C}$. In another study in which ZrO_2 , B_2O_3 and graphite powder mixtures were used to prepare ZrB_2 - ZrO_2 ceramic powders by mechanical activation and annealing at 1400 $^\circ\text{C}$, particle size range was reported between 500-800 nm as a consequence of the neck formation occurred at this temperature (Balci et al., 2012). On the other hand, when the annealing temperature was decreased to 1300 $^\circ\text{C}$ and B was used as a boron source, no neck formation was observed and ZrB_2 - ZrO_2 powders have particle size in the range of 100-300 nm (Balci et al., 2012). Furthermore, Ran et al. (2010) reported the particle size of ZrB_2 powders which were synthesized at temperatures between 1000-1650 $^\circ\text{C}$ by borothermal reduction of ZrO_2 , as 150 and 660 nm at 1000 $^\circ\text{C}$ and 1650 $^\circ\text{C}$, respectively. It was stated that the change in particle size was mostly pronounced at temperature range of 1200-1400 $^\circ\text{C}$ because ZrB_2 particles were subjected to grain growth to form larger particles above 1200 $^\circ\text{C}$. In the present study, the relatively low annealing temperature enabled to obtain sub-micron scaled HfB_2 powders without causing any significant particle coarsening effect, probably by the contribution of the mechanical activation step.

Figure 4.9 (a)-(b) illustrate secondary electron SEM images and the corresponding results of EDX elemental mapping analysis of Hf and B, taken from the powders synthesized by mechanically activated annealing with 20 wt.% excess amount of boron after purification treatments. The figures represent the homogenous distribution of Hf and B elements. The elemental Hf map overlaps almost entirely with elemental B maps (Figure 4.9 (b) and (c)), thus elemental maps of Hf and B indicates the HfB_2 phase. The comparatively weak signals of B may be due to the curtaining of B signals by the strong and dominant signals of Hf.

The elemental analysis results of the mechanically activated powders which were performed by SEM/EDS using the spot mode on the selected points to reveal the phase distributions after annealing (Figure 4.10 (a)) and purification (Figure 4.10 (b))

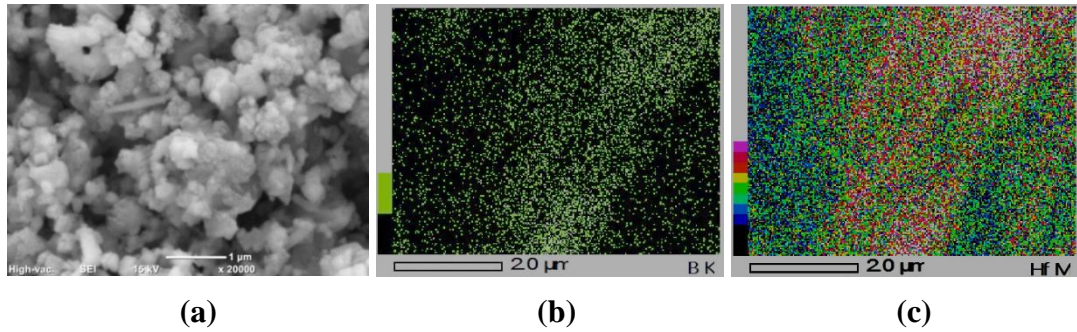


Figure 4.9 : (a) SEM image of synthesized powders with 20 wt.% ex B at 20000X, EDS mapping of (b) B and (c) Hf.

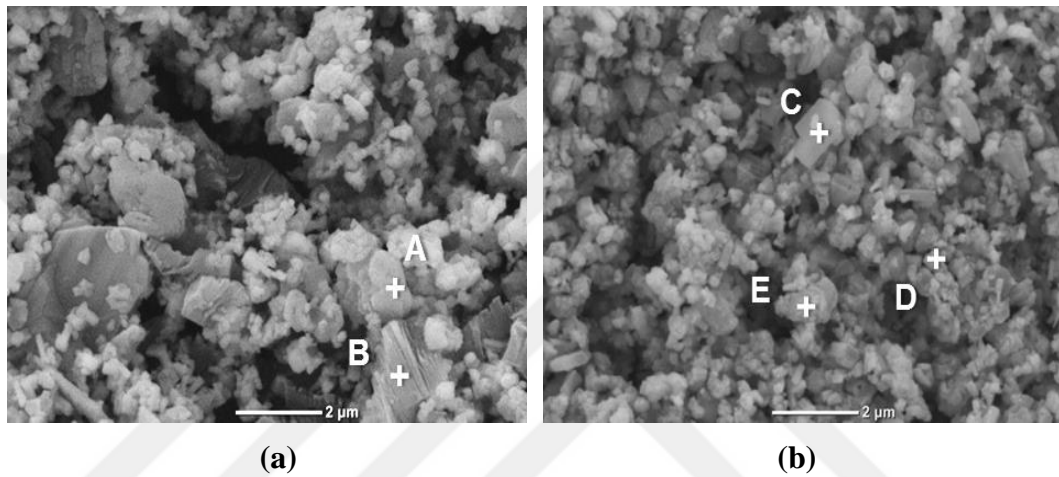


Figure 4.10 : SEM image of the mechanically activated powders containing 20 wt.% excess boron after: (a) annealing and (b) washing with distilled water.

Table 4.1 : SEM/EDS analysis results of different regions marked in Figure 4.10 (a) and (b).

Elements	A	B	C	D	E
B	13.19	22.58	23.18	33.45	28.01
O	20.07	54.57	3.28	4.38	3.75
Hf	66.73	23.15	73.55	62.17	68.24

are listed in Table 4.1. The compositions of two different and distinguishable points A and B shown in Figure 4.10 (a) confirmed that the particles labeled by A comprise of HfB_2 phase together with the B_2O_3 phase, whereas the particles represented by B predominantly consists of the B_2O_3 phase. According to EDS analysis results after purification (particles labelled as C, D and E in Figure 4.10 (b)), powders have a very low oxygen content which can be attributed mainly to the surface oxidation due to the handling in laboratory conditions during the EDS analyses. Moreover, relatively

high boron content of the purified powders indicated the residual elemental B phase in the synthesized HfB_2 powders. Moreover, it was shown that boron powders have α and/or β -rhombohedral crystal structure at 1100 °C (Ağaoğulları et al., 2011). The boron phase could not be detected in the XRD pattern of the synthesized powders after the purification treatments in Figure 4.6 because of its low concentration (under the detection limit which is ~ 2 wt.% of the sample).

During the borothermal reduction of HfO_2 and ZrO_2 , boron oxides and residual boron are most expected impurities after reaction. For the elimination of boron related impurities, high temperature treatments above 1500 °C under the vacuum were suggested (Guo et al., 2012b; Ni et al., 2010; Peshev and Bliznakov, 1968). With the increasing temperature, B_2O_3 are consumed by evaporation and also by reaction with boron to give boron suboxides such as B_2O_2 and BO (Guo et al., 2012b; Ni et al., 2010; Peshev and Bliznakov, 1968). The particle coarsening was also observed due to the high temperature (Guo et al., 2012b; Ran et al., 2010). On the other hand, Guo et al. (2012b) studied on the synthesis of HfB_2 powders and its densification, boron impurities were determined by SEM/EDS analyses in the compacted ceramics obtained from the powders with increasing initial boron content. In their study, ceramics with boron impurities showed higher relative density of 98.6 % whereas ceramics without residual boron reached a relative density of 83.6 %. The positive effect of boron on the relative density explained by the reaction of residual boron with surface oxide impurities (HfO_2 and B_2O_3) allowing to the removal of them (Guo et al., 2012b). Nevertheless, the effect of residual boron content on the densification and properties of HfB_2 ceramics should be further investigated.

In previous studies on the borothermal reduction of Hf and Zr chlorides, HfB_2 nanorods and ZrB_2 nanoplatelets were prepared from mechanically activated $\text{HfCl}_4/\text{ZrCl}_4\text{-B}$ powder blends with 50 wt.% excess boron (Barraud et al., 2005; Guo et al., 2012a). The effect of annealing temperature on the formation of phases was investigated: the presence of HfB_2 , HfO_2 (2 and 8 wt.% for annealing durations of 45 and 60 min, respectively) and FeB were detected at 1100 °C. The effect of B_2O_3 and Fe and/or FeB_x on the formation mechanism of rods was discussed (Barraud et al., 2005). Additionally, it was shown that trace amount of ZrO_2 and Fe_2B existed in the ZrB_2 by the annealing at 1100°C and the $\text{ZrCl}_4\text{-B}$ mixture completely converted to ZrB_2 at 1200 °C (Guo et al., 2012a). ZrB_2 had mainly platelet morphology and

whiskers were also present. The borothermal reduction of HfO_2 was often carried out over $1500\text{ }^\circ\text{C}$ and vacuum was applied for continuous removal of B_2O_3 (Guo et al., 2012b; Ni et al., 2010). The HfB_2 prepared at $1550\text{ }^\circ\text{C}$ had rounded particles with average size of $0.8\text{ }\mu\text{m}$. In this study, borothermal reduction of HfCl_4 -B powder blends with addition of excess amounts of boron was conducted at $1100\text{ }^\circ\text{C}$ which was also inferred from the thermodynamical interpretations to reduce the HfCl_4 loss by evaporation. The particle size of synthesized powders determined as 391 nm after leaching purifications and they showed both faceted rod-like and irregular shapes.

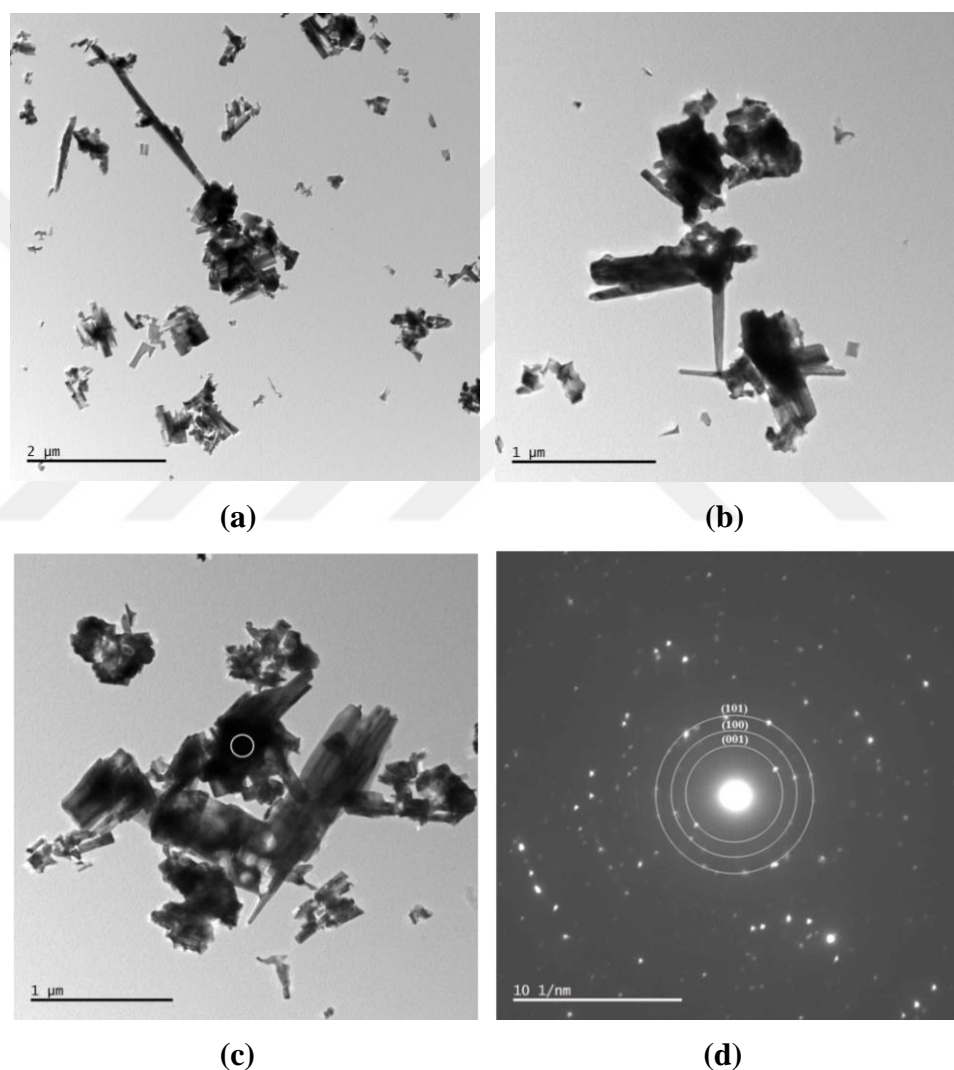


Figure 4.11 : TEM images of the powders milled for 1 h and annealed at $1100\text{ }^\circ\text{C}$: (a), (b) bright-field (BF) images and (d) its corresponding selected area diffraction pattern (SADP) taken from the region marked in (c).

Figure 4.11 (a) through (d) represent the bright field (BF) TEM images and the corresponding selected area diffraction pattern (SADP) taken from the mechanically activated, annealed and subsequently purified powders. The BF images of

synthesized powders illustrate different morphologies in Figure 4.11 (a) to (c) in which rods, elongated and irregular shaped particles exist. The observed particle size of irregular powders varies between 100 and 500 nm, which were also determined in the SEM and PSA results. Additionally, rod-like particles having length of $\sim 0.5\text{-}2\ \mu\text{m}$ were observed in the BF images. The SADP taken from the marked area in Figure 4.11 (c) proves the presence of the polycrystalline hexagonal HfB_2 phase (Figure 4.11 (d)).

In overall, HfB_2 powders were synthesized starting from HfCl_4 and B powder blends via a borothermal reduction route by using mechanical activation, annealing and purification steps. HfB_2 powders with an amount of residual B ($\leq 2\ \text{wt.}\%$) but completely free from undesired phases such as HfO_2 , B_2O_3 and Fe impurity could be evaluated as an economical and nano-scaled precursor for the sintering process of HfB_2 -based ceramics.

4.2 The Mechanochemical Synthesis of HfB_2 -Based Powders from $\text{HfCl}_4\text{-B}_2\text{O}_3\text{-Mg}$ and $\text{HfCl}_4\text{-B-Mg}$ Blends

The HfB_2 -based powders were synthesized by a mechanochemical synthesis route from $\text{HfCl}_4\text{-B}_2\text{O}_3\text{-Mg}$ powder blends. The starting powder blends containing stoichiometric amounts of reactants and those having excess B_2O_3 and Mg were milled in a high-energy ball mill (Spex 8000D Mixer/Mill) at different durations. Additionally, amorphous B was utilized as an alternative boron source in the experiments to observe effect of boron source type. The HfB_2 -based powders were obtained according to the reaction (3.3) and (3.4). Additionally, amorphous B was used in the mechanochemical synthesis route. Thus, the effects of milling duration, excess amounts of reactants (B_2O_3 , B and Mg) and type of boron source on the resultant products were investigated. The synthesized powders were purified by washing with distilled water and acid leaching treatments in order to remove the undesired by-products such as MgCl_2 and MgO . As a result, $\text{HfB}_2\text{-HfO}_2$ and HfB_2 ceramic powders were obtained from the $\text{HfCl}_4\text{-B}_2\text{O}_3\text{-Mg}$ and the $\text{HfCl}_4\text{-B-Mg}$ powder blends, respectively.

4.2.1 The mechanochemical synthesis of HfB₂-based powders from HfCl₄-B₂O₃-Mg blends

The XRD patterns of as-blended HfCl₄-B₂O₃-Mg powder blends and those milled at different durations up to 5 h are shown in Figure 4.12. In the XRD pattern of as-blended HfCl₄-B₂O₃-Mg powders and those milled for 10 min, HfOCl₂.4H₂O (ICDD Card No: 015-0380), HfOCl₂.6H₂O (ICDD Card No: 047-0816) and Mg (ICDD Card No: 35-0821, Bravais Lattice: primitive hexagonal, a=b=0.321, c=0.521) phases were detected. The HfOCl₂.xH₂O compounds formed ((according to the reaction (3.1)) during XRD analyses performed under atmospheric conditions due to the very hygroscopic character of HfCl₄. In addition, the B₂O₃ phase could not be determined in the XRD patterns of the as-blended HfCl₄-B₂O₃-Mg powder blends and those of milled for 10 min because of its amorphous nature.

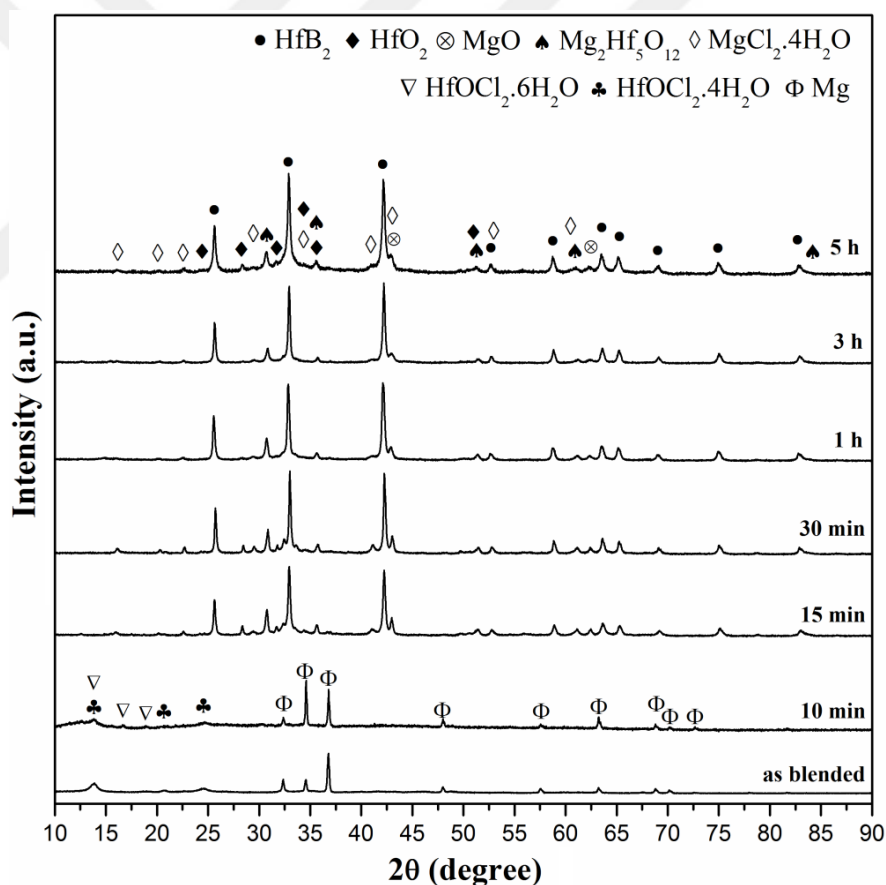


Figure 4.12 : XRD patterns of the as-blended HfCl₄-B₂O₃-Mg powder blends and those milled at different durations up to 5 h.

On the other hand, after milling for 15 min, HfB₂ (ICDD Card No: 038–1398, Bravais lattice: primitive hexagonal, a=b=0.314, c=0.347 nm), HfO₂ (ICDD Card No: 034–0104, Bravais lattice: primitive monoclinic, a=0.528, b=0.518, c=0.511 nm,

$\beta=99.259^\circ$), MgO (ICDD Card No: 089-7746, Bravais lattice: face-centered cubic, $a=b=c=0.420$), $\text{MgCl}_2 \cdot 4\text{H}_2\text{O}$ (ICDD Card No:053-0258, Bravais lattice: primitive monoclinic, $a=0.590$, $b=0.727$, $c=0.842$ nm, $\beta=111.007^\circ$) and $\text{Mg}_2\text{Hf}_5\text{O}_{12}$ (ICDD Card No: 033-0862, Bravais lattice: primitive rhombohedral, $a=b=0.939$, $c=0.870$) phases were detected in the XRD patterns. It can be observed from the Figure 4.12 that the mechanochemical reaction between the reactants starts after a relatively short milling duration of 15 min. Although the HfB_2 formation was observed after milling for 15 min, milling was maintained up to 5 h in with the aim of observing any probable changes in the phases and their intensities. Nevertheless, the phases detected in the XRD patterns and their intensities did not illustrate any obvious difference especially after the milling duration of 1 h. The milling durations over 5 h did not applied because of possible amorphization at prolonged milling durations.

Excess amount of B_2O_3 and Mg were also utilized to examine the effects of reactant amounts on the mechanochemical reaction of $\text{HfCl}_4\text{-B}_2\text{O}_3\text{-Mg}$. The XRD patterns of the $\text{HfCl}_4\text{-B}_2\text{O}_3\text{-Mg}$ powder blends having 30 wt.% excess B_2O_3 and 30 wt.% excess $\text{B}_2\text{O}_3\text{-20 wt.% excess Mg}$ after milling for 3 h are given in Figure 13 (a) and (b), respectively. After 3 h of milling, the determined phases in the Figure 13 (a)-(b) and in those of Figure 4.12 were similar. Moreover, a significant change was

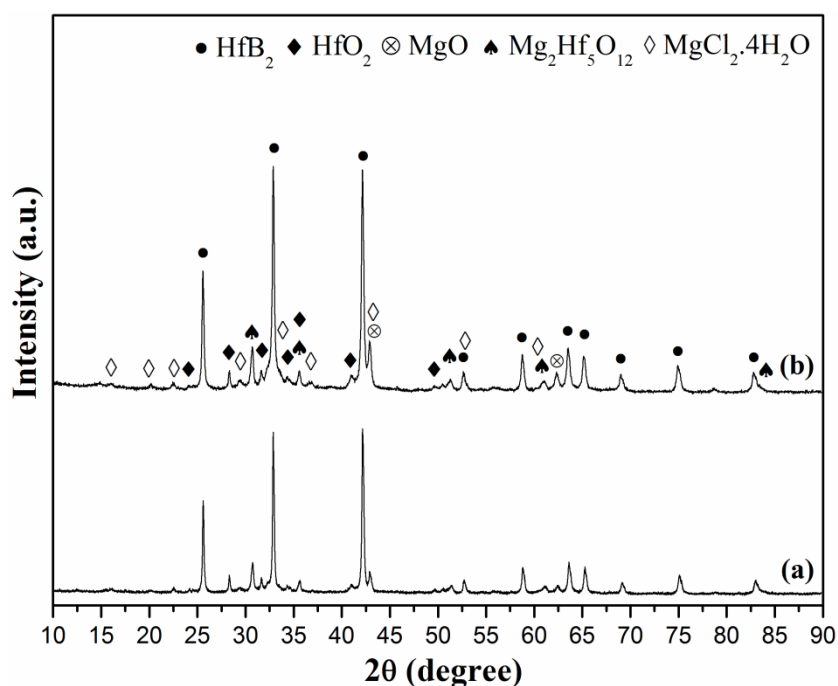


Figure 4.13 : XRD patterns of the $\text{HfCl}_4\text{-B}_2\text{O}_3\text{-Mg}$ powder blends having: (a) 30 wt.% excess B_2O_3 and (b) 30 wt.% B_2O_3 and 20 wt.% excess Mg after 3 h of milling.

not observed in the distribution and intensities of phases. Thus, the following experiments were maintained by utilizing the stoichiometric $\text{HfCl}_4\text{-B}_2\text{O}_3\text{-Mg}$ powder blends. These experimental findings also correspond to the Factsage predictions (in Figure 3.10) which show the usage of Mg over stoichiometric amounts do not increase the amounts of reaction products (HfB_2 , MgCl_2 and MgO).

After the mechanochemical reaction, by-products such as MgCl_2 and MgO were eliminated by purification treatments. The magnesium salts (MgCl_2 and $\text{MgCl}_2\cdot 4\text{H}_2\text{O}$) were leached out by repeated rinsing of the powders with distilled water. In addition, the MgO phase was removed by 4 M HCl leaching, as explained in details in the section 3. XRD patterns of the powders after mechanochemical synthesis and subsequent leaching treatments are illustrated in Figure 4.14. The MgCl_2 , $\text{MgCl}_2\cdot 4\text{H}_2\text{O}$ and MgO phases are not observed in the XRD patterns of synthesized powders after leaching treatments, which prove elimination of these phases. Zhang et al. (2008) prepared LaB_6 powders from $\text{LaCl}_3\cdot 7\text{H}_2\text{O}$, B_2O_3 and Mg blends in an autoclave and after the reaction, MgCl_2 and NaCl impurities were removed by washing the powders with distilled water. After the self-propagating high-temperature synthesis (SHS) reaction of TiO_2 , B_2O_3 and Mg blends, MgO phase was removed via selective acid leaching by leaving behind TiB_2 powders (Lok et al., 2009). Ağaoğulları et al. (2012a) removed the MgO by-product from LaB_6 powders with HCl leaching after the mechanochemical reaction of La_2O_3 , B_2O_3 and Mg powder blends in a high-energy ball mill. In this research, it was stated that the leaching parameters such as HCl concentration, solid/leachant ratio and duration were chosen respectively as 3.6 M, 1 g/10 cm³ and 10 min after a series of pre-experiments.

In the XRD patterns of 15 min and 30 min of milled and purified powders, intensities of the $\text{Mg}_2\text{Hf}_5\text{O}_{12}$ phase are higher than those of 1 h, 3 h and 5 h of milled and purified powders. On the other hand, the peak intensities of HfB_2 , HfO_2 and $\text{Mg}_2\text{Hf}_5\text{O}_{12}$ phases do not show a significant difference after 1 h of milling. The XRD patterns remained mainly unchanged when the milling duration was extended to 5 h. This result pointed out that the duration of mechanochemical synthesis did not affect the phase types of the powders (between 15 min and 5 h) and after a certain time of milling (after 1 h) a steady state condition was reached.

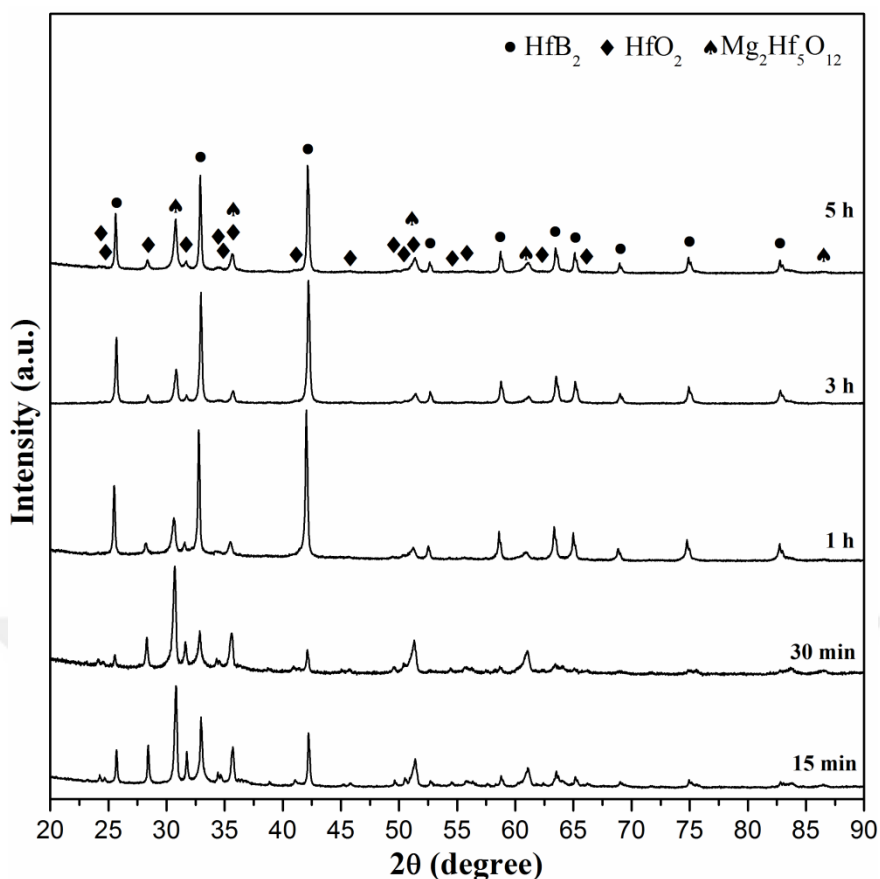


Figure 4.14 : XRD patterns of the $\text{HfCl}_4\text{-B}_2\text{O}_3\text{-Mg}$ powder blends after milling at different durations and subsequent washing and HCl leaching treatments.

The $\text{HfO}_2\text{-MgO}$ phase diagram is given in Appendix A (Wu and Jin, 1997). According to the phase diagram, the $\text{Mg}_2\text{Hf}_5\text{O}_{12}$ phase forms at 28.57 mol.% of MgO. Wu and Jin (1997) showed the stability range of $\text{Mg}_2\text{Hf}_5\text{O}_{12}$ phase between the 1370 and 2173 °C and under this temperature range it decomposes into monoclinic HfO_2 and MgO phases. On the other hand, it was stated that further information is needed on the stability range of the ordered $\text{Mg}_2\text{Hf}_5\text{O}_{12}$ phase (Wu and Jin, 1997). Additionally, the HfO_2 has two polymorphs that appear before melting. These polymorphs involve a tetragonal and a cubic phases and the monoclinic to tetragonal and tetragonal to cubic transformation temperatures were reported as 1830 and 2520 °C, respectively (Wu and Jin, 1997).

Figure 4.15 (a)-(c) illustrate the FTIR spectra of commercial $\text{HfOCl}_2 \cdot 8\text{H}_2\text{O}$ powders and the $\text{HfCl}_4\text{-B}_2\text{O}_3\text{-Mg}$ powder blends after milling for 3 h (in Figure 4.15(b)) and subsequent washing (in Figure 4.15(c)), respectively. The FTIR spectra of $\text{HfOCl}_2 \cdot 8\text{H}_2\text{O}$ powders are given with the aim of comparison. The commercial $\text{HfOCl}_2 \cdot 8\text{H}_2\text{O}$ powders show broad absorption peaks centered at around 1049, 1394,

1608 and 3200 cm^{-1} (in Figure 4.15 (a)). It was previously shown in the literature that the broad vibration peaks between 3650 and 2600 cm^{-1} in the FTIR spectrum of a hydrated hafnium oxychloride are associated with the OH stretching of water molecules (physically adsorbed molecular water) while those at 1616 cm^{-1} associated with their bending mode (Barraud et al., 2006). In the FTIR spectra of $\text{HfCl}_4\text{-B}_2\text{O}_3\text{-Mg}$ powder blends after milling for 3 h, small peaks at the wave numbers of 1421, 1484, 1593 and 3460 cm^{-1} were determined, which indicate the presence of compounds containing hydroxyl group such as hafnium oxychlorides ($\text{HfOCl}_2\cdot 4\text{H}_2\text{O}$ and $\text{HfOCl}_2\cdot 6\text{H}_2\text{O}$) and $\text{MgCl}_2\cdot 4\text{H}_2\text{O}$ at very low amount. Moreover, it is considered that these peaks evolve inevitably because of extremely hygroscopic character of HfCl_4 powders. Although all the powder preparation and milling process were conducted under Ar atmosphere, an amount of hafnium oxychloride compounds can form almost in an unavoidable manner. On the other hand, the absence of the peaks belong to the hafnium oxychloride compounds in the XRD patterns of the 3 h of milled powders (in Figure 4.12) indicates the lower amounts of these oxychloride compounds under the detection limit of XRD (which is 2 wt.% of the overall sample). Additionally, after water washing, there is no peak belongs to O-H bond related compounds in Figure 4.15 (c). Thus, the complete removal of these compounds was achieved by the purification treatments.

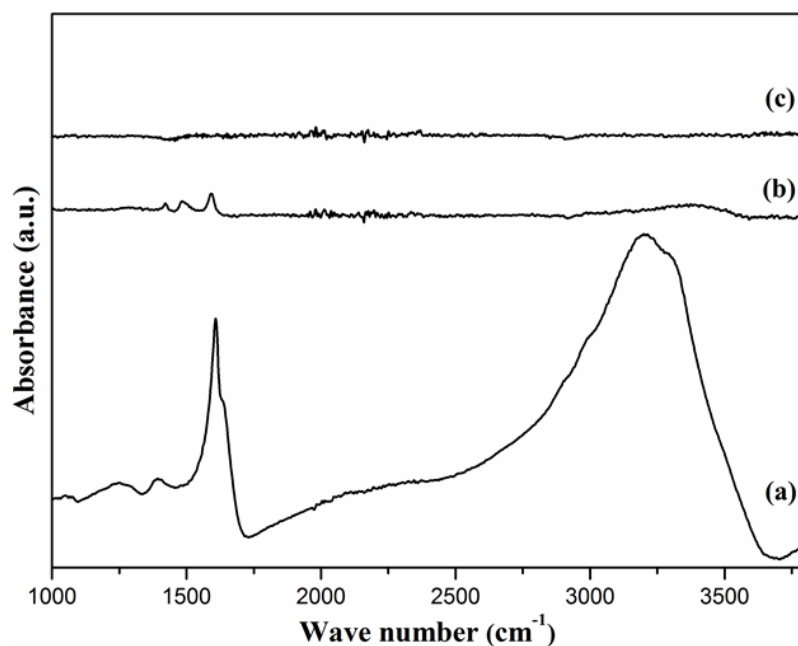


Figure 4.15 : FTIR spectra of (a) commercial $\text{HfOCl}_2\cdot 8\text{H}_2\text{O}$ powders and $\text{HfCl}_4\text{-B}_2\text{O}_3\text{-Mg}$ blends after (b) milling for 3 h, (c) subsequent washing with distilled water.

An annealing treatment was applied to the synthesized powders after purification with the aim of investigating any possible decomposition or transformation of the formed phases. The powders obtained via 3 h of milling of $\text{HfCl}_4\text{-B}_2\text{O}_3\text{-Mg}$ blends and subsequent leaching treatments (by distilled water and 4 M HCl) were annealed at 1000 °C for 3 h. XRD patterns of the annealed powders are represented in Figure 4.16 (a). After the annealing treatment, only phases detected in the XRD patterns are HfB_2 and HfO_2 , whereas the $\text{Mg}_2\text{Hf}_5\text{O}_{12}$ phase was not observed any longer. It was considered that the $\text{Mg}_2\text{Hf}_5\text{O}_{12}$ phase (contains 7.11 wt.% of MgO) decomposed to the HfO_2 and MgO phases upon heating during the annealing treatment at 1000 °C for 3 h. This finding points out that the $\text{Mg}_2\text{Hf}_5\text{O}_{12}$ phase is not stable at/over 1000 °C although its stability range is stated between 1370 and 2173 °C in the $\text{HfO}_2\text{-MgO}$ binary phase diagram (Wu and Jin, 1997). Nevertheless, in the XRD patterns after annealing, the MgO phase is not observed (in Figure 4.16 (a)), which can be explained by its low amount under the detection limit of XRD (which is 2 wt.% of sample). Samad et al. (2004) reported that the $\text{Mg}_2\text{Zr}_5\text{O}_{12}$ phase formed via thermally sprayed coatings of $\text{ZrO}_2\text{-24 wt.% MgO}$ decomposed during hot isostatic pressing at 1100 °C to MgO and ZrO_2 phases. Moreover, increase in the peak intensities of the HfO_2 phase after the annealing can be explained by formation of additional amount of HfO_2 through the decomposition of $\text{Mg}_2\text{Hf}_5\text{O}_{12}$.

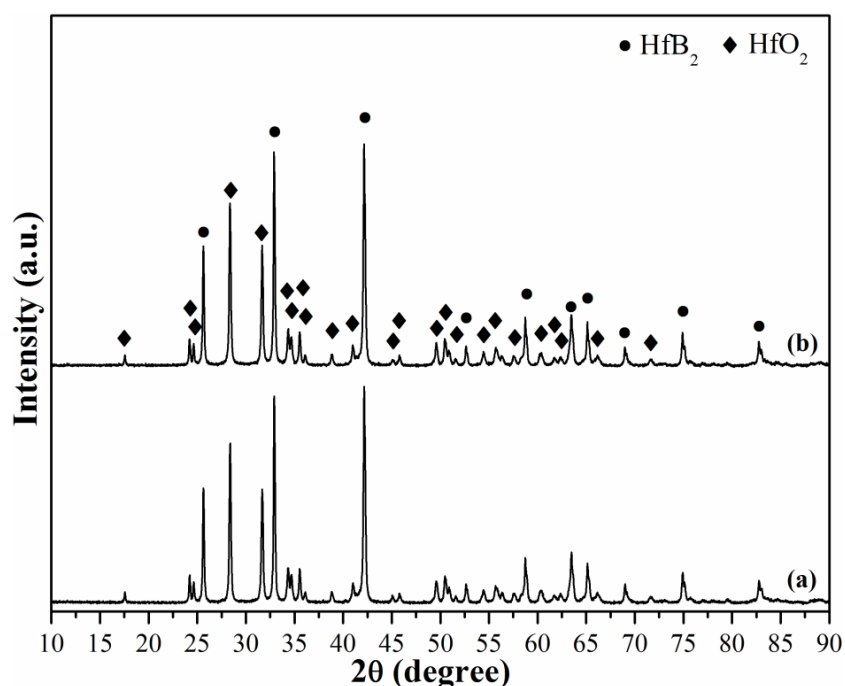


Figure 4.16 : XRD patterns of the 3 h of milled and leached $\text{HfCl}_4\text{-B}_2\text{O}_3\text{-Mg}$ blends after: (a) annealing at 1000 °C for 3 h and (b) subsequent HCl leaching.

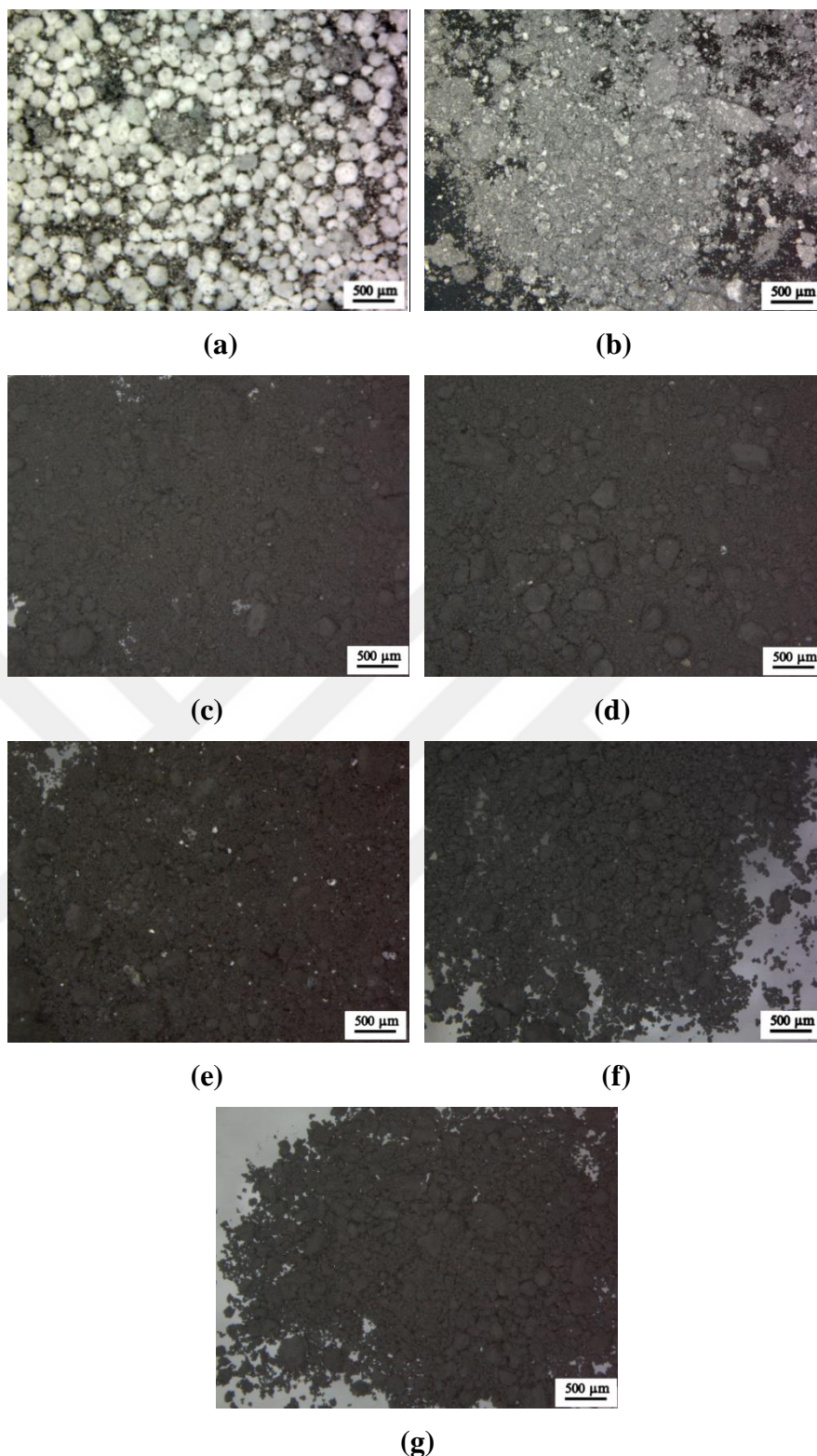


Figure 4.17 : SM images of the $\text{HfCl}_4\text{-B}_2\text{O}_3\text{-Mg}$ powders: (a) as-blended, (b) milled for 10 min, (c) milled for 15 min, (d) milled for 3 h, (e) milled for 5 h, (f) milled for 3 h and purified (g) milled for 3 h milled, purified and annealed at 1000 °C.

A final leaching treatment with 4 M HCl was applied to powders after the annealing so as to elimination of any probable MgO impurity and the XRD patterns of the powders after this final leaching are given in the Figure 4.16 (b). Any significant

difference between the XRD patterns of annealed and subsequently leached powders was not observed as can be seen from the Figure 4.16 (a) and (b).

SM images of the as-blended $\text{HfCl}_4\text{-B}_2\text{O}_3\text{-Mg}$ powders and those milled, leached and annealed ones are illustrated in Figure 4.17 (a)-(g). The SM images of powders throughout the mechanochemical synthesis process can give a general idea about the progress of the intended reactions. As can be seen from the Figure 4.17 (a), the as-blended $\text{HfCl}_4\text{-B}_2\text{O}_3\text{-Mg}$ powders include particles of reactant powders which have relatively different size and illustrate a non-uniform appearance. Additionally, color of the powder blends indicates only a physical mixing instead of a newly formed phase after milling for 10 min in Figure 4.17 (b). On the other hand, by the increase of milling duration to 15 min, the color of $\text{HfCl}_4\text{-B}_2\text{O}_3\text{-Mg}$ powders turned to dark gray which pointed out the formation of new chemical species different from the reactants. And these observations are in good accordance with the XRD findings in Figure 4.12, in which the formation of HfB_2 phase was determined to occur after the 15 min of milling. Figure 4.17 (d) and (e) show SM images of the $\text{HfCl}_4\text{-B}_2\text{O}_3\text{-Mg}$ powder blends after 3 and 5 h of milling, respectively. The lighter or shiny phases between the dark gray powders in Figures 4.17 (c), (d) and (e) might be MgO particles form as by-products of reaction (3.3). After the subsequent purifications with distilled water and 4 M HCl , the synthesized powders gain a homogenous appearance in Figure 4.12 (f). Figure 4.14 (g) illustrates the powders obtained after annealing at $1000\text{ }^\circ\text{C}$ for 3 h and final acid leaching. Any particular change in the appearance of powders after annealing at $1000\text{ }^\circ\text{C}$ and leaching treatment is not observed, which may also be interpreted as an evidence for stability of desired phases such as HfB_2 .

The secondary electron SEM images of the $\text{HfCl}_4\text{-B}_2\text{O}_3\text{-Mg}$ powder blends which were subjected to milling for 3 h and purification are shown in Figure 4.18 (a) and (b) at different magnifications. As seen from the figures, the synthesized powders consist of rounded-shaped particles. In addition, their particle size range can be estimated especially from Figure 4.18 (b) as between 50 and 200 nm.

With the aim of revealing the distribution of different phases in the synthesized powders, SEM/EDX analyses were conducted on the powders. Figure 4.19 (a)-(e)

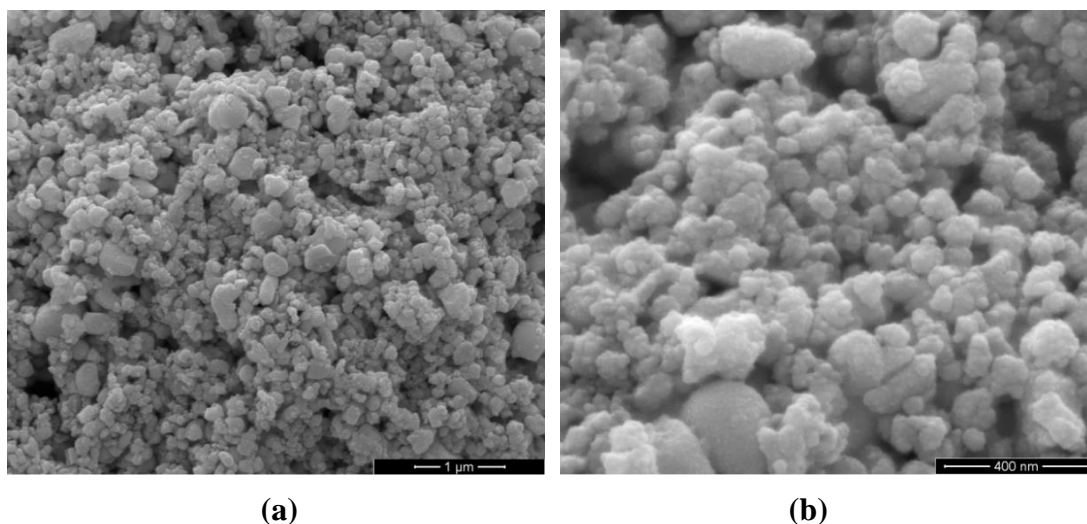


Figure 4.18 : SEM images of the $\text{HfCl}_4\text{-B}_2\text{O}_3\text{-Mg}$ powder blends subjected to milling for 3 h and subsequent purification.

represent the secondary electron (SE) SEM image and related elemental maps of Hf, O, B and Mg for the powders milled for 3 h and subsequently purified with distilled water and 4 M HCl. Figure 4.19 (b) reveals a homogenous distribution of Hf throughout the microstructure. The weak signals belong to B element presented in Figure 4.19 (d) can be explained with the suppression of B signals by the strong signals of Hf, O and Mg. The elemental Hf map coincides almost entirely with elemental B and O maps (Figure 4.19 (c) and (d)) indicating related phases. Besides, it can be said that the elemental O map seems to fill the gaps where B elemental map does not coincidence with the Hf elemental map. Therefore, the elemental maps confirm the formation of HfB_2 and HfO_2 phases and also their uniform distribution throughout the microstructure. Moreover, the elemental Mg map which almost entirely coincidences with the elemental Hf and O maps so it indicates the presence of $\text{Mg}_2\text{Hf}_5\text{O}_{12}$ phase. The removal of MgO phase forms in magnesiothermic reduction reactions during the mechanochemical synthesis of boride compounds is a relatively well known process and it was shown in the previous studies (Ağaoğulları et al., 2012a, Lok et al. 2009, Zhang et al., 2008). Thus, the existence of Mg even after HCl leaching are resulted from the existence of $\text{Mg}_2\text{Hf}_5\text{O}_{12}$ phase, which was also detected in the XRD analysis of purified powders in Figure 4.13.

As a further investigation for the existence of $\text{Mg}_2\text{Hf}_5\text{O}_{12}$ phase, SEM/EDS analysis were conducted on the milled (for 3 h) and purified powders. The secondary electron SEM image and corresponding EDS analysis graph of the powders are shown in

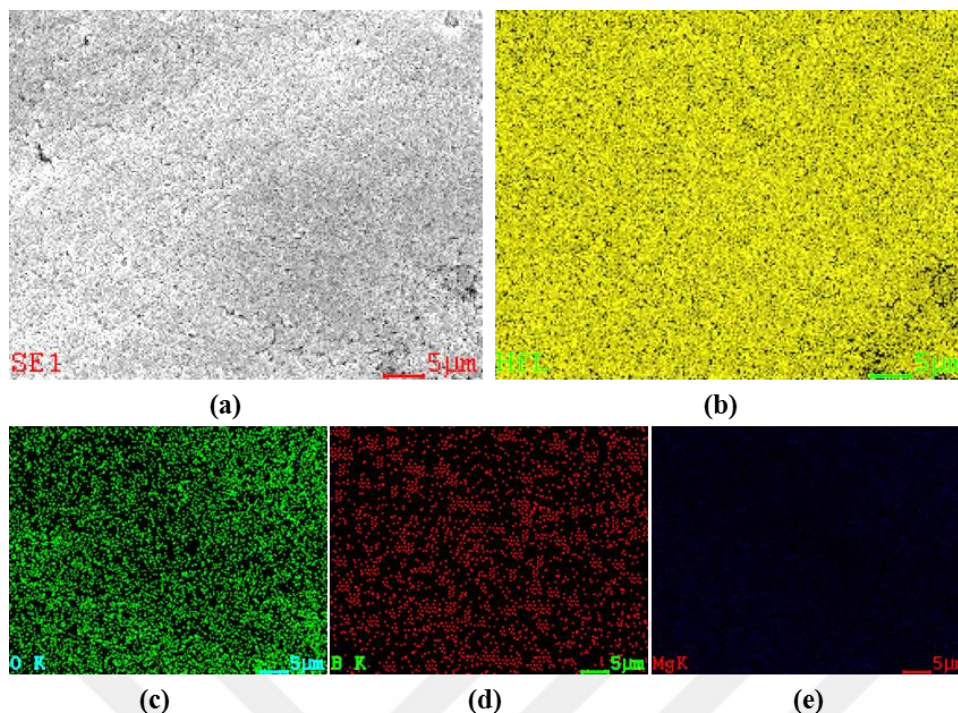


Figure 4.19 : SEM/EDX analyses of milled (for 3 h) and purified powders: (a) SEM image and corresponding elemental maps of (b) Hf, (c) O, (d) B and (e) Mg.

Figure 4.20. According to the general EDS analysis results, the powders include 9.02, 4.83, 0.74 and 85.41 wt.% of B, O, Mg and Hf, respectively. Thus, the Mg content of the purified powders can be taken as an indication for the $Mg_2Hf_5O_{12}$ phase which was also confirmed by the XRD and SEM/EDX analysis.

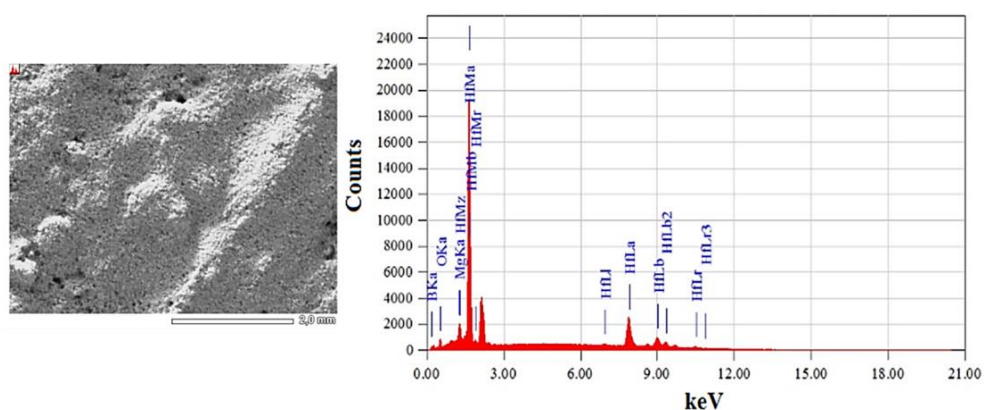


Figure 4.20 : SEM image and corresponding general EDS analysis of the milled (for 3 h) and purified powders.

Additionally, secondary electron SEM image and corresponding EDS analysis of the powders annealed at 1000 °C for 3 h (previously milled for 3 h and purified) and leached with 4 M HCl are given in Figure 4.21. According to the general EDS analysis results, the powders contain 6.60, 6.08 and 87.32 wt.% of B, O and Hf, respectively. After the decomposition of $Mg_2Hf_5O_{12}$ phase to the HfO_2 and MgO

phases by the annealing and the removal of possible MgO phase by acid leaching, Mg element was not found in the final powders.

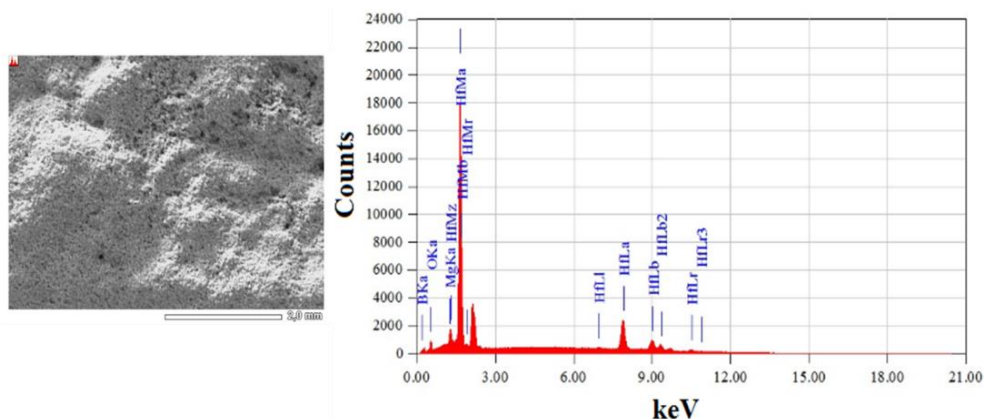


Figure 4.21 : SEM image and corresponding general EDS analysis of the annealed and leached powders (previously milled for 3 h and purified).

Semi-quantitative Rietveld analyses were conducted on the synthesized powders to determine the amounts of HfB_2 phase. The semi-quantitative phase analyses of the milled, purified and annealed powders with the Rietveld refinement method based on their XRD patterns (in Figures 4.14 and 4.16 (b)) are given in Table 4.2. According to the Table 4.2, the HfB_2 amounts in the 1, 3 and 5 h milled and purified powders were determined as 52.8, 53.4 and 52.4 wt.%, respectively. The increasing milling duration did not lead to a remarkable change in the amount of HfB_2 phase. However, a consistency in the amount of the major phase was obtained. It was thought that slight differences in the amounts of the evolved phases might be observed in the mechanochemical synthesis process, which is caused by the incidental conditions of this particular method such as different distribution of the reactant particles in the different regions and interaction between them until steady state conditions are reached (Balcı, 2015). Therefore, it can be said that the system reached a steady state condition in terms of overall mechanochemical reactions after the milling duration of 1 h. In addition, the HfB_2 amount after annealing and leaching treatments was determined as 57.2 wt.%. After the removal of MgO phase evolved by the decomposition of $\text{Mg}_2\text{Hf}_5\text{O}_{12}$ phase during the annealing at 1000 °C, an increase in the HfB_2 amount was observed.

Table 4.2 : Semi-quantitative phase analyses of the $\text{HfCl}_4\text{-B}_2\text{O}_3\text{-Mg}$ powders (after different treatments) obtained from the Rietveld refinement method based on their XRD patterns.

Treatment	HfB_2 amount (wt.%)
Milling for 1 h and purified	52.8
Milling for 3 h and purified	53.4
Milling for 5 h and purified	52.4
Milling for 3 h and annealing at 1000 °C and purified	57.2

Furthermore, the particle size distribution of the powders obtained after different milling durations (1, 3 and 5 h) and subsequent leaching treatments were investigated. The PSA graphs of the $\text{HfCl}_4\text{-B}_2\text{O}_3\text{-Mg}$ powders after milling of 1, 3 and 5 h are given in Figure 4.20 (a)-(c), respectively. The average particle sizes of the powders were determined as 151.4, 140.0 and 129.5 nm, respectively. Although an amount of decrease in the average particle size of the powders by the effect of increasing milling duration was observed, the values were close to each other in general. Hence, it can be asserted that the steady-state conditions were almost reached after 1 h of milling, which was also inferred from the XRD and Rietveld analyses.

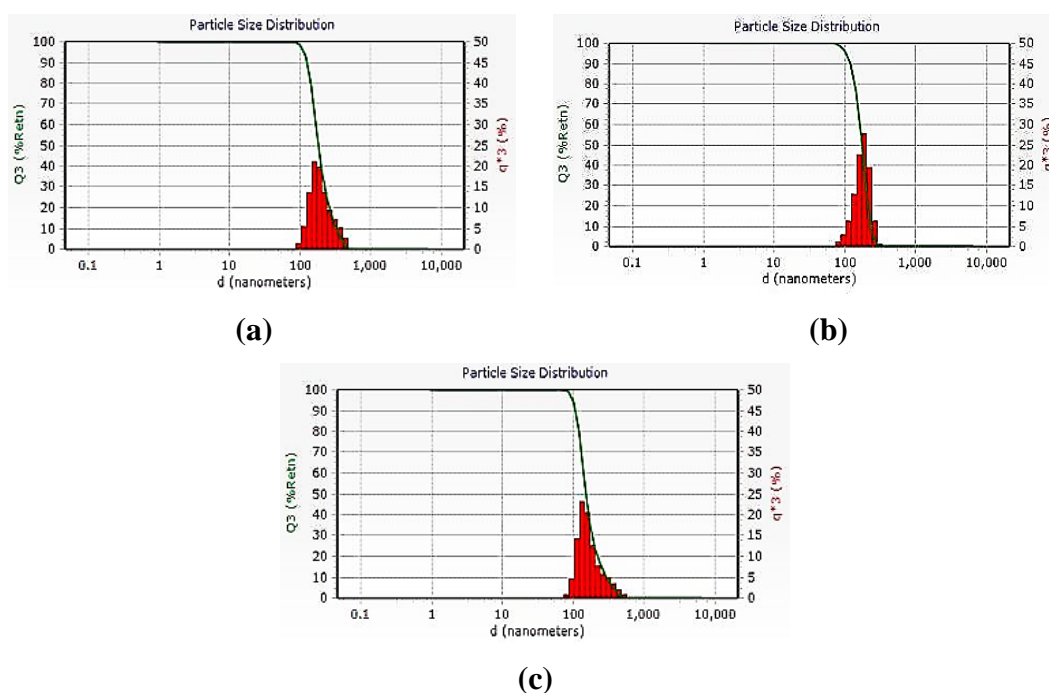


Figure 4.22 : Particle size distributions of the $\text{HfCl}_4\text{-B}_2\text{O}_3\text{-Mg}$ powder blends after milling at different durations and subsequent purification: (a) 1 h, (b) 3 h and (c) 5 h.

XRD analyses were utilized to determine the crystallite size and lattice strain of the $\text{HfCl}_4\text{-B}_2\text{O}_3\text{-Mg}$ powders (using the (001), (100) and (101) reflections) according to milling durations and the related results are illustrated in Table 4.3. As expected, the average crystallite sizes reduced and lattice strain increased with the increasing milling duration. Due to the mechanical deformation imposed into the powders during the milling, particle and crystallite refinement occur and the lattice strain increases (El-Eskandarany, 2001).

Table 4.3 : Average crystallite size and lattice strain of the $\text{HfCl}_4\text{-B}_2\text{O}_3\text{-Mg}$ powders after milling at different durations and purification.

Milling Duration (h)	Crystallite Size (nm)	Lattice Strain (%)
1 h	84.0	0.385
3 h	66.9	0.495
5 h	39.4	0.884

The secondary electron SEM images and PSA graph of the powders after annealing at 1000 °C for 3 h (previously milled for 3 h and purified) and final HCl leaching are shown in Figure 4.21 (a)-(c). The synthesized powders have rounded-shaped morphology similarly with the morphology of powders obtained after milling for 3 h and purification. However, there are also rectangular or angular-shaped particles. The average particle size of the powders was determined as 140.5 nm, which is also in good agreement with the observed particle size in the SEM images. Thus, the annealing treatment conducted at 1000 °C did not cause grain growth and a significant change in the particle size of the synthesized powders.

In order to observe and identify the smaller particles which could not be analyzed by SEM analyses because of the agglomerations, TEM analyses were conducted on the synthesized powders. Figure 4.24 (a), (b), (c) and (e) are the bright-field (BF) images of synthesized powders which are originated from the $\text{HfCl}_4\text{-B}_2\text{O}_3\text{-Mg}$ powder blends after milling for 3 h, annealing at 1000 °C for 3 h and purification. The BF images show rounded and cornered-shaped (like rectangular or cube) particles in sizes varying between 50 and 200 nm, which is also similar to SEM and PSA results. However, there are larger agglomerates consisting of smaller particles in Figure 4.24 (c) and (e). Figure 4.24 (d) is the corresponding SADP of the white-circled region in Figure 4.24 (c) which indicates the presence of the polycrystalline monoclinic HfO_2

phase. In addition, the SADP in Figure 4.24 (f) taken from the marked area in Figure 4.24 (e) proves the presence of the polycrystalline hexagonal HfB_2 phase.

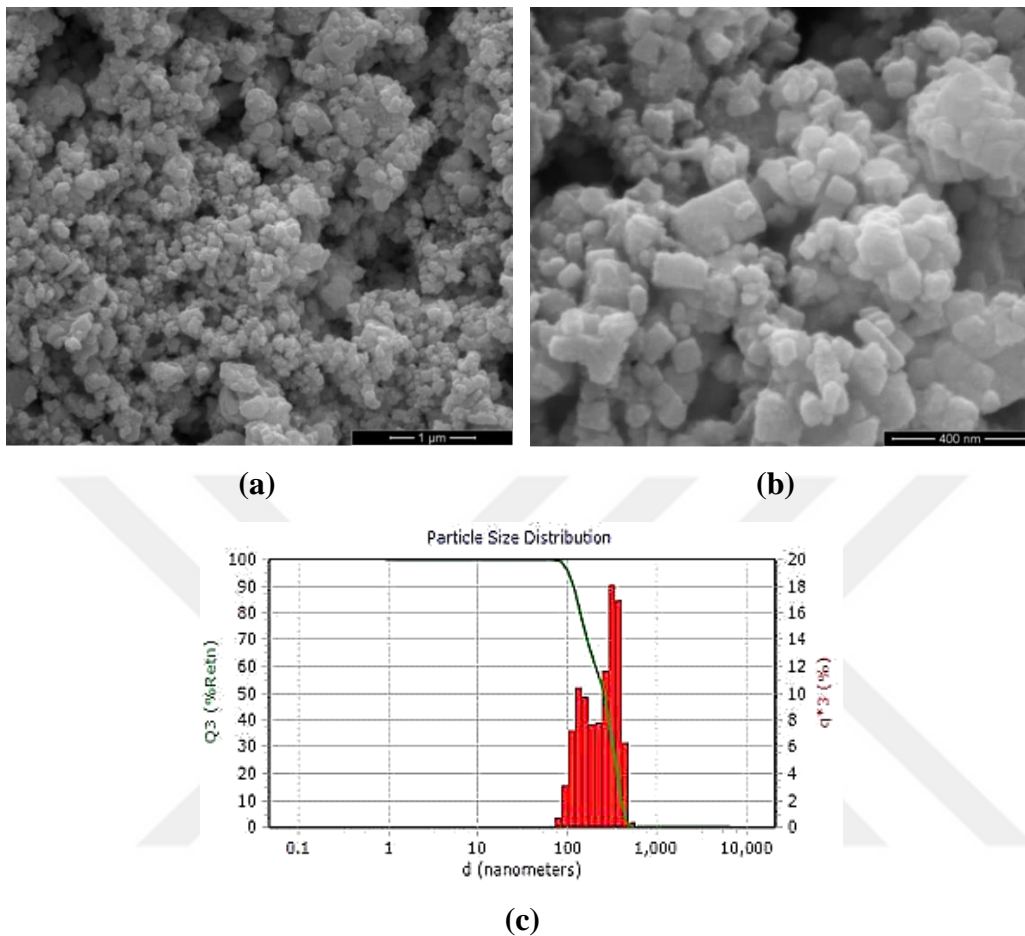


Figure 4.23 : SEM images and particle size distribution of the powders after annealing at 1000 °C for 3 h (previously milled for 3 h and purified) and final HCl leaching.

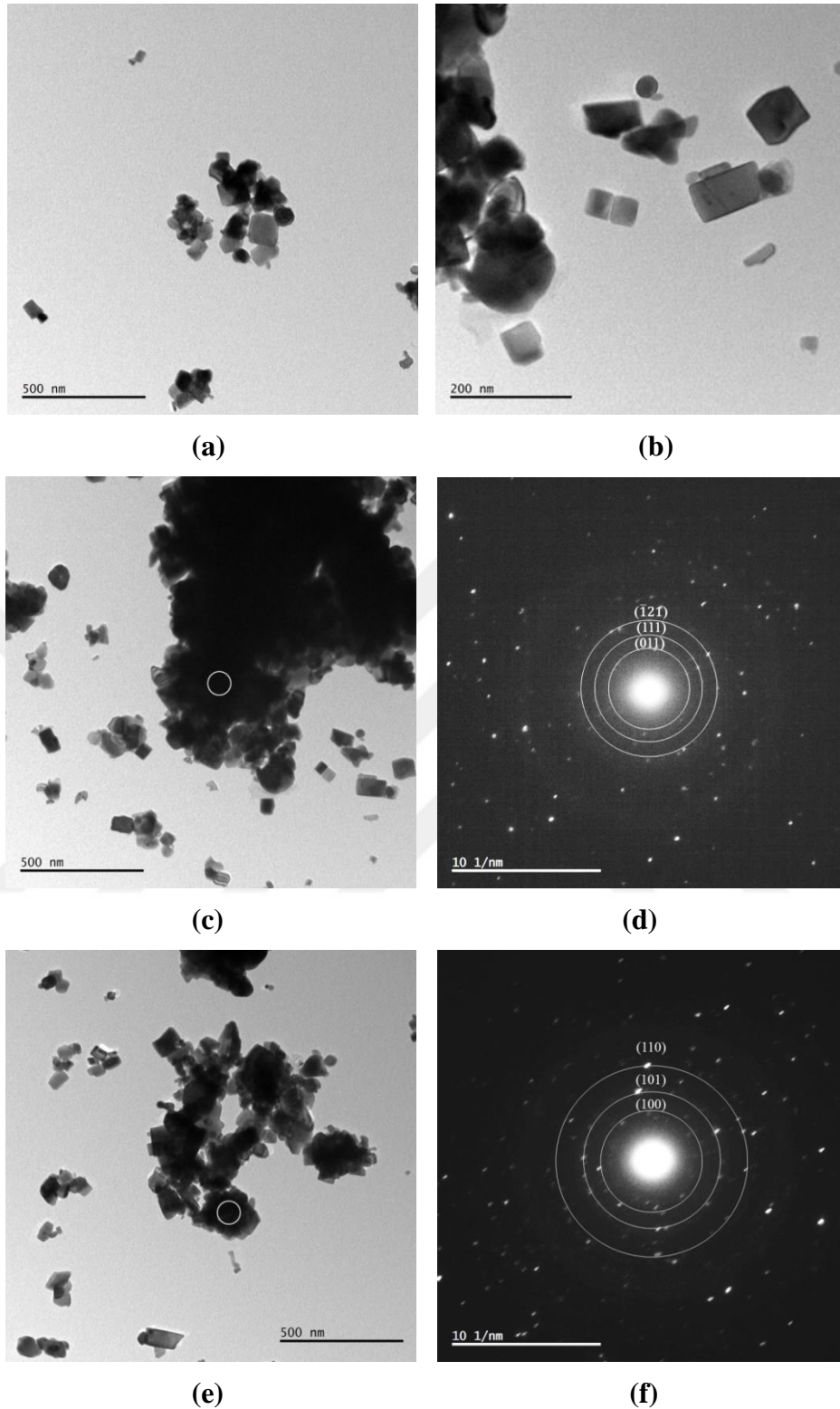


Figure 4.24 : (a) and (b) Bright-field (BF) TEM images of the powders and corresponding selected area diffraction patterns (SADP): (d) SADP taken from the white-circled region in (c), revealing the presence of monoclinic HfO_2 phase, (f) SADP taken from the white-circled region in (e), revealing the presence of hexagonal HfB_2 phase.

4.2.2 The mechanochemical synthesis of HfB_2 powders from HfCl_4 -B-Mg blends

The mechanochemical processing of HfCl_4 -B-Mg powder blends were investigated with the aim of examining the effect of amorphous B as an alternative boron sources. The optimum reaction parameters determined during the mechanochemical processing of the HfCl_4 - B_2O_3 -Mg powders were utilized. Figure 4.25 (a)-(c) show XRD patterns of the stoichiometric as-blended HfCl_4 -B-Mg powders and those milled for 1 and 5 h. In the XRD patterns of the as-blended powders, $\text{HfOCl}_2 \cdot 4\text{H}_2\text{O}$ (ICDD Card No: 015-0380), $\text{HfOCl}_2 \cdot 6\text{H}_2\text{O}$ (ICDD Card No: 047-0816) and Mg (ICDD Card No:035-0821, Bravais lattice: primitive hexagonal, $a=b=0.321$, $c=0.521$ nm) phases were detected. However, B phase could not be detected in the XRD patterns of the as-blended powders (in Figure 4.25) due to its amorphous nature. After the milling duration of 1 h, intensive HfB_2 (ICDD Card No: 038–1398, Bravais lattice: primitive hexagonal, $a=b=0.314$, $c=0.347$ nm) peaks were observed in XRD patterns. Additionally, HfO_2 (ICDD Card No: 034–0104, Bravais lattice: primitive monoclinic, $a=0.528$, $b=0.518$, $c=0.511$ nm, $\beta=99.259^\circ$), MgCl_2 (ICDD Card No:089-1567, Bravais lattice: primitive rhombohedral, $a=b=0.364$, $c=1.766$ nm) and $\text{MgCl}_2 \cdot 4\text{H}_2\text{O}$ (ICDD Card No:053-0258, Bravais lattice: primitive monoclinic,

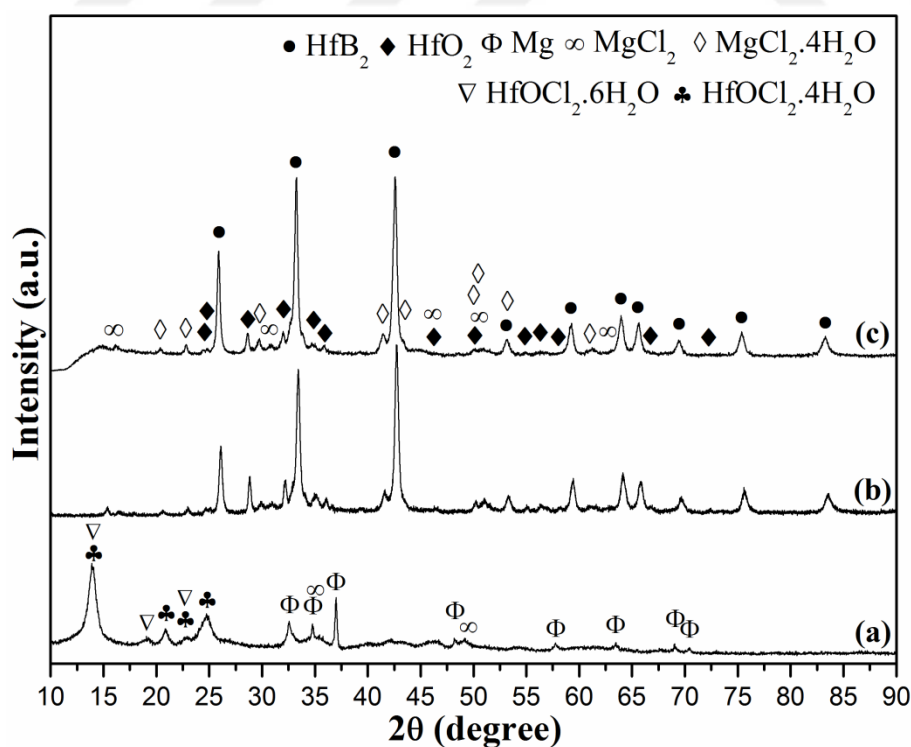


Figure 4.25 : XRD patterns of (a) as-blended stoichiometric HfCl_4 -B-Mg powders and those milled for (b) 1 h and (c) 5 h.

$a=0.590$, $b=0.727$, $c=0.842$ nm, $\beta=111.007^\circ$) peaks were determined in the XRD patterns of the milled powders. The MgCl_2 and $\text{MgCl}_2 \cdot 4\text{H}_2\text{O}$ formed as by-products of the mechanochemical reaction given in the reaction (3.4). However, the formation of HfO_2 phase was a result of unavoidable oxidation of HfCl_4 powders because of their very hygroscopic nature which was also experienced during all the experiments. Moreover, there were no significant differences between the XRD patterns of $\text{HfCl}_4\text{-B-Mg}$ powders milled for 1 and 5 h, in a similar manner with the mechanochemical processing of $\text{HfCl}_4\text{-B}_2\text{O}_3\text{-Mg}$ powders in Figure 4.12.

Different excess amounts of amorphous B were added to $\text{HfCl}_4\text{-B-Mg}$ powder blends with the intention of elimination of the HfO_2 phase. During the borothermal reduction of HfCl_4 powders with amorphous B, it was shown that the single phase HfB_2 powders without any detectable HfO_2 impurity can be synthesized by using amorphous B over the stoichiometric amount. Therefore, the effect of amorphous B amount on the phases formed during the mechanochemical processing of the $\text{HfCl}_4\text{-B-Mg}$ powder blends was investigated with a similar stimulation.

XRD patterns of the $\text{HfCl}_4\text{-B-Mg}$ powder blends having different excess amounts of amorphous B and Mg after milling for 1 h are illustrated in Figure 4.26 (a)-(d). To observe the effect of Mg amount on the formation of HfO_2 phase, 20 wt.% excess amount of Mg was added to the $\text{HfCl}_4\text{-B-Mg}$ powder blends which also included 30 wt.% excess amount of B. However, similar phase distribution was observed for the powders include excess amount of Mg in the Figure 4.26 (c). On the other hand, in the XRD patterns of $\text{HfCl}_4\text{-B-Mg}$ powders with 50 wt.% excess amount of B, the only detected phases were HfB_2 , MgCl_2 and $\text{MgCl}_2 \cdot 4\text{H}_2\text{O}$ without any detectable HfO_2 phase.

The water washing and HCl leaching were applied to the synthesized powders for the removal of magnesium chloride salts and probable Fe impurity. XRD patterns of the stoichiometric $\text{HfCl}_4\text{-B-Mg}$ powders and those having different excess amount of amorphous B after milling for 1 h, washing with distilled water and 4 M HCl leaching are shown in Figure 4.27 (a)-(c). In the XRD patterns of stoichiometric $\text{HfCl}_4\text{-B-Mg}$ powders and those containing 30 wt.% excess B, the HfB_2 and HfO_2 phases were detected. However, it can be said that the intensities of HfO_2 phase in the XRD patterns of powders having 30 wt.% excess B (in Figure 4.27 (b)) decreased compared to those of stoichiometric powders (in Figure 4.27 (a)). In addition, in the

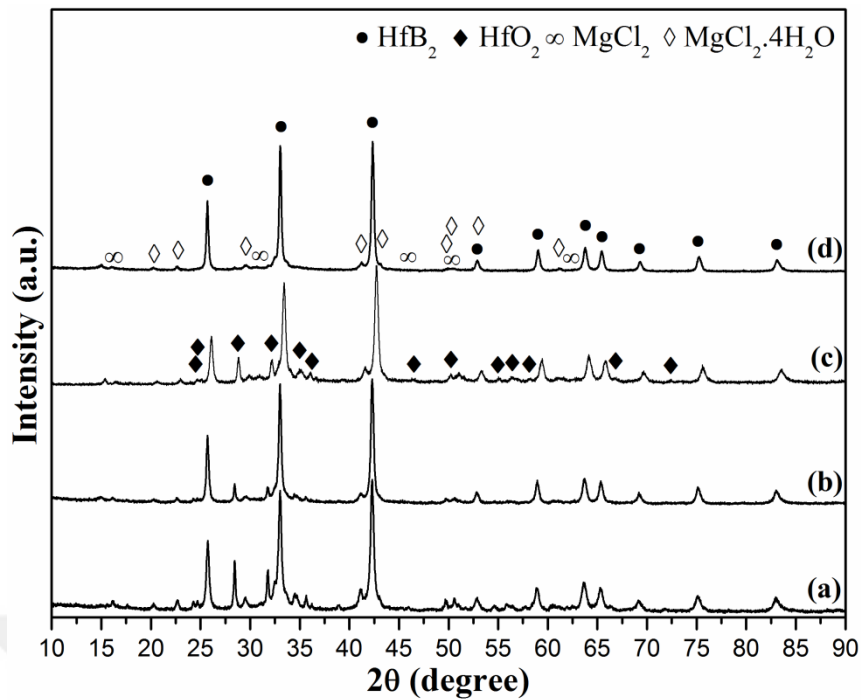


Figure 4.26 : XRD patterns of the HfCl₄-B-Mg powder blends having different stoichiometries: (a) 0 wt.% excess B and Mg (stoichiometric), (b) 30 wt.% excess B, (c) 30 wt.% excess B and 20 wt.% excess Mg and (d) 50 wt.% excess B, after milling for 1 h.

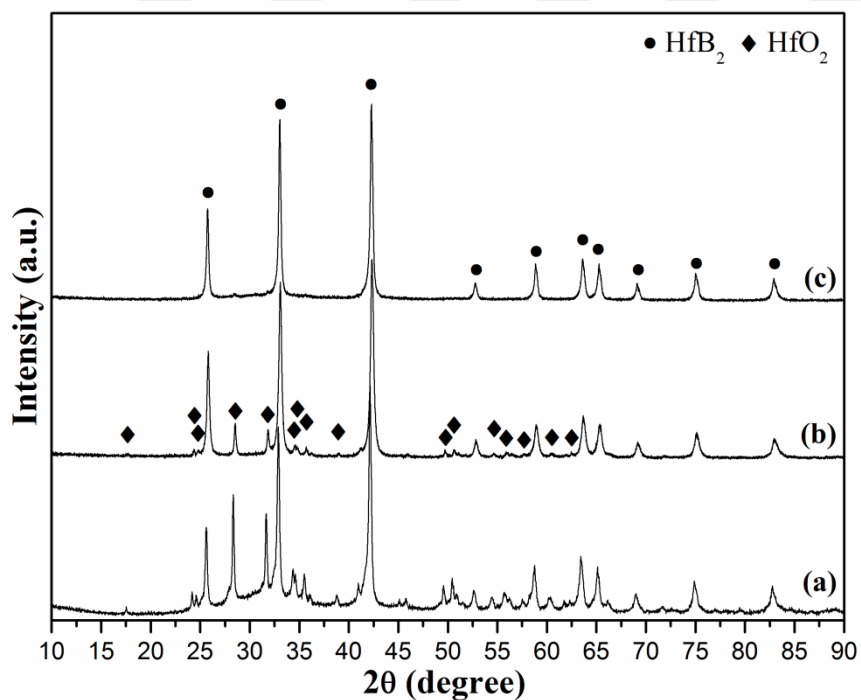


Figure 4.27 : XRD patterns of the HfCl₄-B-Mg powder blends having different excess amount of B: (a) 0 wt.%, (b) 30 wt.% and (c) 50 wt.%, after milling for 1 h and purification.

XRD pattern of HfCl₄-B-Mg powders having 50 wt.% excess amount of B, the HfB₂ phase was determined as single phase. Thus, it was observed that the amount of

amorphous B significantly affects the formation and amount of the HfO_2 phase in the synthesized powders.

The HfCl_4 -B-Mg powder blends having different excess amounts of amorphous B were annealed at 1100 °C for 1 h after milling for 1 h and purification with the aim of observing the any possible phase transformation. XRD patterns of the powders after annealing are illustrated in Figure 4.28 (a)-(c). In the XRD patterns of stoichiometric HfCl_4 -B-Mg blends and those having 30 wt.% excess of B after annealing, the HfB_2 and HfO_2 phases were determined (Figure 4.28 (a) and (b)). In addition, the intensities of HfB_2 phase increased upon heating and an amount of decrease in the HfO_2 peaks was observed. It was considered that the intensities of HfO_2 phase might be suppressed by increased intensities of the HfB_2 phase. Furthermore, HfCl_4 -B-Mg blends having 50 wt.% excess of B have only the HfB_2 phase without any detectable HfO_2 phase after annealing in Figure 4.28 (c).

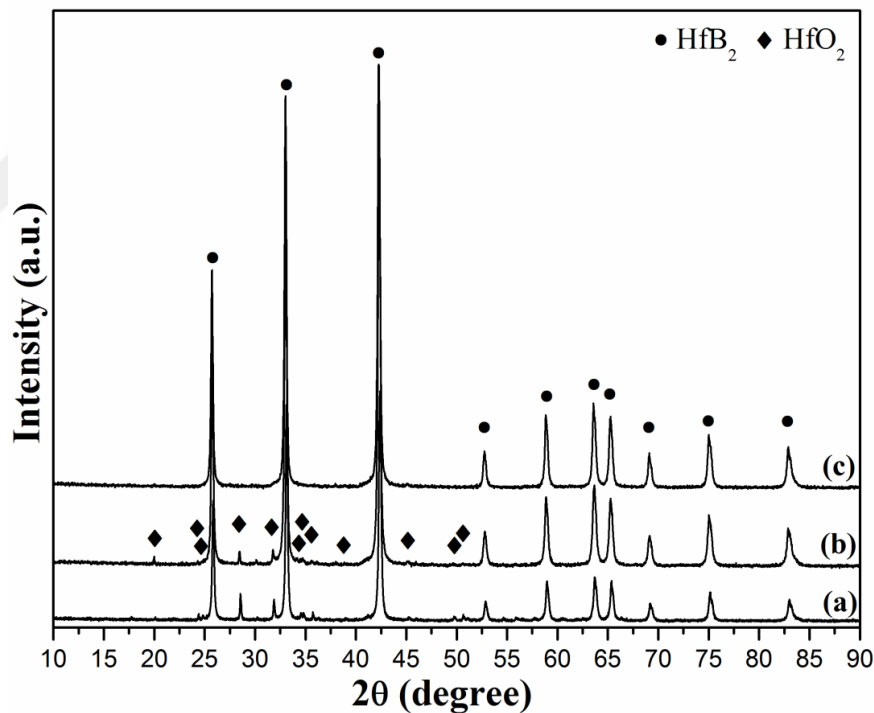


Figure 4.28 : XRD patterns of the HfCl_4 -B-Mg powder blends having different excess amount of B : (a) 0 wt.%, (b) 30 wt.% and (c) 50 wt.%, after milling for 1 h, annealing at 1100 °C for 1 h and purification.

Barraud et al. (2005) investigated the HfB_2 synthesis via mechanically activated annealing of HfCl_4 -B-Mg powder blends. The B and Mg were utilized in excess amounts of 50 wt.%. The HfCl_4 -B-Mg powders blends were milled in a planetary ball mill (Fritsch Pulverisette 7) under Ar atmosphere for 1 h. The ball-to-powder

weight ratio was 20:1 and steel balls and steel vial were used. It was stated that the grinding induced a reduction of partially hydrated HfCl_4 powders, which gave HfH_x and HfB_2 phases. Then, during the annealing, HfH_x decomposed around $500\text{ }^\circ\text{C}$ and reacted with B and MgO to form HfB_2 and HfO , respectively. As a result, annealing the mechanically activated (for 1 h) HfCl_4 -B-Mg blends at $1100\text{ }^\circ\text{C}$ was suggested as a process for synthesis HfB_2 -based powders having average grain size of 300 nm. In addition, relatively small weight fraction of HfO_2 was reported depending on the excess amounts of reactants in the starting blends (Barraud et al., 2005). Moreover, Akgün et al. (2011) suggested mechanochemical synthesis of ZrB_2 powders from ZrO_2 - B_2O_3 -Mg powder blends. It was stated that the ZrB_2 phase formed after milling for 30 h whereas complete conversion of ZrO_2 to ZrB_2 did not take place even with excess amounts of Mg and B_2O_3 and formed ZrB_2 powders contained residual ZrO_2 phase (Akgün et al., 2011).

As a consequence, the HfB_2 - HfO_2 and HfB_2 powders were synthesized from the HfCl_4 - B_2O_3 -Mg and HfCl_4 -B-Mg powder blends via mechanochemical synthesis route at room temperature. It was determined that the usage of different B sources as B_2O_3 and B had significant effect on the formation of HfO_2 phase. It was also shown that the amount of amorphous B in the starting powders of HfCl_4 -B-Mg played an important role for the elimination of the HfO_2 phase.

4.3 The Synthesis of HfB_2 -based Powders by the Mechanically Activated Autoclave Processing of HfCl_4 - B_2O_3 -Mg blends

HfB_2 - HfO_2 ceramic powders were prepared via mechanical activation-assisted autoclave processing of HfCl_4 , B_2O_3 and Mg powder blends conducted at relatively low temperatures. The HfCl_4 , B_2O_3 and Mg starting powders were mechanically activated for 5 min to obtain homogeneously blended precursors with active particle surfaces. The synthesis reaction was performed in a hastelloy autoclave at $500\text{ }^\circ\text{C}$ for 6 and 12 h. Thus, the effects of mechanical activation and reaction duration on the formation yield of HfB_2 phase were investigated in a comparative manner. As-synthesized powders were purified from reaction by-products such as MgO and MgCl_2 by washing and acid leaching treatments.

4.3.1 Phase and thermal analyses of the as-blended and mechanically activated powders

XRD patterns of the as-blended $\text{HfCl}_4\text{-B}_2\text{O}_3\text{-Mg}$ powders and those mechanically activated for 5 min are illustrated in Figure 4.29(a) and (b), respectively. In the XRD patterns of both powders, $\text{HfOCl}_2\cdot 4\text{H}_2\text{O}$, $\text{HfOCl}_2\cdot 6\text{H}_2\text{O}$, Mg and MgCl_2 phases were detected. The crystal structural parameters belonging to different phases encountered in this study are given in Table 4.4. It has been previously observed that the HfCl_4 phase converts into oxychloride and hydrated oxychloride compounds when it interacts with humidity in air (Akçamlı et al., 2015; Barraud et al., 2006). Although blending and mechanical activation processes were conducted at Ar atmosphere, $\text{HfOCl}_2\cdot 4\text{H}_2\text{O}$ and $\text{HfOCl}_2\cdot 6\text{H}_2\text{O}$ phases instead of HfCl_4 are observed because of its highly hygroscopic behavior and atmospheric conditions during the XRD analyses. Moreover, B_2O_3 phase could not be detected in the XRD patterns of the as-blended and mechanically activated powders due to its amorphous nature. The detection of an amount of MgCl_2 phase in the as-blended powders (Figure 4.29(a)) probably arises from the adsorption of the hydrated oxychloride compounds on Mg during blending. The XRD intensity of the MgCl_2 peak at 2θ value of about 34° and the XRD intensities of $\text{HfOCl}_2\cdot 4\text{H}_2\text{O}$ and $\text{HfOCl}_2\cdot 6\text{H}_2\text{O}$ peaks at 2θ value range of $10\text{-}16^\circ$ increased after mechanical activation for 5 min (Figure 4.29(b)). This can be

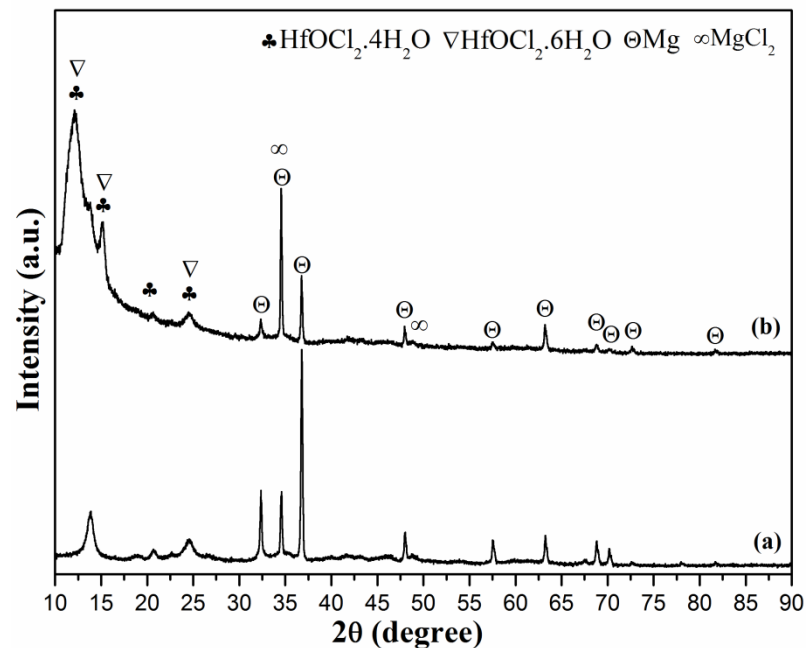


Figure 4.29 : XRD patterns of the (a) as-blended $\text{HfCl}_4\text{-B}_2\text{O}_3\text{-Mg}$ powders and (b) those mechanically activated for 5 min.

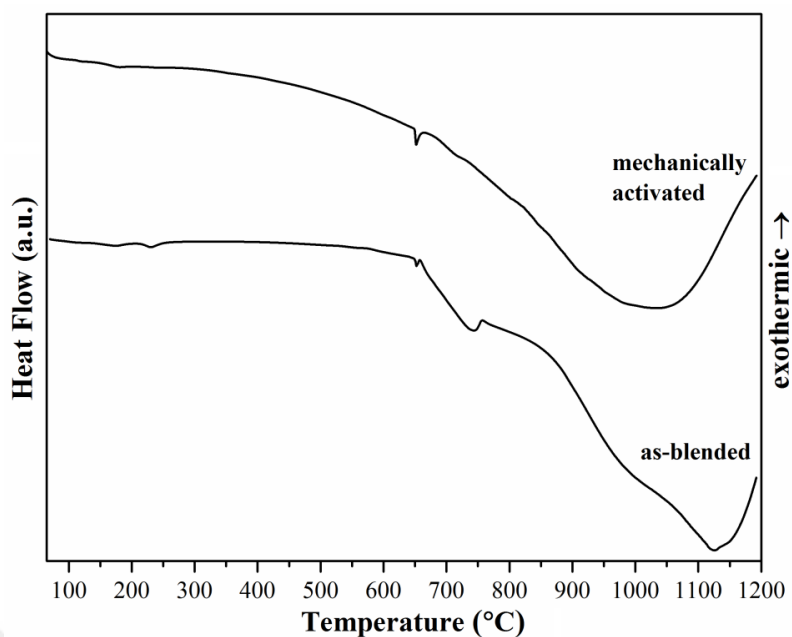
attributed to the formation of active particles and the initiation of reduction reaction, which is also supported by the intensity decrease in the Mg peaks. Extended duration of mechanical activation was not employed for the as-blended powders since a short-time milling is generally required without the occurrence of a partial or complete chemical reaction.

Table 4.4 : The crystal structural information of different phases encountered during autoclave processing of the HfCl₄-B₂O₃-Mg powders.

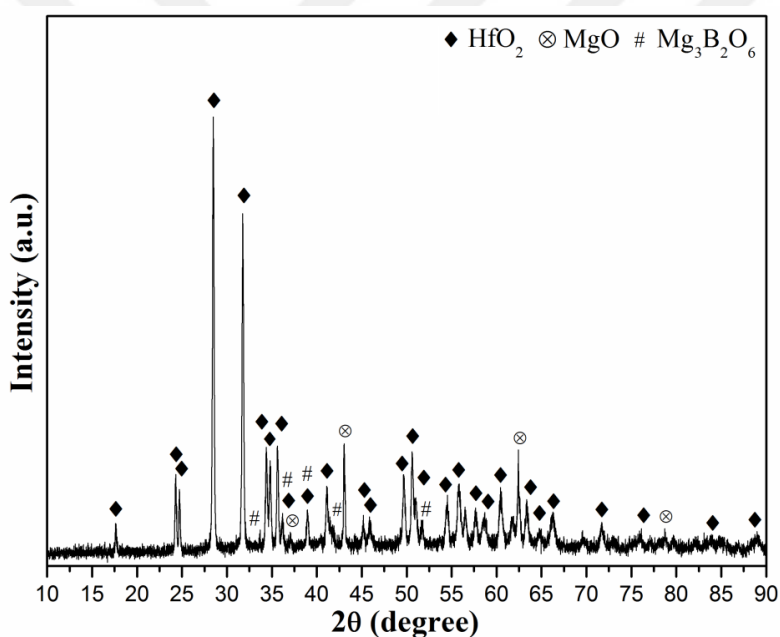
Phase	ICDD Card No	Bravais Lattice	Lattice parameters (nm)
HfOCl ₂ .4H ₂ O	015-0380	-	-
HfOCl ₂ .6H ₂ O	047-0816	-	-
Mg	035-0821	Primitive hexagonal	a=b=0.321, c=0.521
HfB ₂	038-1398	Primitive hexagonal	a=b=0.314, c=0.348
HfO ₂	034-0104	Primitive monoclinic	a=0.529, b=0.518, c=0.512 β=99.26°
HfH _{1.98}	073-2166	Body-centered tetragonal	a=b=0.346, c=0.439
MgO	089-7746	Face-centered cubic	a=b=c=0.422
Mg ₂ Hf ₅ O ₁₂	033-0862	Primitive rhombohedral	a=b=0.939, c=0.870
MgCl ₂	089-1567	Primitive rhombohedral	a=b=0.364, c=0.176
MgCl ₂ .H ₂ O	053-0260	Primitive orthorhombic	a=0.889, b=0.363, c=1.139
MgCl ₂ .6H ₂ O	025-0515	Primitive monoclinic	a=0.987, b=0.711, c=0.608, β=93.74°
Mg ₃ B ₂ O ₆	038-1475	Primitive orthorhombic	a=0.540, b=0.842, c=0.451

DSC scans of the as-blended and 5 min of mechanically activated HfCl₄-B₂O₃-Mg powders are displayed in Figure 4.30(a). As-blended powders have two small endotherms peaking at about 190 and 245 °C corresponding to the dehydration of small amount of H₃BO₃ in the structure of B₂O₃ and sublimation of small amount of HfCl₄ remained in the structure of HfOCl₂.4H₂O and HfOCl₂.6H₂O phases which was not detected by the XRD analysis due to its detection limit (≥ 2 wt.%). These two endotherms are very slight in the mechanically activated powders. It was previously reported that the vaporization of water adsorbed onto the B₂O₃ structure occurred at about 190 °C (Balci et al., 2015). Also, anhydrous HfCl₄ was found to be sublimed at the temperature range of 240-300 °C (Barraud et al., 2006). Surprisingly, the melting of B₂O₃ (T_{melting}=450 °C) was not observed with an endothermic peak in

the as-blended powders. This phenomenon can be attributed to the non-isothermal fast DSC heating conditions carried out in an alumina crucible in which particles of the raw materials react with each other in a very small volume (Balci et al., 2015). There are small endothermic peaks with maximum points at about 650 °C in the as-blended and mechanically activated powders, indicating the melting of Mg. However, this endotherm is more clear in the mechanically activated powders, possibly because of the distributed active Mg particles. The formation of MgO phase cannot be observed from the DSC scans of the powders which it means that a reduction reaction did not take place between the reactant particles. Moreover, an endotherm with an onset temperature of 660 °C and a peak point of 750 °C in the as-blended powders shows the decomposition of $\text{HfOCl}_2 \cdot 4\text{H}_2\text{O}$ and $\text{HfOCl}_2 \cdot 6\text{H}_2\text{O}$ phases. Similarly, the decomposition temperature of partially hydrated ZrCl_4 was reported as below 700 °C (Barraud et al., 2006). A very small exotherm peaking at about 760 °C in the as-blended powders can be attributed to the formation of Mg borate phases which was formerly found to occur at a temperature range of 700-1000 °C in different compositions (MgB_4O_7 , $\text{Mg}_2\text{B}_2\text{O}_5$ and $\text{Mg}_3\text{B}_2\text{O}_6$) (Ağaoğulları et al., 2012b). Furthermore, a very broad endothermic peak with a maximum point of 1120 °C may be an overlapping peak of boiling of residual Mg and emergence of HfO_2 phase as a result of $\text{HfOCl}_2 \cdot 4\text{H}_2\text{O}$ and $\text{HfOCl}_2 \cdot 6\text{H}_2\text{O}$ decompositions. This endotherm shifts to a lower temperature (about 1050 °C) in the mechanically activated powders than that of as-blended one. It contains the decomposition of hydrated oxychloride compounds, emergence of Mg borate and HfO_2 phases and boiling of Mg in the broad overlapping peak without showing any individual endothermic and exothermic peaks. It can be said that mechanically activated powders with active and distributed particles have a simultaneous formation of MgO, Mg borate and HfO_2 phases after penetration of Mg melt through the decomposed $\text{HfOCl}_2 \cdot 4\text{H}_2\text{O}$ and $\text{HfOCl}_2 \cdot 6\text{H}_2\text{O}$ phases. Figure 4.30(b) exemplifies the XRD pattern of the mechanically activated powders after DSC heating. The emerged phases such as HfO_2 , MgO and $\text{Mg}_3\text{B}_2\text{O}_6$ after heating up to 1200 °C confirm the DSC scans of the powders. It should be also noted that HfB_2 phase could not be obtained even after heating of the mechanically activated powders to an elevated temperature without a holding time.



(a)



(b)

Figure 4.30 : (a) DSC scans of the as-blended $\text{HfCl}_4\text{-B}_2\text{O}_3\text{-Mg}$ powders and those mechanically activated for 5 min, and (b) XRD pattern of the mechanically activated powders after DSC heating.

4.3.2. Phase analyses of the powders after autoclave processing

XRD patterns of the as-blended powders and those of mechanically activated after reaction in the autoclave (for 6 and 12 h) are shown in Figure 4.31 (a)-(d). As seen in Figure 4.31 (a)-(b), HfO_2 , $\text{HfH}_{1.98}$, MgO , $\text{Mg}_2\text{Hf}_5\text{O}_{12}$, MgCl_2 and $\text{MgCl}_2 \cdot 6\text{H}_2\text{O}$ phases and a very small amount of HfB_2 phase were detected in the as-blended

powders after autoclave processing for 6 and 12 h. Dissimilar to the as-blended powders after autoclave reaction for 6 h (Figure 4.31(a)), 12 h of processed powders have also $\text{MgCl}_2 \cdot \text{H}_2\text{O}$ phase with a decrease in the peak intensity of MgCl_2 (Figure 4.31(b)). However, autoclave reaction of mechanically activated powders both for 6 and 12 h yielded the major HfB_2 phase in addition to the HfO_2 , MgO , $\text{Mg}_2\text{Hf}_5\text{O}_{12}$, MgCl_2 and $\text{MgCl}_2 \cdot 6\text{H}_2\text{O}$ phases (Figure 4.31(c) and (d)). Extending the reaction duration of the autoclave processing of mechanically activated powders did not affect the nature of emerged phases but it slightly increased their intensities in the XRD peaks. Although the $\text{HfH}_{1.98}$ phase was detected in the as-blended powders after autoclave reaction for 6 and 12 h (Figure 4.31(a) and (b)), there was not an indication of its presence in the mechanically activated ones (Figure 4.31(c) and (d)). In an investigation on the high-energy ball milling of HfCl_4 -B-Mg powder mixtures, Barraud et al. (2005) reported the reduction of partially hydrated HfCl_4 mainly to the HfH_x and subsequently to the HfB_2 phase. The formation of HfH_x ($1.6 < x < 2$) was also determined by Begin et al. (2004) during the milling of HfCl_4 -B-Mg powder blends. It can be stated that 5 min of mechanical activation before autoclave reaction induced the occurrence of HfB_2 without any detection of the $\text{HfH}_{1.98}$ phase. Also, it is surprising to observe the presence of the $\text{Mg}_2\text{Hf}_5\text{O}_{12}$ phase after autoclave reaction of the both as-blended and mechanically activated powders. Indeed, there is no detailed information about the presence of the $\text{Mg}_2\text{Hf}_5\text{O}_{12}$ phase in the archival literature. It was previously introduced in the binary phase diagram of the HfO_2 - MgO system (Wu and Jin, 1997). According to this phase diagram, $\text{Mg}_2\text{Hf}_5\text{O}_{12}$ phase emerges at 28.57 % molar amount of MgO , is stable at the temperature range of 1370-2348 °C and decomposes into monoclinic HfO_2 and MgO phases below this temperature range (Wu and Jin, 1997). Although the autoclave reaction was carried out at 500 °C which is far below than the stability range, the observed $\text{Mg}_2\text{Hf}_5\text{O}_{12}$ phase can be attributed to the pressurized atmosphere (about 22 bar) in the reaction vessel and the higher affinity of $\text{HfOCl}_2 \cdot 4\text{H}_2\text{O}$ and $\text{HfOCl}_2 \cdot 6\text{H}_2\text{O}$ phases compared with that of the stable HfO_2 phase. Furthermore, the differences in the phase composition of the as-blended and mechanically activated powders following autoclave reaction obviously revealed the effect of mechanical activation (Figure 4.31(a)-(d)). The amount of the HfB_2 phase substantially increased due to homogeneous distribution of particles throughout the microstructure and enhancement of their reactivity by means of mechanical activation. Similarly, the effect of mechanical activation on the reaction

yield was also reported in the previous studies pertinent to the preparation of some boron-based products by milling-assisted solid-state synthesis methods (Akçamlı et al., 2016; Aǧaoǧulları et al., 2012b; Balcı et al., 2012; Balcı et al., 2015).

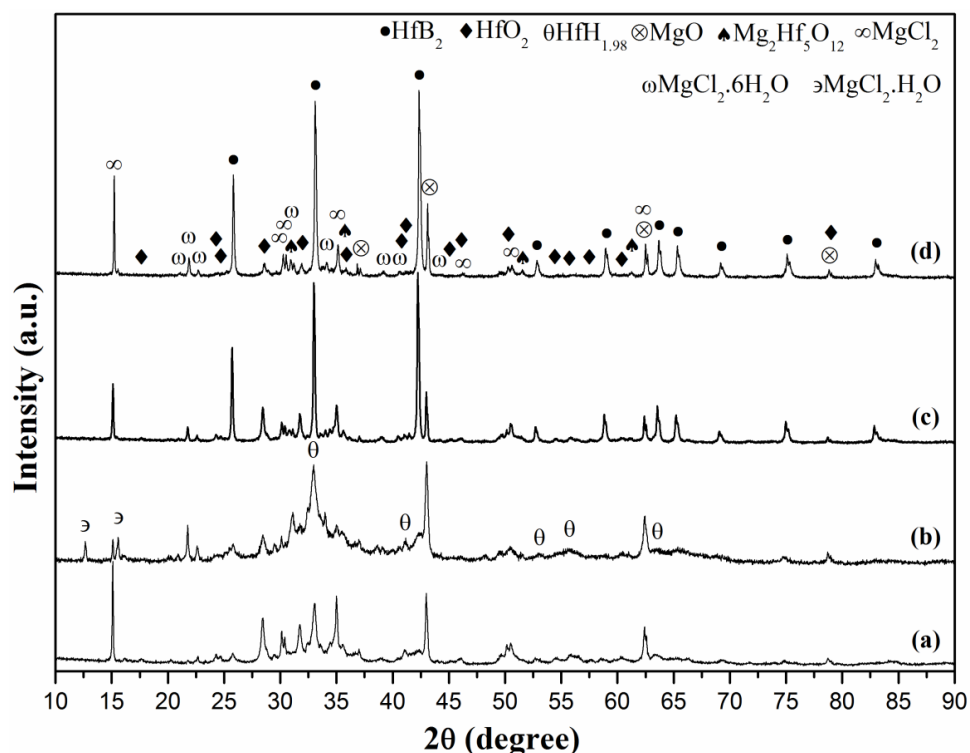


Figure 4.31 : XRD patterns of the as-blended $\text{HfCl}_4\text{-B}_2\text{O}_3\text{-Mg}$ powders and those of mechanically activated for 5 min after autoclave processing at different durations: (a) as-blended powders after 6 h, (b) as-blended powders after 12 h, (c) mechanically activated powders after 6 h and (d) mechanically activated powders after 12 h.

Figure 4.32(a)-(d) illustrates the XRD patterns of the as-blended $\text{HfCl}_4\text{-B}_2\text{O}_3\text{-Mg}$ powders and those mechanically activated for 5 min followed by reaction in the autoclave (for 6 or 12 h) and subsequent washing and leaching treatments. The XRD patterns indicate that MgCl_2 , $\text{MgCl}_2 \cdot 6\text{H}_2\text{O}$, $\text{MgCl}_2 \cdot \text{H}_2\text{O}$ and MgO by-products were completely removed from the powders by washing and HCl leaching. After purification steps, as-blended powders contained $\text{HfH}_{1.98}$, HfO_2 and $\text{Mg}_2\text{Hf}_5\text{O}_{12}$ phases with a very small incubation of HfB_2 (Figure 4.32(a) and (b)). However, there are only HfB_2 , HfO_2 and $\text{Mg}_2\text{Hf}_5\text{O}_{12}$ phases in the mechanically activated powders after autoclave reaction and purification (Figure 4.32(c) and (d)). The XRD intensities of HfO_2 and $\text{Mg}_2\text{Hf}_5\text{O}_{12}$ phases decreased as the duration of autoclave processing increased from 6 to 12 h. Moreover, the Rietveld refinement method was conducted on the purified mechanically activated powders with the aim of determining the estimated amounts of the HfB_2 phase. The HfB_2 amount in the

purified powders synthesized by autoclave processing for durations of 6 and 12 h were calculated as 35.6 and 79.6 %, respectively. Thus, this increase in the amount of HfB_2 proves that extending autoclave processing durations affected the final phase composition by providing a steady-state condition (Figure 4.32(c) and (d)).

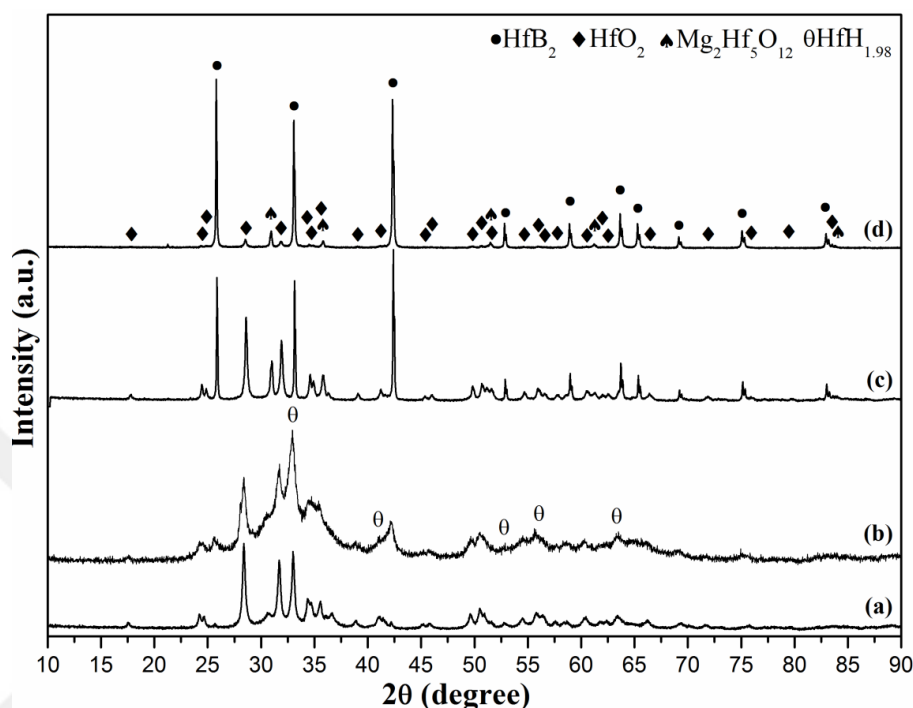


Figure 4.32 : XRD patterns of the as-blended $\text{HfCl}_4\text{-B}_2\text{O}_3\text{-Mg}$ powders and those mechanically activated for 5 min after autoclave processing at different durations and subsequent purification: (a) as-blended powders after 6 h, (b) as-blended powder after 12 h, (c) mechanically activated powders after 6 h and (d) mechanically activated powders after 12 h.

Figure 4.33(a) and (b) show the FTIR spectra of the utilized B_2O_3 and HfCl_4 raw materials for comparison. The B_2O_3 powders show IR absorptions at the wave numbers of 948 cm^{-1} (B–O symmetric stretching), $1055\text{-}1222\text{ cm}^{-1}$ (B–O asymmetrical stretching), $1307\text{-}1496\text{ cm}^{-1}$ (B–O asymmetrical stretching), 2255 and 2368 cm^{-1} (B–H mode), $3018\text{-}3585\text{ cm}^{-1}$ (B–OH mode) (in Figure 4.33(a)) [41-43]. The HfCl_4 powders have IR absorptions at the wave numbers of 929 cm^{-1} (modes of coordinated water), 1044 cm^{-1} (Hf–OH bonds: bridging hydroxide deformation), 1620 cm^{-1} (bending mode of water molecules coordinated to cations), 2050 cm^{-1} (Harmonic and/or combination of vibration bands of Hf–OH), 2363 cm^{-1} (harmonic and/or combination of vibration bands of water) and $2710\text{-}3481\text{ cm}^{-1}$ (OH stretching of water molecules) are determined (Figure 4.33(b)) (Barraud et al., 2006).

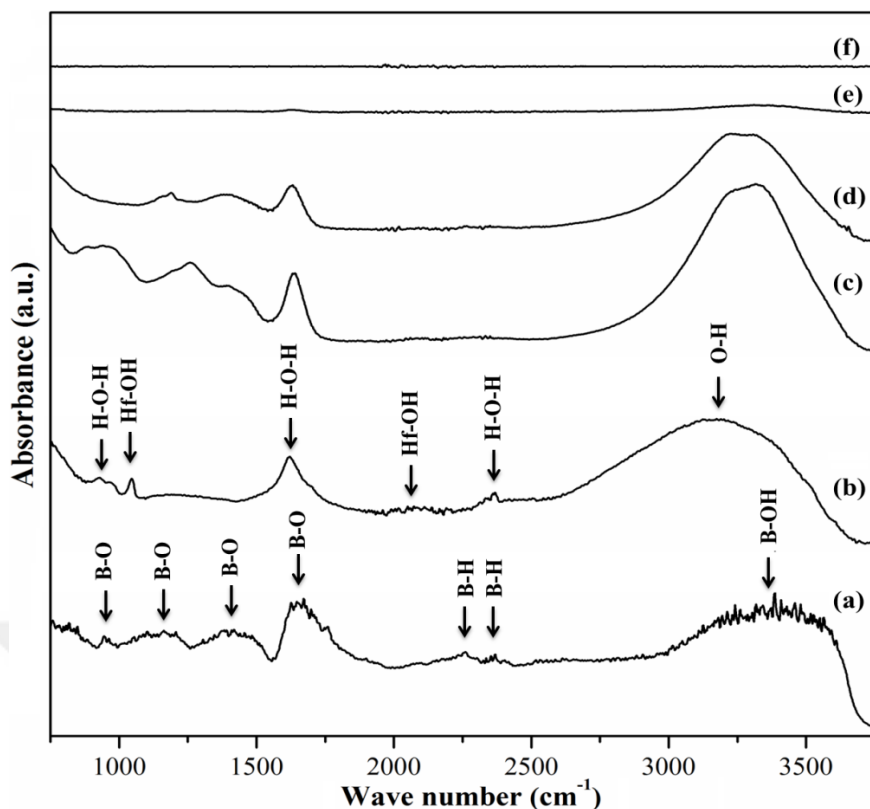


Figure 4.33 : FTIR spectra of the (a) B_2O_3 raw material, (b) $HfCl_4$ raw material, (c) as-blended $HfCl_4$ - B_2O_3 -Mg powders, (d) those mechanically activated for 5 min, (e) those autoclave processed for 12 h and (f) those purified with washing and leaching treatments.

The Hf- OH bonds evolve inevitably because of the extreme hygroscopic character of $HfCl_4$ powders which form $HfOCl_2 \cdot 4H_2O$ and $HfOCl_2 \cdot 6H_2O$ phases. Figure 4.33 (c)-(f) illustrates the FTIR spectra of the as-blended $HfCl_4$ - B_2O_3 -Mg powders and those of mechanically activated for 5 min, subsequently autoclave processed for 12 h and purified, respectively. As expected, the FTIR spectra of the as-blended (Figure 4.33 (c)) and mechanically activated powders (Figure 4.33 (d)) are similar but a small decrease in the peak intensities and slight deflection in the peaks are observed (Akçamlı et al., 2016). In the FTIR spectrum of the $HfCl_4$ - B_2O_3 -Mg powders after mechanical activation for 5 min and autoclave processing for 12 h (in Figure 4.33 (e)), two small absorption peaks in the vicinities of 1625 and 3330 cm^{-1} can be identified, which respectively pertains to hydroxyl groups present in the structure of $MgCl_2 \cdot 6H_2O$ by-product. On the other hand, the absence of the Hf-OH and B-O peaks in the FTIR spectra of the mechanically activated and autoclave processed powders (Figure 4.33 (e)) indicates that there is no unreacted $HfOCl_2 \cdot 4H_2O$, $HfOCl_2 \cdot 6H_2O$ and B_2O_3 phases remained after reaction. On the other hand, in the FTIR spectra of the purified powders (Figure 4.33 (f)), no absorption corresponding

to O-H bands were detected, which indicates the complete elimination of the $\text{MgCl}_2 \cdot 6\text{H}_2\text{O}$ phase.

Figure 4.34 (a) and (b) illustrate the SM images of the as-blended $\text{HfCl}_4\text{-B}_2\text{O}_3\text{-Mg}$ powders and those mechanically activated for 5 min. The progress of the reaction can be followed with the general appearances and color changes of the powders. The differences between the as-blended and mechanically activated powders are quite noticeable. Whereas as-blended powders have white B_2O_3 particles embedded in the dark gray matrix containing $\text{HfOCl}_2 \cdot 4\text{H}_2\text{O}$, $\text{HfOCl}_2 \cdot 6\text{H}_2\text{O}$ and Mg powders, the mechanically activated powders have more uniform size and phase distribution throughout the microstructure. Milling for 5 min provided a close contact between the reactant particles and created activated species for the subsequent autoclave reaction. The SM images of the powders prepared by mechanically activated autoclave processing (for 12 h) and purification treatments are shown in Figure 4.34 (c) and (d), respectively. The general morphologies and colors of the powders changed resulting from the chemical reaction in the autoclave. The shiny or

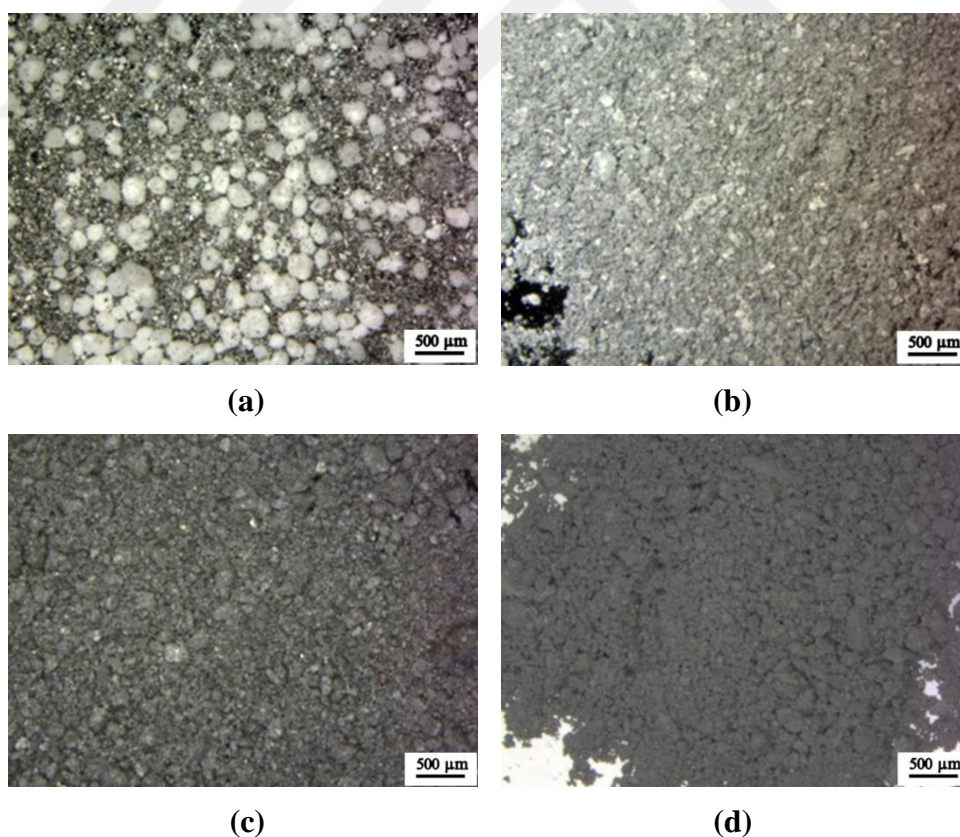


Figure 4.34 : SM images of the (a) as-blended $\text{HfCl}_4\text{-B}_2\text{O}_3\text{-Mg}$ powders, (b) those after mechanical activation for 5 min, (c) those after reaction in the autoclave for 12 h and (d) those after purification.

lighter Mg-based particles such as MgO, MgCl₂ and MgCl₂.6H₂O are clearly observed in Figure 4.34 (c). After the removal of these impurities, the powders exhibit a homogenous microstructure (Figure 4.34(d)).

SEM images of the powders obtained after mechanical activation for 5 min, autoclave reaction for 12 h and purification are shown in Figure 4.35 (a) and (b) at different magnifications. There are large agglomerates smaller than 600 nm, in which spheroidal particles are embedded. Figure 4.35 (c) is the corresponding general EDS analysis of the powders. The EDS measurement shows the existence of Hf, B, O and Mg elements in the microstructure and their compositions were determined as 86.86, 5.89, 6.77 and 0.48 wt.%, respectively. The EDS analysis is in good accordance with the XRD analysis of the purified powders (Figure 4.35 (d)) in which HfB₂, HfO₂ and Hf₂Mg₅O₁₂ phases were determined. Particle size distribution curve illustrated in Figure 4.35 (d) reveals an average value of 189.7 nm. Considering the SEM images and PSA analysis, it can be said that obtained powders have a uniform distribution throughout the microstructure. Although autoclave or solvothermal synthesis methods are quite new applications for preparation of boride compounds, they have been attracting great interest owing to some advantageous such as size control (nano-scaled) and morphology (rod, cube, sheet, i.e.) of the particles (Chen et al., 2012; Ma et al., 2003). Moreover, autoclave synthesis is considered as an environmentally friendly method because the process proceeds in a closed/isolated system and it saves energy by low synthesis temperature (Feng and Li, 2011; Feng and Xu, 2001). It was stated that the usage of relatively mild temperatures which are high enough to trigger crystallization but still low enough to avoid excessive grain growth (ideally in the range of 500-900 °C), enables to obtain nanostructures (Portehault et al., 2011). In a previous study in which HfB₂ powders were prepared by a reaction of HfCl₄ with NaBH₄ at 600 °C in an autoclave, it was stated that the powders had small particle size range of 20-30 nm (Chen et al., 2004c). In another study in which a chemical reaction in an autoclave were utilized for the synthesis of different borides such as TiB₂ and ZrB₂ from related oxides and amorphous B in the presence of elemental Na and S, particle size of the TiB₂ and ZrB₂ products were respectively reported as 100 and 500 nm after related washing and leaching treatments (Chen et al., 2012). It can be said that the particle size of the boride products strongly depends on the decomposition or melting temperature of boron

HfOCl₂.6H₂O phases due to its hygroscopic behavior. While small amount of remained HfCl₄ sublimed in the structures of HfOCl₂.4H₂O and HfOCl₂.6H₂O phases, B₂O₃ and Mg melt diffused through the particles. The decomposition of HfOCl₂.4H₂O and HfOCl₂.6H₂O phases, formation of HfO₂ and MgO phases and initiation of HfB₂ phase occurred simultaneously by the effect of pressurized atmosphere. Meanwhile, an amount of Mg₂Hf₅O₁₂ emerged from the reaction of HfO₂ and MgO phases together with the reduction by-products (MgO, MgCl₂, MgCl₂.6H₂O).

With the aim of revealing the distribution of different phases in the synthesized powders, SEM/EDX analyses were conducted. Figure 4.36 (a)-(e) represent the secondary electron SEM image and related elemental maps for Hf, O, B and Mg belongs to the HfCl₄-B₂O₃-Mg powder blends mechanically activated, autoclave processed and subsequently purified with distilled water and 4 M HCl. Figure 4.36 (b) reveals the homogenous distribution of Hf throughout the microstructure. The weak signals belong to B (in Figure 4.36 (d)) can be explained with the suppression of B signals by the strong signals of Hf, O and Mg. The elemental Hf map coincides almost entirely with elemental B and O maps (Figure 4.19 (c) and (d)) indicating related phases. Therefore, the elemental maps confirm the formation of HfB₂ and HfO₂ phases and also their uniform distribution throughout

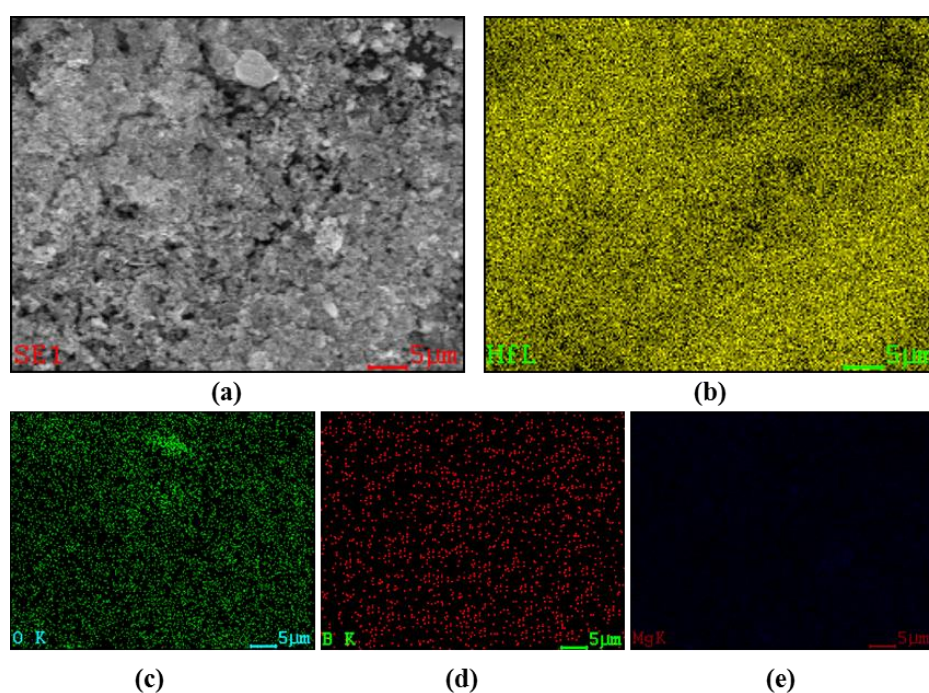


Figure 4.36 : SEM/EDX analyses of the milled (for 3 h) and purified powders: (a) SEM image and corresponding elemental maps for (b) Hf, (c) O, (d) B and (e) Mg.

the microstructure. Moreover, the elemental Mg map which almost entirely coincides with the elemental Hf and O maps so it indicates the $\text{Mg}_2\text{Hf}_5\text{O}_{12}$ phase. The removal of MgO phase by HCl leaching is a relatively well known process and it was shown in the previous studies (Ağaoğulları, 2014; Ricceri et al., 2004). Thus, the existence of Mg even after leaching with 4 M HCl solution should be related with the $\text{Mg}_2\text{Hf}_5\text{O}_{12}$ phase, which was also determined in the XRD analysis of purified powders in Figure 4.32.

Finally, the HfB_2 - HfO_2 powders were synthesized by mechanically activated autoclave processing of the HfCl_4 - B_2O_3 -Mg powder blends. Dissimilarly from the mechanochemical route, during the autoclave processing, the effects of heating and autogen pressure on the types and amounts of obtained phases were observed. It was determined that the amount of the HfB_2 phase in the powders synthesized by autoclave process was higher than that of mechanochemically synthesized ones.

4.4 The synthesis of HfB_2 Powders Blends by Autoclave Processing

The HfB_2 powders were synthesized from HfCl_4 - NaBH_4 -Mg powder blends in the autoclave at 500 °C for 12 h under autogenic pressure conditions. A relatively low synthesis temperature of 500 °C was utilized for the synthesis of HfB_2 powders by taking the advantageous of autoclave synthesis route. Different excess amounts of NaBH_4 were utilized with the intention of investigating their effects on the reaction products. After the autoclave process, additional heat treatments at different temperatures (750, 1000 and 1700 °C) were applied to determine any probable changes in the phases. The single phase HfB_2 powders were achieved to synthesize from the HfCl_4 - NaBH_4 -Mg powder blends having 200 wt.% excess NaBH_4 after a series of treatment which are autoclave processing at 500 °C for 12 h, subsequent annealing at 1000 °C for 3 h and leaching with 4 M HCl.

4.4.1 The synthesis of HfB_2 powders from HfCl_4 - NaBH_4 -Mg powder blends by autoclave processing

XRD patterns of the stoichiometric HfCl_4 - NaBH_4 -Mg powders and those having 100 and 200 wt.% excess amounts of NaBH_4 after the autoclave process at 500 °C for 12 h are shown in Figure 4.37 (a) to (c). After the autoclave reaction, HfB_2 (ICDD Card No: 038–1398, Bravais lattice: primitive hexagonal, $a=b=0.314$, $c=0.347$ nm),

HfO₂ (ICDD Card No: 034–0104, Bravais lattice: primitive monoclinic, a=0.528, b=0.518, c=0.511 nm, β=99.259°), NaCl (ICDD Card No: 005-0628, Bravais lattice: face-centered cubic, a=b=c=0.564 nm), MgCl₂.6H₂O, (ICDD Card No: 025-0515, Bravais lattice: base-centered monoclinic, a=0.987, b=0.711, c=0.608 nm, β=93.740°) and Mg₂B₂O₅ (ICDD Card No: 073-2232, Bravais lattice: primitive triclinic, a=0.619, b=0.922, c=0.312 nm, α=90.400°, β=92.130°, γ=104.320°) phases were determined in the XRD patterns. Additionally, the low intensities of HfB₂ and HfO₂ phases (in the Figure 4.37 (a) to (c)) indicate the low crystallinity of these phases, which can be attributed to the comparatively low synthesis temperature.

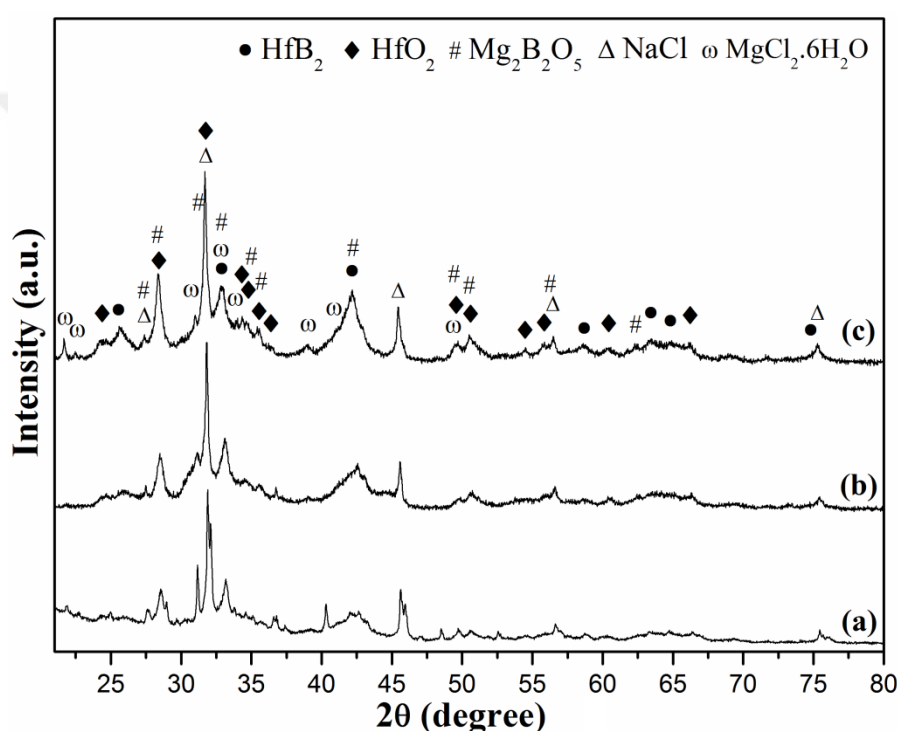


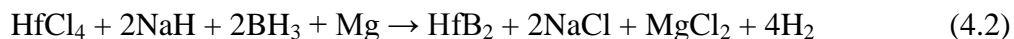
Figure 4.37 : XRD patterns of the HfCl₄-NaBH₄-Mg powder blends having different excess amounts of NaBH₄: (a) 0 wt.%, (b) 100 wt.% and (c) 200 wt.%, after autoclave processing at 500 °C for 12 h.

During the autoclave processing at 500 °C, HfCl₄ (boiling point: 432 °C) and NaBH₄ (boiling point: 500 °C) present in gas-state while Mg exists in solid-state. Therefore, the synthesis reaction is based on a heterogeneous type chemical reaction. The overall reaction is given in the reaction (3.5).

It was stated that the NaBH₄ is decomposed to give BH₃ and NaH at 500 °C according to the reaction (4.1) given below:



The BH_3 reacts further with HfCl_4 to form HfB_2 and HCl , at the same time HCl immediately reacts with NaH and Mg to yield H_2 , NaCl and MgCl_2 according to reaction (4.2):



After the autoclave reaction, the obtained powders were washed with distilled water for the removal of water-soluble chloride salts like NaCl and MgCl_2 . XRD patterns of the powders after washing with distilled water are illustrated in Figure 4.38 (a) to (c). By the removal of water-soluble salts, the determined phases in the XRD patterns were HfB_2 , HfO_2 and $\text{Mg}_2\text{B}_2\text{O}_5$. The presence of HfO_2 and $\text{Mg}_2\text{B}_2\text{O}_5$ phases is caused by the unavoidable evolution of hafnium oxychloride ($\text{HfOCl}_2 \cdot x\text{H}_2\text{O}$) compounds according to reaction (3.1). The $\text{HfOCl}_2 \cdot x\text{H}_2\text{O}$ is decomposed to HfO_2 phase during the reaction upon heating.

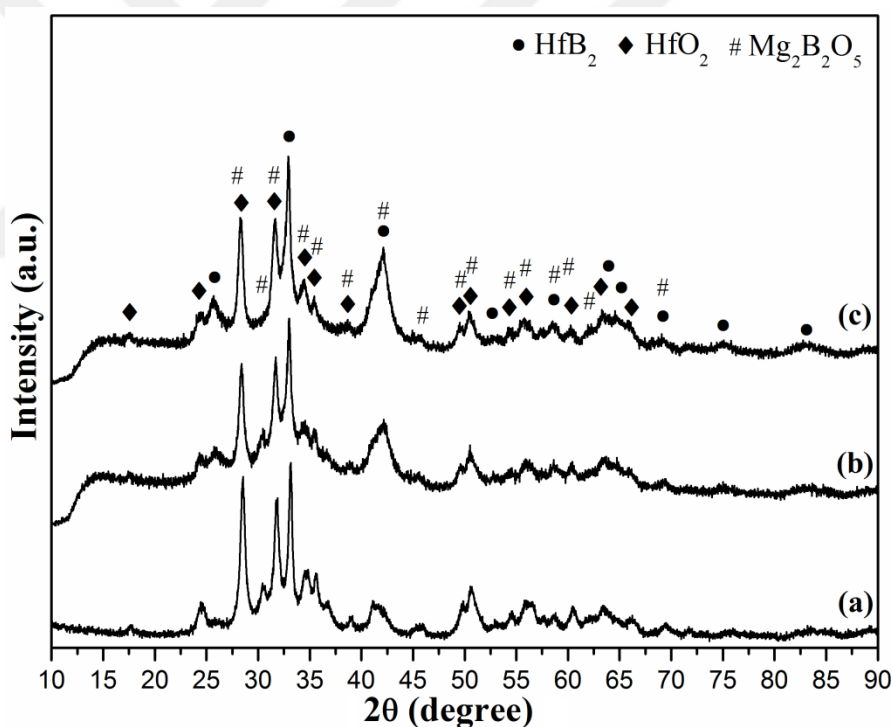


Figure 4.38 : XRD patterns of the HfCl_4 - NaBH_4 - Mg powder blends having different excess amounts of NaBH_4 : (a) 0 wt.%, (b) 100 wt.% and (c) 200 wt.%, after reaction in the autoclave at 500 °C for 12 h and washing with distilled water.

FTIR spectra of the autoclave gases evolved during the reaction of the HfCl_4 - NaBH_4 - Mg blends having 200 wt.% excess NaBH_4 at 500 °C for 12 h are shown in Figure 4.39. After completion of the autoclave reaction, the gaseous products were cooled to the room temperature and were fed into the gas cell of FTIR unit which was heated

to 220 °C for preventing condensation. There are only HCl and H₃BO₃ peaks in the FTIR spectra of reaction gases as can be seen from the Figure 4.39. The formation of H₃BO₃ peaks approximately at the wavenumbers of 1300 and 3030 cm⁻¹ most likely arose from the reaction between the BH₃ and oxygen or humidity (Ağaoğulları et al., 2011). The BH₃ are evolved by the decomposition of NaBH₄ (according to reaction (4.1)) over 400 °C and oxygen or humidity might be derived from the partially hydrated hafnium tetrachloride powders (such as HfOCl₂.4H₂O and HfOCl₂.6H₂O) (Chen et al., 2004a). The HCl peaks at wavenumbers between 2800 and 3200 cm⁻¹ proves the formation of HfB₂ according to the overall reaction (3.5) (Ağaoğulları et al., 2011). In addition, any peaks belonging to the HfCl₄ gas was not determined in the FTIR analysis, which can be explained by its total consumption during autoclave process for 12 h.

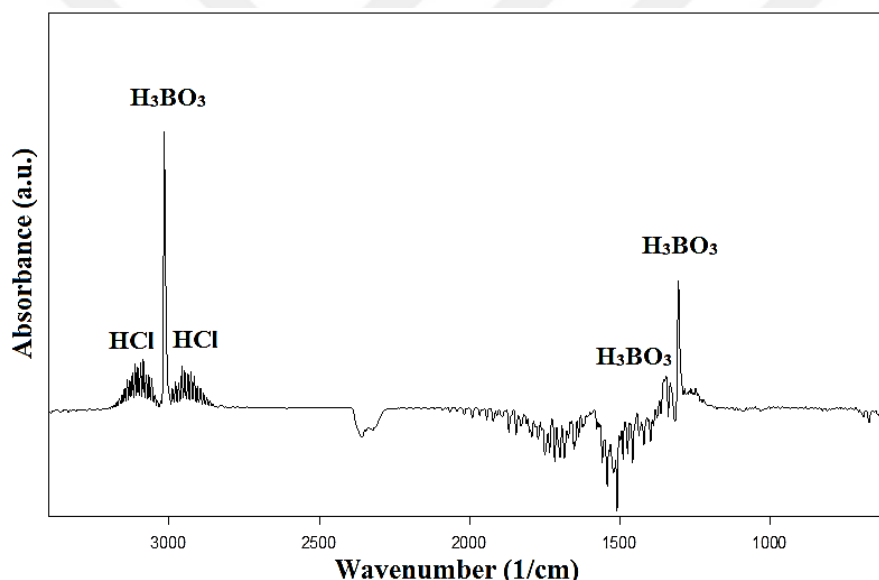


Figure 4.39 : FTIR spectra of autoclave gases evolved during the reaction of HfCl₄-NaBH₄-Mg blends having 200 wt.% excess NaBH₄ at 500 °C for 12 h.

After the autoclave process conducted at 500 °C for 12 h and washing with distilled water, the obtained powders were annealed at higher temperatures in order to increase peak intensities and to investigate the any changes in the detected phases. Two different annealing temperatures (750 and 1000 °C) were selected to observe the effect of annealing temperature on the formed phases.

XRD patterns of the HfCl₄-NaBH₄-Mg powder blends having different excess amounts of NaBH₄ after the autoclave process, washing with distilled water and annealing at 750 °C for 3 h are given in Figure 4.40 (a)-(c). The XRD patterns of

powders after annealing at 750 °C do not show a significant difference compared to the synthesized and water-washed ones, as can be seen from the Figure 4.38 and Figure 4.40. However, an amount of increase in the intensities was observed by the effect of the heat treatment.

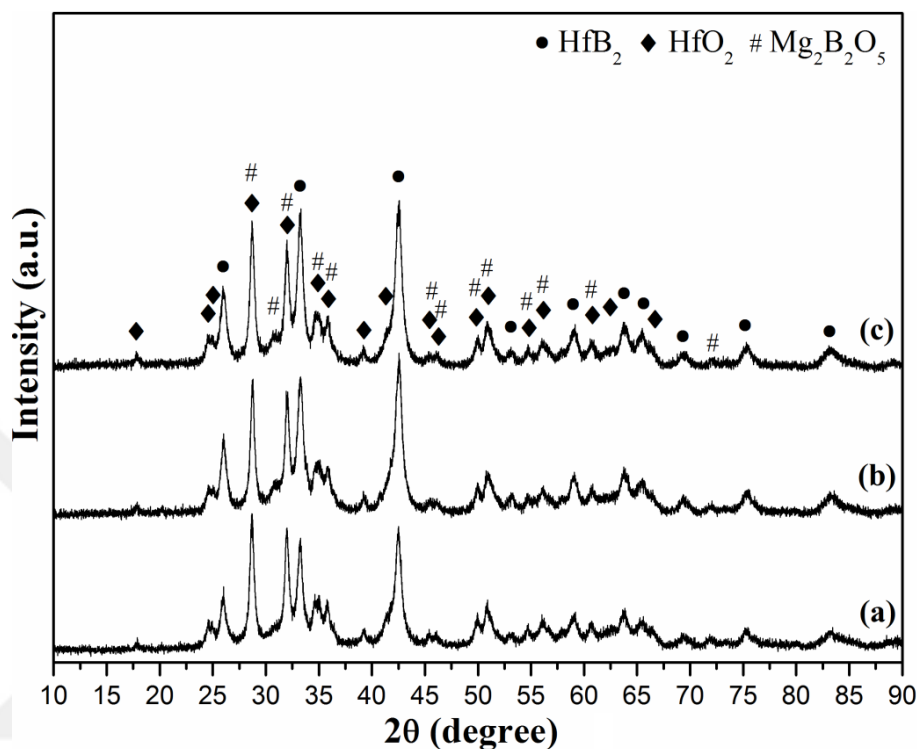


Figure 4.40 : XRD patterns of the HfCl₄-NaBH₄-Mg powder blends having different excess amounts of NaBH₄ : (a) 0 wt.%, (b) 100 wt.% and (c) 200 wt.%, after reaction in the autoclave at 500 °C for 12 h, washing with distilled water and annealing at 750 °C for 3 h.

The XRD patterns of the HfCl₄-NaBH₄-Mg powders after reaction in the autoclave for 12 h, leaching with distilled water and annealing at 1000 °C for 3 h are given in Figure 4.41 (a)-(c). The increase in the annealing temperature gave rise to significant changes in the intensities of the different phases. Especially in the XRD patterns of HfCl₄-NaBH₄-Mg powders with 200 wt.% excess NaBH₄, very few amount of HfO₂ were detected. On the other hand, the amount of HfO₂ phase is higher in the XRD patterns of stoichiometric HfCl₄-NaBH₄-Mg powders and in those including 100 wt.% of excess NaBH₄. In addition, the Mg₂B₂O₅ phase was determined in the XRD patterns of HfCl₄-NaBH₄-Mg powders having different excess amounts of NaBH₄ after the annealing at 1000 °C.

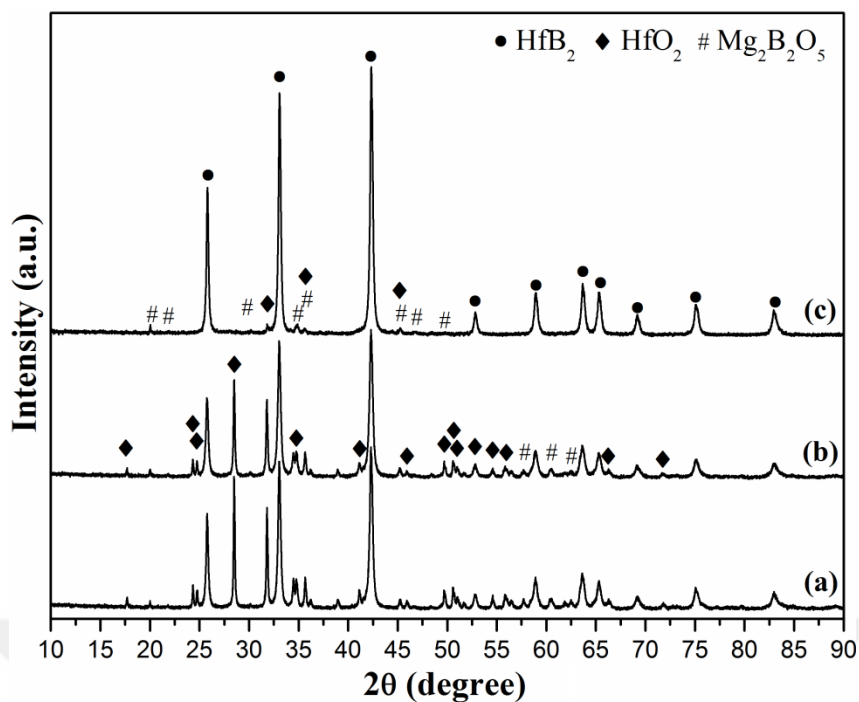


Figure 4.41: XRD patterns of the $\text{HfCl}_4\text{-NaBH}_4\text{-Mg}$ powder blends having different excess amounts of NaBH_4 : (a) 0 wt.%, (b) 100 wt.% and (c) 200 wt.%, after reaction in the autoclave at $500\text{ }^\circ\text{C}$ for 12 h, washing with distilled water and annealing at $1000\text{ }^\circ\text{C}$ for 3 h.

XRD pattern of the $\text{HfCl}_4\text{-NaBH}_4\text{-Mg}$ powders containing 200 wt.% excess NaBH_4 after reaction in the autoclave, washing with distilled water, annealing at $1000\text{ }^\circ\text{C}$ and subsequent HCl leaching are shown in Figure 4.42. The magnesium borate phase

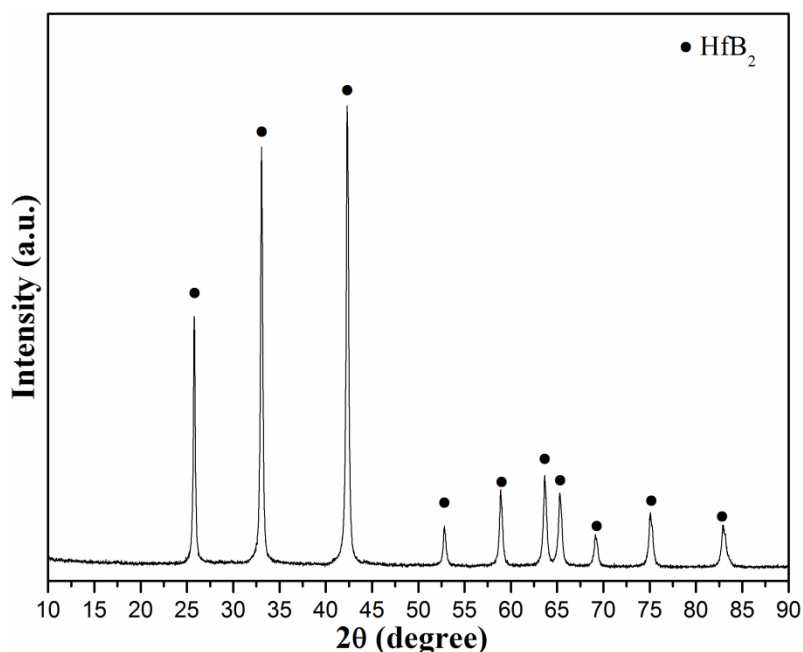


Figure 4.42 : XRD pattern of the $\text{HfCl}_4\text{-NaBH}_4\text{-Mg}$ powder blends having 200 wt.% excess amounts of NaBH_4 after reaction in the autoclave at $500\text{ }^\circ\text{C}$ for 12 h, washing with distilled water, annealing at $1000\text{ }^\circ\text{C}$ for 3 h and leaching with 6 M HCl.

was dissolved out by 6 M HCl leaching. By the elimination of the $\text{Mg}_2\text{B}_2\text{O}_5$ phase, the HfB_2 phase was observed as a single phase in the XRD pattern. Even though slight amount of HfO_2 was detected after heat treatment at 1000 °C, any peaks belonging to the HfO_2 phase was not determined in the XRD patterns of powders after HCl leaching. This situation might be induced by the suppression of HfO_2 phase by the intensive peaks of HfB_2 phase.

An additional heat treatment was conducted at 1700 °C for 6 h to reveal the presence of residual HfO_2 phase or any impurity which could not be detected in the XRD patterns of powders annealed at lower temperatures. The XRD pattern of the HfCl_4 - NaBH_4 -Mg powders containing 200 wt.% excess amount of NaBH_4 after reaction in the autoclave, washing with distilled water, annealing at 1700 °C for 6 h and purification with 6 M HCl is given in Figure 4.43. In the XRD pattern, the HfB_2 phase with very low amount of HfO_2 phase was detected. In addition, any other residual impurity was not determined within the detection limit of XRD, thus it was shown that synthesized HfB_2 powders have high purity.

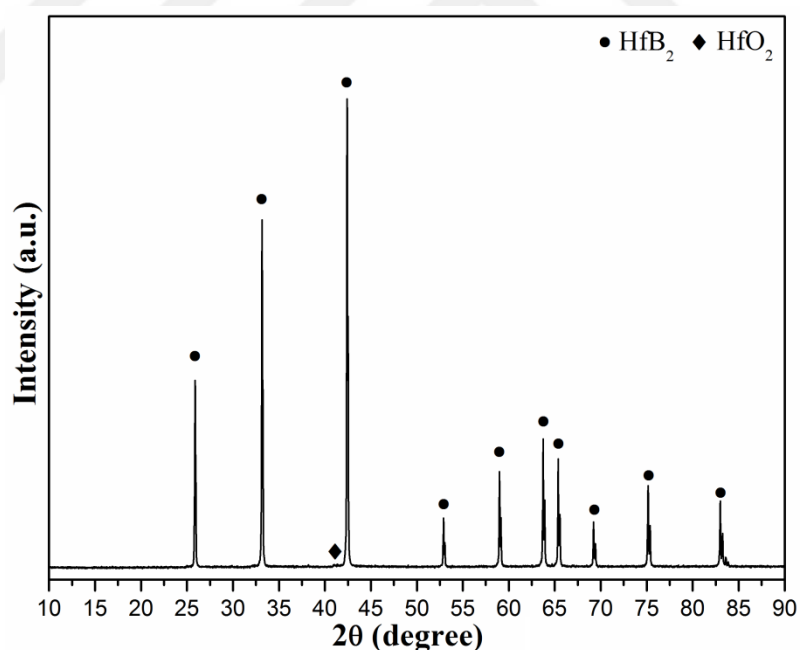


Figure 4.43 : XRD patterns of the HfCl_4 - NaBH_4 -Mg powder blends having 200 wt.% excess amount of NaBH_4 after reaction in the autoclave at 500 °C for 12 h, washing with distilled water, annealing at 1700 °C for 6 h and leaching with 6 M HCl.

The SM images of the HfCl_4 - NaBH_4 -Mg powders having 200 wt.% excess NaBH_4 after reaction in the autoclave at 500 °C for 12 h and subsequent washing with distilled water are shown in Figure 4.44 (a) and (b), respectively. The as-synthesized

powders obtained after the autoclave processing have a lighter gray color and inhomogeneous structure in Figure 4.44 (a). After the rinsing, they have a similar appearance with a darker color. In addition, shiny or lighter particles in Figure 4.44 (a) and (b) might be metal chloride salts or MgO. SM images of the synthesized powders after the annealing at 1000 °C and subsequent purification are illustrated in Figure 4.44 (c) and (d), respectively. The synthesized powders illustrate more uniform appearance after annealing treatment whereas some lighter impurities (lighter particles) are still noticeable. On the other hand, by the elimination of these impurities by related leaching treatments powders gain a pure and homogenous appearance.

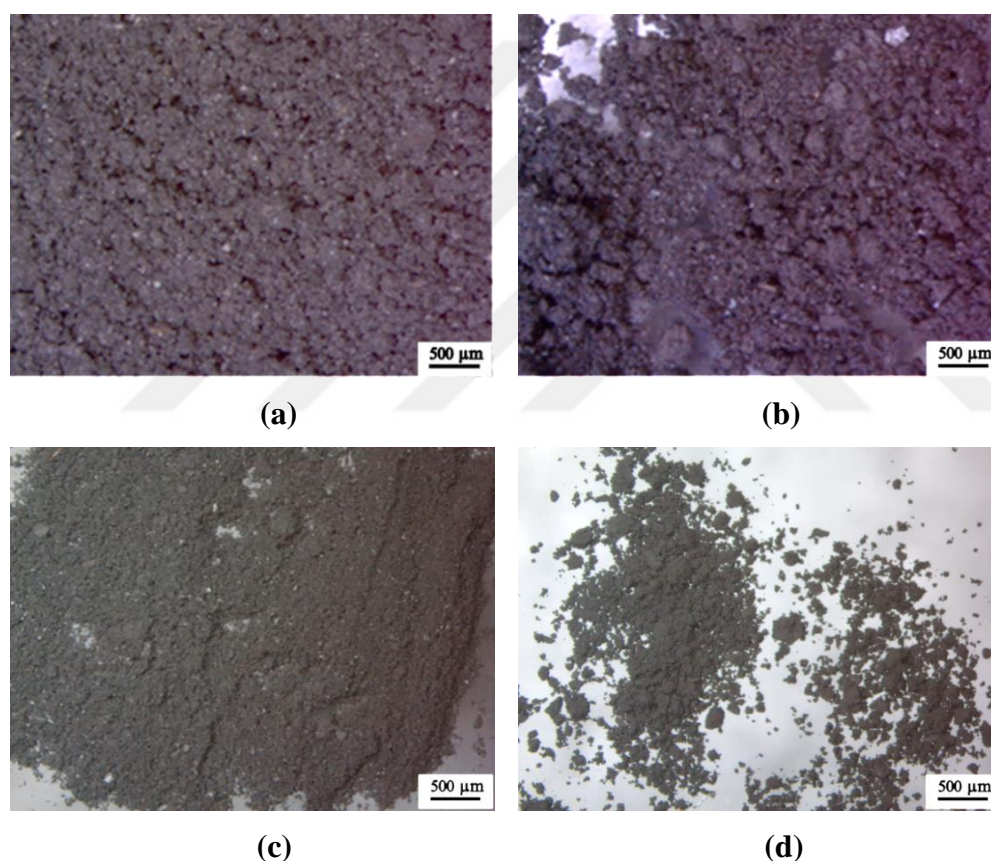


Figure 4.44 : SM images of the $\text{HfCl}_4\text{-NaBH}_4\text{-Mg}$ powder blends having 200 wt.% excess NaBH_4 after: (a) processing in the autoclave at 500 °C for 12 h and subsequent, (b) washing with distilled water, (c) annealing at 1000 °C and (d) leaching with 6 M HCl.

Figure 4.45 (a) and (b) illustrate secondary electron SEM images of the $\text{HfCl}_4\text{-NaBH}_4\text{-Mg}$ powders having 200 wt.% excess NaBH_4 after the autoclave process (at 500 °C for 12 h) and subsequent washing with distilled water at different magnifications. The powders include irregular particles and uneven particle size

distribution after the autoclave synthesis and subsequent water washing. Figure 4.45 (c) presents the results of general EDS analysis of the same powders shown in Figure 4.45 (a) and (b). The EDS analysis demonstrates the presence of Hf, B, O and Mg elements after the autoclave process and washing. The EDS analysis results complies well with XRD findings in Figure 4.38 (c) having HfB_2 , HfO_2 and MgO phases.

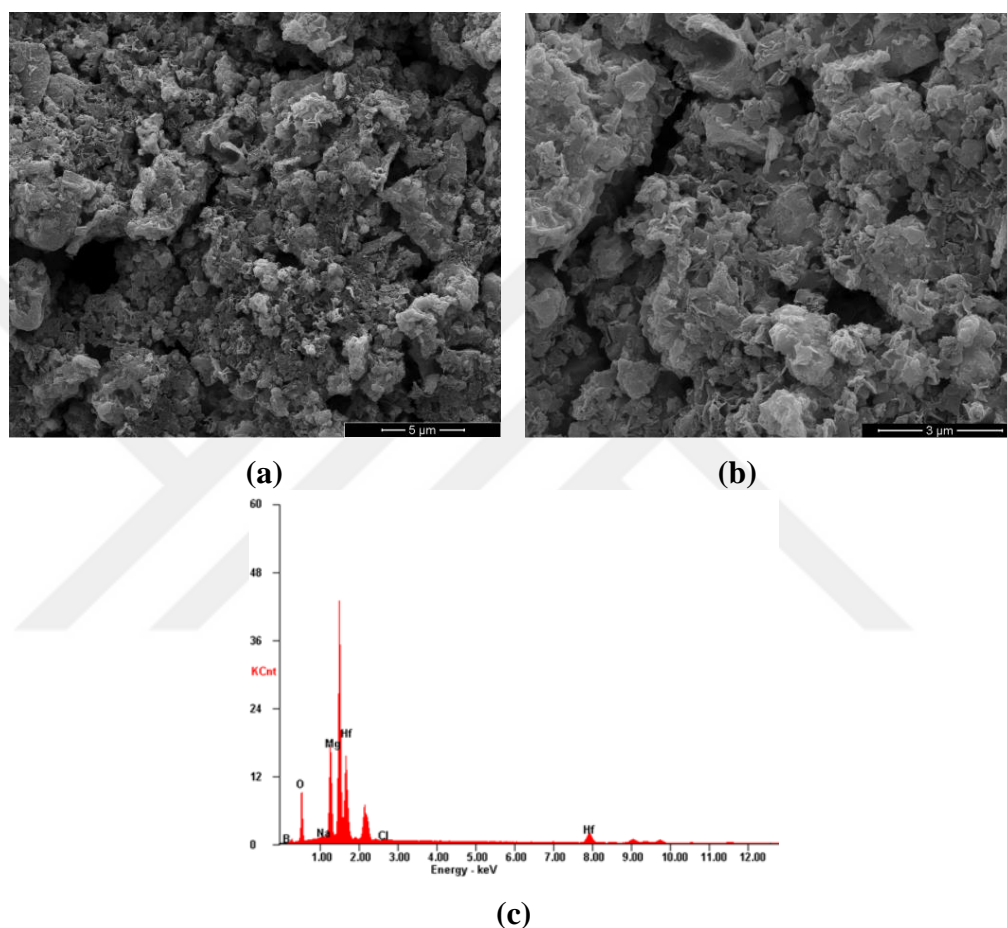


Figure 4.45 : (a)-(b) SEM images of the HfCl_4 - NaBH_4 -Mg powders having 200 wt.% excess NaBH_4 after reaction in the autoclave and washing with distilled water at different magnifications and (c) its corresponding EDS analysis.

Figure 4.46 (a) and (b) illustrate secondary electron SEM images of HfCl_4 - NaBH_4 -Mg powders having 200 wt.% of excess NaBH_4 after the autoclave process (at 500 °C for 12 h), washing with distilled water, annealing at 1000 °C for 3 h and subsequent leaching with 6 M HCl at different magnifications. In the SEM images, powders having rounded-shaped morphology having observable particle size less than 200 nm are monitored. The graph of general EDS analysis which was conducted on the synthesized powders is given in Figure 4.46 (c). The EDS analysis revealed the presence of Hf, B and O elements. The O amount in the powders was

measured as 4.56 wt.% which is attributed to the surface oxides formed during the handling of the powders at laboratory conditions and the presence of very few amount of probable HfO_2 phase. The PSA graph of the powders is illustrated in Figure 4.36 (d) and the average particle size of powders was measured as 145.2 nm which was compatible with the SEM images.

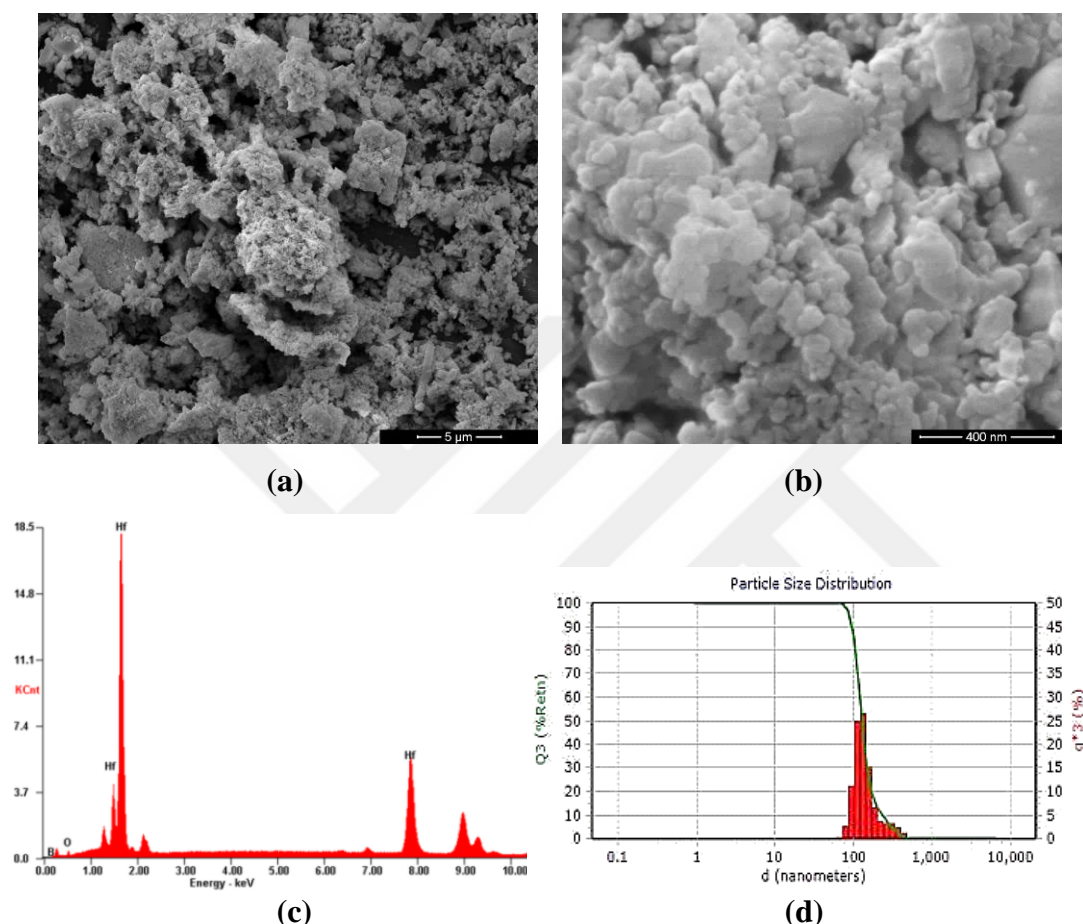


Figure 4.46 : (a)-(b) SEM images of the HfCl_4 - NaBH_4 -Mg powders having 200 wt.% excess NaBH_4 after reaction in the autoclave, washing with distilled water, annealing at 1000 °C for 3 h and leaching with 6 M HCl, corresponding (c) EDS analysis and (d) PSA analysis.

Chen et al. (2004b) prepared nanocrystalline HfB_2 powders in a stainless steel autoclave with quartz tube by the reaction of 5 mmol HfCl_4 and 30 mmol NaBH_4 (200 mol.% excess) at 600 °C. It was stated that both the crystallinity and crystallite size of the HfB_2 increased by increasing temperature over 500 °C. On the other hand, no HfB_2 formation was observed when the temperature was lower than 450 °C. The formation reaction was based on the interaction between the HfCl_4 and BH_3 (formed by the decomposition of NaBH_4 at about 500 °C). It was also stated that the

increasing pressure in the autoclave could be beneficial for the HfB₂ formation (Chen et al., 2004b). The overall reaction was described as in (3.5).

Additionally, ZrB₂ powders were prepared by a similar reaction between ZrCl₄ and NaBH₄ in a stainless steel autoclave with a quartz liner at the temperatures between 450 and 700 °C for 6, 12 and 24 h (Chen et al., 2004c). Similar results were reported with the HfB₂ synthesis mentioned above and it was stated that when reaction time was less than 6 h, the formation reaction was not completed and the crystallinity was relatively poor. However, varying the reaction time between 12 and 24 h did not significantly affect either the crystallinity or the crystallite size.

Chen et al. (2004a) also prepared nanocrystalline TiB₂ powders by the reaction of TiCl₄ (analytical pure liquid, T_B: 136.4 °C) and NaBH₄ at a temperature range of 500-700 °C in an autoclave by a similar method with HfB₂ and ZrB₂ synthesis. The TiB₂ had 20 nm particle size at 600 °C.

Cai et al. (2010) synthesized nanocrystalline Co₂B via a reaction of CoCl₂ with NaBH₄ in the temperature range of 500-600 °C in an autoclave. The formation reaction of Co₂B was given as follows:



According to Cai et al. (2010) when the temperature increases up to 500 °C, NaBH₄ begins to decompose forming BH₃ and NaH gases in relation to reaction (4.1). The BH₃ reacts with CoCl₂, and Co₂B forms together with HCl and H₂ by-products. It was asserted that the high pressure enables the formation of crystalline Co₂B at these low temperatures. The crystallinity or the yield of the Co₂B did not change significantly varying the duration of the reaction between 10 and 24 h. Thus, this was considered as an indication for rapid progress of the reaction between CoCl₂ and NaBH₄, once it is triggered. The average particle size of Co₂B was stated as 80 nm (Cai et al., 2010).

LaB₆ powders were prepared in a stainless steel autoclave (25 ml capacity) starting from LaCl₃.7H₂O, NaBH₄ and Mg at 400 °C (Zhang et al., 2008). It was stated that the reaction temperature and time played an important role on the formation of LaB₆ powders and no LaB₆ formation observed if the temperature below 350 °C, also varying the reaction time between 4 and 12 h did not cause a significant change in

the crystallinity or morphology of the powders. The mean particle size of powders was 30 nm (Zhang et al., 2008).

Feng et al. (2004) proposed a solvothermal route for synthesis of Ni_2B powders. The reaction took place between NiCl_2 and NaBH_4 at 420 °C by using benzene as solvent. Anhydrous NiCl_2 (4.1 g) and NaBH_4 (0.6 g) were placed in a stainless steel autoclave, then benzene was added to the autoclave up to 70% of the total volume and it was kept at 420 °C for 12 h. The sublimation and decomposition point for the NiCl_2 and NaBH_4 were stated as 300 and 400 °C, respectively. Accordingly, a gas-gas reaction between the NiCl_2 and BH_3 occurred and the Ni_2B was obtained. Feng et al. (2004) interpreted the role of NaCl by-product as vital to obtain nanocrystalline Ni_2B powders. It was stated that the NaCl prevented the agglomeration of Ni_2B powders and improved the dispersivity, so it ensured to acquire highly crystalline Ni_2B powders with an average size of 20 nm.

Figure 4.47 (a) through (d) represent the bright field (BF) TEM images and the corresponding selected area diffraction pattern (SADP) taken from the HfCl_4 - NaBH_4 -Mg powders having 200 wt.% of excess NaBH_4 after the autoclave process (at 500 °C for 12 h), washing with distilled water, annealing at 1000 °C for 3 h and subsequent leaching with 6 M HCl. Figure 4.47 (c) is a BF image taken from a general region showing agglomerates comprising polygonal/spheroidal-shaped particles in sizes varying between 50 and 200 nm, which were also determined in the SEM and PSA results. However, there are spheroidal particles having sizes below 300 nm, which are attached to the large agglomerates. The SADP (Figure 4.47 (d)) taken from the region marked in Figure 4.47 (c) reveals the polycrystalline hexagonal HfB_2 phase.

Consequently, the HfB_2 powders were prepared by the autoclave processing of the HfCl_4 - NaBH_4 -Mg powder blends after annealing and purification steps in high purity and nanoscale. The results showed that the usage of excess amount of NaBH_4 is need to obtain single phase HfB_2 powders and elimination of HfO_2 phase.

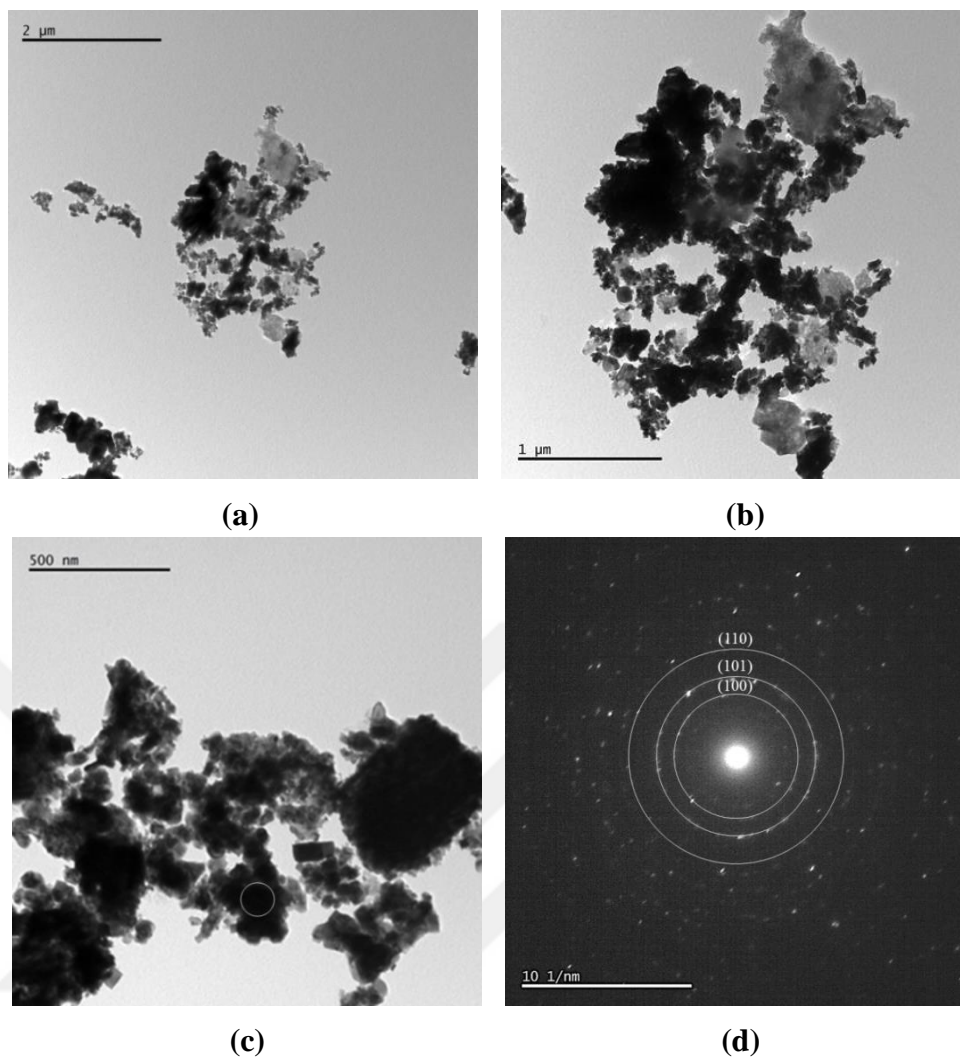


Figure 4.47 : TEM images of the powders milled for 1 h and annealed at 1100 °C: (a), (b) bright-field (BF) images and (c) and (d) its corresponding selected area diffraction pattern (SADP).

4.5 The other powder blends investigated for HfB₂-based powder synthesis by autoclave processing

The HfB₂-based powder synthesis was also investigated by utilizing different powder blends in scope of the autoclave process. For this purpose, four different powder systems which are HfCl₄-H₃BO₃-Mg; HfCl₄-B (in the presence of NaCl-KCl-MgCl₂); HfOCl₂.8H₂O-B₂O₃-Mg and HfCl₄-B-Mg were additionally studied. However, any HfB₂ formation could not be observed in XRD analyses after the autoclave processing of these powder blends.

XRD patterns of the HfCl₄-H₃BO₃-Mg powders having different excess amounts of H₃BO₃ (from stoichiometric to 450 wt.% excess) and 30 wt.% of excess Mg after autoclave process at 500 °C for 12 h, are shown in Figure 4.47 (a)-(d). In the XRD

patterns of obtained powders HfO_2 , MgO , MgCl_2 , $\text{MgCl}_2 \cdot 4\text{H}_2\text{O}$ phases were determined. Additionally, a crust layer showing different appearance from the loose powders and deposited on sidewalls of the autoclave vessel was observed. In the XRD patterns of this layer (in Figure 4.48 (d)), $\text{Mg}_3\text{B}_7\text{O}_{13}\text{Cl}$ phase was determined. This phase might form by the effect of pressure evolved in the autoclave during the reaction for 12 h. On the other hand, any HfB_2 formation was not detected in the XRD patterns of powders after autoclave processing.

Figure 4.49 represents the XRD patterns of the $\text{HfCl}_4\text{-H}_3\text{BO}_3$ (250 wt.% excess)- Mg (30 wt.% excess) powder blends after autoclave process at 500 °C for 12 h and 6 M HCl leaching. The only phase detected in the XRD pattern after the purification was HfO_2 .

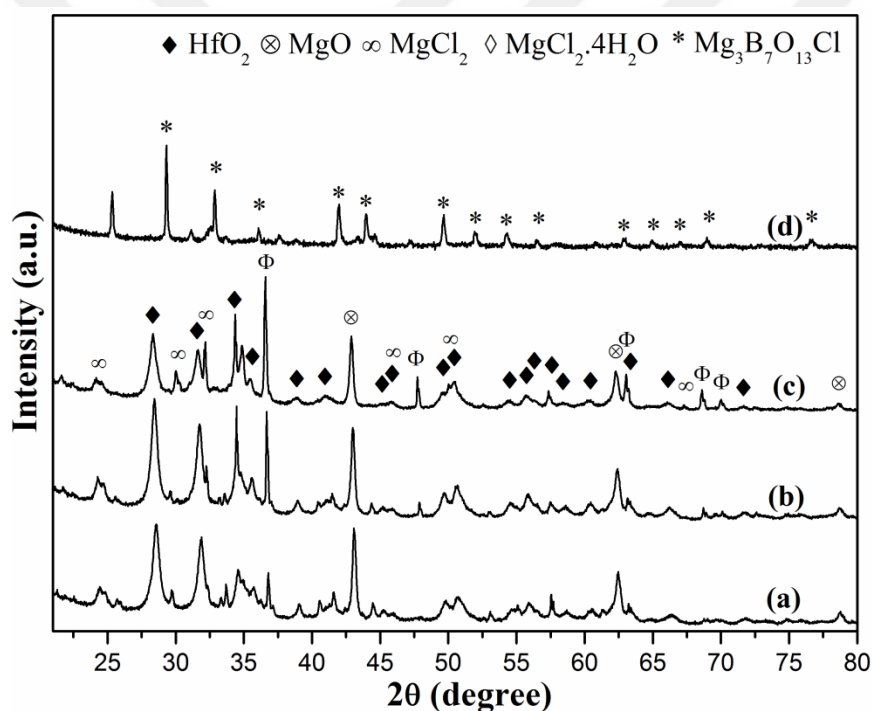


Figure 4.48 : XRD patterns of the $\text{HfCl}_4\text{-H}_3\text{BO}_3\text{-Mg}$ powder blends after autoclave process at 500 °C for 12 h, with different stoichiometries : (a) $\text{HfCl}_4\text{-H}_3\text{BO}_3$ (450 wt.% excess)- Mg (250 wt.% excess), (b) $\text{HfCl}_4\text{-H}_3\text{BO}_3$ (250 wt.% excess)- Mg (30 wt.% excess), (c) $\text{HfCl}_4\text{-H}_3\text{BO}_3\text{-Mg}$ (30 wt.% excess) and (d) $\text{HfCl}_4\text{-H}_3\text{BO}_3$ (450 wt.% excess)- Mg (250 wt.% excess)- crust layer.

Figure 4.50 (a) and (b) show SM images of loose powders and crust layer obtained after the autoclave reaction (at 500 °C for 12 h) of $\text{HfCl}_4\text{-H}_3\text{BO}_3$ (250 wt.% excess)- Mg (30 wt.% excess) powders, respectively. The phase difference between the powder products and crust layer can be easily observed from the SM images in accordance with XRD analyses.

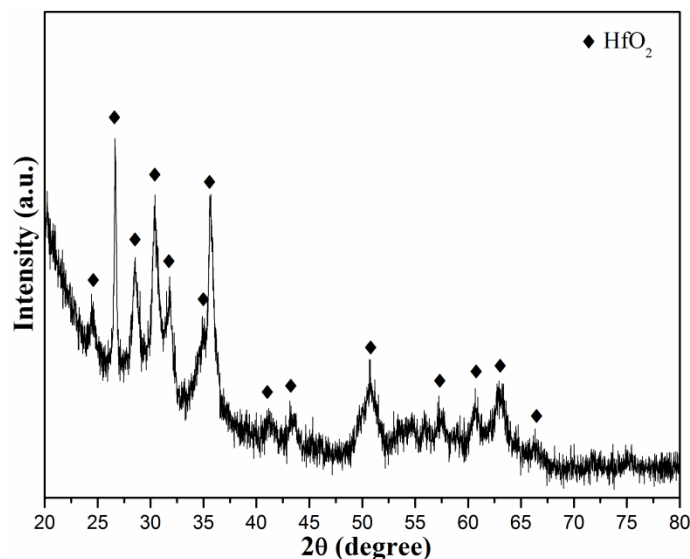


Figure 4.49 : XRD patterns of the HfCl₄-H₃BO₃ (250 wt.% excess)-Mg (30 wt.% excess) blends after the autoclave process at 500 °C for 12 h and 6 M HCl leaching.

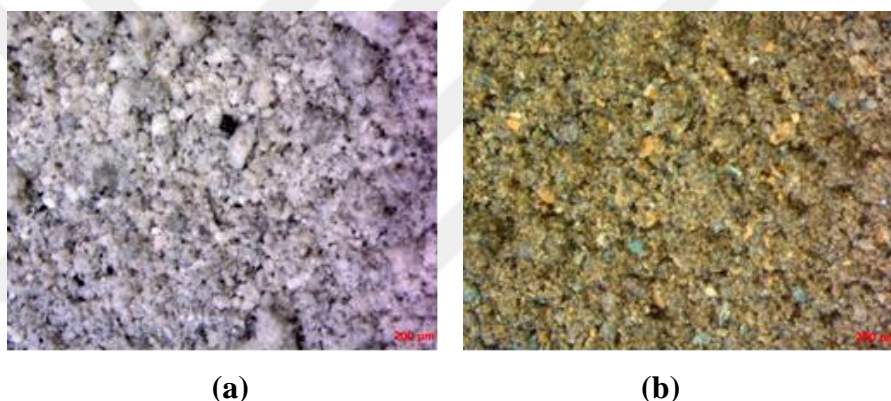


Figure 4.50 : SM images of the HfCl₄-H₃BO₃ (250 wt.% excess)-Mg (30 wt.% excess) blends after the autoclave process at 500 °C for 12 h: (a) powder products and (b) crust layer.

Figure 4.51 represents XRD pattern of the HfCl₄-B powder blends after the autoclave synthesis in presence of NaCl-KCl-MgCl₂ (as an inorganic solvent) at 500 °C for 12 h under starting pressure of 5 bar and washing with distilled water. The NaCl-KCl-MgCl₂ salt mixture (with molar ratios of 20, 20 and 60 wt.%, respectively) has the eutectic temperature of 396 °C (Williams, 2006). The molten salt route was applied during the autoclave synthesis to enhance the diffusion of reactants through a liquid phase (Williams, 2006). After the autoclave process, products were washed with distilled water to remove NaCl, KCl and MgCl₂ salts. The final products were vacuum dried at 105 °C. In the XRD pattern of the products after washing with distilled water, the only detected phase was HfO₂, whereas no HfB₂ formation was observed.

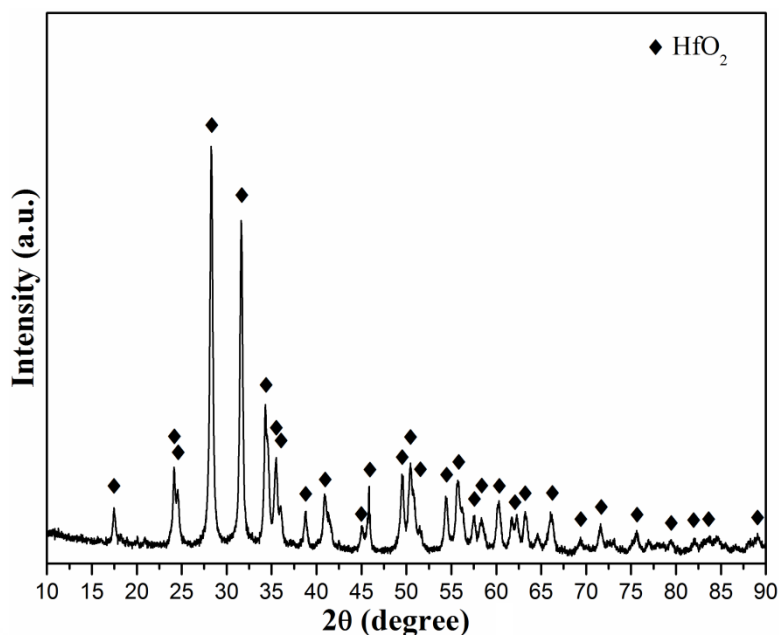


Figure 4.51 : XRD pattern of the HfCl₄-B powder blends (in the presence of NaCl-KCl-MgCl₂ molten salt) after the autoclave process at 500 °C for 12 h under the starting pressure of 5 bar and subsequent water washing with distilled water.

Ma et al. (2003) synthesized CrB nanorods by a reduction-boronation route at 650 °C using a molten salt in an autoclave. CrCl₃ (0.015 mol), amorphous B (0.015 mol), metallic Na (0.045 mol) and 30 g of anhydrous AlCl₃ were placed into a stainless steel autoclave and it was heated to 650 °C for 10 h. Single-crystalline nanorods of CrB₂ with a diameter of 10–30 nm and a maximum length of 1.5 μm were obtained. The growth of CrB₂ nanorods was described as vapor–liquid–solid mechanism. It was reported that the molten AlCl₃ salt provides a liquid medium and accelerates the reaction kinetics by enhancing diffusion. It should be noted that the AlCl₃ has a boiling point of 186 °C. To obtain a molten AlCl₃ medium, a pressure level higher than approximately 20 bar should be provided in the autoclave so as to keep away the AlCl₃ from boiling. Also, the high pressure which was provided by the evaporation of AlCl₃ may benefit the vapor–liquid–solid nucleation for the CrB phase. Hence, the molten salt flux might affect the facilitation of the growth mechanism of the CrB nanorods. It was also stated that the CrB formation could not be achieved at temperatures lower than 600 °C, in contrast when the temperature increased over 700 °C an obvious increase in the diameter of CrB rods was determined. Furthermore, an optimum reaction time was found as 10 h to complete the boronation reaction (Ma et al., 2003).

Figure 4.52 shows the XRD pattern of the HfCl₄-B-Mg powder blends after the autoclave synthesis at 500 °C for 12 h under starting pressure of 5 bar. In the XRD pattern of the obtained powders, HfO₂, MgCl₂, MgCl₂.4H₂O and Mg phases were detected. On the other hand, HfB₂ phase was not observed in the XRD patterns. The XRD analysis showed that no reaction between the HfCl₄, B and Mg took place to form HfB₂ phase.

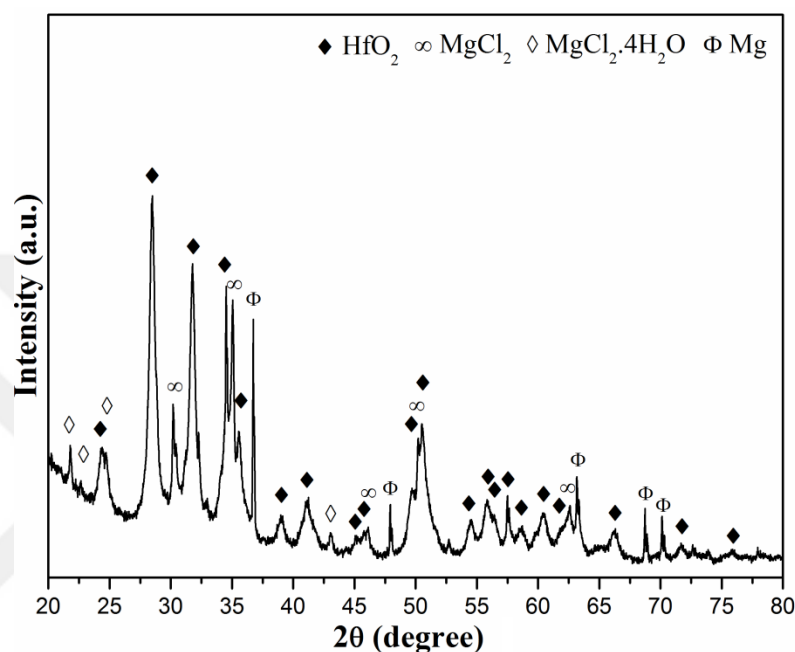


Figure 4.52 : XRD pattern of the HfCl₄-B-Mg powder blends after the autoclave process at 500 °C for 12 h under the starting pressure of 5 bar.

XRD pattern of the HfOCl₂.8H₂O-B₂O₃-Mg powder blends after the autoclave synthesis at 500 °C for 12 h is illustrated in Figure 4.53. In the XRD patterns, HfO₂, MgO, Mg₂(BO₃)₂ and MgCl₂.4H₂O phases were determined. It was considered that the B₂O₃ reacted with MgO during the autoclave process to produce magnesium borate phase (Mg₂(BO₃)₂). On the other hand, the XRD pattern of the products in Figure 4.53 does not indicate any HfB₂ formation after the autoclave reaction for 12 h. It can be asserted that the HfOCl₂.8H₂O phase decomposed to yield HfO₂ at 500 °C, but no reaction between the HfOCl₂.8H₂O, B₂O₃ and Mg took place to yield HfB₂ phase.

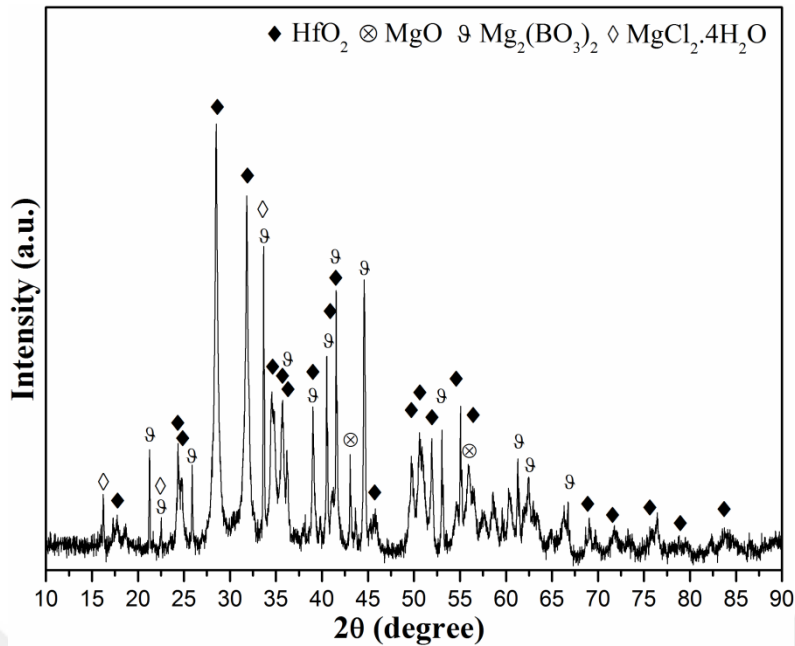


Figure 4.53 : XRD pattern of the $\text{HfOCl}_2 \cdot 8\text{H}_2\text{O}$ - B_2O_3 -Mg powder blends after the autoclave process at 500 °C for 12 h under the starting pressure of 5 bar.

4.6 Consolidation and Bulk Properties of the HfB_2 and HfB_2 - HfO_2 Powders

The synthesized and purified powders were consolidated to investigate the microstructural and mechanical properties of the bulk HfB_2 -based products. Effects of production method, powder composition and sintering technique on the microstructural and mechanical properties of the samples were investigated. The powders obtained by utilizing optimum process parameters and in high qualities were used in the sintering experiments. The samples were selected as to represent the synthesis method or phase composition properties of synthesized powders. Two different sintering techniques as cold pressing/pressureless sintering (PS) (without and with Co addition) and spark plasma sintering (SPS) techniques were applied to consolidation of powders. The PS of powders without Co addition was conducted at 1700 °C for 6 h, whereas pressureless sintering with Co addition was applied at 1500 °C for 5 h. Also, SPS of powders was performed at 1700 and 1900 °C for 15 min under pressure of 60 MPa.

Hafnium diboride powders originated from the borothermal reduction of HfCl_4 powders after milling for 1 h, annealing at 1100 °C for 1 h and purification were consolidated by PS with addition of 2 wt.% Co aid (HfB_2 -B-2CoPS). The HfB_2 - HfO_2 powders originated from mechanochemical processing of the HfCl_4 - B_2O_3 -Mg powders blends by milling for 3 h, HCl leaching, annealing at 1000 °C for 3 h and

final leaching were consolidated by PS with addition of 2 wt.% Co (HfBO-M-2CoPS) and SPS at 1700 °C for 15 min (HfBO-M-SPS). HfB₂-HfO₂ powders originated from autoclave processing of the HfCl₄-B₂O₃-Mg powders after reaction for 12 h and purification were consolidated by PS (without Co addition) (HfBO-A-PS) and SPS (HfBO-A-SPS). HfB₂ powders originated from autoclave processing of the HfCl₄-NaBH₄-Mg powder blends (with 200 wt.% excess amount of NaBH₄) after reaction for 12 h, annealing at 1000 °C for 3 h and purification were consolidated by PS with addition of 2 wt.% Co (HfB-A-2CoPS) and SPS (HfB-A-SPS). The synthesis methods, raw materials and sintering conditions of the consolidated samples are listed in Table 4.5. In addition, the sintered samples were identified with short names and given in the Table 4.5.

Table 4.5 : The raw materials, synthesis method, sintering techniques and names of sintered powders.

Raw material	Method	Sintering Technique	Sintering Conditions	Sample Name
HfCl ₄ -B	Borothermal reduction	PS -2wt.% Co	1500 °C, 5 h	HfB-B-2CoPS
HfCl ₄ -B ₂ O ₃ -Mg	Mechanochemical synt.	PS -2wt.% Co	1500 °C, 5 h	HfBO-M-2CoPS
HfCl ₄ -B ₂ O ₃ -Mg	Mechanochemical synt.	SPS	1700 °C, 15 min, 60 MPa	HfBO-M-SPS
HfCl ₄ -B ₂ O ₃ -Mg	Autoclave process.	PS	1700 °C, 6 h	HfBO-A-PS
HfCl ₄ -B ₂ O ₃ -Mg	Autoclave process.	SPS	1700 °C, 15 min, 60 MPa	HfBO-A-SPS
HfCl ₄ -NaBH ₄ -Mg	Autoclave process.	PS -2wt.% Co	1500 °C, 5 h	HfB-A-2CoPS
HfCl ₄ -NaBH ₄ -Mg	Autoclave process.	SPS	1900 °C, 15 min, 60 MPa	HfB-A-SPS

4.6.1 Microstructural characterization and density of the sintered samples

Figure 4.54 shows the OM images of the sintered hafnium diboride and hafnium diboride-hafnium oxide powders consolidated by different conditions and techniques (PS and SPS). Apparently, it can be seen that the sintered samples have high densification rates and low porosity amount at the lower magnifications obtained by OM. On the other hand, the HfBO-A-PS sample (in Figure 4.54(d)) has a higher porosity amount and lower densification rate compared to spark plasma sintered one (in Figure 4.54(e)). Therefore, Figure 4.54 (d) reveals that the PS technique which were applied at 1700 °C for 7 h (without any sintering aid), was not sufficient to reach a high densification rate, as expected. On the other hand, sintering the same powders by SPS technique provide significant amount of improvement in the

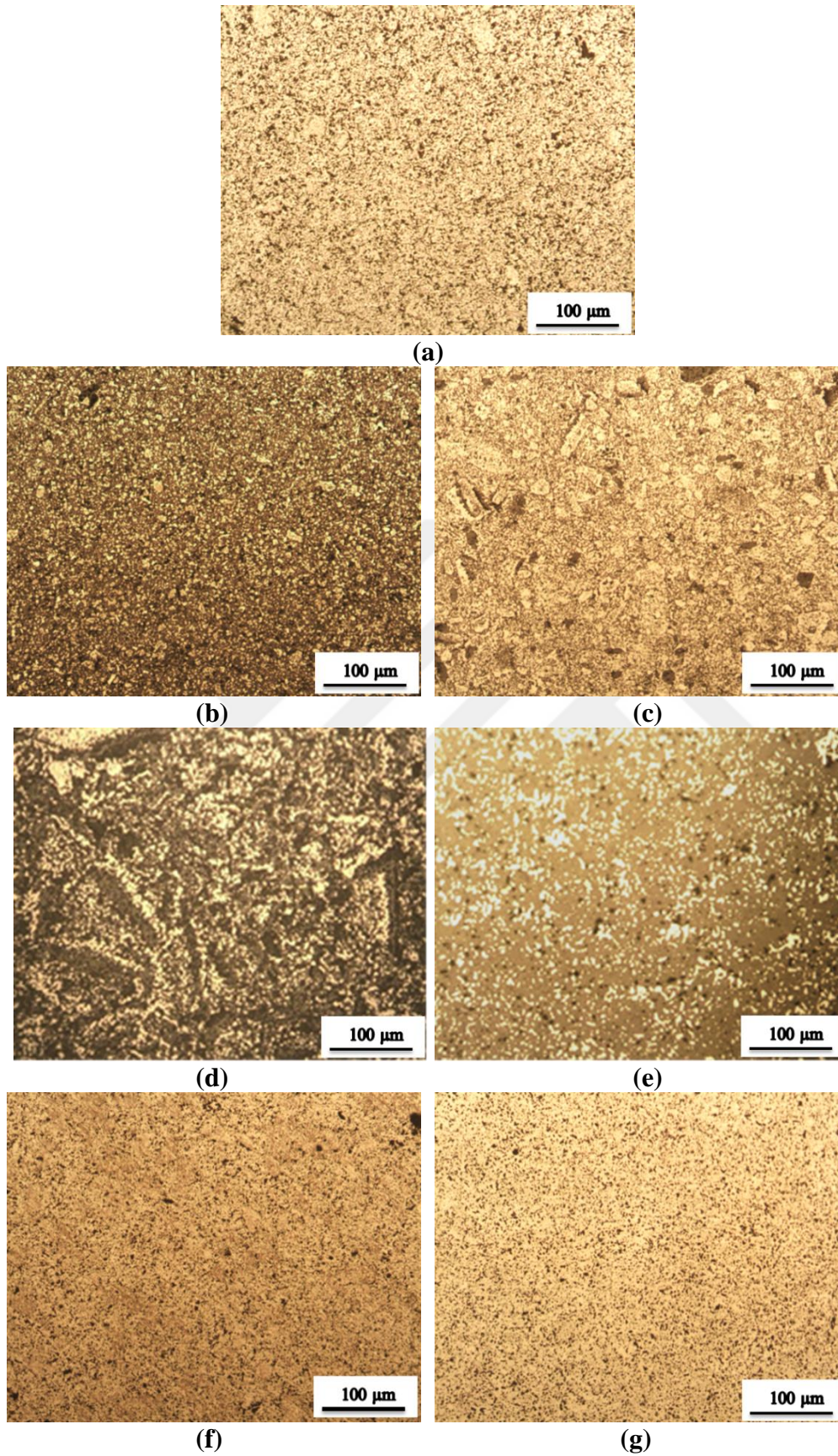


Figure 4.54 : OM images of the sintered samples: (a) HfB-B-2CoPS, (b) HfBO-M-2CoPS, (c) HfBO-M-SPS, (d) HfBO-A-PS, (e) HfBO-A-SPS, (f) HfB-A-2CoPS and (g) HfB-A-SPS.

densification rate and the porosity amount decreased significantly. In addition, by comparison of HfBO-A-PS and HfBO-M-2CoPS samples, it can be said that a comparative improvement in the densification rate was obtained by sintering aid. Moreover, by comparing the OM images of HfB-A-2CoPS and HfB-A-SPS (in Figure 4.54 (f) and (g)), it can be said that the sample sintered by SPS technique (in Figure 4.54 (f)) has higher densification rate and finer microstructure compared to the pressurelessly sintered sample (in Figure 4.54 (g)). Also, a similar situation is observed for the HfBO-M-2CoPS and HfBO-M-SPS samples. Therefore, in general SPS technique provides higher densification over the PS technique with and without 2wt.% Co addition.

Figure 4.55 (a)-(b) illustrate SEM images of some HfB₂ and HfB₂-HfO₂ samples consolidated by PS and SPS techniques. The microstructure of the HfBO-A-PS sample includes high amount porosities and indicates in sufficient densification. However, the HfBO-A-SPS sample has comparatively denser structure with lower porosity amount. Also, the SEM image of the HfB-M-SPS sample sintered with SPS

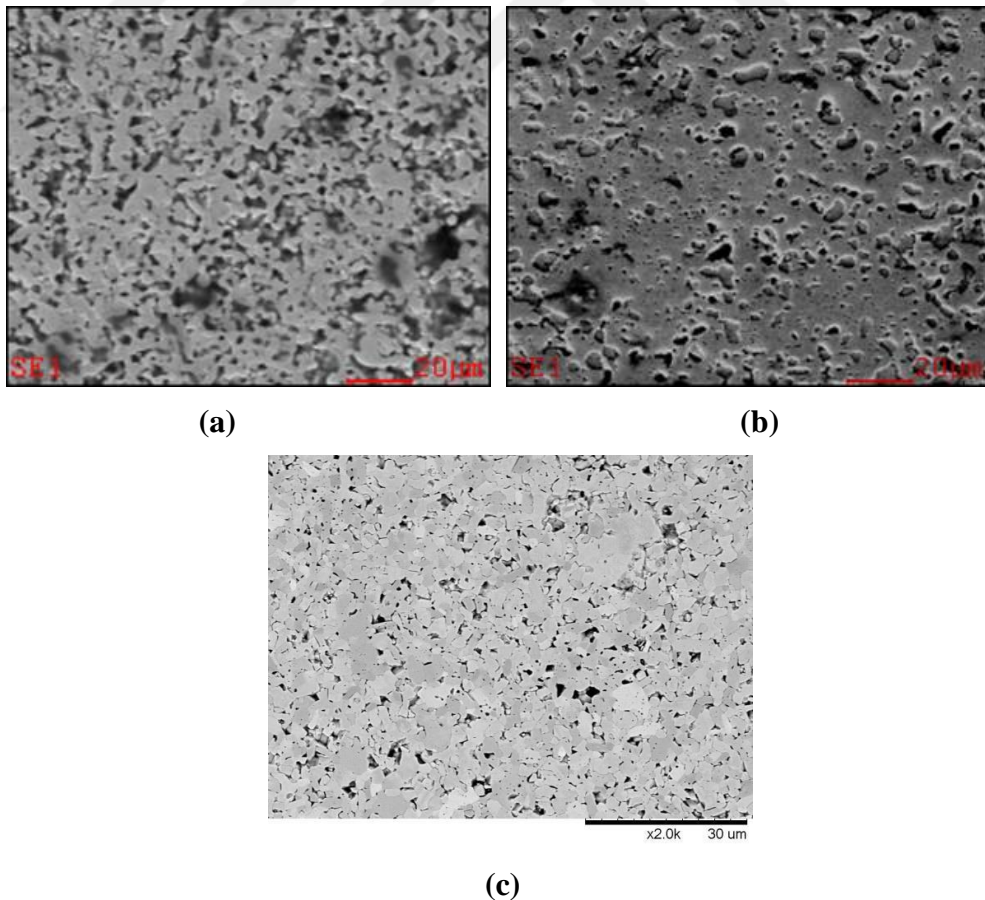


Figure 4.55 : SEM images of the sintered samples: (a) HfBO-A-PS, (b) HfBO-A-SPS and (c) HfB-A-SPS.

at 1900 °C is given in Figure 4.55 (c). The HfB-M-SPS sample represents monolithic HfB₂ structure with some amount of porosity.

The sintered samples were subjected to the XRD analyses for determining the any probable phase transformation and contamination that could occur during sintering process. Figure 4.56 (a)-(e) show the XRD patterns of the HfB-B-2CoPS, HfBO-M-2CoPS, HfBO-M-SPS, HfBO-A-PS, HfBO-A-SPS, HfB-A-2CoPS and HfB-A-SPS samples, respectively. In the XRD patterns of HfB-B-2CoPS, HfB-A-2CoPS and HfB-A-SPS samples, the only detected phase was HfB₂ which conform well to the XRD patterns of corresponding powders in Figures 4.6 and 4.42. In addition, in the XRD patterns of HfBO-M-2CoPS and HfBO-M-SPS samples (Figure 4.56 (b) and (c)), HfO₂ and HfB₂ phases were determined which were also detected in the XRD patterns of related powders in Figure 4.16 (b). Therefore, it can be said that during the sintering experiments of HfB-B-2CoPS, HfBO-M-2CoPS, HfBO-M-SPS, HfB-A-2CoPS and HfB-A-SPS samples, any phase transformation or contamination did not occur. On the other hand, in the XRD patterns of HfBO-A-PS and HfBO-A-SPS samples, the only detected phases were HfB₂ and HfO₂, whereas any contamination or other undesired phases were not determined. The Hf₂Mg₅O₁₂ phase (which was observed in the XRD patterns of powders in Figure 4.32 (d)) was not detected in the XRD patterns of the sintered samples. It was considered that this phase decomposed to HfO₂ and MgO phases by the effect of high temperature during sintering. Nevertheless, the MgO phase could not be determined in the related XRD patterns after sintering (might be because of its low concentration under the detection limit of XRD (which is ~2 wt.% of the sample)). In addition, it was previously determined that the Hf₂Mg₅O₁₂ phase formed during the mechanochemical synthesis of HfB₂-HfO₂ powders was also decomposed by the heat treatment at 1000 °C for 3 h. In another study, decomposition of the Mg₂Zr₅O₁₂ phase (formed in thermally sprayed coatings of ZrO₂- 24 wt.% MgO) to MgO and ZrO₂ phases was observed after hot pressing at 1100 °C (Samad et. al., 2004).

The secondary electron SEM image, and corresponding elemental maps (Hf, B, O and Mg) taken from the HfBO-A-PS sample are shown in Figure 4.57 (a)-(e). The elemental maps of Hf, B and O indicate the presence and uniform distribution of these elements throughout the microstructure. The elemental B map (Figure 4.57 (c))

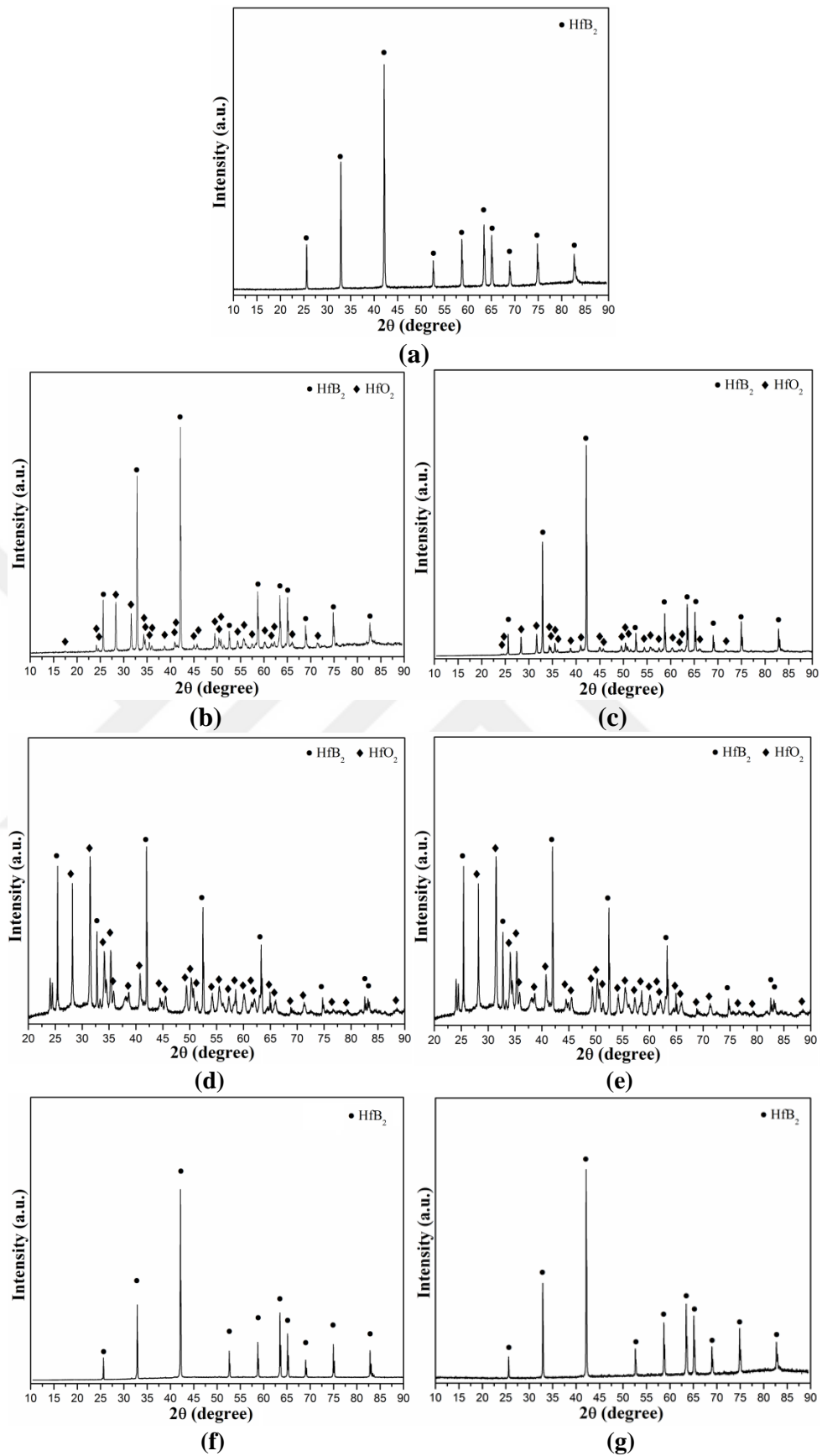


Figure 4.56 : XRD patterns of the sintered samples: (a) HfB-B-2CoPS, (b) HfBO-M-2CoPS, (c) HfBO-M-SPS, (d) HfBO-A-PS, (e) HfBO-A-SPS, (f) HfB-A-2CoPS and (g) HfB-A-SPS.

coincides almost entirely with the Hf elemental map (Figure 4.57 (b)), suggesting the presence of a hafnium diboride phase. The O elemental map seems to fill the gaps where the B elemental map does not coincide with the Hf elemental map. In addition, the existence of Mg is verified by the elemental map of Mg in Figure 4.57 (e), which can be explained by MgO phase evolved by the decomposition of $\text{Mg}_2\text{Hf}_5\text{O}_{12}$ phase. As a result, the formation of $\text{Mg}_2\text{Hf}_5\text{O}_{12}$ phase during the mechanochemical and autoclave processing of the $\text{HfCl}_4\text{-B}_2\text{O}_3\text{-Mg}$ powder blends and its decomposition upon the heating both by annealing and sintering experiments were in accordance with each other. Thus, the elemental mapping in Figures 4.57 confirms the presence of the HfB_2 and HfO_2 phases and the absence of any impurity, as observed in the XRD patterns in Figure 4.56 (a) and (b).

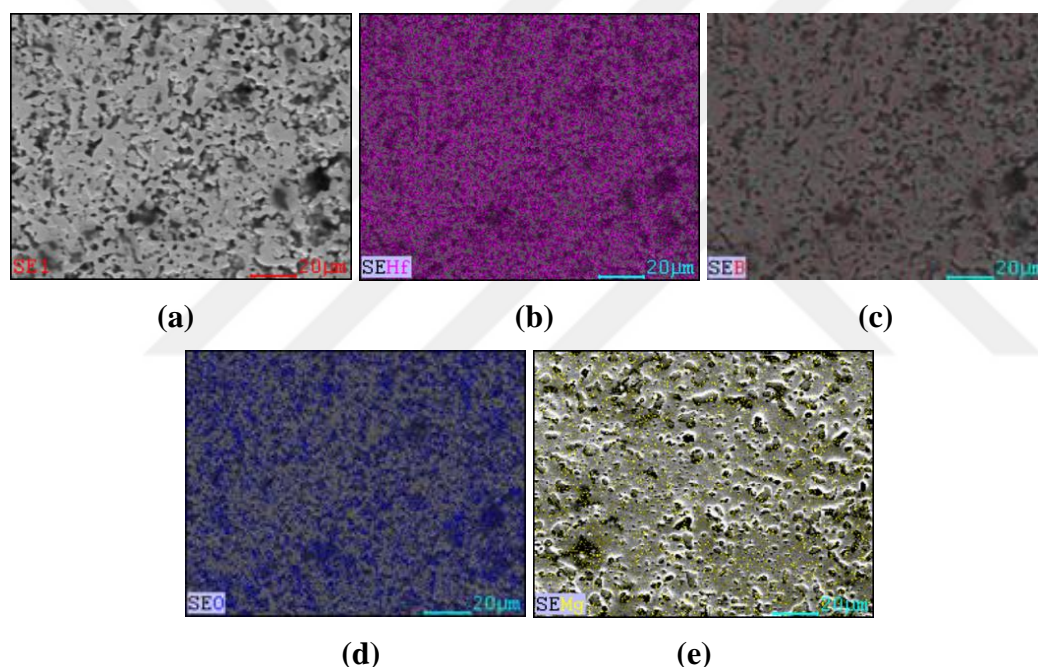


Figure 4.57: SEM/EDX analysis of the HfBO-A-PS sample: (a) SEM image, and elemental maps for (b) Hf, (c) B, (d) O and (e) Mg.

The Archimedes and relative densities of the sintered samples are given in Table 4.6. Theoretical density values of the sintered samples were calculated by taking into account of the amounts of different phases in the synthesized powders, which were determined by the Rietveld method. The HfBO-A-PS sample exhibits the lowest relative density value as 83.22 %, which is lower about 8 % than that of HfBO-A-SPS sample. The lower relative density of HfBO-A-PS sample can be attributed to the insufficient sintering conditions. Zou et al. (2010) reported the relative density of HfB_2 pressurelessly sintered at 2350 °C for 2 h as 85.6%. The

higher relative density value of HfBO-A-PS sample compared to the study of Zou et al. (2010) can be explained by the positive effect of the HfO₂ phase. Li et al. (2009) prepared ZrB₂-ZrO₂ ceramics with ZrO₂ content varied from 15 to 30 vol.% by hot pressing at 1850 °C for 60 min under a uniaxial pressure of 30 MPa. It was stated that higher content of ZrO₂ was apparently beneficial for the densification of ZrB₂-ZrO₂ ceramics. On the other hand, relative density value of the HfBO-A-SPS sample showed significant amount of increase. Thus, better results were obtained by SPS technique than PS in regard of sintering rates of HfB₂-HfO₂ powders. The relative density values of HfBO-A-PS and HfBO-A-SPS samples conform well to the microstructures presented in the SEM images of the samples given in Figure 4.55 (a) and (b).

Table 4.6: Density values of the sintered samples.

Sample Name	Theoretical Density (g/cm³)	Archimedes Density (g/cm³)	Relative Density (%)
HfB-B-2CoPS	11.16	10.05	90.05
HfBO-M-2CoPS	10.64	9.77	91.82
HfBO-M-SPS	10.55	10.00	93.79
HfBO-A-PS	10.89	9.28	83.22
HfBO-A-SPS	10.89	9.93	91.11
HfB-A-2CoPS	11.16	10.06	90.14
HfB-A-SPS	11.21	10.47	94.18

The relative density of the HfBO-M-2CoPS sample was determined as 91.82%, whereas the density of the HfBO-M-SPS sample was 93.79%. The SPS technique provided an improvement in the densification rate of HfB₂-HfO₂ powders synthesized by mechanochemical reaction. In addition, a comparison between the density values of HfBO-M-SPS and HfBO-A-SPS samples can be made, which were determined as 93.79% and 91.11%, respectively. The main differences of HfBO-M-SPS and HfBO-A-SPS samples are their synthesis methods and the existence of probable MgO phase. The density difference of about 2.7% can be due to the effect of MgO phase and different morphologies and particle sizes of sintered powders. In addition, the relative density values of HfB-A-2CoPS and HfB-A-SPS samples show a similar trend according to the sintering technique. The HfB₂ powders originated from autoclave processing of the HfCl₄-NaBH₄-Mg powders reached

a higher densification rate by SPS at 1900 °C for 15 min, under pressure of 60 MPa. Moreover, the HfB-A-SPS sample shows the highest relative density value of 94.18%. Anselmi-Tamburini et al. (2006) sintered commercial HfB₂ powders (with grain size of 44 μm) by SPS at 1900 °C for 10 min and the relative density was reported as 86.8%. The higher densification rate of HfB₂ powders obtained in this study is due to significant difference in regard of the average particle size of sintered powders. Accordingly, it can be said that the relatively low particle size of synthesized powders (145 nm) and close contact points between particles (observed in the SEM investigations) have a positive effect on the sintering rate. The HfB₂ powders originated from borothermal reduction of HfCl₄ powders reached a relative density of 90.05% by the PS with addition of 2 wt. % of Co (HfB-B- 2CoPS). The relative density of HfB-A-2CoPS sample originated from autoclave processing of the HfCl₄-NaBH₄-Mg powders was determined as 90.14%. Thus, the relative densities of HfB₂ powders obtained via different synthesis methods illustrate close values after pressureless sintering with Co addition. As a result, it can be said that the pressureless sintering conditions (at 1700 °C for 6 h) without sintering addition is not adequate for sintering of hafnium diboride-based powders. In addition, pressureless sintering with 2 wt.% Co addition (at 1500 °C for 5 h) provided an amount of increase where as it was not sufficient to achieve a full density. Reaching high density values for HfB₂ without any sintering aid is very difficult due to their very high melting point and low grain boundary and volume diffusion rates (Fahrenholtz et al., 2007; Telle et al., 2000; Zou et al., 2010).

The Vickers microhardness values of the sintered products are given in Table 4.7. The HfBO-A-PS sample has the lowest hardness value (8.25 GPa) among the samples due to the insufficient densification rate, as expected. However, the hardness value of HfBO-A-PS sample reached to 14.60 GPa by the spark plasma sintering technique as a result of improvement in the densification. Sciti et al. (2007) prepared monolithic HfB₂ ceramics by SPS at 2200 °C for 5 min under 65 MPa with the relative density and hardness value of 80% and 7.0 GPa, respectively. In the same study, relative density and hardness value of HfB₂ include 3 vol.% MoSi₂, 3-4 vol.% HfO₂ and spark plasma sintered at 1750 °C for 3 min under 100 MPa were 100% and 22 GPa, respectively (Sciti et al., 2007). The hardness values of HfBO-M-2CoPS and HfBO-M-SPS samples were respectively determined as 14.72 and 19.45 GPa.

The hardness values of HfB₂-HfO₂ powders originated from the mechanochemical processing of HfCl₄-B₂O₃-Mg powder blends increased by SPS technique. Thus, the hardness values of samples are in accordance with the densification rates. The hardness of the HfB-B-2CoPS sample was measured as 14.91 GPa. Also, a comparison can be made between the hardness values of the HfBO-M-SPS and the HfBO-A-SPS samples. The different hardness values of HfBO-M-SPS and HfBO-A-SPS samples originated respectively from the mechanochemical and autoclave synthesis of HfB₂-HfO₂ powders can be explained by the amount and presence of different phases, as well as dissimilarities in particle size and morphologies of powders. In addition, the highest hardness value was observed for the HfB-A-SPS by means of SPS technique and higher sintering temperature of 1900 °C. Thus, the microhardness values of the sintered samples were in the same trend with their density values given in Table 4.6.

Table 4.7 : Hardness values of the sintered samples.

Sample Name	HV_{0.2} (GPa)
HfB-B-2CoPS	14.91±0.88
HfBO-M-2CoPS	14.72±1.49
HfBO-M-SPS	18.45±1.55
HfBO-A-PS	8.25±1.49
HfBO-A-SPS	14.60±1.37
HfB-A-2CoPS	14.85±1.03
HfB-A-SPS	20.99±0.98

Wear volume loss and relative wear resistance values of the selected HfB₂ and HfB₂-HfO₂ samples are presented in Table 4.8. The HfBO-A-PS sample has the highest wear volume loss value; the most likely cause is the insufficient densification rate and it was taken as a reference for calculating the relative wear resistance values of other samples. Relative wear resistances were calculated with acceptance of the relative wear resistance of the HfBO-A-PS as 1, and dividing the wear volume loss values of the HfBO-A-PS sample to those of the other samples. As seen from the Table 4.8, PS and SPS samples of HfB₂-HfO₂ powders originated from autoclave process have the wear volume loss of 13.6x10⁻³ and 5.53x10⁻³ mm³, respectively. Thus, the SPS technique enhanced the relative wear resistance of the HfB₂-HfO₂ composite by 2.5 times. Additionally, the relative wear resistance of the HfB₂-HfO₂

composites (HfBO-M-2CoPS and HfBO-M-SPS) originated from mechanochemical processing of the HfCl₄-B₂O₃-Mg powder blends showed an amount of increase by SPS technique along with the increase in the density and hardness values. In addition, the HfB-A-SPS sample showed the lowest wear volume loss value. Therefore, the microhardness and wear volume loss values of the sintered samples conform well to their relative density values.

Table 4.8: Wear volume loss and relative wear resistance of the sintered samples.

Sample Name	Wear Volume Loss ($\times 10^{-3} \text{ mm}^3$)	Relative Wear Resistance
HfBO-M-2CoPS	7.39	1.84
HfBO-M-SPS	4.30	3.16
HfBO-A-PS	13.60	1
HfBO-A-SPS	5.53	2.46
HfB-A-SPS	1.85	7.35

There is limited number of study on the wear properties of bulk hafnium diboride ceramics in the open literature. However, some studies on wear characteristics of hafnium diboride thin films deposited on different substrates were reported (Chowdhury et al., 2015; Tayebi et al., 2012). Also, there are only few studies on the wear properties of the sintered metal borides (Ağaoğulları, 2014; Balcı, 2015; Chakraborty et al., 2014). As a comparison for wear results, bulk LaB₆ and SmB₆ samples (with relative density of 96.80 and 96.84 %) prepared by cold press and PS at 1700 °C for 5 h respectively showed wear volume loss of 11.7×10^{-3} and $19.3 \times 10^{-3} \text{ mm}^3$ as a result of sliding wear test conducted under an applied force of 4 N (Ağaoğulları, 2014). Balcı (2015) reported the wear volume loss values of NbB₂ (sintered by SPS, having relative density of 83.75%) as $11.5 \times 10^{-4} \text{ mm}^3$. In addition, ZrB₂-TiB₂ composites with TiB₂ content up to 30 wt.% (sintered via hot pressing at 2200 °C for 2 h under the pressure of 50 MPa, with relative density of 98.4%) showed wear volume loss values ranging between 10.8×10^{-4} and $0.31 \times 10^{-4} \text{ mm}^3$ (Chakraborty et al., 2014).

Figure 4.58 (a) and (b) show SEM images of wear tracks from the HfBO-A-PS and the HfBO-A-SPS samples, respectively. The wear track profiles of the HfBO-A-PS and the HfBO-A-SPS samples are shown in Figure 4.58 (c) with the aim of making representative evaluation between them. The high amount of

porosities in the microstructure of PS sample probably leads to severe material loss during sliding. The PS sample exhibits some micro-grooves along the sliding direction. On the other hand, the surface of SPS sample has a smoother appearance which can be explained by the higher resistance against material removal from the surface by means of its higher density and hardness values.

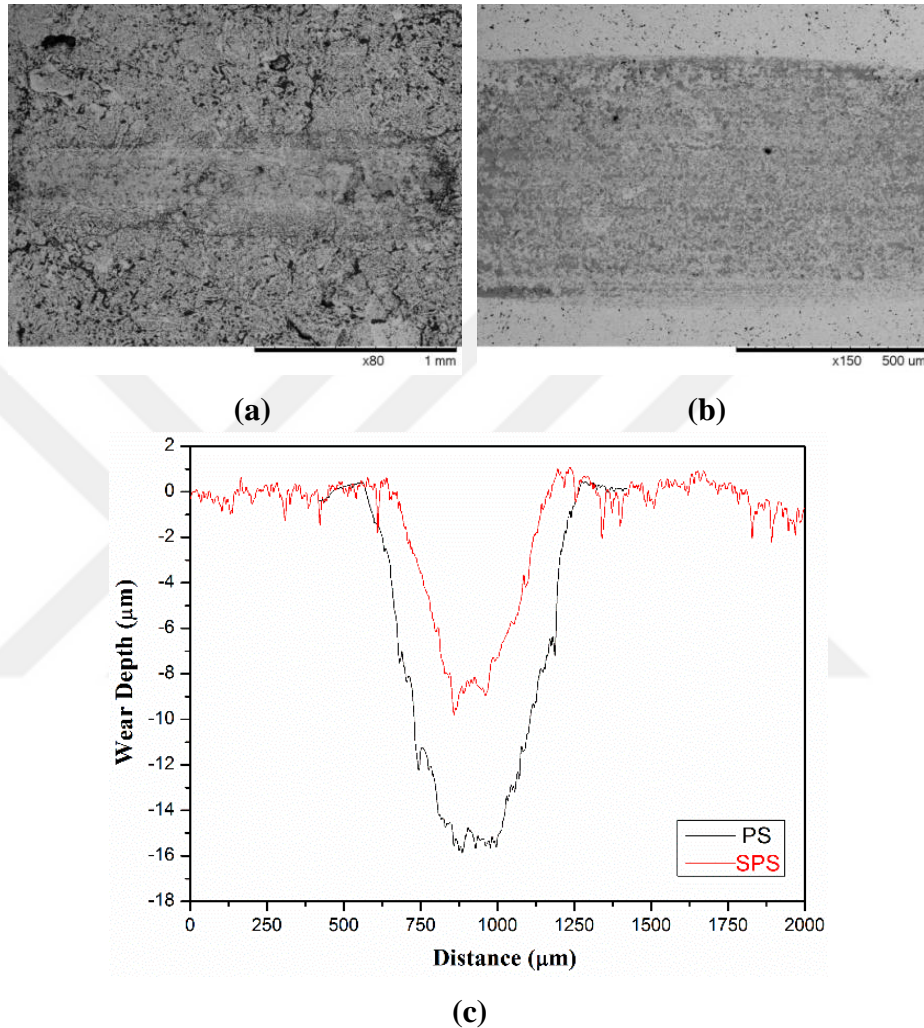


Figure 4.58 : Worn surface SEM images of the sintered samples: a) HfBO-A-PS, b) HfBO-A-SPS and (c) their corresponding wear profiles.

Figure 4.59 illustrates the mean friction coefficient values of the HfBO-M-2CoPS, HfBO-M-SPS and HfB-A-SPS samples. Friction coefficient of the sintered HfBO-M-2CoPS sample sliding against alumina counterface is about 0.54 and a slightly higher friction coefficient value of about 0.60 is observed for the SPS sample (HfBO-M-SPS). In addition, the HfB-A-SPS sample has the highest friction coefficient value among the samples which is about 0.64. Chakraborty et al. (2014) determined the friction coefficients of ZrB_2 - TiB_2 (with TiB_2 up to 30 wt.%) samples

between in the range of 0.31 to 0.532. Additionally, the friction coefficient values of vanadium and niobium borides sintered by SPS were reported as 0.49 and 0.53, respectively (Balci, 2015). Therefore, it can be said that the friction values of the HfBO-M-2CoPS, HfBO-M-SPS and HfB-A-SPS samples were close to reported values in the literature and compatible with each other.

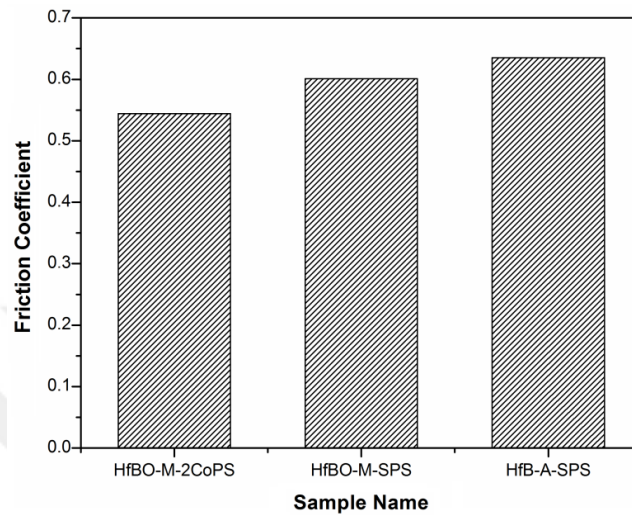


Figure 4.59 : Mean friction coefficients of the sintered hafnium diboride-based samples.

5. CONCLUSIONS

In this dissertation, it was aimed to synthesis high purity hafnium diboride-based powders through economical raw materials and methods. In this thesis, hafnium diboride-based powders were synthesized by three different methods and the synthesized powders were consolidated by two different sintering techniques. The mechanically activated borothermal reduction at reduced temperatures (compared to high temperature methods), mechanochemical route as a room temperature solid-state synthesis method and low temperature autoclave synthesis were applied. These methods utilized to synthesis these high temperature ceramic powders as alternative ways to conventional methods and they provides several advantages such as usage of economical raw materials, utilization of simple equipment, reduction in reaction temperature and obtaining fine particle sizes. The detailed characterization investigations were conducted on the synthesized powders and sintered products.

The results of this thesis can be summarized mainly in five sections including the mechanically activated borothermal synthesis, mechanochemical synthesis, autoclave processing of the two different powder system ($\text{HfCl}_4\text{-B}_2\text{O}_3\text{-Mg}$ and $\text{HfCl}_4\text{-NaBH}_4\text{-Mg}$) blends and consolidation of synthesized powders.

In the mechanically activated borothermal reduction method, HfB_2 powders were successfully synthesized from the $\text{HfCl}_4\text{-B}$ powder blends by a combined method of mechanical activation and annealing processes. Based on the results obtained in this study, the following conclusions can be drawn:

- The thermodynamical predictions pointed out that the reaction between HfCl_4 and amorphous B could be completed at the temperature range of 1100-1200 °C by keeping the formation of gaseous hafnium chloride by-products at a possible minimum level. The experimental assessment of the formation mechanism of HfB_2 indicated the borothermal reduction of HfO_2 phase formed by the decomposition of hafnium oxide halides.

- It was determined that the boron amount in the starting blends plays an important role on the formation of HfO₂ phase. By the utilization of less than 20 wt.% excess amounts of boron, HfO₂ was detected as a secondary phase together with the major HfB₂ phase.
- Washing with distilled water and leaching with HCl were applied to the annealed powders for the elimination of undesired B₂O₃ phase and Fe impurity. Although the XRD patterns of the mechanically activated and annealed powders, with 20 wt.% excess boron, did not include any peaks belong to the B₂O₃ phase, the FTIR and AAS analyses proved the existence of this phase.
- The EDS analysis results obtained from randomly selected points indicated the residual boron phase in the synthesized powders with 20 wt.% excess boron content.
- The HfB₂ powders showed faceted rod-like morphology after purification. The presence of liquid B₂O₃ phase during the annealing step might enhance the diffusion mechanism and the nucleation at solid-liquid interface and promote the formation of rod-like morphology.
- The average particle size of the obtained powders was 391 nm. The oxygen content of the synthesized powders was about 3.5 wt.% which was attributed to the surface oxidation.

During the mechanochemical synthesis of hafnium diboride-based powders, the HfCl₄-B₂O₃-Mg powder blends were utilized and amorphous B was alternatively used in order to investigate the effect of different boron sources. The results of this section can be summarized as:

- The mechanochemical reaction between the HfCl₄-B₂O₃-Mg took place after milling for 15 min. However, the mechanochemical synthesis reaction reached a steady state condition after milling for 1 h and the additional milling durations did not cause a significant difference on the amount and distribution of obtained phases.
- The MgCl₂ (having different hydration levels) and MgO by-products and probable Fe impurity were removed by washing the powders with distilled water and HCl leaching treatments.

- HfB_2 , HfO_2 and $\text{Mg}_2\text{Hf}_5\text{O}_{12}$ phases were determined in the XRD patterns of synthesized powders after milling from 1 h to 5h and purification treatments.
- The $\text{Mg}_2\text{Hf}_5\text{O}_{12}$ phase decomposed to HfO_2 and MgO phases during the annealing of synthesized powders (via 3 h of milling and purification treatments) at 1000 °C for 3 h.
- After the annealing and final leaching with HCl , the HfB_2 - HfO_2 ceramic powders were obtained. The synthesized powders included 57.2 wt.% HfB_2 and 52.8 wt.% HfO_2 according to the semi-quantitative Rietveld method.
- The synthesized HfB_2 - HfO_2 powders had average particle sizes between 129.5 and 151.4 nm according to the milling duration and rounded or cornered-shaped morphologies.
- TEM images showed particles having rounded or cornered-shaped (like cubes) morphology and particle size about 200 nm and below. TEM analyses proved the existence of HfB_2 and HfO_2 phases.
- In addition, amorphous B was utilized as alternative boron source in the mechanochemical synthesis method to investigate the effect of different boron sources on formed phases. In the XRD patterns of the HfCl_4 -B-Mg blends having 50 wt.% excess amorphous B, the only determined phase was HfB_2 after 1 h of milling and related purification treatments. The heat treatment of obtained powders at 1100 °C for 1 h did not cause any change in the determined phases.

In the autoclave processing of the HfCl_4 - B_2O_3 -Mg powders, the HfB_2 - HfO ceramic powders were synthesized at relatively low temperatures. The following results can be summarized for this section:

- The HfB_2 -based ceramic powders were synthesized by means of a short time mechanical activation and a chemical reaction in the autoclave at 500 °C.
- The effects of mechanical activation and the duration of autoclave reaction were investigated as important process parameters. The formation yield of HfB_2 phase increased with increasing reaction duration from 6 to 12 h. The optimum results were obtained with mechanical activation and 12 h of autoclave reaction.
- The undesired by-products such as MgO and MgCl_2 were removed by water and acid leaching treatments and pure powders were obtained.

- In the XRD patterns of synthesized powders, the $\text{Mg}_2\text{Hf}_5\text{O}_{12}$ phase was detected, which was also determined throughout the mechanochemical processing of the $\text{HfCl}_4\text{-B}_2\text{O}_3\text{-Mg}$ blends.
- The synthesized powders showed spherical morphology with larger agglomerates and the average particle size of the resultant $\text{HfB}_2\text{-HfO}_2$ powders was determined as 189.7 nm.

In the autoclave processing of $\text{HfCl}_4\text{-NaBH}_4\text{-Mg}$ powder blends, the HfB_2 powders were successfully synthesized at low temperature. The obtained results can be summarized as:

- In the XRD patterns of stoichiometric $\text{HfCl}_4\text{-NaBH}_4\text{-Mg}$ powders and those having different excess amounts of NaBH_4 after autoclave processing and washing with distilled water, the HfB_2 , HfO_2 and magnesium borate phases were determined.
- The NaCl , MgCl_2 (with different hydration levels) and magnesium borate by-products were removed by washing with distilled water and HCl leaching throughout the different stages of the process.
- Additional heat treatments at higher temperatures were applied to synthesized powders. After the annealing at 1000 °C for 3 h and 1700 °C for 6 h and subsequent HCl leaching, single-phase high purity HfB_2 powders were obtained.
- The NaBH_4 amount was determined as an important factor to obtain single phase HfB_2 powders and prevent the formation HfO_2 as a secondary phase.
- The HfB_2 powders had rounded-shaped morphology and average particle size of 145.2 nm after annealing at 1000 °C and purification. The oxygen content of the synthesized powders was about 4.56 wt.% which was attributed to the surface oxidation and probable HfO_2 phase.

The selected HfB_2 and $\text{HfB}_2\text{-HfO}_2$ powders obtained with optimum process conditions throughout the different powder synthesis methods were consolidated by two different sintering techniques which were pressureless sintering and spark plasma sintering. The results of sintering experiments can be summarized as follows:

- Any contamination from consolidation processes was not detected in the XRD analyses of sintered samples. However, the $\text{Mg}_2\text{Hf}_5\text{O}_{12}$ phase observed after the autoclave processing of the $\text{HfCl}_4\text{-B}_2\text{O}_3\text{-Mg}$ blends was decomposed during the consolidation of powders both by PS and SPS.

- The relative density values of HfB₂-HfO₂ powders originated from autoclave processing of the HfCl₄-B₂O₃-Mg blends reached to 83.22 and 91.11% with PS and SPS, and their microhardness values were 8.25±1.49 and 14.60±1.37 GPa, respectively. The insufficient densification rate of PS sample was due to the very high melting point and low grain boundary and volume diffusion rates of these ceramics. A high amount of porosity was observed in microstructure of PS sample in OM and SEM investigations.
- The HfB₂-HfO₂ powders originated from mechanochemical processing of the HfCl₄-B₂O₃-Mg blends reached to 91.82% densification when consolidated by PS with 2 wt.% Co addition. The relative density of the same powders was reached to 93.79% by SPS. The microhardness values of PS and SPS sample were 14.72±1.49 and 18.45±1.55 GPa, respectively.
- The relative density of HfB₂ sample originated from mechanically activated borothermal method after PS with 2 wt.% Co addition was 90.05% and the microhardness was 14.91±0.88 HV. The HfB₂ powders obtained by autoclave processing of the HfCl₄-NaBH₄-Mg blends reached to relative density and hardness of 90.14% and 14.85±1.03 GPa with the same technique. Thus, the densification rates of HfB₂ powders originated from different synthesis methods were in a similar level.
- The highest relative density and hardness value of HfB₂ powders (originated from autoclave processing of the HfCl₄-NaBH₄-Mg blends) were obtained by SPS technique (at 1900 °C for 15 min) as 94.18% and 20.99±0.98 GPa, by means of advantages of this special method and higher sintering temperature.
- The higher densification rates were obtained by SPS technique and also the presence of HfO₂ phase in the HfB₂ powders facilitated the densification rate with respect to monolithic HfB₂ structure. Also, the microhardness, wear volume loss and mean friction coefficients values of sintered samples showed similar trends with densification rates.

In addition, the followings can be stated as suggestions for future work to carry the research further:

- i) Different sintering aids such as silicide compounds and other metallic agents in varying amounts can be investigated to provide the full densification of the bulk samples. Although there are some studies on the sintering of hafnium

diborides with some silicide compounds, they generally use commercial powders with rather coarser particle size, ii) Thermal oxidation resistance of sintered samples can be explored at high temperatures.



REFERENCES

- Ağaoğulları, D., Balcı, Ö., Öveçoğlu, M.L. and Duman, İ.** (2011). Synthesis of α - and β -rhombohedral boron powders via gas phase thermal dissociation of boron trichloride by hydrogen, *Metallurgical Materials Transaction B*, 42, 568-574.
- Ağaoğulları, D., Öveçoğlu, M.L. and Duman, İ.** (2012a). Synthesis of LaB_6 powders from La_2O_3 , B_2O_3 and Mg blends via a mechanochemical route, *Ceramics International*, 38, 6203–6214.
- Ağaoğulları, D., Balcı, Ö., Gökçe, H., Öveçoğlu, M.L. and Duman, İ.** (2012b). Synthesis of Magnesium Borates by Mechanically Activated Annealing, *Metallurgical Materials Transaction A*, 43, 2520–2523.
- Ağaoğulları, D.** (2014). *Synthesis, development and characterization of some rare-earth metal hexaboride powders and their sintered products. (Ph.D. dissertation)*, I.T.U., İstanbul, Turkey.
- Ağaoğulları, D., Balcı, Ö., Öveçoğlu, M.L., Suryanarayana, C. and Duman, İ.** (2015). Synthesis of bulk nanocrystalline samarium hexaboride, *Journal of European Ceramic Society*, 35, 4121–4136.
- Akçamlı, N., Ağaoğulları, D., Balcı, Ö. Öveçoğlu, M.L. and Duman, İ.** (2015). Synthesis of HfB_2 powders by mechanically activated borothermal reduction of HfCl_4 , *Ceramics International*, 42, 3797–3807.
- Akçamlı, N., Ağaoğulları, D., Balcı, Ö. Öveçoğlu, M.L. and Duman, İ.** (2016). Synthesis of triclinic and hexagonal SmBO_3 powders by mechanically activated annealing of Sm_2O_3 and B_2O_3 blends, *Ceramic International*, 42, 10045–10057.
- Akgün, B., Çamurlu, H.E., Topkaya, Y. and Sevinç, N.** (2011). Mechanochemical and volume combustion synthesis of ZrB_2 , *International Journal of Refractory Metals and Hard Materials*, 29, 601–607.
- Anselmi-Tamburini, U., Kodera, Y., Gasch, M, Unuvar, C., Munir, Z.A., Ohyanagi, M. and Johnson, S.M.** (2006). Synthesis and characterization of dense ultra-high temperature thermal protection materials produced by field activation through spark plasma sintering (SPS): I. Hafnium Diboride, *Journal of Materials Science*, 41, 3097–3104.
- Avvakumov, E., Senna, M. and Kosova, N.** (2001). *Soft Mechanochemical Synthesis*. Dordrecht, Netherlands: Kluwer Academic Publisher.
- Balaz, P.** (2008). *Mechanochemistry in Nanoscience and Minerals Engineering*. Kosice, Slovakia: Springer.

- Balaz, P., Achimovicova, M., Balaz, M., Billik, P., Cherkezova-Zheleva, Z., Criado, J. M. and Wieczorek-Ciurowa, K.** (2013). Hallmarks of mechanochemistry: from nanoparticles to technology, *Chemical Society Reviews*, 42, 7571–7637.
- Balci, Ö., Ağaoğulları, D. and Duman, İ.** (2010). The production of HfO₂-HfB₂ composite powder from HfO₂, B₂O₃ and Mg by solid state reaction and subsequent annealing, *Solid State Science and Technology*, 18, 91–98.
- Balci, Ö., Ağaoğulları, D., Öveçoğlu, M.L. and Duman, İ.** (2012). ZrB₂-ZrO₂ ceramic powders from ZrO₂-B₂O₃/B system by high energy ball milling and annealing assisted process, *Ceramics International*, 38, 2201–207.
- Balci, Ö.** (2015). *Fabrication of Vanadium and Niobium Borides via Milling-Assisted Solid State Synthesis Methods and Sintering Techniques.* (Ph.D. dissertation), I.T.U., İstanbul, Turkey.
- Balci, Ö., Ağaoğulları, D., Ovalı, D., Öveçoğlu, M.L. and Duman, İ.** (2015). In situ synthesis of NbB₂-NbC composite powders by milling-assisted carbothermal reduction of oxide raw materials, *Advanced Powder Technology*, 26, 1200–1209.
- Bargeron, C.B., Benson, R.C., Newman, R.W., Jette, A.N. and Phillips, T.E.** (1993). Oxidation Mechanisms of Hafnium Carbide and Hafnium Diboride in the Temperature Range 1400°C and 2100 °C, *Johns Hopkins APL Technical Digest*, 14, 29–36.
- Barraud, E., Begin-Colin, S. and Caer, G.L.** (2005). Nanorods of HfB₂ from mechanically-activated HfCl₄ and B-based powder mixtures, *Journal of Alloys Compounds*, 398, 208–218.
- Barraud, E., Begin-Colin, S., Caer, G.L., Villieras, F. and Barres, O.** (2006). Thermal decomposition of HfCl₄ as a function of its hydration state, *Journal of Solid State Chemistry*, 179, 1842–1851.
- Begin-Colin, S., Caer, G.L., Barraud, E. and Humbert, O.** (2004). Mechanically activated synthesis of ultrafine rods of HfB₂ and milling induced phase transformation of monocrystalline anatase particles, *Journal of Materials Science*, 39, 5081–5089.
- Bellosi, A., Monteverde, F. and Sciti, D.** (2006). Fast Densification of Ultra-High-Temperature Ceramics by Spark Plasma Sintering, *International Journal of Applied Ceramic Technology*, 3, 32–40.
- Berkowitz-Mattuck, J.B.** (1966). High-Temperature Oxidation III. Zirconium and Hafnium Diborides, *J. Electrochem. Soc.*, 113, 908–914.
- Bittermann, H. and Rogl, P.** (1997). Critical Assessment and Thermodynamic Calculation of the Ternary System Boron-Hafnium-Titanium (B-Hf-Ti), *Journal of Phase Equilibria*, 18, 24–47.
- Blum, Y.D., Marschall, J., Hui, D., Adair, B. and Vestel, M.** (2008). Hafnium Reactivity with Boron and Carbon Sources Under Non-Self Propagating High-Temperature Synthesis Conditions, *Journal of American Ceramics Society*, 91, 1481–1488.

- Boldyrev, V. V.** (1986). Mechanochemistry of inorganic solids, *Indian National Science Academy*, 52, 400-417.
- Boldyrev, V. V.** (2006). Mechanochemistry and mechanical activation of solids, *Russian Chemical Reviews*, 75(3), 177-189.
- Boldyrev, V. V. and Tkacova, K.** (2000). Mechanochemistry of solids: past, present and prospects, *Journal of Materials Synthesis and Processing*, 8, 121-132.
- Brochu, M., Gauntt, B., Zimmerly, T., Ayala, A. and Loehman, R.** (2008). Fabrication of UHTCs by Conversion of Dynamically Consolidated Zr+B and Hf+B Powder Mixtures, *Journal of American Ceramic Society*, 91, 2815-2822.
- Butyagin, P. Y.** (1984). Structural disorder and mechanochemical reactions in solids, *Uspekhi Khimii*, 53, 1769-1789.
- Cacciamani, G., Riani, P. and Valenza, F.** (2011). Equilibrium between MB₂ (M=Ti, Zr, Hf) UHTC and Ni: A thermodynamic database for the B–Hf–Ni–Ti–Zr system, *CALPHAD: Computer Coupling of Phase Diagrams and Thermochemistry*, 35, 601–619.
- Cai, P.J., Wang, H., Liu L.H. and Zhang L.** (2010). Low temperature synthesis of nanocrystalline Co₂B, *Journal of the Ceramic Society of Japan*, 118(11), 1102-1104.
- Cai, T., Qiu, W.F., Liu, D., Han, W.J., Ye, L., Zhao, A.J. and Zhao T.** (2013). Synthesis, Characterization, and Microstructure of Hafnium Boride-Based Composite Ceramics Via Pre ceramic Method, *Journal of American Ceramic Society*, 96, 1999–2004.
- Carney, C., Paul, A., Venugopal, S., Parthasarathy, T., Binner, J., Katz, A. and Brown, P.** (2014). Qualitative analysis of hafnium diboride based ultra high temperature ceramics under oxyacetylene torch testing at temperatures above 2100°C, *Journal of the European Ceramic Society*, 34, 1045–1051.
- Chakraborty, S., Debnath, D., Mallick, A.R. and Das, P.K.** (2014). Mechanical and thermal properties of hot pressed ZrB₂ system with TiB₂, *International Journal of Refractory Metals and Hard Materials*, 46, 35–42.
- Cheminant, P., Deschanel, X., Boulanger, L. and Thorel, A.** (1997). Microstructural damage in hafnium diboride under neutron irradiation, *Key Engineering Materials*, 132-136, 643–646.
- Cheminant-Coatanlem, P., Boulanger, L., Deschanel, X. and Thorel, A.** (1998). Microstructure and nanohardness of hafnium diboride after ion irradiations, *Journal of Nuclear Materials*, 256, 180–188.
- Chen, L., Gu, Y., Shi, L., Yang, Z., Ma J. and Qian Y.** (2004a). A reduction – boronation route to nanocrystalline titanium diboride, *Solid State Communications*, 130, 231–233.
- Chen, L., Gu, Y., Yang, Z., Shi, L., Ma J. and Qian, Y.** (2004b). Preparation and some properties of nanocrystalline ZrB₂ powders, *Scripta Materialia*, 50, 959–961.

- Chen, L., Gu, Y., Shi, L., Yang, Z., Ma, J. and Qian, Y.** (2004c). Synthesis and oxidation of nanocrystalline HfB₂, *Journal of Alloys and Compounds*, 368, 353-356.
- Chen, B., Yang, L., Heng, H., Chen, J., Zhang, L., Xu, L., Qian, Y. and Yang, J.** (2012). Additive-assisted synthesis of boride, carbide, and nitride micro/nanocrystals, *Journal of Solid State Chemistry*, 194, 219–224.
- Chowdhury, S., Polychronopoulou, K., Cloud, A., Abelson, J.R. and Polycarpou, A.A.** (2015). Nanomechanical and nanotribological behaviors of hafnium boride thin films, *Thin Solid Films*, 595, 84–91.
- Cutler, R.A.** (1991). Engineering Properties of Borides, In S. J. Schneider (Ed.), *Ceramics and Glasses: Engineered Materials Handbook*, Vol. 4, (pp. 787–803), ASM International, Materials Park, OH.
- Demazeau, G.** (2008a). Solvothermal processes: new trends in Materials Chemistry, *Journal of Physics.: Conference Series*, 121, 1-5.
- Demazeau, G.** (2008b). Solvothermal reactions: an original route for the synthesis of novel materials, *Journal of Materials Science*, 43, 2104-2114.
- Demazeau, G.** (2010). Solvothermal Processes: Definition, Key Factors Governing the Involved Chemical Reactions and New Trends, *Z. Naturforsch*, 65, 999–1006.
- Delogu, F. and Mulas, G.** (2010). Kinetic processes and mechanism of mechanical alloying, In M. Sopicka-Lizer (Ed.), *High-energy Ball Milling: Mechanochemical Processing of Nanopowders* (pp.92–100). Cambridge, UK: Woodhead Publishing Limited, CRC.
- El-Eskandarany, M. S.** (2001). *Mechanical Alloying for Fabrication of Advanced Engineering Materials*. Norwich, N.Y: Noyes Publications.
- Fahrenholtz, W.G., Hilmas, G.E., Talmy, I.G. and Zaykoski, J.A.** (2007). Refractory diborides of zirconium and hafnium, *Journal of American Ceramics Society*, 90, 1347–1364.
- Fahrenholtz, W.G.** (2014). A Historical Perspective on research related to ultrahigh temperature ceramics, In Fahrenholtz, W.G., Wuchina, E.J., Lee, W.E. and Zhou, Y (Ed.), *Ultra-High Temperature Ceramics: Materials for Extreme Environment Applications*, (pp. 6–32). US, John Wiley & Sons, Inc.
- Fahrenholtz, W.G., Wuchina, E.J., Lee, W.E. and Zhou, Y.** (2014). Introduction, In Fahrenholtz, W.G., Wuchina, E.J., Lee, W.E. and Zhou, Y (Ed.), *Ultra-High Temperature Ceramics: Materials for Extreme Environment Applications*, (pp. 1–5). US, John Wiley & Sons, Inc.
- Fang, Z. and Dixon, D.A.** (2013). Hydrolysis of ZrCl₄ and HfCl₄: The initial steps in the high-temperature oxidation of metal chlorides to produce ZrO₂ and HfO₂, *Journal of Physical Chemistry C*, 117, 7459–7474.
- Feng, X., Bai Y.J., Lu, B., Zhao, Yang, J. and Chi, J.R.** (2004). Synthesis of nanocrystalline Ni₂B via a solvo-thermal route, *Inorganic Chemistry Communications*, 7, 189–191.

- Feng, S. and Li, G.** (2011). Hydrothermal and Solvothermal Syntheses, In R. R. Xu, W. Q. Pang, Q. S. Huo (Ed.), *Modern Inorganic Synthetic Chemistry*, (pp. 63–95). Amsterdam, Netherlands:Elsevier.
- Feng, S. and Xu, R.** (2001). New Materials in Hydrothermal Synthesis, *Accounts of Chemical Research*, 34, 239–247.
- Fuller, J. and Sacks, M.D.** (2004). Special section on Ultra-High Temperature Ceramics (UHTC), *Journal of Materials Science*, 39, 5885–6066.
- Gasch, M.J., Ellerby, D.T. and Johnson, S.M.** (2004). *Handbook of Ceramic Composites*, New York: Springer.
- Ghosh, D. and Subhash, G.** (2013). *Recent Progress in Zr(Hf)B₂ Based Ultrahigh Temperature Ceramics*, In S. Somiya (Ed.), *Handbook of Advanced Ceramics*, (pp. 267-299). Elsevier Inc.
- Gilman, P. S. and Benjamin, J. S.** (1983). Mechanical alloying, *Annual Review of Materials Science*, 13, 279–300.
- Golla, B.R. and Basu, B.** (2014). Spark Plasma Sintering of Nanoceramic Composites, *Comprehensive Hard Materials*, 2, 177–205.
- Gösset, D. and Kryger, B.** (1993). Advances in control assembly materials for water reactors Proceedings of a Technical Committee meeting, held in Vienna, 29 November-2 December 1993, *Boron and hafnium base absorbers for advanced pwr control rods*, Commissariat à l' énergie atomique, CEN Saclay, Gif-sur-Yvette, France.
- Guo, J., Li, J. and Kou, H.** (2011). Chemical Preparation of Advanced Ceramic Materials, In R. R. Xu, W. Q. Pang, Q. S. Huo (Ed.), *Modern Inorganic Synthetic Chemistry*, (pp. 429–454). Amsterdam, Netherlands:Elsevier.
- Guo, S., Ping, D.H. and Kagawa, Y.** (2012a). Synthesis of zirconium diboride platelets from mechanically activated ZrCl₄ and B powder mixture, *Ceramics International*, 38, 5195–5200.
- Guo, W.M., Yang, Z.G. and Zhang, G.J.** (2012b). Synthesis of submicrometer HfB₂ powder and its densification, *Materials Letters*, 83, 52–55.
- Guo, S., Naito, K. and Kagawa, Y.** (2013). Mechanical and physical behaviors of short pitch-based carbon fiber-reinforced HfB₂-SiC matrix composites, *Ceramics International*, 39, 1567–1574.
- Gutman, E. M.** (1998). *Mechanochemistry of Materials*. Cambridge, UK: Cambridge International Publishing.
- Jayaraman, S., Yang, Y., Kim, D.Y., Girolami, G.S. and Abelson, J.R.** (2005). Hafnium diboride thin films by chemical vapor deposition from a single source precursor, *Journal of Vacuum Science and Technology A*, 23, 1619–1625.
- Jayaraman, S., Gerbi, J.E., Yang, Y., Kim, D.Y., Chatterjee, A., Bellon, P., Girolami, G.S., Chevalier, J.P. and Abelson, J.R.** (2006). HfB₂ and Hf-B-N hard coatings by chemical vapor deposition, *Surface Coatings Technology*, 200, 6629–6633.

- Jung, S.H., Oh H.C., Kim, J.H., Choi, S.C., Lee, S.H. and Kim, H.D.** (2013). Pretreatment of zirconium diboride powder to improve densification, *Journal of Alloys and Compounds*, 548, 173–179.
- Juretschke, H.J. and Steinitz, R.** (1958). Hall effect and electrical conductivity of transition-metal diborides, *Journal of Physics and Chemistry of Solids*, 4, 118–127.
- Kobayashi, H., Shimosaka, K. and Mitamura, T.** (1993). Preparation and formation process of HfB₂ fine powders by Mg-thermite method, *Journal of Ceramics Society of Japan*, 101, 446–450.
- Kravchenko, S.E., Burlakova, A.G., Korobov, I.I., Shulga, Y.M., Dremova, N.N., Volkova, L.S., Kalinnikov, G.V., Shilkin, S.P. and Andrievskii R.A.** (2015). Preparation of Hafnium Diboride Nanopowders in an Anhydrous Na₂B₄O₇ Ionic Melt, *Inorganic Materials*, 51, 380–383.
- Kuznetsov, S.A.** (2012). Electrodeposition of hafnium and hafnium-based coatings in molten salts, *Chemical Papers*, 66, 511–518.
- Levine, S.R., Opila, E.J., Halbig, M.C., Kiser, J.D., Singhd, M. and Salem, J.A.** (2002). Evaluation of ultra-high temperature ceramics for aeropropulsion use, *Journal of the European Ceramic Society*, 22, 275–2767.
- Levitas, V. I.** (2004). Continuum mechanical fundamentals of mechanochemistry, In V. Domnich, Y. Gogotsi (Eds.), *High Pressure Surface Science and Engineering* (pp.161-292). Bristol, UK: Institute of Physics, IOP Publishing Ltd.
- Li, W., Zhang, X., Hong, C., Han, W. and Han, J.** (2009). Preparation, microstructure and mechanical properties of ZrB₂-ZrO₂ ceramics, *Journal of the European Ceramic Society*, 29, 779–786.
- Licheri, R., Orru, R., Musa, C., Locci, A.M. and Cao, G.** (2009). Consolidation via spark plasma sintering of HfB₂/SiC and HfB₂/HfC/SiC composite powders obtained by self-propagating high-temperature synthesis, *Journal of Alloys and Compounds*, 478, 572–578.
- Liu, Y., Li, Q. and Fan S.** (2003). Self-catalytic growth of aluminum borate nanowires, *Chemical Physics Letters*, 375, 632-635.
- Lok, J.Y., Logan, K.V. and Payyapilly J.J.** (2009). Acid Leaching of SHS Produced Magnesium Oxide/Titanium Diboride, *Journal of the American Ceramic Society*, 92(1), 26–31.
- Ma, J., Gu, Y., Shi, L., Chen, L., Yang, Z. and Qian, Y.** (2003). Reduction-boronation route to chromium boride (CrB) nanorods, *Chemical Physics Letters*, 381, 194–198.
- Ma, D., Liu, H., Yang, H., Fu, W., Zhang, Y., Yuan, M., Sun, P. and Zhou, X.** (2009). High pressure hydrothermal synthesis of cuprous oxide microstructures of novel morphologies, *Materials Chemistry and Physics*, 116, 458–463.

- Makarenko, G.N., Krushinskaya, L.A., Timofeeva, I.I., Matsera, V.E., Vasil'kovskaya, M.A. and Uvarova, I.V.** (2015) Formation of diborides of groups IV-VI Transition metals during mechanochemical synthesis, *Powder Metallurgy and Metal Ceramics*, 53, 514-521.
- Mallik, M., Kailath, A.J., Ray, K.K. and Mitra, R.** (2012). Electrical and thermophysical properties of ZrB₂ and HfB₂ based composites, *Journal of the European Ceramic Society*, 32, 2545-2555.
- Massalski, T.B.** (1990). *Binary alloy phase diagrams*. Materials Park, OH: ASM International.
- McCormick, P. G. and Froes, F. H.** (1998). The fundamentals of mechanochemical processing, The Member of The Minerals, *Metals and Materials Society*, 50, 61-65.
- Mishra, S.K., Das, S.K., Ray, A.K. and Ramachandrarao, P.** (2002). Effect of Fe and Cr Addition on the Sintering Behavior of ZrB₂ Produced by Self-Propagating High-Temperature Synthesis, *Journal of the American Ceramic Society*, 85, 2846-2848.
- Monteverde, F.** (2007). Ultra-high temperature HfB₂-SiC ceramics consolidated by hot-pressing and spark plasma sintering, *Journal of Alloys and Compounds*, 428, 197-205.
- Monteverde, F. and Bellosi, A.** (2005). The resistance to oxidation of an HfB₂-SiC composite, *Journal of European Ceramic Society*, 25, 102-1031.
- Monteverde, F.** (2008). Hot pressing of hafnium diboride aided by different sinter additives, *Journal of Materials Science*, 43, 1002-1007.
- Monteverde, F., Bellosi, A. and Scatteia, L.** (2008). Processing and properties of ultra-high temperature ceramics for space applications, *Materials Science and Engineering A*, 485, 415-421.
- Moon, O.M., Kang, B.C., Lee, S.B. and Boo, J.H.** (2004). Temperature effect on structural properties of boron oxide thin films deposited by MOCVD method, *Thin Solid Films*, 464-465, 164-169.
- Morris, M.A. and Morris, D.G.** (1991). Ball-milling of elemental powders-compound formation and/or amorphization, *Journal of Materials Science*, 26, 4687-4696.
- Motojima, S., Funahashi, K. and Kurosawa, K.** (1990). ZrB₂ coated on copper plate by chemical vapor deposition, and its corrosion and oxidation stabilities, *Thin Solid Films*, 189, 73-79.
- Murty, B.S. and Ranganathan, S.** (1998). Novel materials synthesis by mechanical alloying-milling, *International Materials Reviews*, 43, 101-41.
- Musa, C., Orru, R., Sciti, D., Silvestroni, L. and Cao, G.** (2013). Synthesis, consolidation and characterization of monolithic and SiC whiskers reinforced HfB₂ ceramics, *Journal of European Ceramic Society*, 33, 603-614.
- Nasseri, M.M.** (2015) The Investigation of Neutron Interactions with HfB₂ -A Simulation Study, *Transactions of the Indian Ceramic Society*, 74, 177-180.

- Nguyen, Q.N., Opila, E.J. and Robinson, R.C.** (2004). Oxidation of Ultrahigh Temperature Ceramics in Water Vapor, *Journal of Electrochemical Society*, 151, 558-562.
- Ni, D.W., Zhang, G.J., Kan, Y.M. and Wang, P.L.** (2008). Synthesis of monodispersed fine hafnium diboride powders using carbo/borothermal reduction of hafnium dioxide, *Journal of European Ceramic Society*, 91, 2709–2712.
- Ni, D.W., Zhang, G.J., Kan, Y.M. and Wang, P.L.** (2010). Hot pressed HfB₂ and HfB₂-20 vol.% SiC ceramics based on HfB₂ powder synthesized by borothermal reduction of HfO₂, *International Journal of Applied Ceramics Technology*, 7, 830-836.
- Ni, D.W., Liu, J.X. and Zhang, G.J.** (2012a). Microstructure refinement and mechanical properties improvement of HfB₂-SiC composites with the incorporation of HfC, *Journal of European Ceramic Society*, 32, 2557-2563.
- Ni, D.W., Liu, J.X. and Zhang, G.J.** (2012b). Pressureless sintering of HfB₂-SiC ceramics doped with WC, *Journal of European Ceramic Society*, 32, 3627–3635.
- Okamoto, N.L., Kusakari, M., Tanaka, K., Inui, H. and Otani, S.** (2010). Anisotropic elastic constants and thermal expansivities in monocrystal CrB₂, TiB₂, and ZrB₂, *Acta Materialia*, 58, 76–84.
- Opeka, M., Talmy, I. G., Wuchina, E. J., Zaykoski, J. A. and Causey, S.J.** (1999). Mechanical, thermal and oxidation properties of refractory hafnium and zirconium, *Journal of European Ceramic Society*, 19, 2405–2414.
- Opeka, M.M., Talmy, I.G. and Zaykoski, J.A.** (2004). Oxidation-Based Materials Selection for 2000°C+Hypersonic Aerosurfaces: Theoretical Considerations and Historical Experience, *Journal of Materials Science*, 39, 5887–5904.
- Otani, S., Korsukova, M.M. and Mitsuhashi, T.** (1998). Preparation of HfB₂ and ZrB₂ single crystals by the floating-zone method, *Journal of Crystal Growth*, 186, 582–586.
- Öveçoğlu, M. L.** (1987). *Development of a dispersion strengthened Al-Fe-Ce alloy by mechanical alloying and related theoretical modeling of dislocations in composite materials. (Ph.D. dissertation)*. Stanford University, San Francisco.
- Pastor, H.** (1977). XIV. Metallic Borides: Preparation of Solid Bodies - Sintering Methods and Properties of Solid Bodies. In V.I. Matkovich (Ed.), *Boron and Refractory Borides* (pp. 457–493). Berlin, Germany: Springer-Verlag.
- Peshev, P. and Bliznakov, G.** (1968). On the borothermic preparation of titanium, zirconium and hafnium diborides, *Journal of Less Common Metals*, 14, 23–32.

- Portehault, D., Devi S., Beaunier, P., Gervais, C., Giordano, C., Sanchez, C. and Antonietti, M.** (2011). A General Solution Route toward Metal Boride Nanocrystals, *Angewandte Chemie International Edition*, 50, 3262–3265.
- Post, B., Glaser, F.W. and Moskowitz, D.** (1954). Transition metal diborides, *Acta Metallurgica*, 2, 20–25.
- Putkonen, M. and Niinisto, L.** (2006). Atomic layer deposition of B₂O₃ thin films at room temperature, *Thin Solid Films*, 514, 145–149.
- Ran, S., Biest, O.V. and Vleugels, J.** (2010). ZrB₂ Powders synthesis by borothermal reduction, *Journal of European Ceramic Society*, 93, 1586–1590.
- Rhodes, W.H., Clougherty, E.V. and Kalish, D.** (1970). Research and Development of Refractory Oxidation-Resistant Diborides, Part II, Volume IV. Mechanical Properties, Technical Report.
- Ricceri, R. and Matteazzi, P.** (2004). A Fast and Low-Cost Room Temperature Process for TiB₂ Formation by Mechanochemistry, *Materials Science and Engineering: A*, 379, 341–346.
- Saito, N., Ikeda, H., Yamaoka, Y., Glaeser, A.M. and Nakashima, K.J.** (2012). Wettability and transient liquid phase bonding of hafnium diboride composite with Ni–Nb alloys, *Journal of Materials Science*, 47, 8454–8463.
- Samad, A.A. Lugscheider, E., Bobzin, K. and Maes, M.** (2004). Thermal Spray 2004: Advances in Technology and Application, *Proceedings of the International Thermal Spray Conference*, (pp.903–907), Osaka: Book News, Inc., January 1-4.
- Samsonov, G.V.B., Kovenskaya, A. and Serebryakova T.I.** (1971). Some physical characteristics of the diborides of transition metals of groups IV and V., *Russian Physics Journal*, 14, 11–4.
- Savino, R., Fumo, M.S., Silvestroni, L. and Sciti, D.** (2008). Arc-jet testing on HfB₂ and HfC-based ultra-high temperature ceramic materials, *Journal of European Ceramic Society*, 28, 1899–1907.
- Schwab, S.T., Stewart, C.A., Dudeck, K.W., Kozmina, S.M., Katz, J.D., Bartram, B., Wuchina, E.J., Kroenke, W.J. and Courtin, G.** (2004). Polymeric Precursors to Refractory Diborides, *Journal of Materials Science*, 39, 6051–6055.
- Sciti, D., Silvestroni, L. and Nygren, M.** (2008). Spark plasma sintering of Zr- and Hf-borides with decreasing amounts of MoSi₂ as sintering aid, *Journal of the European Ceramic Society*, 28, 1287–1296.
- Sichkar, S.M. and Antonov, V.N.** (2013). Electronic structure, phonon spectra and electron-phonon interaction in HfB₂, *Low Temperature Physics*, 39, 1–9.
- Silvestroni, L. and Sciti, D.** (2007). Effects of MoSi₂ additions on the properties of Hf- and Zr–B₂ composites produced by pressureless sintering, *Scripta Materialia*, 57, 165–168.

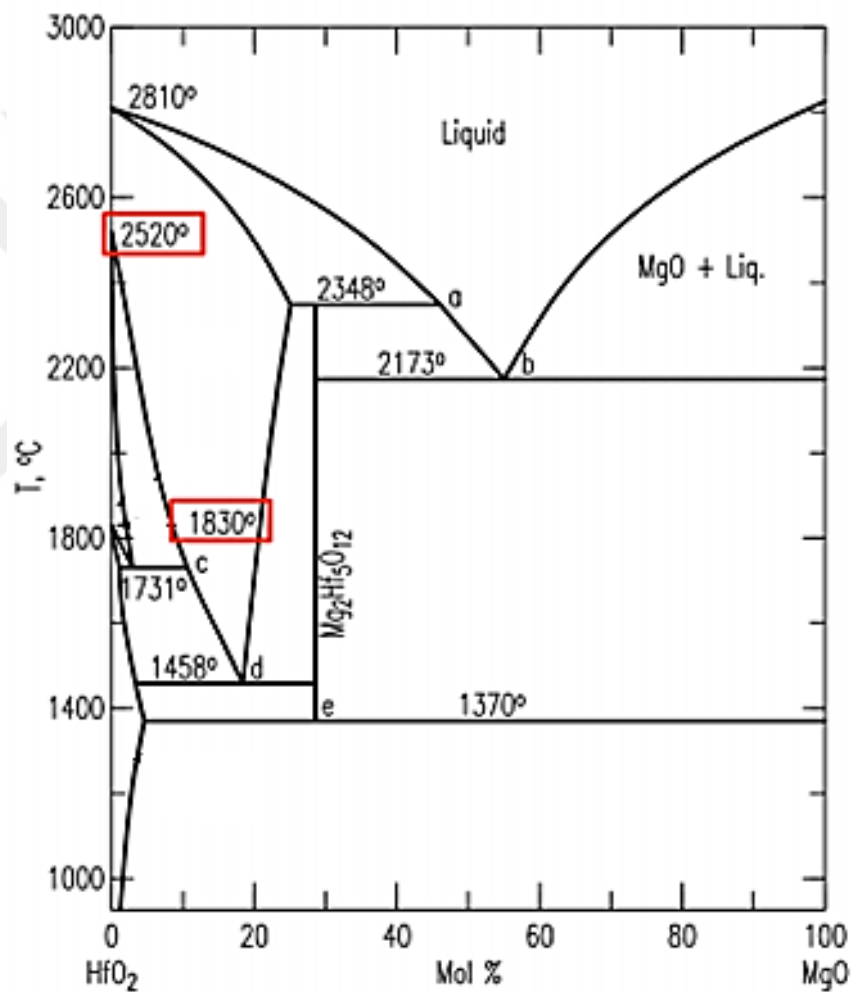
- Simeone, D., Hablot, O., Micalet, V., Bellon, P. and Serruys, Y.** (1997). Contribution of recoil atoms to irradiation damage in absorber materials, *Journal of Nuclear Materials*, 246, 206–214.
- Simonenko, E.P., Sevast'yanov, D.V., Simonenko, N.P., Sevast'yanov, V.G. and Kuznetsov, N.T.** (2013). Promising ultra-high-temperature ceramic materials for aerospace applications, *Russian Journal of Inorganic Chemistry*, 58, 1669–1693.
- Sonber, J.K., Murthy, T.S.R.Ch., Subramanian, C., Sunil, K., Fotedar, R.K. and Suri, A.K.** (2010). Investigations on synthesis of HfB₂ and development of a new composite with TiSi₂, *International Journal of Refractory Metals and Hard Materials*, 28, 201–210.
- Sonber, J.K. and Suri, A.K.** (2011). Synthesis and consolidation of zirconium diboride: review, *Advances in Applied Ceramics*, 110, 321–333.
- Soni, P.** (2001). *Mechanical Alloying: Fundamentals and Applications*. Cambridge, UK: Cambridge International Science Publishing.
- Sopicka-Lizer, M.** (2010). Introduction to mechanochemical processing, In M. Sopicka-Lizer (Ed.), *High-energy Ball Milling: Mechanochemical Processing of Nanopowders*, (pp.1–5). Cambridge, UK: Woodhead Publishing Limited, CRC.
- Suryanarayana, C.** (2001). Mechanical alloying and milling, *Progress in Materials and Science*, 46, 1-184.
- Suryanarayana, C.** (2004). *Mechanical Alloying and Milling*, Marcel Dekker, Inc., New York, USA.
- Suryanarayana, C. and Norton, M.G.** (1998). *X-Ray Diffraction: A Practical Approach*. New York, USA: Plenum Press.
- Suryanarayana, C., Ivanov, E. and Boldyrev, V.V.** (2001). The science and technology of mechanical alloying, *Materials Science and Engineering A*, 304-306, 151–158.
- Takacs, L.** (2002). Self-sustaining reactions induced by ball milling, *Progress in Materials Science*, 47, 355–414.
- Tayebi, N., Yanguas-Gil, A., Kumar, N., Zhang, Y., Abelson, J.R., Nishi, Y., Ma, Q. and Rao, V.R.** (2012). Hard HfB₂ tip-coatings for ultrahigh density probe-based storage, *Applied Physics Letters*, 101, 091909, 1–5.
- Telle, R., Sigl, L.S. and Takagi, K.** (2000). Handbook of Ceramic Hard Materials, In Riedel, R., (Ed.), *Boride-Based Hard Materials*, (pp.802–945), Weinheim, Germany: Wiley-VCH.
- Tripp W.C. and Graham, H.C.** (1971). Thermogravimetric Study of the Oxidation of ZrB₂ in the Temperature Range of 800 to 1500 °C, *Journal of Electrochemical Society*, 118, 1195–1199.
- Upadhy, K., Yang, J.M. and Hoffman, W.P.** (1997). Materials for ultrahigh temperature structural applications, *American Ceramics Society Bulletin*, 76, 51–56.

- Url-1** <<http://ceramics.org/wp-content/uploads/2011/08/applications-uhtc-johnson.pdf>>, date retrieved: 05.02.2016.
- Url-2** <<http://pubs.rsc.org/en/content/articlelanding/2014/cs/c3cs60219b#!divAbstract>>, date retrieved: 05.02.2016.
- Venugopal, S., Boakye, E.E., Paul, A., Keller, K., Mogilevsky, P., Vaidhyanathan, B., Binner, J.G.P., Katz, A. and Brown, P.M.** (2013). Sol–gel synthesis and formation mechanism of ultra-high temperature ceramic: HfB₂, *Journal of American Ceramic Society*, 97, 1–8.
- Venugopal, S., Paul, A., Vaidhyanathan, B., Binner, J.G.P., Heaton, A. and Brown, P.M.** (2014). Synthesis and spark plasma sintering of sub-micron HfB₂: Effect of various carbon sources, *Journal of the European Ceramic Society*, 34, 1471–1479.
- Wang, C.R., Yang, J.M. and Hoffman, W.P.** (2002). Thermal stability of refractory carbide/boride composites, *Materials Chemistry and Physics*, 74, 272-281.
- Wang, Q., Pan, D., Jiang, S., Ji, X., An, L. and Jiang, B.** (2006). A solvothermal route to size- and shape-controlled CdSe and CdTe nanocrystals, *Journal of Crystal Growth*, 286, 83–90.
- Wang, H., Lee, S.H. and Kim, H.D.** (2012). Nano-Hafnium Diboride Powders Synthesized Using a Spark Plasma Sintering Apparatus, *Journal of American Ceramic Society*, 95, 1493–1496.
- Wang, H., Lee, S.H. and Feng, L.** (2014a). HfB₂–SiC composite prepared by reactive spark plasma sintering, *Ceramics International*, 40, 11009–11013.
- Wang, H., Lee, S.H., Kim, H.D. and Oh, H.C.** (2014b). Synthesis of ultrafine hafnium diboride powders using solution-based processing and spark plasma sintering, *International Journal of Applied Ceramic Technology*, 11, 359–363.
- Wang, Y., Feng, J., Feng, B., Song, X. and Cao, J.** (2015). Anisotropic growth of Ni₃(BO₃)₂ nanowhiskers on nickel substrates and its application in the fabrication of superhydrophilic surfaces, *RSC Advances*, 5, 28950–28957.
- Weimer, A. W.** (1977). Carbide, Nitride and Boride Materials Synthesis and Processing. London, UK: Chapman & Hall.
- Weng, L., Zhang, X., Han, J., Han, W. and Hong, C.** (2009). The effect of B₄C on microstructure and thermo-mechanical properties of HfB₂-based ceramics. *Journal of Alloys and Compounds*, 473, 314–318.
- Wieczorek-Ciurawa, K.** (2010). Mechanochemical synthesis of metallic-ceramic composite powders, In M. Sopicka-Lizer (Ed.), *High-energy Ball Milling: Mechanochemical Processing of Nanopowders* (pp. 193–223). Cambridge, UK: Woodhead Publishing Limited, CRC.

- Wieczorek-Ciurowa, K., Oleszak, D. and Gamrat, K.** (2007). Mechanosynthesis and process characterization of some nanostructured intermetallics/ceramics composites, *Journal of Alloys Compounds*, 434-435, 501–504.
- Williams D.F.** (2006). Assessment of candidate molten salt coolants for the NGNP/NHI heat-transfer loop, Retrieved November 12, 2015 from <http://web.ornl.gov/~webworks/cppr/y2006/rpt/124838.pdf>.
- Wu, K. and Jin, Z.** (1997). Thermodynamic assessment of the HfO₂-MgO system, *Calphad: Computer Coupling of Phase Diagrams and Thermochemistry*, 21(3), 411–420.
- Wu, W.W., Zhang, G.J. and Sakka, Y.** (2013). Nanocrystalline ZrB₂ powders prepared by mechanical alloying, *Journal of Asian Ceramic Societies*, 1, 304–307.
- Xie, R.C. and Shang, J.K.** (2007). Morphological control in solvothermal synthesis of titanium oxide, *Journal of Materials Science*, 42, 6583–6589.
- Yang, Y., Jayaraman, S., Kim, D.Y., Girolami, G.S. and Abelson, J.R.** (2006). Crystalline texture in hafnium diboride thin films grown by chemical vapor deposition, *Journal of Crystal Growth*, 294, 389–395.
- Yang, J., Zeng, J., Yu, S.H., Yang, L., Zhang, Y.H. and Qian, Y.T.** (2000). Pressure-Controlled Fabrication of Stibnite Nanorods by the Solvothermal Decomposition of a Simple Single-Source Precursor, *Chemistry of Materials*, 12, 2924–2929.
- Zapata-Solvas, E., Jayaseelan, D.D., Brown, P.M. and Lee, W.E.** (2013). Thermal properties of La₂O₃-doped ZrB₂- and HfB₂-based ultra-high temperature ceramics, *Journal of the European Ceramic Society*, 33, 3467–3472.
- Zhang, D.L.** (2004). Processing of advanced materials using high-energy mechanical milling, *Progress in Materials Science*, 49, 537–560.
- Zhang, G.J., Guo, W.M., Ni, D.W. and Kan, Y.M.** (2009). Ultrahigh temperature ceramics (UHTCs) based on ZrB₂ and HfB₂ systems: powder synthesis, densification and mechanical properties, *Journal of Physics Conference Series*, 176, 1–12.
- Zhang, M., Yuan, L., Wang, X., Fan, H., Wang, X., Wu, X., Wang, H. and Qian, Y.** (2008). A low-temperature route for the synthesis of nanocrystalline LaB₆, *Journal of Solid State Chemistry*, 181, 294–297.
- Zhou, Y., Wang, J., Li, Z., Zhan, X. and Wang, J.** (2014). First-Principles investigation on the chemical bonding and intrinsic elastic Properties of transition metal diborides TmB₂ (TM=Zr, Hf, Nb, Ta, and Y), In *Fahrenholtz, W.G., Wuchina, E.J., Lee, W.E. and Zhou, Y. (Ed.), Ultra-High Temperature Ceramics: Materials for Extreme Environment Applications*, (pp. 60–82). US, John Wiley & Sons, Inc.
- Zou, J., Zhang, G.J. and Kan Y.M.** (2010). Pressureless densification and mechanical properties of hafnium diboride doped with B₄C: From solid state sintering to liquid phase sintering, *Journal of the European Ceramic Society*, 30, 2699–2705.

APPENDICES

APPENDIX A: The binary phase diagram of $\text{HfO}_2\text{-MgO}$ showing both the transformation temperatures of HfO_2 and the formation of $\text{Mg}_2\text{Hf}_5\text{O}_{12}$ adapted from Wu and Jin, 1997.





CURRICULUM VITAE



Name Surname : Nazlı AKÇAMLI
Place and Date of Birth : İstanbul, 02.05.1982
E-Mail : nzakcamli@hotmail.com

EDUCATION

- **B.Sc.** : 2004, Istanbul University, Faculty of Engineering, Department of Chemical Engineering.
: 2005, Istanbul University, Faculty of Engineering, Department of Metallurgical and Materials Engineering.
- **M.Sc.** : 2009, Istanbul University, Department of Metallurgical and Materials Engineering.

PROFESSIONAL EXPERIENCE AND REWARDS:

- 28.01.2015-07.02.2016, Research Assistant, Bursa Technical University, Faculty of Natural Sciences, Architecture and Engineering, Department of Metallurgical and Materials Engineering.
- 2015-2016, Project Researcher, Bursa Technical University, BAP Project.
- 2014-2015, Project Scholarship, The Scientific and Technological Research Council of Turkey, TÜBİTAK.
- 2013-2015, Project Scholarship, National Boron Research Institute, BOREN, Turkey.
- 2005-2012, Research and Development Engineer, Goldaş Kuyumculuk San. İth. İhr. A.Ş..

PUBLICATIONS, PRESENTATIONS AND PATENTS ON THE THESIS:

- **Akçamlı, N., Ağaoğulları, D., Balcı, Ö., Öveçoğlu, M.L., Duman, İ., 2015.** Synthesis of HfB₂ powders by mechanically activated borothermal reduction of HfCl₄, *Ceramics International*, 42, 3797-3807.
- **Akçamlı, N., Ağaoğulları, D., Balcı, Ö., Duman, İ., Öveçoğlu, M.L., 2014.** Mechanochemically assisted synthesis of HfB₂ from HfCl₄ and B powder blend, 3rd International Conference on Recent Trends in Structural Materials, COMAT 2014, November 19-21, 2014, Plzen, Czech Republic.
- **Akçamlı N., Ağaoğulları D., Balcı, Ö., Duman, İ., Öveçoğlu, M.L., 2014.** Mechanochemical Synthesis of HfB₂-HfO₂ Ceramic Powders from HfCl₄-B₂O₃-Mg System, 3th International Ceramic Glass Porcelain Enamel Glaze and Pigment Congress, SERES 2014, October 15-17, 2014, Eskişehir, Turkey.

OTHER PUBLICATIONS, PRESENTATIONS AND PATENTS:

International Articles (SCI, SCIE)

- **Akçamlı, N., Ağaoğulları, D., Balcı, Ö. Öveçoğlu, M.L., Duman, I. (2016).** Synthesis of triclinic and hexagonal SmBO₃ powders by mechanically activated annealing of Sm₂O₃ and B₂O₃ blends, *Ceramics International*, 42, 10045–10057.

Other International Articles

- **Akçamlı, N. and Oktay, E., 2012.** Ag-Cu ve Ag-Cu-Ge Alaşımlarının Mekanik ve Mikroyapısal Özellikleri, 15th International Metallurgy & Materials Congress (IMMC'16), September 13-15, 2012, İstanbul, Turkey. [IMMC'16-2012 Abstracts Book, Metallurgy of Non-ferrous Metals, 761-766].
- **Akçamlı, N. and Oktay, E., 2010.** Germanyumun Gümüşün Mikroyapı ve Mekanik Özelliklerine Etkisi”, 15th International Metallurgy & Materials Congress (IMMC'15), November 11-13, 2010, İstanbul, Turkey. [IMMC'15-2010 Abstracts Book, Metallurgy of Non-ferrous Metals, 1150-1157].

International Conference Papers

- **Akçamlı, N., Gökçe, H., Kalemtaş, A., Uzunsoy, D., 2015.** The effect of graphene nanoplatelets (GNPs) addition on the microstructural and mechanical properties of aluminum, 2nd Graphene and Related Technologies: from Laboratory to Industry, October 15-16, 2015, İstanbul, Turkey.
- **Kırmızı, K., Akçamlı, N., Uzunsoy, D. 2015.** Fabrication and Characterization of Aluminum-Graphene Nano Platelets (GNP) Composites, ICNES (International Congress on Natural and Engineering Science), September 09-13, 2015, Sarajevo.

- Ađaođulları, D., **Akçamlı, N.**, Balcı, Ö., Duman, İ., Öveçođlu, M.L., 2014. Preparation of samarium borate powders via mechanically activated annealing, 3rd International Conference on Recent Trends in Structural Materials, COMAT 2014, November 19-21, 2014, Plzen, Czech Republic.
- Ađaođulları, D., Balcı, Ö., **Akçamlı, N.**, Duman, İ., Öveçođlu M.L., 2014. The Effect of Reaction Temperature on the Synthesis of Elemental Boron Powders, 17th International Metallurgy and Materials Congress, IMMC 2014, September 11-13, 2014, İstanbul, Turkey.
- **Akçamlı, N.**, Balcı, Ö., Ađaođulları, D., Duman, İ., Öveçođlu, M.L., 2014. Thermodynamical Interpretations and Experimental Studies on the Formation of Amorphous Boron Powders via CVD Method using various H₂ Flow Rates, International Conference on Structural Nano Composites, NANOSTRUC 2014, May 20-21, 2014, Madrid, Spain.
- **Akçamlı, N.**, Oktay, E., 2012. Ag-Cu ve Ag-Cu-Ge Alařımlarının Mekanik ve Mikroyapısal Özellikleri, 16th International Metallurgy & Materials Congress (IMMC'16), September 13-15, 2012, İstanbul, Turkey.
- **Akçamlı, N.**, Oktay E., 2010. Germanyumun Gümüřün Mikroyapı ve Mekanik Özelliklerine Etkisi", 15th International Metallurgy & Materials Congress (IMMC'15), November 11-13, 2010, İstanbul, Turkey.

